Author:
Ingram, Stephen T

Title:
Causes, Magnitudes and Atmospheric Implications of Kinetically Limited Diffusion in Organic Aerosol

Causes, Magnitudes and Atmospheric Implications of Kinetically Limited Diffusion in Organic Aerosol

Stephen Ingram

October 29, 2019

A dissertation submitted to the University of Bristol in Accordance with the Requirements for award of the degree of Doctor of Philosophy in the Faculty of Science.

School of Chemistry

Words: 72,600

Abstract

In order for a molecule to evaporate from an aerosol particle, first it must diffuse to the surface. Similarly, once a molecule has condensed onto a droplet, it is compelled by a gradient in chemical potential to diffuse inwards. These processes can be the rate limiting step in the equalising of concentrations between the gas and condensed phases. Here, several novel studies have been conducted, both computationally and in a laboratory, exploring different aspects of this phenomenon and the rate at which it proceeds. The experiments have been designed to reduce the current uncertainties in atmospheric science, by relying on proxies for common atmospheric molecules.

Firstly, molecular dynamics simulations have investigated the process by which a single water molecule diffuses through a dehydrated organic structure. The course taken was found not to be continuous, but rather proceeded by a random walk of hops between cavities. Displacement was integrated and the diffusion coefficients were found to be consistent with existing experimental literature.

A methodology is presented for the extraction of diffusion coefficients from the growth and shrinkage rates of levitated organic droplets. The method was validated using sucrose aerosol, revealing that water equilibration is generally fast, although it can exceed several hours when particle viscosities approach that of a glass.

Once water diffusion was parameterised at different humidities, attention was turned to the evaporation of organic molecules, assuming the water flux would be unchanged by the presence of another solute. Several aerosol systems were studied, each with differing viscosities, volumes and volatilities of the evaporating molecule. Kinetic modelling was found to predict evaporation effectively when semivolatile organics were assumed to obey the Stokes-Einstein relation. This result is deemed highly significant to the modelling of gas-particle partitioning.

Finally, an atmospherically relevant oxidation reaction was initiated in the presence of a single seed droplet. By tracking resonances in the Raman spectrum, it was observed that mass accreted onto the droplet surface. Several experiments were conducted investigating the proportion of the coating that evaporates at different humidities.

Acknowledgements

There are too many people to thank for making these past four years such an enjoyable, bizarre, exhilirating time.

In the Reid group I would especially like to thank Bryan, Grazia, Rose, Flo, Jim, Chu, and Micheal Cotterell. They helped me in myraid ways over the years. I learned a lot from Aleks around optics tables, board games tables and pool tables. She epitomised everything I think an experimental scientist should be. Finally, Al and Mara, we'll always have Cuba.

The Glowacki group has expanded many times over in the past few years, but I will still remember when it was myself, Mike O'Connor and Rob Arbon. To me, Rob epitomises everything a computational scientist should be. Special thanks go to Robin, Helen, Simon, Balasz and Dasha for many out there discussions.

At the NERC doctoral training partnership, who I am immensely grateful for for funding, Sara Tonge has been a constant source of assistance and good humour for everyone in the cohort. She was always incredibly personable in our interactions.

I'm deeply grateful to Bex for making every moment we spend together full of joy. She's supported me through many highs and lows and I'm lucky to have met her.

Around the department, I'd like to thank Tom Oliver and Wuge Briscoe for keeping things weird every time I bumped into them.

Finally, I couldn't have done it without Jonathan and Dave. Jonathan has been incredibly supportive of me and the project even from before I started. He possesses a nearly inhumanly knowledgeable about chemistry, physics and environmental science, and gives people the space to shape their research and explore their curiosity.

Every conversation I had with Dave was mind expanding in one way or another, he is truly a genius and it has been a privelege to work with him.

I declare that the work in this dissertation was carried out in accordance with the requirements of the University's *Regulations and Code of Practice for Research Degree Programmes* and that it has not been submitted for any other academic award. Except where indicated by specific reference in the text, the work is the candidates own work. Work done in collaboration with, or with the assistance of, others, is indicated as such. Any views expressed in the dissertation are those of the author.

SIGNED: STEPHEN INGRAM DATE: 29/10/19

Contents

"I have no doubt that, although progressive changes are to be expected in physics, the present doctrines are likely to be nearer to the truth than any rival doctrines now before the world. Science is at no moment quite right, but it is seldom quite wrong, and has, as a rule, a better chance of being right than the theories of the unscientific. It is, therefore, rational to accept it hypothetically."

- Bertrand Russell, *My Philosophical Development*, **1959**

"Science is a high stakes game."

- Dana Scully, *The X Files,* **1995**

Chapter 1

Introduction

> "The furnaces of the world are now burning about 2,000,000,000 tons of coal a year. When this is burned, uniting with oxygen, it adds about 7,000,000,000 tons of carbon dioxide to the atmosphere yearly. This tends to make the air a more effective blanket for the earth and to raise its temperature. The effect may be considerable in a few centuries."
>
> - Francis Molena, *Popular Mechanics,* **1912**

1.1 The Aerosol Phase

It is actually rather difficult produce a definition of the word aerosol that includes everything that is generally agreed *to be* an aerosol, and excludes everything that is generally agreed *not* to be. The examples that perhaps most commonly spring to mind are the plumes released from deodorant or spray cans, and they satisfy the definition contained in most theses on this subject: a liquid or solid suspended in a gas phase. These are both examples of man-made aerosol that are engineered for a specific purpose, and the common usage of the word seems to be associated

with such systems. Yet this is erroneous: In all but the most pristine of natural environments, one cubic centimeter of the air at ground level contains tens of thousands of particles[1], many of which were formed by natural processes.

Note that the presence of an ensemble of particles is not a necessary or sufficient condition. The experiments that I have conducted measure the properties and dynamic responses of only one at a time. As such, a better definition is needed which captures more of the complexity I have just described. Let us adopt the following: One or more small objects, which are more dense than their surroundings. The crucial aspect of this definition is the existence of a gradient in density, as it strongly suggests the possibility of *mass transport* between the particles and the suspending fluid. That is precisely what that thesis concerns.

1.2 Aerosols in the Atmosphere

As a function of altitude, the concentration of atmospheric particles that are not cloud droplets tends to be highest at ground level. There is a slight decrease in number concentration at the top of the planetary boundary layer, around 3.5 km above ground level, before an increase in the troposphere[2]. Where each particle originated, how, and what it has since been exposed to will all potentially influence its properties or how it behaves.

What is the benefit to investigating aerosol properties? Aside from the benefit to scienctific knowledge, in a 'blue skies' manner, of a deeper understanding of how multiphase and multi-component chemical systems act, it is imperative that greater knowledge of atmospheric aerosol chemistry and physics is attained, for several reasons:

1. An increasing proportion of us are projected to live in cities in the coming decades, which unfortunately coincides with a general degradation in air quality[3]. Partly, this is due to particulate matter, of which smog is the most obvious example. It is currently difficult to predict with much confidence when and where urban aerosol will be concentrated, but will be crucial from a human health perspective.

2. Aerosol are constantly adjusting in composition through gas-particle exchange phenomena. Which compounds stay in the condensed phase, and which do not, influences the radiative balance of the atmosphere: particles reflect and refract sunlight whereas vapour does not.[1] Crucially, if the light wavelength is infrared, heat is expelled into space, cooling the Earth each day. This is known as the direct effect. If the number concentration, or optical properties, of aerosol were to change, it could alter the climate. Indeed, some suggestions have currently considered the deliberate engineering of particles that could stop, or slow, the climate from being altered in this manner[4]. The scientific basis for such scenarios is not currently well defined, and the side effects of deliberately emitting particles that interact with the climate system cannot be well predicted.

3. When subject to a specific set of physical conditions, aerosol particles can experience runaway growth as water vapour condenses onto them (see section 1.3.2). If enough droplets in one particular location grow sufficiently, eventually a cloud will be formed[5]. Clouds also insulate the Earth from exposure to the entirety of solar radiation, which causes additional cooling. This is the indirect effect.

Despite significant research into processes 2 and 3, it still remains unclear, to the best of our available knowledge, the extent to which the presence of atmospheric aerosol cools the planet[6]. Nonetheless, a huge amount of scientific research has been conducted into the behaviour of particulate matter. The deficiency in our knowledge is in a sense a result of the complexity of the climate system: too many processes interrelate and feed back with one another. Disentangling each of the effects is difficult.

The remainder of the chapter will focus on the state of the aerosol science. Sections 1.2 - 1.4 move approximately through the lifetime of a droplet. Firstly, the formation mechanisms of so called *primary* and s*econdary* droplets will be introduced, with specific attention paid to the gas phase organic chemistry involved in the latter. Next, the extended periods of time that organic aerosol are suspended in the atmosphere will give rise to the oxidation of the constituent

[1] Or at least, not enough to appreciably influence the amount of radiation leaving the atmosphere.

molecules within the particles. Some of these studies, and the chemistry that appears to be occurring, will be described. If the transformation, or the changes in temperature, pressure or humidity are significant enough, it can induce severe physicochemical changes, such as phase transitions. Some examples of these are provided, and their atmospheric relevance justified with reference to cutting edge field, laboratory, or simulation works.

As the glass transition in organic aerosol is a significant recent discovery, and crucially important to the research that has been undertaken for this thesis, special attention will be paid to concepts in glass physics that will become useful later.

Finally, it should be appreciated that single particle experiments of the type employed here are somewhat rare in the literature, and therefore many of the publications that will be referenced throughout this thesis will have used different techniques to study aerosol. The more common technique of initiating particle formation in relatively small chambers ('smog chambers'), that are intended to replicate atmospheric conditions, shall be described.

1.2.1 Primary Sources

Often the particles that are suspended in the air were emitted as aerosol at ground level. In some cases, such as atmospheric dust or sand in desert environments, the same particle may survive multiple aerosolisation events, settling back to Earth by deposition each time. In other cases, like sea spray, particles are continuously generated and reabsorbed by the ocean churning, or the waves etc. at the surface. The key attribute is that the particle was created by physical rather than chemical means.

The sources that contribute most to the observed aerosol count vary depending on location and time of year, as a significant proportion of every type manage to get uplifted to high altitude, at which point they can be transported significant distances over land or ocean by tropospheric currents[7]. A number of very striking representations of this type of long range transport have been recently produced by NASA, combining satellite observations and emissions estimates to visualise the aerosol dispersion within the atmosphere using their GEOS-5 (Goddard Earth Ob-

serving System) climate model[8]. Several stills are presented in Figure 1.2.1. Panels (a) and (d) show parcels of aerosol forming which are comprised of several types that have mixed since emission: Saharan dust and Secondary aerosol mixing above the East China Sea, and Sea spray and wildfire dust mixing across the Pacific Ocean, respectively.

One feature that recurs consistently in these videos is the interaction between aerosol and weather events, perhaps best shown in panel (b). Tropical storms, hurricanes and polar storms contain huge masses of sea spray aerosol and transport them long distances. During transport, it is common for a plume of particles to experience many severe changes in the ambient conditions of the atmopshere they are suspended in, inducing changes at the interface, or perhaps even deeper within the particle.

One aerosol source noticeable in the figures is anthropogenic, i.e. man-made: sulphate rich aerosol are generated by industrial activity, and smoke is formed during incomplete combustion when fossil fuels are burned.

1.2.2 Secondary Sources and New Particle Formation

Until relatively recently, spontaneous formation of aerosol particles in the gas phase was considered a theoretical curiosity with little practical or atmospheric application. While reports such as that of Aitken in 1900[9] suggested new particle formation was possible in some conditions, most atmospheric aerosol were believed to be primary particles. Then, starting in 1995, a number of seminal works by Weber[10], Kulmala[11] and many of their coworkers were produced, reporting the formation of secondary aerosol observed in sites across the world[12].

The process follows a similar pattern almost everywhere it is observed. Sunrise initiates a rapid burst of new particle formation and growth in rural environments, as a result of several factors operating in concert: the rising temperature increases evaporation rates from vegetation, as well as expanding the boundary layer, which increases the mixing of precursor vapours[13]. The latter effect then drives further volatile organic compound (VOC) evaporation. Simultaneously, the sunlight causes photochemical reactions that form oxidants and reactive oxygen species[14].

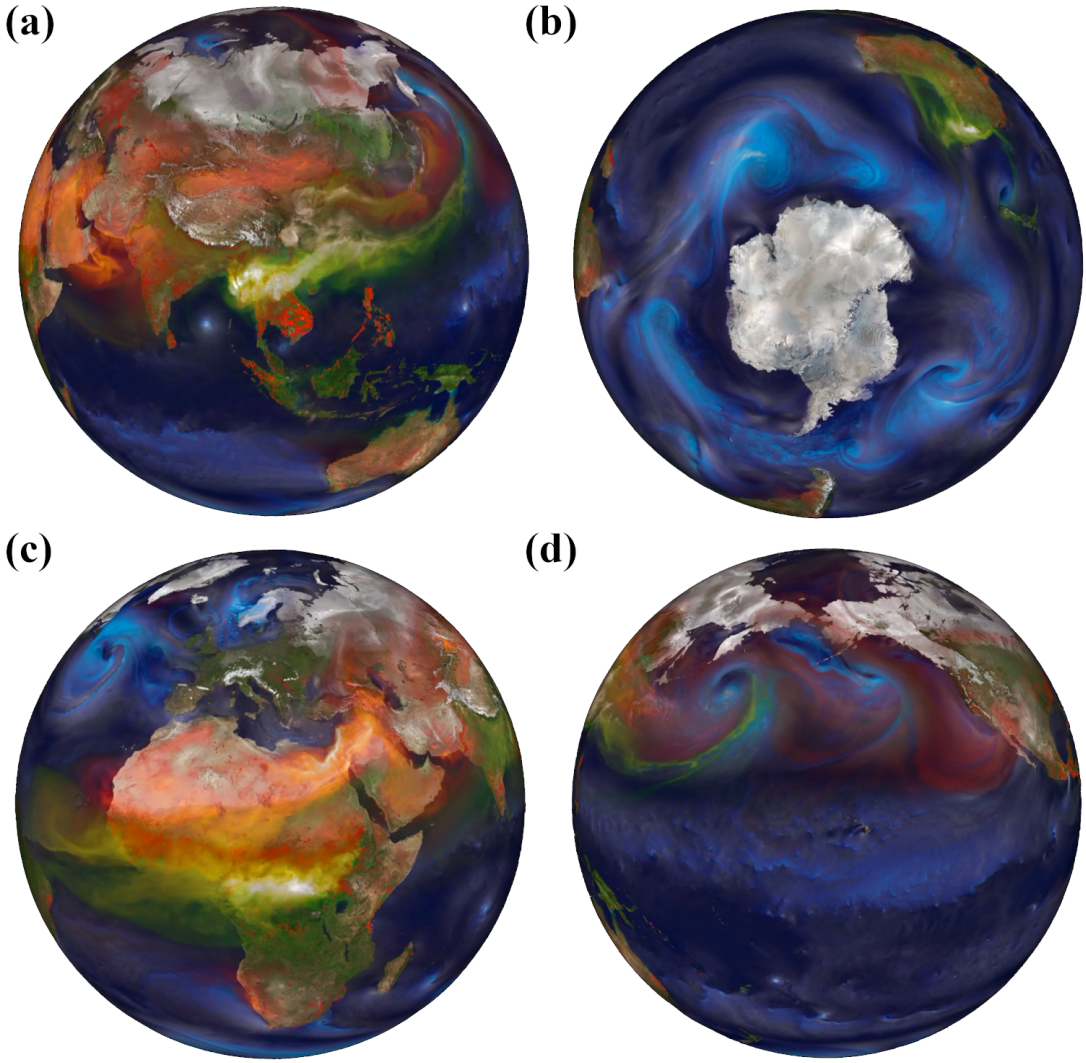

Figure 1.2.1: Still images from a GEOS-5 model of aerosols in the Earths atmosphere, produced by NASA. Simulation represents May 2005 to May 2007. Stills were chosen to represent the complexity of different aerosol emitted into the atmosphere, by the same land mass. In addition, Features shown in each panel are (a) Asia, (b) Antarctica, (c) Africa and Europe, and (d) the Pacific Ocean. Legend: Desert dust is coloured orange, forest fire dust is red, sea spray is blue, secondary aerosol is green, smoke and sulphate rich particles are white. Reproduced from NASA/Godard Space Flight Center.

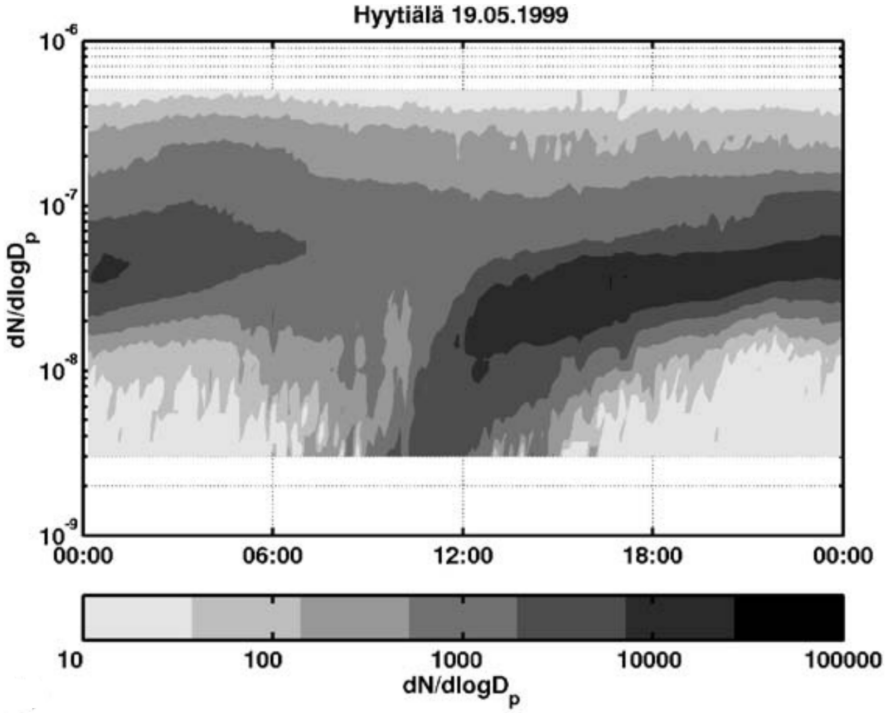

Figure 1.2.2: Prototypical data showing an increase in aerosol concentrations, follow by growth, observed in the morning, reproduced from ref. 11. The plume visible on the left hand portion of the graph (midnight) is the end of the previous days SOA mass.

Thus, both reactants become more concentrated.

Figure 1.2.2 presents a so-called 'banana plot' of particle radii against time of day, showing a broad increase in concentration and radius in the morning[15]. The name refers to the appearance of the high particle count feature.

Sulphur is a major elemental component of primary particulate emissions, in the form of volcanic ash, as well as aerosol produced by many industrial processes. It is a trace component of the atmosphere more generally. Several oxides, in addition to sulphuric acid, can be found at the parts per trillion volume (pptv) concentration at all altitudes and in almost every continent[16]. The ambient concentrations of sulphur compounds vary throughout the year, which has been found to correlate with both the rate of new particle formation[17] and also the sulphate mole fraction[18] measured in the newly formed aerosol. Clearly it is playing a role, but it is difficult to unpick precisely what. In trying to elucidate the mechanism behind the observations, it has been

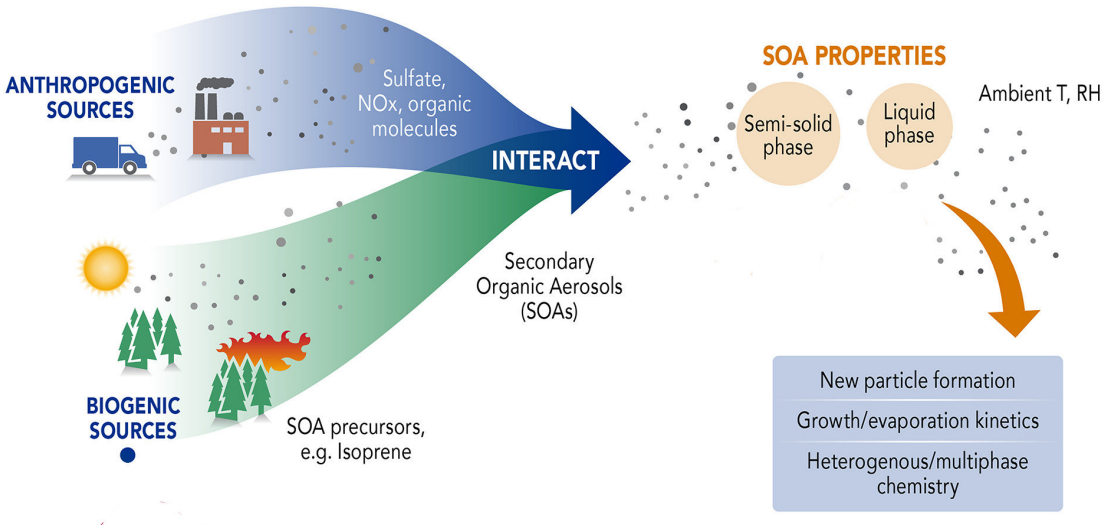

Figure 1.2.3: Schematic of different stages in a Secondary Organic Aerosol particles lifetime, adapted from Shrivastava et al.[19] From left to right: emission, nucleation, growth, and possible changes in phase state.

proposed that secondary aerosol formation proceeds first through the formation of molecular clusters of sulphate and ammonium.

VOCs are emitted in large quantities in both urban and rural environments at most times of the year. Vegetation naturally emits isoprene (Figure 1.2.3) and monoterpenes in the hundreds of Tg year^{-1} in response to external stresses or naturally during their life cycles[20]. Many such molecules are susceptible to a rapid chain of essentially barrierless chemical reactions initiated by collision with small molecules, or other reactive organic gases. These will be described in more detail in the coming sections of this chapter. For the time being, it is important to stress that such a process usually results in a lowering of vapour pressure, expressed as a saturation value (the pressure that would exist above a pure liquid containing only that molecule). The pressure of organic matter that is actually in the gas phase will not change, meaning that oxidation tends to[2] transform molecules such that they are closer to saturated. Molecules will then seek to condense onto particulate matter, if any is present.

Monoterpenes are an important class of biogenic compound that contribute significantly to

[2]This is not necessarily the case. See subsequent sections.

new particle formation and growth[21]. Their chemical forumla, $C_{10}H_{16}$, contains three double bond equivalents, suggesting significant capacity for oxidation until the carbon chain is fully saturated with oxygen or hydrogen groups.

Urban environments produce VOCs which are distinct from those found in the natural world. Generally speaking, they are aromatic molecules, such as toluene, benzene or xylene[22]. In the literature, naphthalene is often used as a model precursor[23]. The resulting oxidation and new particle formation pathways of anthropogenic and biogenic VOCs are distinct from each other, due to the aromatic system needing to be disrupted for oxygen atoms to form bonds with the carbon backbone. A number of source apportionment studies[24](and references therein) operating in megacities and have consistently found that the most common particles collected[3] in major population centers across the northern hemisphere are secondary particles.

1.2.3 Organic Chemistries of the Boundary Layer and Troposphere

Oxidation of VOCs

The most common reaction pathway that biogenic VOCs undergo after emission is gas phase oxidation. Of most interest to this thesis are oxidation reactions which produce compounds of higher molecular weights than their precursors, which are sometimes referred to as 'functionalisation' reactions. The functional groups introduced depend on the oxidant, and the hydroxyl radical, ·OH, is the most frequent oxidant encountered. Ozone and nitrate are less common, and so ozonolysis and nitration can be considered sub classes of the oxidation phenomenon. Nitration reactions tend to dominate during the night time[25], when photochemical production of ozone or hydroxyl is absent.[4]

Arguably the most important VOC emitted into the atmosphere is isoprene, as it is by far the most common[27]. Additionally its primary oxidation pathway can switch between functionalisation and fragmentation, as a result of subtle changes in the concentrations of NO_x and

[3] by number, rather than volume or mass

[4] That is not to say ozone is not present during the night; it can be produced through other radical propagation reactions[26].

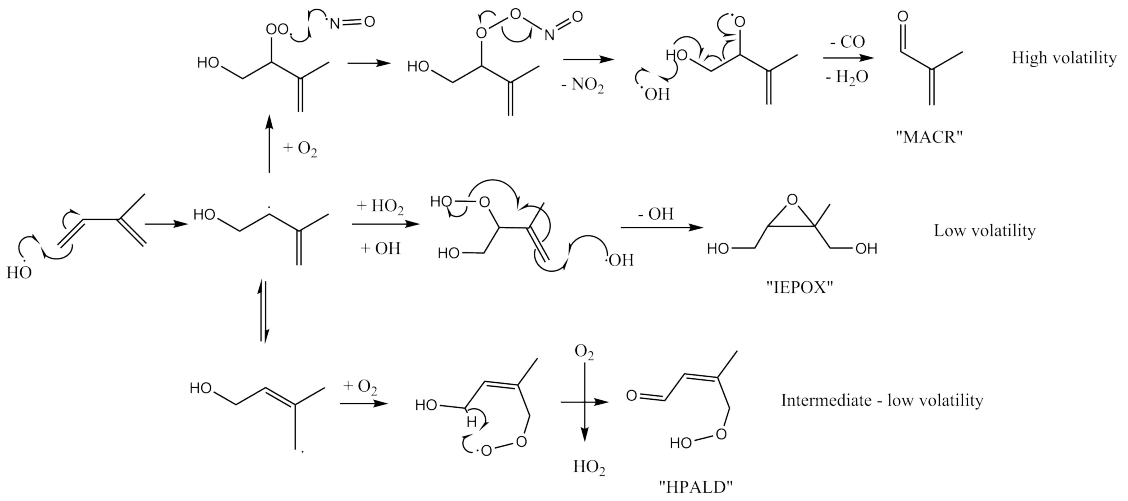

Figure 1.2.4: Simplified reaction schemes of common pathways that take place during isoprene OH oxidation.

O_2.[5] Clearly, the resulting mass yield of particulate matter will be highly sensitive to the most frequent type of isoprene oxidation that is happening[28]. The reaction with the hydroxyl radical begins with the formation of a bond between the oxygen and one of the alkene groups in isoprene (scheme 1.2.4). The radical centre formed on the adjacent carbon is then intercepted by at least one O_2 moiety, at which point three possibilities emerge:

- High NO_x conditions fragment the molecule, producing methacrolein and converting NO to NO_2 in the process[28, 19] (top reaction). The mean molecular weight goes down and everything stays within the gas phase.

- When the atmospheric molecule HO_2 is present, multiple rearrangements followed by ·OH additions can happen in rapid succession (middle reaction), generating epoxydiols (IEPOXs). These are semivolatile, water soluble[29], and highly reactive with respect to sulphate compounds[30]. As a result, IEPOXs are one of the most common single constituents found in SOA worldwide[31, 32].

- In the absence of an excess of either of the aformentioned species, the reaction can only

[5] including other common dioxygen radicals HO_2 or RO_2

proceed by isomerisation, producing hydroperoxy-aldehydes, (HPALDs, bottom reaction)[33]. Generally speaking, these are insufficiently heavy to condense onto droplets and so remain vapours. They are known to be important in the catalytic production of hydroxyl, as the peroxide bond is weak and can be cleaved easily[34, 35].

Another reaction mechanism that has been afforded significant investigation in the literature is that of α-pinene with ozone. Ozone is concentrated mostly in the stratosphere and troposphere[26], although there is still some present in the planetary boundary layer[13]. Averaged globally, α-pinene is the most common monoterpene in the atmosphere, although its yearly emissions are less than one tenth of that of isoprene[27]. The reaction is central to the studies described in Chapter 8, and an understanding of the products will inform the choice of molecules that are aerosolised in earlier experiments.

In the late 90s, several important works began to study the mechanism: first, it was conducted in the dark by Hoffmann et al. and shown to produce organic aerosol at quite high yields[36], whilst at the same time known products of the ozonolysis reaction (including *cis*-pinonic acid[37]) were observed in the particle phase above, among other sites, a boreal forest in Portugal[38].

The early stages of the oxidation mechanism can be found in many publications[39, 40, 41]; one has been reproduced in Figure 1.2.5 above. The ozone attacks the π system of the double bond and forms a primary ozonide, which then decomposes into two possible Criegee intermediates. Crucially, the ozonide is a bicyclic molecule, and so the two halves remain connected by the dimethylcyclobutane group on the other side of the ring, even after the bonds break.

In the absence of collisions with other oxidants, the peroxy half of the criegee moiety will cleave a hydrogen, undergoing a 1,4-shift and reforming an alkene adjacent itself. As shown in the figure, the conformation of the C-O-O bonds with respect to the backbone will influence which hydrogen is removed (middle versus right hand channels). Very soon afterwards, the weakened peroxy bond breaks and a hydroxyl is released back into the gas phase.

The chemistry that can occur afterwards is very complex and branches much further, not least because hydroxyl itself will react with both the parent VOC and many of the oxidation

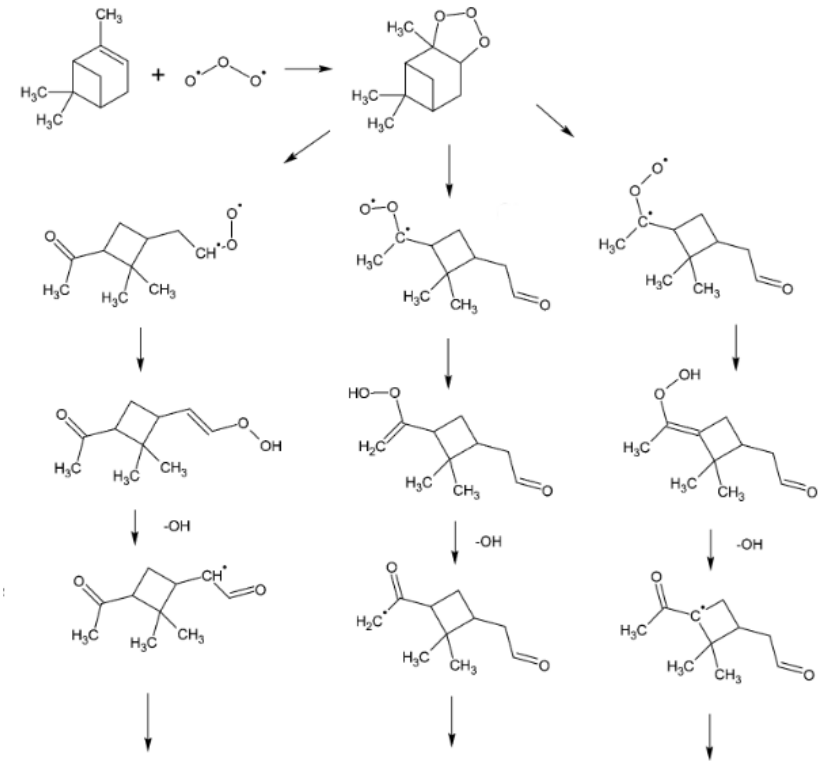

Figure 1.2.5: The ozonolysis mechanism of α-pinene. From top to bottom: formation of a primary ozonide, decomposition into Criegee intermediates, intermolecular proton transfer, loss of a hydroxyl radical.

products[42, 43]. One statement that can be made with confidence is that the ozonolysis process almost always leads to a net increase in molecular mass as it proceeds, and a more significant lowering of the saturation vapour pressure than occurs in isoprene oxidation[44].

Autoxidation of VOCs

While autoxidation chemistry has been recognised as an important pathway for chemical ageing during combustion, as well as other bulk phase chemical and biological systems,[45] it was an open question for some years whether tropospheric molecules would have sufficient energy to undergo transformations of this kind on an appreciable timescale.

The first clue that autoxidation was occuring to at least some of the VOCs were high concentrations of species with the formula $C_{10}H_{16}O_{9\text{-}11}$ in freshly formed monoterpene SOA: Mass

spectroscopic analysis of particulate matter formed in high α-pinene conditions captured in field[46] and chamber[47] studies have indepentently observed high yields of molecules with this formula, i.e. containing the same number of carbon and hydrogen as the parent monoterpene, but many more oxygen atoms. This seemed to suggest that whatever was oxidising the monoterpene only contained oxygen and no other elements. More conventional oxidation mechanisms could not explain the production of this coumpound as repeated collisions with other radicals would insert additional nitrogen, carbon or hydrogen into the elemental formula[48].

A more general example of the autoxidation pathway is presented in Figure 1.2.6. This mechanism also explains how the molecular weight of a VOC can increase drastically when the oxidant concentration is low: it only requires one collision to initiate, after which the Criegee intermediate rearranges through an intermolecular hydrogen abstraction process. Multiple O_2 molecules can potentially add to the resulting carbon centered radical in rapid succession, each cleaving a different C-H bond and allowing the process to continue. Hydrogen atoms are not lost from the molecule but instead migrate along the backbone, as in Figure 1.2.5. Various *ab initio* calculations have calculated that the turnover for autoxidation of cyclohexane[49], α -phellandrene,[50] and α-pinene[51, 40] ozonides all to be fast. It is easy to see why: molecular oxygen accounts for nearly 21% of all molecules in the atmosphere, and so a given VOC molecule will collide with O_2 at a much higher frequency than with any other oxidant.

Autoxidation seems to be very important for new particle formation and SOA growth[52] but many uncertainties remain[53]. It may be, for instance, that VOCs emitted from agriculturally developed (i.e. crop) land will be the minority component in the reaction scheme, whereas above forest canopies they will be in excess relative to oxidants[19]. Recently, a large collaboration led by Trostl et al. attempted to extrapolate from measurements conducted as part of the CLOUD chamber experiment at CERN (see section 1.5.1) into atmospheric conditions[54]. It was shown that highly oxidised organics can drive new particle formation by themselves under certain conditions, without the presence of sulphur or ammonium compounds[54]. The inclusion of autoxidation in the reaction scheme was required to replicate the observations[55].

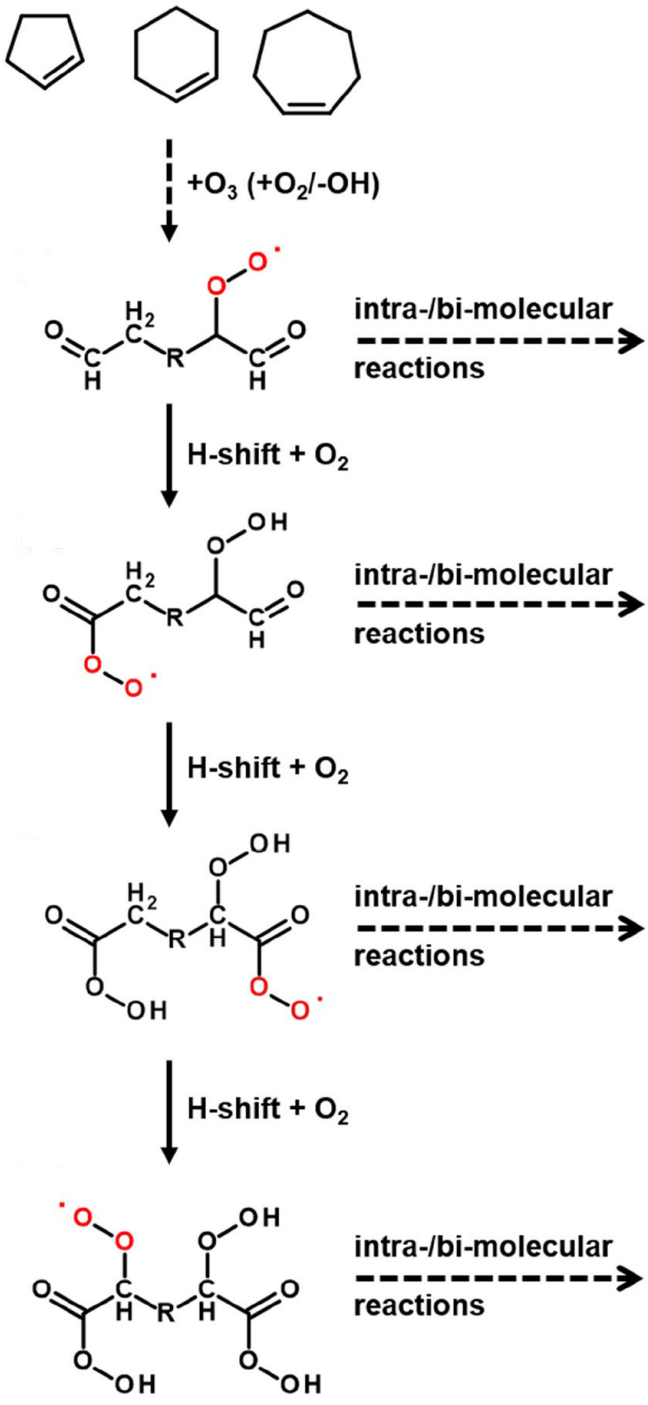

Figure 1.2.6: Generalised mechanism of autoxidation in an oxygen atmosphere, reproduced with permission from Ehn. et al.[41]

Other fates of Criegee Intermediates

It is becoming apparent that Criegee intermediates are crucial to the formation of SOA particles via the ozonolysis oxidation pathway. Many studies also substantiate that the mixture of chemical species found within the particles will be very different depending on which compounds intercept Criegee intermediates whilst they are in the gas phase. Given their very high reactivity, an exhaustive exploration of all possible reactions is not possible in this context, but some key mechanisms are worth introducing.

• Criegee intermediates can themselves act as oxidants, as they possess delocalised unpaired electrons. One reaction of particular atmospheric relevance is the conversion of SO_2 to SO_3[56, 57] under ambient atmospheric conditions (reaction 1). Similarly, NO can be oxidised to NO_2 , resulting in the loss of the terminal oxygen from the Criegee species, and the formation of a closed shell (i.e. non radical) aldehyde compound. (reaction 2). Reaction with NO_2 also occurs readily, although it appears to proceed via addition. The product is a stable adduct of the two species, and NO_3 is not observed[58].

• Collision with water has a variable frequency, depending on the RH, however the resultant reaction (reaction 3 where R = H) tends to be facile[59, 60] once the collision has happened.

• In a similar way to the original ozonolysis reaction, Criegee intermediates can undergo 3+2 cycloaddition to alkenes (reaction 4), including monoterpenes. The rate constants are found to be much lower than reactions 1 - 3, but some authors suggest the reaction could still be important under certain atmospheric conditions[61].

• Radical chain propagation can occur when RO_2 radicals intercept a species that is partially autoxidised. Two such species, with at least one O_2 molecule added to their backbones, can form an adduct through their terminal radical centers. Such a molecule would contain *four* oxygens bonded in a row, which is highly kinetically unstable with respect to O_2 production (reaction 5). The produced organics are alkoxy molecules of the form RO·.

• Reactions can occur at the air-particle interface, especially with polar or highly charged species, as electrostatic effects can significantly increase the probability of collision. This effect

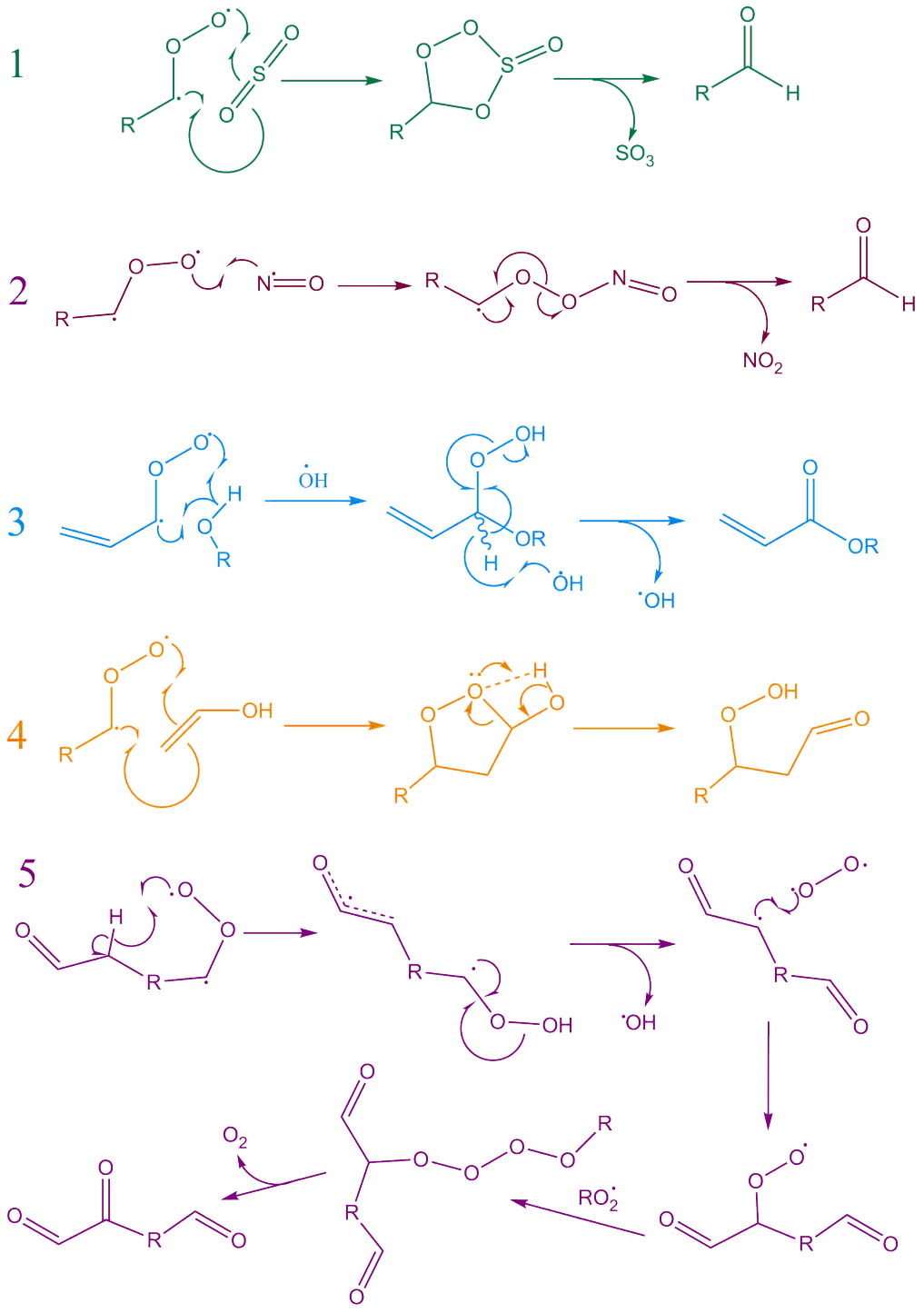

Figure 1.2.7: Some examples of reactions between Criegee intermediates and common atmospheric molecules. *R* represents saturated or unsaturated aliphatic groups.

has been found to be especially strong with the head groups of surface active organics[62, 63]. If carboxylic acid or enol groups are present in the surfactants, there are at least three possible mechanisms by which the carbonyl oxide of the Criegee intermediate can add into various bonds[64].

• The organic vapours which condense during new particle formation must be present at supersaturated concentrations. For this to come about, either the partial pressure must increase or the saturation pressure of the oxidised product must rapidly decrease as a result of a reaction. Gas phase oligomerisation[65], where Criegees insert into C-H bonds on unreacted VOCs, is a method by which the latter can occur.

Taken together, the literature suggests that the concentration of sulphur and nitrogen compounds, the humidity, and the amount of unreacted VOC remaining will all influence the chemical structures present in an evolving SOA plume. Additionally, the presence or absence of molecular oxygen will slow the rapid production of low volatility compounds.

1.3 Processing and Ageing of Organic Aerosol in the Atmosphere

There are probably as many unique examples of atmospheric processing as there are particles in the atmosphere; the array of reactants and reactions a particle may be subject to is much too large to list explicitly. It is also highly dependent on the formation pathway, and the constituents of the early nuclei. Nonetheless, a few general processes can be extracted, and a number of important trends can be identified that tend to occur commonly as the aerosol is aged. An understanding of such processes should allow us to choose, and aerosolise, compounds during experiments in order to produce particles that approximate different stages in the atmospheric lifetime of an SOA particle.

As in the previous section, specific attention will be paid to organic aerosol, although different particle types such as polycyclic aromatic hydrocarbons[66, 67] may be susceptible to oxidation reactions similar to those described here. Analytical chemistry studies performed on particulate matter sampled directly during field campaigns will be referenced, in addition to sim-

ilar observations made on laboratory produced aerosol. The combination will be used to understand the broad changes in molecular structure that occur as a result of atmospheric processing.

1.3.1 Environmental Chemistry of Aerosols

In some mass spectrometry studies of freshly produced SOA it has been possible to identify of the order of ten components that are each around twice as concentrated as the rest of the mixture[68, 69]. Nonetheless, they do not constitute the majority of the organic mass, and so it must be treated as a highly complex multicomponent mixture. What is unclear is how the properties of the organic mass on the single particle level will arise collectively from the properties of the individual molecules and ions within it. Certainly parameters such as vapour pressure and reactivity will vary over orders of magnitude within the mixture, yet each particle will exhibit one evaporation profile, one reaction rate with respect to oxidation, et cetera.

Another layer of complexity arises from the interactions of different VOCs when they are oxidised simultaneously in the same atmosphere. Recent studies in the literature can be separated into those that investigate biogenic-biogenic interactions and biogenic-anthropogenic interactions. In a recent example of the former, McFiggans et al.[70] investigated the coupled oxidation of isoprene and α-pinene, discovering that the mixture produces a much reduced yield of condensed aerosol mass in comparison to the oxidation of either VOC by itself. It was hypothesised that the isoprene peroxy radicals (see Fig. 1.2.4) will react competitively with first stage α-pinene oxidation products, reducing the yield of α-pinene dimers and also of hydroxyl radicals in the gas phase.

A very important work was published by Kalberer et al. in 2004[71]. It proved that oligomerisation reactions can happen in the particle phase as well as the gas phase[72], forming significantly larger molecules than dimers. The system involved the oxidation of an anthropogenic VOC, 1,3,5,-trimethylbenzene. They found that the decomposition of the aromatic ring produced methylglyoxal sub-units, which added to each other consecutively in a reversible condensation reaction[73]. Since water is a byproduct of this kind of chemistry, it strongly suggests that de-

hydration of aerosol can, in itself, shift the equilibrium position of reactions that are occurring within the particles, converting semivolatile mass to involatile mass in the process[74].

Observations from various authors since have revealed the prevalence of oligomers in SOA; both atmospheric measurements[75], as well as SOA produced from various VOCs in laboratories[76, 77, 78] broadly agree with one another.

There is mounting evidence, and one would intuitively predict, that as the volatile components contained within the organic mass evaporate, the molecular mass of the remaining compounds will increase and the chemical structures will be more oxidised and more crosslinked. A complex array of chemical and physical processes such as this cannot be solved explicitly whenever one wants to predict the evolving size and properties of an aerosol plume; computationally it would not be feasible. Therefore, we require a simpler, heuristic quantity from which the atmospheric effects of aerosol can be approximated.

For instance, one can represent the oxidation state of ambient organic aerosol using the mean oxygen to carbon (O:C) ratio of the organic constituents[69, 79, 80]: As a particle is aged by the gas phase species it encounters, the organic backbones of the constituent molecules are gradually saturated with C-O, C-OO or C=O bonds, and the ratio approaches (or exceeds) 1.

Other parameters and two dimensional maps have been proposed that aim to capture information regarding the 'age' of stable organic molecules. One is the mean oxidation state per carbon atom, usually written as OS_c. This quantity, plotted in conjunction with either carbon chain length[81] or compound volatility[47], is capable of differentiating between the pathways of atmospheric reactions[82]: Oligomerisation reactions increase molecular weight but do not change OS_c. Different functionalisation reactions either increase or decrease weight but usually increase the oxidation state. The final pathway, fragmentation, leads to a reduction in vapour pressure and chain length, but an increase in oxidation state. Similarly, some studies have plotted the observed O:C and H:C ratios of SOA from the field and the laboratory as perpendicular axes, in an attempt to find correlations within their elemental composition[83].

It may be that photo-oxidation and radical oxidation will continue to crosslink the organic

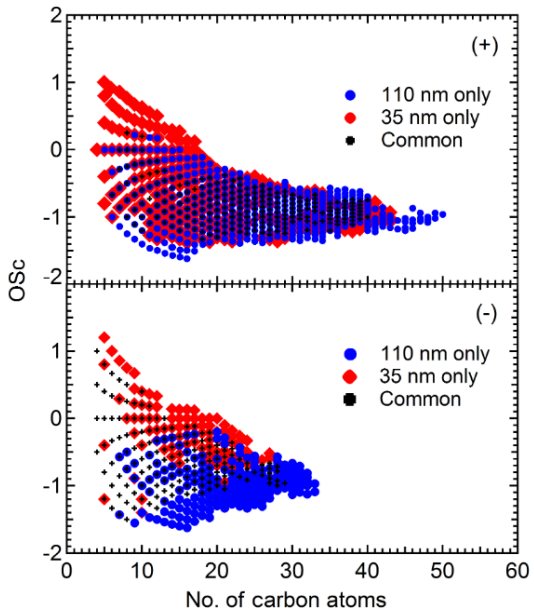

Figure 1.3.1: 'Map' of compounds observed in SOA produced by the oxidation of β-Pinene, with oxidation state and chain length forming the two dimensions. Reproduced from Tu et al.[81]

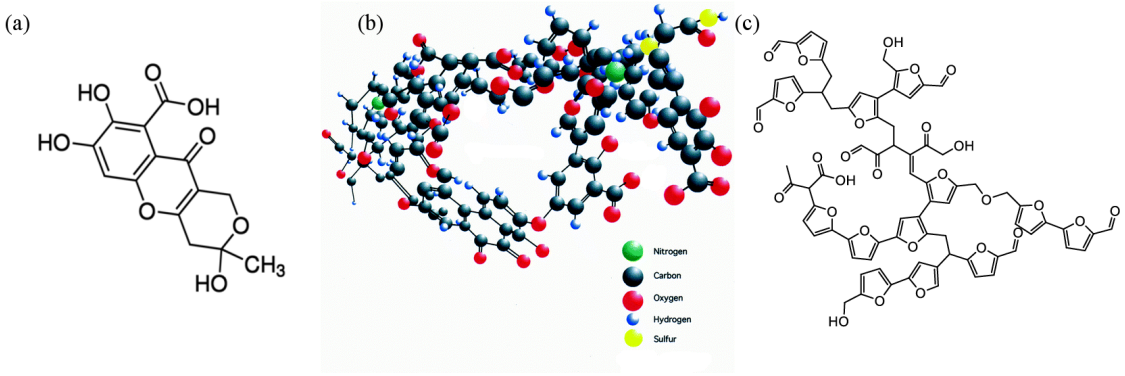

Figure 1.3.2: Examples of proposed chemical structures of humic like substances in the geochemistry literature. (a) Fulvic acid (reproduced from Sigma Aldrich Inc. website) (b) A highly aromatic structure containing N and S proposed by von Wandruszka 2000[84]. (c) Furan based structure proposed by Filiciotto et al.[85]. These elements and functional groups are known to be present in SOA.

species present in the particle phase in unpredictable ways. The logical conclusion of this type of condensed phase chemistry are so called 'Humic like' substances (HULIS). HULIS were first discovered in the geochemistry community[84]. Humic acid is a well known soil nutrient, and is observed in freshwater streams. As a class of molecules, HULIS are quite ill defined: their main identifying features are very large molecular masses, high O:C ratios, and molecular structures containing a combination of aromatic, aliphatic, and carboxylic acid groups. It is also highly likely that sulphur and nitrogen will be present in the chemical formula[86]. Several different structures of humic substances are shown in Figure 1.3.2. Each humic-like molecule will likely have a unique structure, elemental composition and molecular mass, and so it is impossible to determine analytically their exact structure. Fulvic acid (panel (a)) is often considered as a prototypical humic substance, as it is more water soluble and lighter than much of the observed HULIS. Interestingly, it has been observed to possess a very similar mass spectrum to that of highly oxidised SOA[87].

Despite being involatile, HULIS have been observed in particulate matter sampled from a number of urban sites in China[88], South Korea[89], and Brazil[90], as well as rural and suburban environments in east Asia[86]. Their prevalence in such a wide range of natural environments suggests that they are formed in the particle phase, perhaps via multiple pathways. It may even be that Humic like molecules will be present in some form within all organic aerosol once it has been sufficiently processed by the atmosphere. It may not, however, always be the case that ageing will increase the mass loading of particulate matter: A recent study by Romonosky and coworkers at UC Irvine found that hydrolysis reactions tend to break up large molecules and liberate more volatile species if a large excess of water is present in the SOA[91].

Brown carbon is a related class of aerosol, containing a unique subset of organic material that is produced by particle phase reactions. The molecules are defined by a characteristic absorbance profile in the visible spectrum, which may influence the radiative balance of the atmosphere[92]. Mass spectrometry[93] and computational[94] studies have identified imidazole, a nitrogen containing heterocycle, as a significant contributor to the absorbance. Its production occurs in the

particle phase and seems to follow a multistep reaction involving glyoxal and ammonia.

Each of the structural properties that have been introduced here (O:C ratio, molecular weight, crosslinking) should be considered when designing an aerosol science experiment that is intended to replicate SOA.

1.3.2 Hygroscopic Growth

Were there not aerosols present in every layer of the atmosphere, it is likely that rain would not exist as we understand it. Instead, water would be removed from the atmosphere at ground level, by condensing on every available solid object in each affected area. In reality, aerosols remove some of the water from the atmosphere by absorbing it. Hygroscopic growth is the name given to this process, and its magnitude is dependent on the humidity, and the affinity for water each particle expresses. The trend in uptake across all humidities can be reffered to as the *hygroscopicity* of a substance, which can be assumed to be independent of particle radius.

To be precise, the quantity of humidity used in this thesis will be *relative* humidity:

$$RH = \frac{p_{water}(T)}{p^{\circ}_{water}(T)}. \tag{1.3.1}$$

p_{water} is the partial pressure of water in an atmosphere and p°_{water} is the saturation pressure.[6] When expressed as a decimal, the RH will be equal to the water activity of the gas phase, regardless of the temperature, but the mass of water that must be present to maintain the RH generally increases as the surrounding air gets hotter. It will be expressed as percentages throughout the thesis.

Recalling the banana plots from section 1.2.2, we know that 'fresh' SOA falls in the diameter range 20 - 100 nm[12, 95], and that the particles grow slowly over time into the approximate range 100 - 400 nm[96, 97] if they continue to be exposed to semivolatile vapours[98]. It is less well known how much water can be absorbed at equilibrium[7] by SOA, across the range of

[6] as defined previously, the pressure that would exist in equilibrium directly above pure liquid water.

[7] The timescale of the growth, and whether a given particle is ever capable of reaching equilibrium, is a different topic. That will be the subject of Chapter 2.

humidities they are likely to encounter.

What is uncontroversial is that organic aerosol is less hygroscopic than inorganic aerosol[99, 100]. An early study by Varutbangkul et al.[99] systematically investigated the ozonolysis of several VOCs, finding that hygroscopic growth generally becomes poorer as the organic molecules become larger (C_5H_n versus $C_{10}H_{16}$ versus $C_{15}H_{24}$). This publication predates by one year the κ-Kohler theory[101] of hygroscopic growth, and so uses mathematical functions to relate increasing volume to water activity that have since fallen out of use. κ-Kohler theory has been adopted readily by a large proportion of the aerosol science community (the original publication has been cited nearly 1400 times). Briefly, it proposes a dimensionless quantity κ, that can be though of as a measure of the hygroscopicity of a substance. It can be calculated via the equation:

$$\kappa = \frac{V_{water}}{V_{dry}} \left(\frac{1}{a_w} - 1 \right). \tag{1.3.2}$$

V_{water} is the volume of water solvating the material present in the droplet, whose volume is equal to V_{dry}. Strictly speaking, κ should be reported at a given activity, and frequently a_w = 0.95 is used[80]. However, its value is commonly assumed to be invariant with activity. This assumption is advantageous because it implies that a single value of κ can be used to prescribe the particle growth factor (GF) across the entire RH range[8], spanning zero to a fully saturated atmosphere. GF is defined as the ratio of the radius to the dry radius (or diameter to dry diameter):

$$GF = \frac{a(RH)}{a_{dry}} \tag{1.3.3}$$

An example contour plot of growth factors extending up to 100% humidity is presented in Figure 1.3.3 (originally from Duplissy. et al.[100]). As κ increases, the radius grows by more at a given RH.

SOA particles contain around picograms (10^{-12}g) of material, and so the mass of water condensing is similarly small. The low mass might mean that molecular scale effects influence the

[8]There is a singularity in equation 1.3.2 when a_w = 1. In the original publication, Petters and Kreidenweis[101] suggested that the treatment only applies to sub and supersaturated atmopsheres, rather than saturated. As such, the 'entire RH range' refers to 0 < RH < 99%.

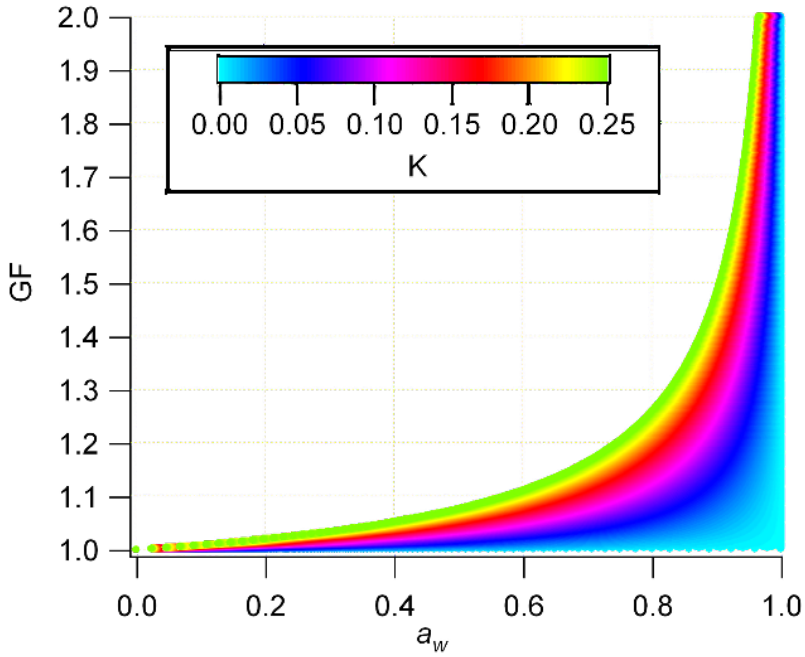

Figure 1.3.3: Examples of growth factors as a function of the parameter κ, reproduced from Duplissy et al.[100] Note that usually $\kappa < 1$.

hygroscopic growth observed on the scale of droplets: the amount of water that can stably bond to a single organic molecule through Van der Walls forces, hydrogen bonding etc. is a useful piece of information when determining the maximum equilibrium water content of a given aerosol phase. In turn, this will be determined by the compounds that manage to find their way into the particle phase.

It turns out the literature is not entirely in agreement on this point. A very recent study by Hu et al.[102] has challenged the conventional view of hygroscopic growth of SOA, by creating an experiment where semivolatile organics are continuously resupplied into the atmosphere of the chamber, promoting co-condensation: a process where an increase in organic mass drives the uptake of water to equalise the water activity. They observed growth factors in excess of 4, and a κ value of 8.48, both of which are enormous in comparison to anything else published in this field. Yet they make a convincing case that their experiment is more atmospherically relevent. Their logic was that, in the atmosphere, almost all SVOCs present will be above their saturation

and so these effects will drive much larger particles than normal chamber experiments would observe.

Cloud Activation

Cloud droplets tend to form in atmospheres supersaturated with water (RH > 100%). A runaway water condensation process is initiated and individual aerosol particles can increase in diameter over tenfold, entering the micron scale regime[103]. The precise amount of water that can be absorbed by any of the solutes present is less important in a supersaturated than a subsaturated environment, because the equilibrium state the particle wishes to approach is a pure water phase containing no solute.

The interaction between SOA and clouds is, by all accounts, quite subtle: A wide array of studies[104, 105, 106] support that neither biogenic nor anthropogenic SOA make very efficient cloud condensation nuclei. Interestingly, it was recently found[107] that SOA coatings of up to 60 nm can be present on mineral dust and the core particle will still maintain its cloud activation properties. It may therefore be that ice can nucleate from solutions in which secondary organic matter is dissolved, but if it comprises the entire particle it may not be able to induce nucleation efficiently.

Microphysical modelling[108] of the structure and dynanics of multiple particles (sometimes referred to as 'box modelling') has suggested that the effect of semivolatile organic evaporation is to even further reduce the nucleation activity of SOA. Different studies have produced contradictory results about which kinds of atmospheric conditions lead to the most pronouced change[103, 109]. Clearly, further research is needed into the influence of different volatility aerosol on the cloud formation process

It is also useful to distinguish between homogeneous and heterogeneous ice nucleation: the former occurs when the entirety of an aqueous droplet crystallises in a highly supercooled atmosphere[110], and the latter occurs when a layer of ice grows onto a particle surface[111, 112, 113]. Which mechanism of nucleation a particle can undergo will be influenced heavily by

its phase state, and hence whether water condenses *into* or *onto* its surface. Recently, Ruehl et al.[114] published an important contribution in *Science,* suggesting that the presence of some surface active components in the SOA mass could depress the surface tension of a growing droplet. Their experiments investigated ammonium sulphate seed particles coated with different widths of α-pinene SOA, and showed that when the volume fraction of organics was sufficiently high, the surface tension reduction was large enough to counteract the low hygroscopicity of the remaining organics. Therefore, the critical supersaturation needed for cloud activation was still lowered[114].

Aircraft measurement studies by Cziczo et al.[115], which sampled aerosol in Central America, reveal that proportionally fewer SOA particles become cloud droplets than exist as aerosol in the ambient atmosphere, and that dust particles coated with organics are less common in clouds than those that are not. Both of these results suggest that their cloud activation properties are distinctly lower than inorganic aerosol.

1.4 Phase Transitions in Organic Aerosol

It is common for the atmospheric chemistry literature to differentiate between *internally* and *externally* mixed parcels of aerosol. Briefly, the former refers to the equalising of concentrations between the surface and core of a single particle,[9] whereas external mixing refers to whether molecules are distributed between every particle in the plume in a way that equalises concentration. This subsection will focus on *internal* mixing, specifically enthalpic barriers that can restrict it, and the resultant demixing processes.

It is also useful at this point to conceptualise the distinction between events, or thermodynanmic quantities, that are state functions and path functions. The distinction will be important when comparing the glass transition to other forms of phase transition. Briefly, an observable is a path function if its magnitude under a given set of conditions is influenced by the preparation of

[9] or, for instance, between surfaces on opposite sides of the droplet.

the system. By contrast, a state function is only dependent on the conditions at the time ('state') and not the path taken between the initial and final states.

1.4.1 Liquid-Liquid Phase Separation

Enthalpic effects can arise from the different forms of molecular interactions present in aerosol as its composition changes: organic solutes will experience a different environment when in proximity to each other versus when they are locally solvated by water. If the strength of this 'hydrophobic effect' outweighs the entropic benefit of the organics remaining mixed with water, then the free energy of the biphasic state will be lower than that of the mixed state and phase separation will occur.

The different reaction and oxidation pathways decribed in section 1.3 produce compounds that vary drastically in their water solubility. It therefore seems reasonable to assume that at least some of the particle phase components of SOA will not be miscible with aqueous solutions at the concentrations present.[10] The key questions appear to be: under what conditions might demixing occur, and how?

Many studies and conference presentations in recent years by the group of Cari Dutcher have provided insights into the exact mechanism by which demixing proceeds in the particle phase. Their experiments involve immobilising large droplets within microfluidic channels and observing them using high time resolution imaging. Instead of suspension in air, the droplets were formed by injection into silicone oils. The silicone media are designed with tunable refractive indices, which allows a crude determination to be made of the internal droplet concentration, on the basis of the imaged contrast between it and the surrounding fluid. The technique has recently been used to investigate droplets containing varying ratios of organic and inorganic compounds. They discovered that liquid-liquid phase separation (LLPS) always occurs after the insoluble compounds exceed their saturation concentration[116]. Phase separated aerosol tends to adopt

[10] As we are only considering secondary particles, it is likely that sodium or ammonium compounds will also be present given the formation mechanism. They will partition into the aqueous phase.

core-shell morphologies (more on these in Chapters 3 and 8) where the lower surface tension phase preferentially becomes the shell[117] (see Figure 1.4.1).

A comparison of LLPS in α-pinene SOA produced by four methods was recently undertaken by Ham et al.[118], using high magnification imaging. It was found that ozonolysis produces SOA that undergoes phase separation at around 95% RH, whereas photooxidation of α-pinene does not create any water insoluble compounds. Interestingly, the presence or absence of ammonia had no observable effect on the LLPS characteristics[118]. The result suggests that after it has participated in the nucleation mechanism, ammonia will not significantly alter the multiphase chemistry that forms low volatility compounds.

Nandy and Dutcher[116] also shed light on the dynamical features of the transition: the initial stages of the phase transition occur everywhere in the droplet at once, via a spinodal decomposition like mechanism[119, 120, 121].[11]

A comprehensive study of the phase state of aerosol sampled from many environments was conducted by Takahama, Liu and Russell of the Scripps Institute of Oceanography. They utilised X-ray microscopy[122], finding two general classes of particles that adopt a core-shell morphology: organic or soot aerosol with a layer of carboxylic acids surrounding the interface, and fully phase separated aqueous/organic droplets, with the organic phase becoming the shell. Interestingly, all but one of the particles were spherical, suggesting a low viscosity. The spectroscopic data revealed that some water resided in the organic phase and some organics in the aqueous phase, meaning that there may be some application for ternary mixing rules to determine the compositions of both the core and shell in these droplets. A similar scanning X ray imaging method was used by O'Brien et al.[117] to chart how the organic : inorganic ratios of both phases changed as core shell droplets were dried. They found that water was lost from both phases at low RHs. Interestingly, under humid conditions, it was observed that the outer phase can become mostly water and yet still not mix with the core.

[11] Briefly, instead of a single phase nucleating and growing within the other, instantaneous fluctuations in concentration allow many small nuclei to form at once, which then coalesce essentially randomly to form one coherent phase.

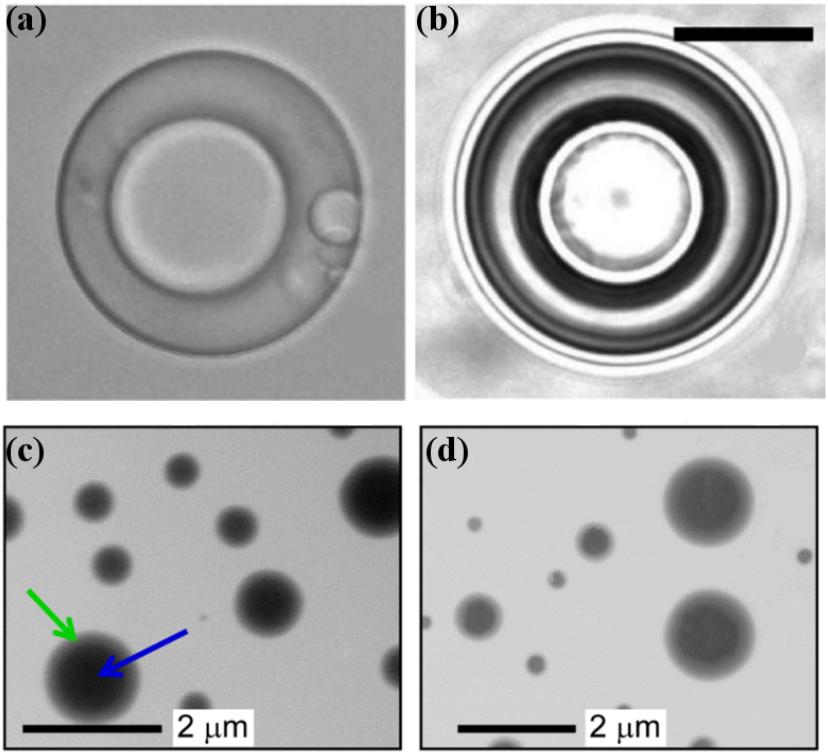

Figure 1.4.1: Observation of phase separated droplets in the literature. (a) 3-methylglutaric acid : ammonium sulphate at a molar ratio 2:1 (b) 3-mathyladipic acid : ammonium sulphate at a molar ratio 2:1 (scale bar is 50 μm). (c) and (d) 4-dihydroxy-3-methoxybenzeneacetic acid : ammonium sulphate at a molar ratio 1:1 in an RH of (c) 66% and (d) 20%. (a) and (b) are Brightfield images reproduced from Nandy and Dutcher[116] and (c) and (d) are electron microscopy images reproduced from O'Brien et al.[117]

1.4.2 The Glass Transition

Glasses are an interesting state of matter which possess a semingly contradictory combination of properties. They have the material properties of a solid, but the instantaneous molecular structure of a liquid. Specifically, they lack long range translational order, or a 'lattice', yet molecular motion is still highly restricted[123] (see Figure 1.4.2).

Interestingly, the glass transition is not a true phase transition, in the sense that there is no discontinuity in the key thermodynamic descriptors of the sample, such as density or internal energy[124]. Instead, the kinetic energy of the system gradually decreases and the object under

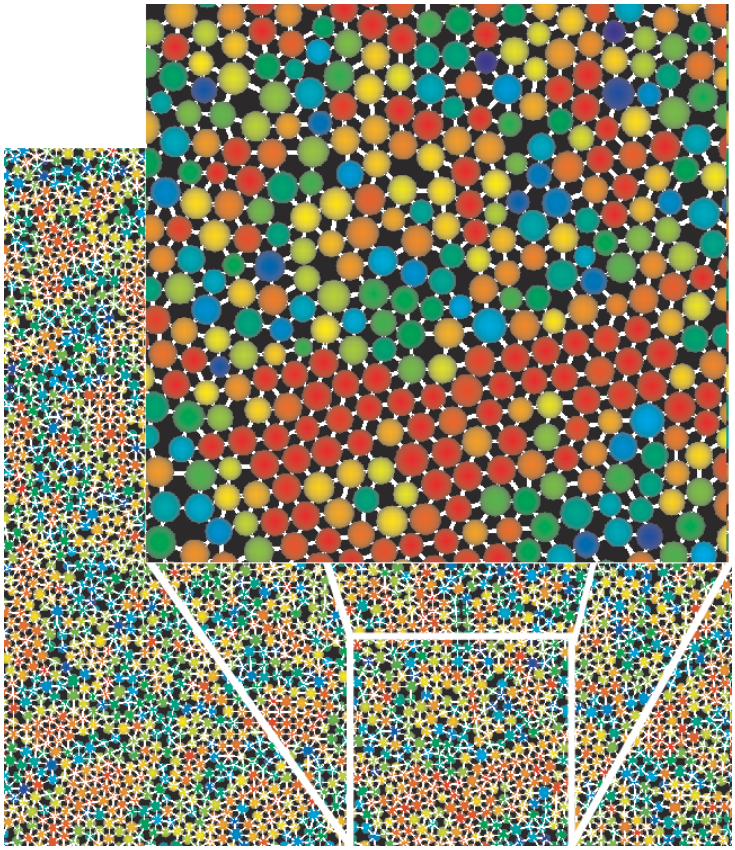

Figure 1.4.2: Example molecular structure of a glass formed of colloidal spheres, reproduced with permission from Tanaka et al.[123] The spheres are coloured according to the extent of local hexagonal order they experience.

study hardens, but without any spontaneous reorganisation occurring at the molecular level. As a result, the 'end state' is somewhat ill-defined and the rate at which the transition occurs can influence the structure formed. Some properties exhibited by glasses, such a specific volume, tend to adopt path function like behaviour[125].

While many of the compounds traditionally associated with glassy behaviour are inorganic minerals, a subset of organic molecules can act as 'glass formers'[126, 127], which tend to have low molecular weights (relative to polymers) and a high capacity for hydrogen bonding[128, 129]. Recalling the atmospheric chemistry described previously in this Chapter, it is entirely reasonable to assume that SOA particles exist as glasses at least some of the time.

Early Observations

The first suggestion that atmospheric aerosol could undergo a glass transition was made by Zobrist et al. in 2008[130]. The publication drew on two major factors in asserting this: the viscous nature of many organic species in their pure state,[12] and the humidity dependent composition of aerosol heavily implied the existence of a moisture driven glass transition. Interestingly, the arrest of molecular diffusion occurs due to dehydration rather than the decreasing kinetic energy of the molecules, as in a 'conventional' glass transition as the temperature is lowered below the glass transition temperature. Following a change in gas relative humidity (RH), there occur large increases in organic solute concentration close to the surface[132, 133].

Therefore, temperature and humidity both play an effect in the vitrifying of droplets. At low temperatures, the rate of ice formation in the aerosol phase will be slower than it would otherwise be in the bulk phase as generally no heterogeneous nucleation sites are present in the particles. Dehydration can therefore cause concentrations of solute to be accessed that significantly arrest diffusion, even at high relative humidities[134]. If molecular motion is slowed and sufficient water is driven from the particle, the system is confined to a metastable, amorphous 'solid-melt' type structure[135]. No kinetic pathway is available to undergo a phase[136] transition and form an equilibrium crystal phase[137]. A diverse range of laboratory and ambient aerosol measurements have amassed data to support this hypothesis in the intervening years[138, 95]. Some of the most important will be described presently.

Advances in Experimental Techniques

Many different techniques have been developed to measure particle viscosity, some of which are sensitive to different magnitudes and different particle sizes. Indeed, it is now possible to chart changes in viscosity to a rather high degree of precision as a function of humidity[139]. One drawback any new method must overcome is the incredibly small sample masses involved

[12] With the notable exception of cis-Pinonic acid and 3-methyl-1,2,3-butanetricarboxylic acid[131], it is extremely difficult to buy or synthesise any of the molecules known to reside in SOA. As such, compounds with similar molecular weight and hygroscopic responses are often used as proxies.

when probing the aerosol phase, where even generating a large ensemble over many hours will be unlikely to provide more than μg of material. As a result, many of these techniques require high magnification or high time resolution imaging.

One of the more ingenious methods developed in recent years is fluorescence lifetime imaging, or FLIM[133]. It operates by doping particles with a fluorophore whose molecular structure contains two rings, connected by a straight chain of sp^1 hybridised carbon atoms. Upon absorption of a photon, the rings can rotate in the excited state such that their planes are perpendicular to one another, a conformation that must relax back to planar in order for the molecule to relax electronically (Chapter 3 contains a schematic example of the fluorescence process). The particles studied can be either deposited on a coverslip[133] or, more recently, the technique has been extended to study optically levitated aerosol[140]. Arguably the most important discovery that has been made using fluorescence imaging is that processes like oxidation[141] and dehydration[142] do not change viscosity in a uniform way throughout the particle. Instead there is a considerable degree of heterogeneity, both between the surface and the core, but also on even smaller length scales.

As viscosity defines the resistance of a material to stress or deformation, several experimentalists have resorted to simply deforming aerosol particles and measuring their subsequent responses. Bounce fraction[143] and 'Poke and Flow'[144] techniques are two such examples. The former involves accelerating an ensemble of particles at a surface and measuring the proportion that rebound ('bounce') successfully, versus adhering or simply exploding. This is rather severe, not to mention destructive of the sample, and is also difficult to extract quantitave information unless a suitable material can be used to calibrate the apparatus in advance. Nonetheless, among other publications, it has been used to successfully determine changes in the proportion of liquid like particles in Beijing throughout the year[145], and to investigate viscosities of α-pinene SOA present at different mass loadings[146]. Both of those studies have contributed to what appears to be an emerging consensus in the literature that water transport in SOA is usually fast (a result of the liquid like state), at least in the planetary boundary layer[147]. This has been

corroborated recently by observations of aerosol sampled from both urban[148] and rural[149] sites.

Poke and Flow is somewhat similar to bounce fraction but relies on stationary particles being pierced by a metal rod, and then recovering a spherical shape at a rate that is calibrated to systems of known viscosity. It has been used to investigate both isoprene[150] and α-pinene[151] SOA recently, showing broad agreement with previous literature[144]. It is not sensitive to highly viscous states (i.e. under dry conditions) as the droplets are prone to shattering.

Coalescence of particles is a useful method of quantifying viscosity, since it requires a change in shape on the same length scale as the particle itself. Contactless coalescence is possible using optical trapping[152], with an added advantage that the surface tension of the droplet is also determined simultaneously[153]. Rothfuss and Petters have developed a novel *ensemble* coalescence method[154], wherein many pairs of droplets are created and sized as they travel through a temperature and RH controlled environment. The proportion of coalesced particles that fully relax to a spheical shape in a given set of conditions can then be related to whether a glass transition has occurred. As of now, the apparatus has been used to study viscous aerosol coated in surfactants[155], the systematic effect of hydroxyl functional groups on viscosity[156], and ternary organic + inorganic aerosol[157].

Some authors have designed computational models which can simulate both the dynamics of aerosol and a gas phase in concert, allowing a representation of viscous aerosol to be inserted into a representation of the atmosphere. For instance, Zaveri et al.[158] developed MOSAIC (Model for Simulating Aerosol Interactions and Chemistry) which has since been used in over one hundred studies (at the time of writing), and introduced into the Met Office's WRF-CHEM (Weather Research and Forecasting with coupled Chemistry) model[136], allowing the mixing state and gas-particle partitioning to be solved explicitly.

Recent models by Topping and O'Meara[159] have begun to employ analytical solutions to molecular diffusion rather than numerical evaluations. How and why these differ from each other will be explored in Chapter 2 and so will not be expanded any further here, aside from to note

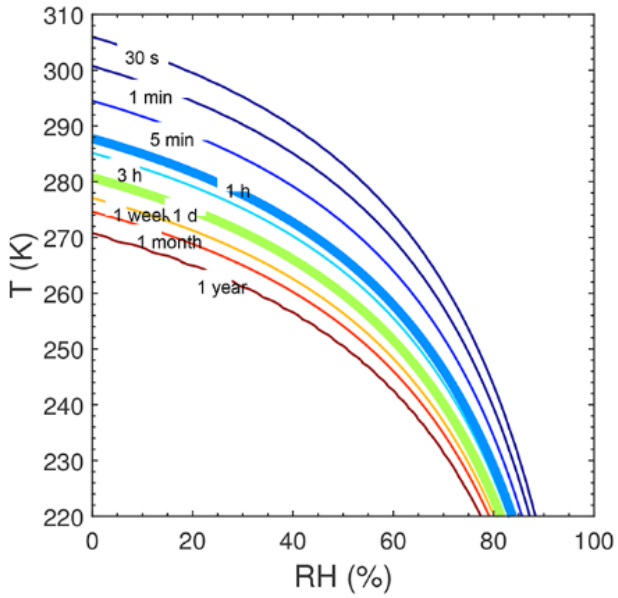

Figure 1.4.3: Simulated timescales for the uptake of a semivolatile compound to reach equilibrium with SOA particles as a function of humidity and temperature, reproduced from Li and Shiraiwa[160]. The involatile mass is assumed to possess a glass transition temperature of 270 K. See reference and supplement for model information.

that they claim the speed increase from doing so is significant enough that they could in theory be input into global climate models.

Shiraiwa and Seinfeld demonstrated from numerical modelling[161] that the mean equilibration times of a condensing species is strongly dependent on the mass loading of aerosol in the atmosphere, i.e. the amount or *pre-existing* particles present, in addition to RH and temperature. They found that in more pristine environments, indicative of remote areas such as the Hyytiala forest in Finland or Jungfrau-joch in the Swiss Alps, fewer particles are present and so consequently the uptake time takes on the order of days to weeks when the bulk diffusion coefficient is 10^{-15} m^2s^{-1}. A more recent study probed the influence of volatility and glass transition temperature, finding a strong effect of both[160]. One such example is presented in Figure 1.4.3.

Clearly, it is becoming desirable to identify instances where gaps in the current scientific understanding of aerosol microphysics tend to limit our ability to predict atmospheric phenomena, and focus particular attention on those areas[162]. Firstly, it is useful to reappraise how

that has been done, in addition to how atmospheric conditions have been reproduced by others in laboratory settings.

1.5 Laboratory Techniques

A laboratory environment provides an opportunity to control for at least some of the complexity of an aerosol system, as the literature cited until now should attest: The existence of the glassy state in organic aerosol has been established through years of accumulated research, involving both field campaigns and measurements made on aerosol prepared in laboratories. That the same dynamical behaviour is seen in these 'synthetic' aerosol plumes as in the real atmosphere allows us to have confidence that similar chemical mechanisms are occurring in the lab as in the atmosphere. What follows is an overview of the experiments that are commonly conducted in the literature, the information that can be generated from them, and brief discussions of their strengths and weaknesses. Once again, introducing the research into SOA will be the primary focus.

1.5.1 Particle Formation or Generation

Smog Chamber Experiments

As it turns out, it is relatively straightforward to induce new particle formation within a laboratory environment. The methods that have evolved to achieve this generally conform to one of three types: smog chambers (either batch or continuous flow) and flow tubes. The purpose of this subsection is to briefly introduce the techniques themselves. Enough studies employing them have been and will be referenced elsewhere in this Chapter. What they have in common are the controllable presence of VOCs, oxidants, NO_x, water vapour and photochemistry.

Flow tubes are perhaps an evolution of the shock-tube technique used in combustion chemistry to study rate constants, and are expectedly a more extreme method of particle formation. They involve rapid air flow, allowing efficient mixing of precursors with oxidants. Processes can

be investigated in a highly time resolved way because spectroscopic instruments can be placed along the tube in any position, corresponding to very fine increments of time after nucleation. An early flow tube study[13] which professed to be applicable to the aerosol formation process was conducted by Ulrich Poschl et al. in 2001[164]. They probed the ozone and water uptake onto soot particles coated in benzo-pyrene, and calculated the first order oxidation rate, as well as the enthalpy change of ozone and water absorption. Later, a flow tube experiment more compatible with study of new particle formation and tropospheric aerosol was described by the group of Barbara Finlayson-Pitts[165].

Batch reactors operate in an essentially closed system, with the exception of ultraviolet illumination. The reaction is studied spectroscopically and the particles are collected once the system is judged to have reached a steady state. One potential drawback of operating in a batch mode is that some of the reactants may be consumed entirely during the experiment, meaning that the relative concentrations of certain key species will continuously change over time[166]. This is not a realistic simulation of atmospheric processes, as the resupply of a given reactant can usually occur if it is present at a high enough saturation.

Continuous flow reactors are arguably more common in the current literature. They allow a better analysis to be made of the evolving properties of an ensemble of aerosol. Usually, chambers are outfitted with multiple pieces of analytical equipment. For instance, the AIDA[167] chamber (Aerosol Interaction and Dynamics in the Atmosphere) contains a Condensation Particle Counter, both Scanning Mobility and Aerosol Particle Sizers, and two mass spectrometers to monitor gas and particle phase chemistry. Similarly, the group of Jacqui Hamilton in the University of York have pioneered the analysis of organic aerosol using gas chromatography[168] on samples generated in a photochemical flow reactor.

Some smog chambers go to great lengths to increase their atmospheric relevance. Many are outdoors, and transparent, allowing terrestrial solar radiation to directly interact with the chemistry occuring within. Clearly, they must reside in a somewhat warmer climate for this to

[13]Regarding atmospheric *chemistry*, many works by Nobel laureate Mario Molina utilised flow tubes, and predate the Poschl work by several decades[163].

be of any use. The EUPHORE (European Photoreactor) operated by the Mediterranean Center for Environmental Studies in Valencia, Spain is one prominent example. One of its studies has already been referenced, which investigates oligomerisation in α-pinene chemistry[78]. Another example is a highly interdisciplinary collaboration that proved that ammonium compounds must be present for efficient production of imidazole compounds to occur from glyoxal[169] (see section 1.3.1).

Arguably the largest and most sophisticated chamber currently in operation is the CLOUD (Cosmics Leaving OUtdoor Droplets) experiment at CERN[170]. Its original purpose was to investigate the potential for cosmic rays to influence the rate of new particle formation, a hypothesis that eventually proved to be incorrect[14]: the mechanisms described in section 1.2.2 remain the best current explanation of how aerosol nucleates, and ionisation of molecules by collision with high energy subatomic particles has little to no impact on the process[171]. More recently, the researchers at CLOUD have begun to focus on the role of organics in nucleation[172].

1.5.2 Measurements of Diffusional Kinetics

It was stated previously that the glass transition does not involve discontinuities in intermolecular bonding or motion. In fact, many experiments conducted on mimics of atmospheric aerosol support this, since dynamic changes in size can only be reproduced by assuming that diffusion slows smoothly as water activity decreases, rather than instantaneously at the glass transition RH[173, 97, 174, 175].

Net diffusion of matter is a process that requires a thermodynamic driving force, which can be either entropic (the equalisation of a concentration gradient) or enthalpic (insoluble molecules demixing from solution) in nature. While each molecule may move in a chaotic, Brownian way, the cumulative effect is mass transport towards the new equilibrium state. Conversely, if there is no disequilibrium, molecular motion does not stop, but instead the lack of coherence has the effect of cancelling each other out to create no effective change in the distribution over time.

[14] Perhaps a more accurate term would be 'negligible'.

A diffusion coefficient, D, therefore represents an average across many similar processes which operate across a range of efficiencies.

Some publications that refer to measuring diffusion actually approximate it by measuring viscosity and converting from one to the other through the Stokes-Einstein equation[176, 143, 177, 178]:

$$D = \frac{k_B T}{6\pi\eta a}, \tag{1.5.1}$$

which equates the diffusion coefficient of a species, D, to the ratio of the thermal energy, $k_B T$, supplied by the surroundings to the friction that that species experiences (via Stokes' Law). η is the local viscosity and a is the hydrodynamic radius of the diffusing molecule. The origins, assumptions and failures of this equation will be the subject of significant discussion in later Chapters (namely 5 and 7), so those aspects will not be discussed presently.

A recent laboratory study by Ullmann et al. published independent measurements of viscosity and diffusion in thin films of limonene SOA. The diffusion was estimated through the dissipation of photobleached molecules impregnated into the sample[179], and found to conform to equation 1.5.1 within the error of the measurement.

There are currently two single particle strategies by which the dependence of the diffusion constant of water on composition in viscous aerosol can be determined. In the first strategy, particles are exposed to step changes in humidity that drive water loss from the particle surface. The rate of water loss from the surface is extremely rapid; often, the core of the particle cannot respond rapidly enough to equalise the water activity before diffusion is effectively arrested near the surface. The radial heterogeneity that is 'dried in' to the particles is well documented[132, 122]. and modelling the subsequent internal water transport phenomena is central to extracting diffusion coefficients from experiments conducted on optically trapped and electrodynamically levitated particles[180, 112, 181].

In a second strategy, the water activity is maintained at a constant value but the gas phase water is instantaneously switched from normal to deuterated water, leading to progressive iso-

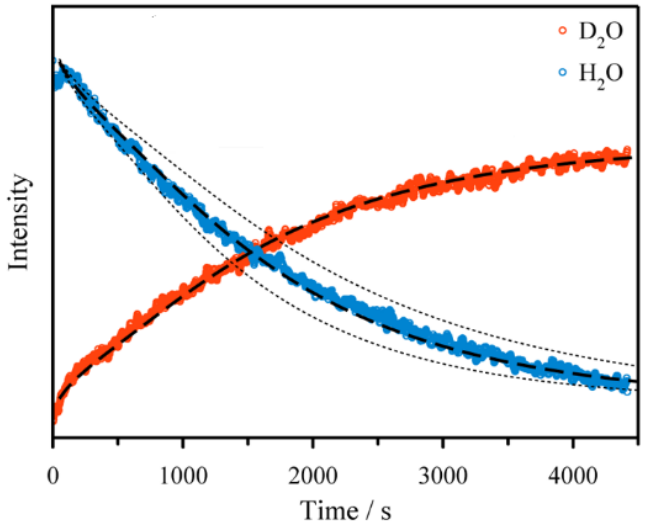

Figure 1.5.1: Charting the exchange of water for deuterated water in a single droplet using Raman spectroscopy. Points are the integrated intensities of the O-H (blue) and O-D (red) Raman bands. Figure has been reproduced from Davies et al.[182]

topic exchange within the particle. The change in isotopic ratio can be studied by integrating the O-H and O-D stretching frequencies in the Raman signal of the droplet[183]. As the 'water' activity is not changing *per se*, the equilibrium composition of the droplet is constant and well defined throughout the experiment, and so the extent to which the exchange has taken place is easily calculable. Therefore, the rate of D_2O uptake is directly coupled to the diffusion constant of water at that relative humidity. This method has been used to study particles either deposited on a substrate[184] or optically trapped[182]. Indeed, a similar approach has been extended to study the slow diffusional mixing of non-deuterated and deuterated sucrose between two contacting phases at low water activity, highlighting the conformity of sucrose diffusion constants to the Stokes-Einstein equation, whilst supporting that water transport is significantly faster[185]. More broadly, the diffusion constants of large organic molecules in viscous aerosol or through viscous shells on aerosol particles have been inferred from kinetic measurements of the rates of volatilisation of tracer compounds including, for example, pyrene[174].

1.6 Outlook and Thesis Overview

It has hopefully become apparent that the impacts of organic aerosol can be wide ranging, influencing for instance cloud cover[186, 187, 188], particulate matter concentrations in cities[189, 190], and the radiative balance of the atmosphere[191]. Yet the key processes governing the evolution of atmospheric aerosol take place on time and length scales much smaller than the current resolution of climate models. It is therefore desirable to identify instances where gaps in the current scientific understanding of aerosol microphysics tend to limit our ability to predict atmospheric phenomena, and focus particular attention on those areas.[162]

If we wish to investigate particles that replicate the properties of SOA, it is important to understand the molecular features of the products of organic chemistry that takes place in the atmosphere. Several oxidation schemes of common VOCs were presented in this Chapter in this vein. On the basis of the common products of isoprene and α-pinene, we can say that SOA molecules contain high levels of oxygentation, as well as the presence of acid, aldehydes or ketone functional groups in the backbone. It seems that larger molecular masses and an increased presence of ring structures (aliphatic, rather than aromatic) are the hallmarks of organic aerosol that has been further oxidised in the particle phase.

The physical properties of organic constituents can be changed by atmospheric processing and in turn change dynamic processes that the aerosol mass undergoes: gas-particle partitioning can be slowed and cease to maintain an equilibrium between the gas and particle phases. Chapter 2 will describe analytical and numerical models that can be used to distinguish between whether evaporation and condensation is occuring in an equilibrium or a non-equilibrium state. It will introduce concepts such as the folding time, bulk versus gas diffusion coefficients, and internal concentration gradients, which will become central to the discussions presented later in the thesis. It will include mathematical treatments of Fickian diffusion and a proof of a useful relationship between vapour pressure and particle surface area.

Chapters 3 and 4 will introduce the methods that have been used to generate data throughout my studies. They have been split as my working time invovled both laboratory and computational

studies, conducted in two different research groups.

The laboratory apparatus used was an aerosol optical tweezer, which is capable of the reproduceable capture and levitation of individual aerosol particles with radii of the order of microns (μm). The independent variable in all of the experiments which will be discussed was the gas phase, specifically the humidity and the presence or absence of VOC oxidation chemistry. Two mass flow configurations will be described that allow these conditions to be either maintained or changed rapidly at the discretion of the researcher. Mie theory will be introduced and two prototypical solutions to it will be presented, involving the scattering of either a homogeneous sphere, or a sphere coated with a small layer containing a different refractive index. Understanding both of these scattering patterns will be essential to the interpretation of spectra in later experiments.

Computational methods have also been employed in this thesis, namely molecular dynamics (MD). Chapter 4 will describe many of the key algorithms that underpin molecular dynamics packages, methods that can be used to set up and run simulations, and the general procedures that can be applied to interpret the resultant trajectories. It involves some subjectivity on the part of the user to decide which chemical systems and length scales are most appropriate to investigate. Effort will be made to describe the factors that one should consider when intuiting such things.

The technique has been applied to the problem of predicting the diffusion coefficients of water through organic matter at varying levels of dehydration, as well as the mechanism by which diffusion happens. This will be the focus of Chapter 5. The study relied on a large dataset combining simulations in which a single water molecule was tracked over a long timescale with others in which more water rich volumes of organic matter are investigated. The size regimes probed are significantly smaller than SOA and so can be considered a representation water transport close to the droplet interface.

Next, three distinct laboratory projects are described, each of which involve probing the responses of optically levitated droplets to perturbations in their external environment: specifically, relative humidity and the oxidation of a volatile organic compound in the surrounding gas phase.

Generally speaking, we wish to understand the extent of kinetic slowing due to diffusion through measurement of the lag between the adjustment of the gas phase conditions and a characteristic time for the particle to respond.

Chapters 6 is a large investigation of water evaporation in viscous organic aerosol. It presents a function that, when assumed to represent the smooth variation in diffusion as water is removed from aerosol, accurately reproduces changes in size induced through steps in RH. The function contains two variables which can be fit from many different experiments for each organic solute, or solutes, investigated. Comparison with several literature studies will be done, and the importance of what could be described as the thermodynamics within any diffusion model will be discussed; namely, how solute concentration and water activity are interrelated.

Organic solutes that are themselves volatile, or semivolatile, are investigated in Chapter 7. The applicability of the Stokes-Einstein equation to the prediction of their evaporation rates is also tested, and found to be appropriate. A variety of experimental viscosity data was 'hard-coded' into the diffusion model, bypassing the need for the optimisating variables.

Finally, Chapter 8 contains a more open ended set of experiments investigating the evaporative properties of the distribution of molecules produced when α-pinene is oxidised by ozone. A thin coating of SOA material is produced on both inorganic and organic particles in dry air, which is then allowed to evaporate into both dry and humid air. How reversible the condensation is observed to be should allow us to disentangle the competing effects of viscosity and volatility the product distribution. The optical properties of the coating are also extracted, as a by-product of the Mie theory approach, and compared with literature values.

Chapter 2

Kinetic Factors Influencing Gas-Particle Partitioning in Aerosol

"The fiction is already there. The writer's task is to invent the reality." - J.G. Ballard

---

A plume of aerosol suspended in a parcel of air can be thought of as an enormous interface, separating the interiors of individual droplets from the surrounding gas. In contrast to the liquid state, the proportion of molecules that may be considered 'at the surface' of the condensed phase is radically larger in an aerosol. Therefore, any change in the dynamic equilibrium of the plume that drives addition to, or subtraction from, droplet surfaces may substantially alter the total chemical composition of the aerosol. Indeed, many of the most important meteorological impacts of atmospheric aerosol are governed by surface processes.

The aim of this chapter is to describe the factors controlling the evaporation of, and condensation on to, aerosol particles. Primary focus will be given to water and organic vapours.

First, the thermodynamics of equilibrium partitioning are introduced. This culminates with a proof of the Maxwell treatment of evaporation, a useful relationship that will be utilised in Chapter 7 to infer the vapour pressure of a given species above a droplet's surface. Then, stepping

up in complexity, an analytical model of gas uptake into a single particle is described. Such a model allows a rudimentary prediction of the conditions under which equilibrium will be maintained between the gas and particle phases, or under which kinetic limitations ('slowing') will be observed.

The utility of this model is that it could be used to scan the parameter space of a laboratory experiment in advance, to approximately determine which experiments are likely to be fruitful: For instance, one could estimate the conditions most likely to produce a viscous aerosol that will slow water transport above a certain timescale, or determine the amount of a VOC that may need to be injected into a chamber experiment that will yield a given SOA mass.

Finally, two approaches to modelling intraparticle diffusion will be described. As we will see, in particles experiencing severe kinetic slowing of partitioning, the diffusional flux to or from the surface is the rate limiting process. Hence it becomes important, once evaporation experiments have been conducted, to rigorously understand the evolving internal structure of the droplet under study.

2.1 Gas-Particle Partitioning of Volatile Compounds

The vapour phase reactions that drive new particle formation in the Earth's atmosphere are highly complex and branching, as introduced in the previous chapter. Nonetheless, a generalised physical picture of the process can be constructed.

A chemical species can undergo functionalisation pathways, among others such as oligomerisation, as it is oxidised. Progression along such pathways will lead to a decrease in volatility, thereby driving uptake from the gas into the aerosol phase.[192] We would like to predict the quantitative relationship between these parameters: Namely, how much more uptake can be expected given a specific decrease in volatility of a condensing molecule.

The mass loading of the aerosol plume may also influence the thermodynamically favoured partitioning state: the more condensed phase available, the larger the mass of vapour taken up. Conversely, any dilution of the aerosol plume, perhaps through changes in atmospheric temper-

ature or pressure, will drive re-evaporation. This effect will also be neglected, as we will only consider the condensation of a single species onto a single droplet. The surrounding gas phase must therefore be treated as a 'thermodynamic bath' of sorts, with a constant background mass concentration of aerosol, and a constant partial pressure, p_∞, of the condensing molecule. The assumption that these do not change will greatly simplify the mathematics of the problem. Indeed, when considering single particles levitated using an optical tweezer setup, it can sometimes be assumed that $p_\infty = 0$. This will become apparent in Chapter 3.

2.1.1 Condensation of Semivolatile Species

In both urban and rural environments, aerosol populations will come into contact with many thousands of organic species suspended in the atmosphere around them. Each molecule will have its own propensity to condense, defined by its equilibrium saturation in the gas phase.

$$C^* = \frac{p_{svoc}\gamma_{svoc}M_{svoc}}{RT} \tag{2.1.1}$$

Where γ_{svoc} is the activity coefficient of the SVOC within the condensed phase of the aerosol, and p is its partial pressure, and T is the temperature. Depending on which units M_{svoc}, the molecular mass, and R, the gas constant, are expressed in, a factor of 10^6 may need to be introduced to convert C* to μg cm^{-3}.

Once again it should be noted that every substance present has a unique C*. If its mass in the ambient atmosphere of a droplet exceeds its C* value, vapours will begin to condense. If not, it will remain in the gas phase, or volatilise from the aerosol phase, if any is present.

There is a molecular aspect to the process which we are neglecting for the time being: Whenever each molecules collides with the interface of the droplet, it can rebound or adhere,[193] and the probability of adhering can be expressed via an accomodation coefficient. What happens next, i.e. whether the condensing molecules are capable of diffusing away from the droplet interface, and on what timescale, will be the focus of later subsections. For now, we are interested in describing the flux of a molecule as a function of its volatility.

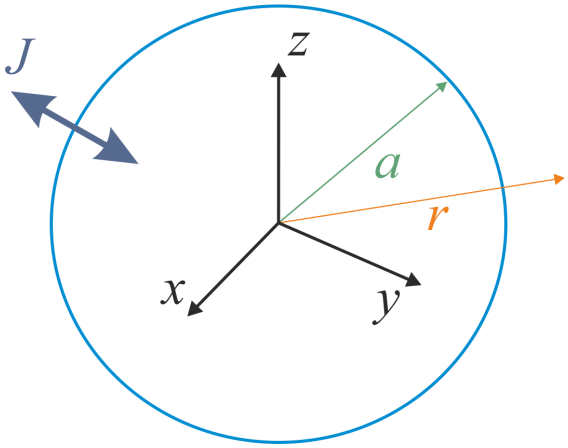

Figure 2.1.1: Schematic representation of the coordinate system used in this proof.

2.1.2 The Maxwell Treatment of Evaporation

Fick's first law states that the flux, J, of a gas phase species in a particular direction, will act in such a way as to neutralise any concentration gradient:

$$J = -D_g \frac{\partial C}{\partial r} \tag{2.1.2}$$

Where D_g is the diffusion constant in the gas phase, and C is some measure of the concentration. This law is itself a consequence of the Second Law of Thermodynamics, as any state in which $\frac{\partial C}{\partial r} = 0$ will have a higher entropy than a state in which more molecules are concentrated in one location than another. Note the use of spherical coordinates here; r denotes radial distance from the centre of the coordinate system. In this proof the evaporating droplet, of radius a, lies at the origin.

The dimensionality of flux is [moles][distance]$^{-2}$[time]$^{-1}$. Unfortunately, such a quantity is not often inferrable from experimental data, such as when the molecular mass of the partitioning species is not known, or when multiple species are evaporating simultaneously. It is more useful, therefore, to convert J to the *mass flux* out of the droplet, for instance in units of kg s^{-1}. The conversion is achieved through multiplication by Avogadro's constant, followed by the surface area of the droplet.

$$\frac{dm}{dt} = N_A \cdot 4\pi r^2 \cdot J \tag{2.1.3}$$

Substituting equation 2.1.2 into the above generates:

$$\frac{dm}{dt} = -N_A 4\pi r^2 D_g \frac{\partial C}{\partial r} \tag{2.1.4}$$

Which can be simplified further by replacing the partial derivative of concentration at the particle surface with the gradient in gas phase density ρ. More specifically, if we assume that $N_A \partial C = d\rho$, then it follows that

$$|\frac{dm}{dt}| = 4\pi r^2 D_g \frac{d\rho}{dr} \tag{2.1.5}$$

Where the direction of the flux has been ignored by taking the absolute value. This has the effect of making the next few equations general to both evaporation and condensation. By integrating both sides,

$$4\pi D_g \cdot \int d\rho = |\frac{dm}{dt}| \cdot \int \frac{1}{r^2} dr \tag{2.1.6}$$

we produce a function of the vapour density of the partitioning species, that decays radially outwards from the edge of the droplet into the gas phase:

$$\rho(r) = B - \frac{|dm/dt|}{4\pi r D_g}. \tag{2.1.7}$$

Here, B is the constant of integration that represents the asymptote of the decay at $r \to \infty$. By evaluating this limit, it can be seen that equation 2.1.7 collapses to $B \to \rho_\infty$. Physically, this means that the flux seeks to equalise the gas density directly above the droplet $\rho(r)$ to that of the ambient atmosphere ρ_∞.

The mass change can therefore be rewritten as

$$\frac{dm}{dt} = 4\pi r D_g(\rho_\infty - \rho(r)) \tag{2.1.8}$$

This is a general equation for droplet growth and shrinkage, and can be found in the early treatment of Fukuta and Walter[194]. In this case the modulus is not taken as the equation is now sensitive to the direction of the partitioning: For evaporation $\rho_\infty < \rho(r)$, whereas for condensation the inverse is true, $\rho_\infty > \rho(r)$. For the purposes of this thesis, several further steps are required to produce an equation that directly relates observable quantities from our experiments to more atmospherically relevant properties such as pressure or mass loading. Specifically, particle radius is used.

Firstly, if the species under consideration is semivolatile, then its saturation partial pressure p_∞ should be low enough that it will behave as an ideal gas, meaning that

$$\rho(r) = \frac{m_{svoc,gas}}{V} = \frac{p_{svoc}(r)}{RT} \cdot M_{svoc} \tag{2.1.9}$$

Where T is the temperature of both the particle and gas phases, which are assumed to remain equal throughout the evaporation process. As only $\rho(r)$ and $p_{svoc}(r)$ are functions of r, partial pressure can be substituted for density using the identity 2.1.9:

$$\frac{dm}{dt} = \frac{4\pi r M_{svoc} D_g}{RT}(p_{svoc}(r) - p_\infty) \tag{2.1.10}$$

One boundary condition that must now be applied is mass conservation,

$$\frac{dm}{dt} = \frac{dm_{svoc,gas}}{dt} = -\frac{dm_{svoc,droplet}}{dt} \tag{2.1.11}$$

which is to say that the flux *to the surface* is equal to flux *from the surface*. From here it is possible to directly relate the gas phase properties of the semivolatile to the droplet size. If we define the initial mass fraction of semivolatile in the droplet, F_{svoc}

$$F_{svoc} = \frac{m_{svoc,droplet}}{m_{droplet}} \tag{2.1.12}$$

then the initial, and indeed evolving, mass of semivolatile can be expressed as a function of droplet volume:

$$m_{svoc,droplet} = \frac{4}{3}\pi a^3 \rho_{droplet} F_{svoc} \tag{2.1.13}$$

In representative atmospheric conditions, semivolatile species are unlikely to be the only organic compounds present in a particle (there may, for instance, be nonvolatile components, in addition to water). Therefore, $\rho_{droplet}$ is the density of the entire droplet, including all other components.

Rearranging 2.1.13 such that a becomes the subject, we have

$$a^3 = \frac{3}{4\pi}\frac{m_{svoc,droplet}}{\rho_{droplet} F_{svoc}} \tag{2.1.14}$$

Then, using the chain rule, the above can be inserted into the mass flux equation, linking the change in particle volume during evaporation to the pressure above the surface $p_{svoc}(a)$:

$$\frac{da^3}{dt} = \frac{da^3}{dm_{svoc,droplet}} \cdot \frac{dm_{svoc,droplet}}{dt} = \frac{3aM_{svoc}D_g}{RT\rho_{droplet}F_{svoc}}(p_{svoc}(a) - p_\infty) \tag{2.1.15}$$

This is sufficient to interpret the kinds of experimental data that will be generated in this thesis. However, the dependence of the right hand side on radius, *a,* somewhat complicates this expression, and so one final manipulation is needed. Using the mathematical identity

$$\frac{da^3}{dt} = \frac{da^3}{da^2} \cdot \frac{da^2}{dt} = \frac{3a}{2} \cdot \frac{da^2}{dt} \tag{2.1.16}$$

the factor of a can be removed, yielding

$$\frac{da^2}{dt} = \frac{2M_{svoc}D_g}{RT\rho_{droplet}F_{svoc}}(p_{svoc}(a) - p_\infty). \tag{2.1.17}$$

Put concisely, this shows that an evaporating sphere comprised of one chemical species will lose its *surface area* at a constant rate. Working backwards, it also strongly suggests that any change in an observed value of $\frac{da^2}{dt}$ will be primarily due to a change in p_{svoc}, or p_∞.[1]

[1]The qualifier 'primarily' is used as the density and temperature will also fluctuate during an experiment. The influence of changes in mass fraction on the observed radius changes can be accounted for using Raoult's law, which will be described in section 2.3.1

2.2 An Analytical Solution to Vapour Condensation Onto a Sphere

If there is *more than one* chemical species in an evaporating droplet then concentration will decay over time. This process is captured by Fick's *second* law, which states that the rate at which C changes can be related to the change in flux as a function of distance. Combining this statement with equation 2.1.1 gives a differential equation in C:

$$\frac{\partial C}{\partial t} = \nabla J = \frac{\partial}{\partial x} + \frac{\partial}{\partial y} + \frac{\partial}{\partial z}(-D\frac{\partial C}{\partial r}) \tag{2.2.1}$$

Converting to spherical coordinates generates:

$$\frac{\partial C}{\partial t} = \frac{1}{r^2}\frac{\partial}{\partial r}(r^2 D\frac{\partial C}{\partial r}) \tag{2.2.2}$$

$$\frac{\partial C}{\partial t} = \frac{D}{r}[2\frac{\partial C}{\partial r} + r\cdot\frac{\partial^2 C}{\partial r^2}] \tag{2.2.3}$$

We wish to solve this two dimensional problem, in order to integrate the evolving value of C for a variety of diffusion coefficients D. Here D is more general, applying to both the particle and gas phases.

In a spherically symmetric droplet with an interface, we can define three boundary conditions that may help simplify the problem:

1. Due to radial symmetry, there is no flux across the centre of the droplet:

$$\frac{\partial C(0,t)}{\partial t} = 0 \tag{2.2.4}$$

2. The surface evaporation rate is linearly related to how far from equilibrium the concentration is

$$-D\frac{\partial C(a,t)}{\partial r} = k(C(a,t) - A_0) \tag{2.2.5}$$

where A_0 represents the value in equilibrium with the saturation mass concentration (equation 2.1.1) of the condensing molecule under consideration.

3. No semivolatile is present in the particle at *t=0*:

$$C(r,0) = 0. \tag{2.2.6}$$

To begin with, we shall normalise the concentration against A_0. If we assume a separation of variables, which is to say that the space and time dependence can be decomposed into radial and temporal functions,

$$\frac{C(r,t) - A_0}{-A_0} = R(r) \cdot T(t) \tag{2.2.7}$$

then the left hand side of the above differential equation becomes:

$$\frac{\partial C}{\partial t} = R(r)T' \tag{2.2.8}$$

(note that A_0 is constant with respect to time). Similarly, the right hand side becomes:

$$\frac{D}{r}[2\frac{\partial C}{\partial r} + r \cdot \frac{\partial^2 C}{\partial r^2}] = D \cdot R''T + \frac{2D}{r} \cdot R'T. \tag{2.2.9}$$

Where $R' = \frac{dR(r)}{dr}$ and $R'' = \frac{d^2R(r)}{dr^2}$. Equating and dividing through by RTD generates

$$\frac{T'}{DT} = \frac{R''}{R} + \frac{2}{r} \cdot \frac{R'}{R}. \tag{2.2.10}$$

Neither side of this equation is a function of the variable of the other, and so they must both be constant. We shall solve each side separately.

The radial dimension

If we define $\beta^2 = -\frac{T'}{DT}$ then

$$R'' + \frac{2}{r}R' + \beta^2 R = 0 \tag{2.2.11}$$

This is close to the simplest way the Ordinary Differential Equation (ODE) can be stated. For the final step, the following identity can be created using the product rule:

$$\frac{d^2}{dr^2}(R \cdot r) = R'' \cdot r + 2R' \tag{2.2.12}$$

Therefore equation 2.2.11 can be redefined as a function of $R \cdot r$:

$$(R \cdot r)'' + \beta^2 (R \cdot r) = 0 \tag{2.2.13}$$

Which has a known general solution

$$R \cdot r = \sigma_1 \sin(\beta r) + \sigma_2 \cos(\beta r) \tag{2.2.14}$$

To determine the values of the coefficients σ, we should return to the boundary conditions. Firstly, boundary condition 2.2.4 becomes

$$\frac{\partial R \cdot r}{\partial t}_{r=0} = R(0) = 0 \tag{2.2.15}$$

As the sine function passes through (0,0) and cosine through (0,1), straight away we can say that there is no cosine density in the solution, and therefore $\sigma_2 = 0$. This implies an infinite sequence of solutions of the form

$$R(r) = \frac{a}{r} \sin(\beta_n \frac{r}{a}) \tag{2.2.16}$$

where a is the particle radius. Substituting the above into the second boundary condition, 2.2.5, gives

$$-D \frac{\partial \frac{a}{r} \sin(\beta_n \frac{r}{a})}{\partial t}_{r=a} = kR(a). \tag{2.2.17}$$

This requires use of the product rule to evaluate, generating

$$-D[\frac{\beta_n}{a} \cos(\beta_n \frac{r}{a}) - \frac{a}{r^2} \sin(\beta_n \frac{r}{a})]_{r=a} = k \sin(\beta_n) \tag{2.2.18}$$

or, more concisely,

$$\frac{D}{ak} \cdot \frac{\sin(\beta_n) - \beta_n \cos(\beta_n)}{\sin(\beta_n)} = 1. \tag{2.2.19}$$

The accuracy of any solution to the radial dimension therefore relies on evaluating as many roots β_n of the above as is computationally feasible, assuming the values of k and D are known. Indeed, there has also been an implicit assumption throughout this proof that D is *symmetric*, by which it is meant that every compound in the droplet diffuses at the same speed.

The time dimension

The time dimension of the concentration function is considerably simpler. We start by rearranging the definition of β, and inserting the sum iterator n, giving:

$$\frac{\partial T(t)}{\partial t} = -\beta_n^2 DT(t) \tag{2.2.20}$$

This differential equation has an exponential solution of the form:

$$T(t) = \exp(-\beta_n^2 Dt) \tag{2.2.21}$$

By multiplying *T(t)* and *R(r)* we can now produce the general solution to the evolving concentration within the system:

$$C(r,t) - A_0 = \sum_{n=1}^{\infty} A_n \exp(-\beta_n^2 Dt) \cdot \frac{a}{r} \sin(\beta_n \frac{r}{a}) \tag{2.2.22}$$

Proving the identity of the coefficients A_n and their relationship to β_n is considerably more involved. The reader is directed to the supplement to the paper of Liu, Zaveri and Seinfeld for the full proof[195]. Suffice to say, the accuracy with which the solution can be found still depends on the number of roots that are evaluated. If n is large enough, this model can tell us a large amount about the time dependence of compositional changes within droplets. In fact, it is a realistic enough solution that it has been possible to model the isotope exchange of water and deuterated water in viscous aerosol using slight modifications to equation 2.2.22[184, 196].

Recent studies have used the physics described here to approximate gas-particle exchange in different aerosol systems: In addition to the original analytical solution proposed by Liu et

al.[195], the Zaveri group have continued to refine the treatment, introducing particle phase reaction kinetics into the solution[97]. This latter development was itself found to be of use in the interpretation of SOA formation[197]. O'Meara et al. have described several[198, 159] adaptable models of simple chemical systems, using both Fickian and Maxwell-Stefan approaches to molecular diffusion. Assuming an appropriate length resolution representation of the particle interior, the solution to the differential equation 2.2.2 will describe the time evolution of the amount of a condensing chemical species in the particle.

Here we will consider a slightly modified version of such a model.

2.2.1 Gas and Bulk Phase Diffusion Limitations to Equilibration

As stated at the beginning of the Chapter, our intention is to construct a model that may be used in rational experiment design: to assess the relative timescales of water and SVOC volatilisation from an aerosol particle, in order to determine the range of experimental conditions where they could most easily be analysed separately. Such an assessment should allow us to identify, in advance, the conditions under which the water loss rate is likely to be slowed beyond a certain value. Additionally, any model that allows the radius to vary would be able to identify the approximate timescale over which the loss of a known SVOC will drive a desired size change. As we will see in later chapters, this is useful for ensuring any measurement of the vapour pressure of a species is statistically significant. Of course, in any of the above cases, there may be uncertainty in the literature as to the value of bulk phase diffusion constants which would make precise predictions difficult. But that is, in a sense, the point.

To this end, an analytical model of the gas-particle partitioning of semi-volatile species has been described by Mai et al.,[199] that is based on the above treatment. It simulates the condensation kinetics of water or hypothetical SVOCs into a particle experiencing a small, but nonzero, change in the external gas phase saturation of each species.

For this thesis, a new version of this model was coded. Firstly, an assumption has been made that condensation and evaporation are reversible within this context, i.e. a positive or negative

value of $\frac{\partial C}{\partial t}$ will not influence the solutions determined by the ODE. Secondly, to connect some of the more abstract variables to physically measurable quantities, we have defined

$$L = \frac{ak}{D} = \frac{v_b^{-1}}{v_i^{-1} + v_g^{-1}} \tag{2.2.23}$$

Where the different v_b, v_i, and v_g parameters are the bulk, interfacial, and gas phase velocities of the condensing molecule respectively. L is therefore a characteristic, dimensionless number that defines approximately whether motion in the particle phase is faster or slower than in the surrounding gas phase. The original publication defined the different velocities according to:

$$v_b = \frac{D_{svoc}}{a}, v_i = \frac{v\alpha}{4H}, v_g = \frac{D_g}{aH} \tag{2.2.24}$$

Where H is the Henry's law volatility constant for the condensing molecule, and α is the accomodation coefficient. a and D_{svoc} are as defined in earlier sections of this Chapter. Here we have fully adopted the above framework: α was set to 1 and n to 100. The velocity, v, is defined by the mean value of the Boltzmann distribution of the condensing species at 296K,

$$v = \sqrt{\frac{2RT}{M_r}} \tag{2.2.25}$$

and indirectly through the Henry's Law coefficients:

$$H = \frac{\rho_{droplet}}{C*} \tag{2.2.26}$$

where the density, $\rho_{droplet}$, is likely to increase and mass loading, $C*$, is likely to decrease as molecular weight becomes larger.

2.2.2 Systematic study of the Characteristic time for Equilibration of Atmospherically Relevant Small Molecules

We wish to understand which process is the bottleneck to uptake. Here we have chosen to investigate water (whose atmospheric relevance is clear), malonic acid and cis-pinonic acid, as

prototypical molecules that partition between the gas and aerosol phases. cis-pinonic acid is a first generation oxidation product of α-pinene, that has been observed in SOA mass[200, 201], and has known surface activite[202, 62] properties. Malonic acid is a diacid of similar volatility to pinonic acid and will be used as a proxy molecule for SVOCs in several of the studies described in later Chapters.

A small note on nomenclature before the main discussion: The folding timescales for each component within the particle, τ, were defined as the timesteps at which the integrated concentration reaches a factor of *1/e* of its equilibrium value. This method was also employed in the original publication, in recognition of the exponential nature of the uptake process.[199] These may also be referred to as *mixing* or *equilibration* times, depending on the mechanism of uptake, and the strength of the concentration gradient formed between the surface and the center. The magnitude of the final concentration (A_0 in the notation of the previous subsection) does not influence the calculation, meaning that compounds of vastly different volatilities can be compared.

The tunable parameter in the model is the condensed phase diffusion coefficient for each species under consideration. Values are varied logarithmically within atmospherically relevant bounds (10^{-12} - 10^{-19} m^2 s^{-1}). All other parameters resemble as closely as possible the physical and molecular properties of the molecule in question.

Firstly, we can see that at the limit of very slow diffusion, the mixing times rise exponentially. All three compounds show identical dependences of diffusion on mixing time. It is therefore within this regime that the approximate relationship

$$\tau = \frac{r^2}{\pi^2 D_{svoc}} \tag{2.2.27}$$

holds[147, 203, 204]. Note that there are no terms that relate to the physical or molecular properties of the SVOC. The relationship therefore cannot account for situations in which compounds with the same D_{svoc} mix on different timescales. Indeed, this is exactly what is predicted by the model.

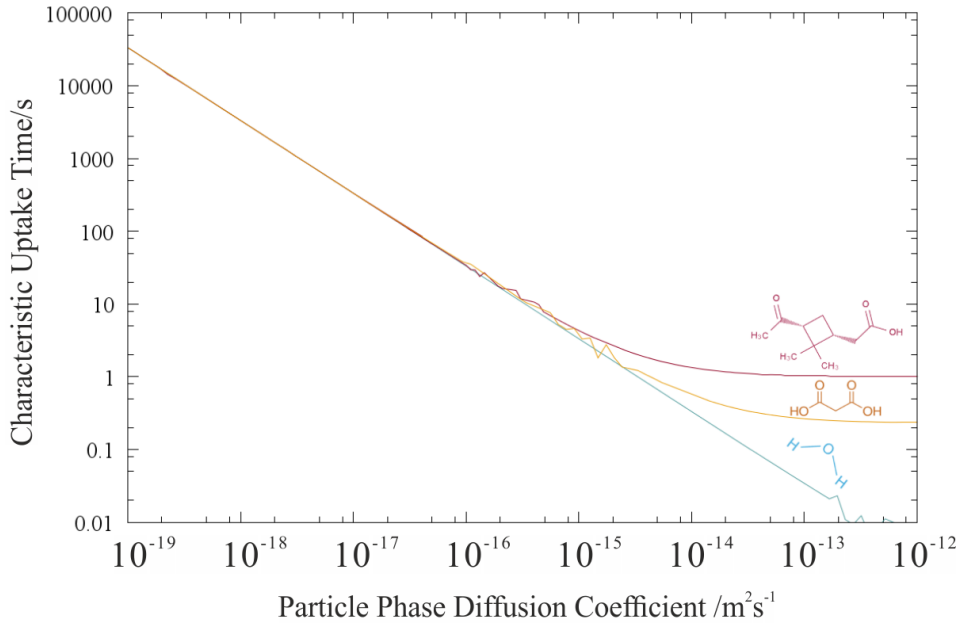

Figure 2.2.1: Concentration folding timescales, calculated over a wide range of particle phase diffusion coefficients D for two condensing volatile organic compounds (VOCs), in addition to water. The particle radius is 200 nm, and the model timescale is continuously adjusted as the uptake slows.

At the limit of fast diffusion, they become separated and the uptake of organic compounds transitions into a regime where it is almost constant with respect to D. This is the gas diffusion regime. Comparing the right hand intercept at 10^{-12} m^2s^{-1} for a 200 nm radius particle, the trend in timescales directly follows the volatility, as expressed by the Henry's Law coefficients in the Table below.

Compound	Henry's Law Constant	Gas Diffusion Velocity/ms^{-1}
Water	4.3×10^4	522.91
Malonic Acid	6.60×10^7	217.48
cis-Pinonic Acid	2.86×10^8	163.45

Interestingly, there seems to be an interplay between the the gas velocity and the volatility (as expressed through the Henry's law constant) in determining the limiting rate of uptake. The two trends are coupled, in that the more volatile molecules tend to have a lower molecular weight,

which shifts the Boltzmann distribution of speeds to higher values (in this case a temperature of 296 K was assumed). Yet the separation of timescales at $D = 10^{-12}$ m^2s^{-1} is less than the four orders of magnitude that separate the H coefficients. This suggests that an accurate description of gas phase kinetics is crucial to prediction of τ for semivolatile molecules.

Around the intermediate regime between the two limits, numerical instabilities begin to appear in the solutions to the equations. They causes fluctuations in the amount of predicted uptake, which manifests in the 'jagged' appearance of the organic curves in this region. Such behaviour may be the result of the shell width in the model (2 nm) being too small, approaching the length of one molecule. Nonetheless the microphysics appears to have been captured accurately: Three examples of rates at which the induced concentration gradients make their way from the interface backwards into the particle are presented in Figure 2.2.2. Panels a-c represent decreasing rates of bulk diffusion, and so increasing degrees of kinetic limitation.

Inspection of the intermediate regime reveals aspects of the two limiting behaviours: the first 50 s proceed by the growth of a condensing layer, from the surface down, as in panel (c). Conversely, once the semivolatile reaches the core of the droplet (50-100 s) the remaining uptake occurs via rapid increases in concentration at all radial coordinates, as in panel (a).

We also consider the equilibration timescales for particles of radius 5μm in Figure 2.2.3, a size of more relevance to particles that may be trapped during optical tweezer studies. The trends have a similar appearance but are shifted to longer timescales by almost three decades. In this case, the self-diffusion coefficient below which all three timescales collapse to v (equation 2.2.25) is 10^{-15} m^2s^{-1}, with the same divergence at the gas diffusion limit as observed for the 200 nm particle. Comparing the timescales of the two organics at this limit, it can be seen that equilibration takes substantially longer in the larger particle (80 vs 0.2 s for malonic acid). Such a large increase reflects that the mixing process scales with the volume of material in the droplet rather than the radius. Indeed, τ begins to exceed the mean atmospheric lifetime of such a droplet below a diffusion value of approximately 10^{-18} m^2 s^{-1}.[2] This may have implications for

[2]Seinfeld and Pandis[203] gives the lifetime of a 1μm droplet as 11.8 days, or 1.02*10^6s

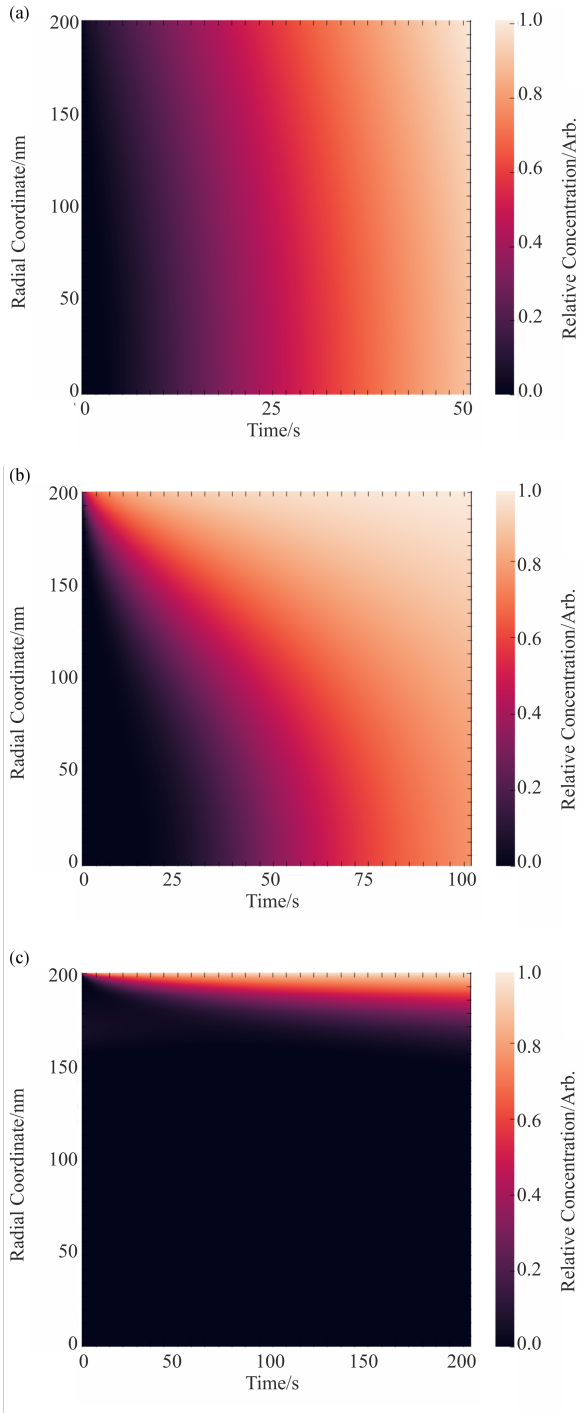

Figure 2.2.2: Internal dynamics of the simulated 200 nm particle during uptake of cis-Pinonic acid (red line on previous figure), assuming varying values of D_{svoc}: (a) 10^{-15} (b) 10^{-16} and (c) 10^{-18} m^2s^{-1}. The interface is at the top, the core of the particle is the bottom. The colour scales have been normalised for clarity.

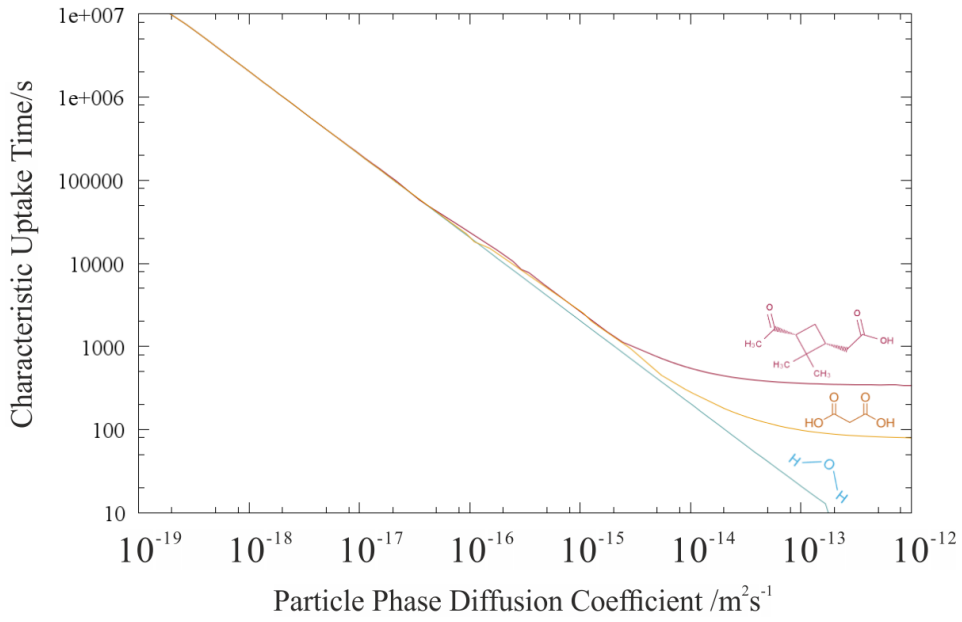

Figure 2.2.3: As in Figure 2.2.1, concentration folding times expressed as a function of diffusion coefficients. In this case, the particle radius is 5μm. All other parameters are as described in the main text.

the atmospheric relevance of any kinetic measurements made on optically tweezed particles in this thesis.

2.2.3 Water Partitioning as a Special Case

Interestingly, the partitioning of water follows a different trend to that of the organics in both particles. τ_{water} continues to decrease in the same logarithmic fashion as D_w increases across the entire range, whereas the SVOC volatilisation enters the gas limited regime described above.

While these simulations do not probe D_w values approaching the self diffusion coefficient (2×10^{-9} m^{2}s^{-1}), any onset of a gas diffusion limited state for water uptake will occur at mixing times substantially less than 1 s. This renders them almost immeasurable by the techniques that will be employed in this thesis, and cetainly too fast to be explicitly included in atmospheric models. As semivolatile organics have lower equilibrium vapour pressures than water, particle phase transport of organics will be slower than τ_{water}. Therefore, the above figures show that

the water content of a gas-particle system will always be able to adjust to compositional change during the change itself; the water 'co-condenses'.

The fact that water equilibrates faster than the organic compounds is a consequence of it exhibiting a faster rate of resupply to the particle surface. In fact, the diffusion from the far gas phase to the surface to is so fast in the model that the surface and core concentrations always equilibrates more slowly within the range of D_w probed. In addition, the higher saturation concentration of water means that, proportionally, the amount of molecules 'leaving' the vapour phase during mass uptake by the aerosol will be lower.

Within the analytical treatment of the model, both of these effects are a consequence of the molecular weight of water being lower than the organics. Therefore, through equations 2.2.23-26, the gas velocity will be much higher than the bulk velocity and the consequently L will be much smaller than 1. Indeed, this may go some way to explaining the unique properties water exhibits in this context: It is about as light as it is possible for a molecule to be that still exists in equilibrium with a condensed phase under atmospheric conditions.

Once it has partitioned into the condensed phase, D_w is usually found to be significantly faster than D_{svoc}, at any given particle composition. Figures 2.2.1 and 2.2.3 therefore do not directly map onto RH, as each of the three molecules will have a unique dependency of the uptake timescale on water activity. To investigate further, the ratio τ_{svcc}/τ_{water} has been calculated as a function of RH for both particle sizes, and is presented in Figures 2.2.4 and 2.2.5.

In producing these figures we have assumed that D_w varies according to a sigmoidal equation (see section 2.4), where $D_{w,org}$ is 10^{-16} m^2s^{-1}. D_{SVOC} is assumed to follow the Stokes-Einstein relationship[176] with a hypothetical viscosity range of 10^{-3} Pas to 10^{7} Pas between relative humidities of 100% and 0% respectively. This assumption will be tested more rigorously against experimental data for a variety of semivolatile species in Chapter 7 of this thesis. Malonic acid was defined with a Stokes flow diameter of 4.7$\mathring{A}$, and cis-Pinonic acid of 6.5$\mathring{A}$. Other model parameters are as follows: Temperature = 296 K, accommodation coefficient α = 1, particle density $\rho_{droplet}$ = 1.4 gcm^{-3}, gas phase diffusion coefficient = 10^{-5} m^2s^{-1}.

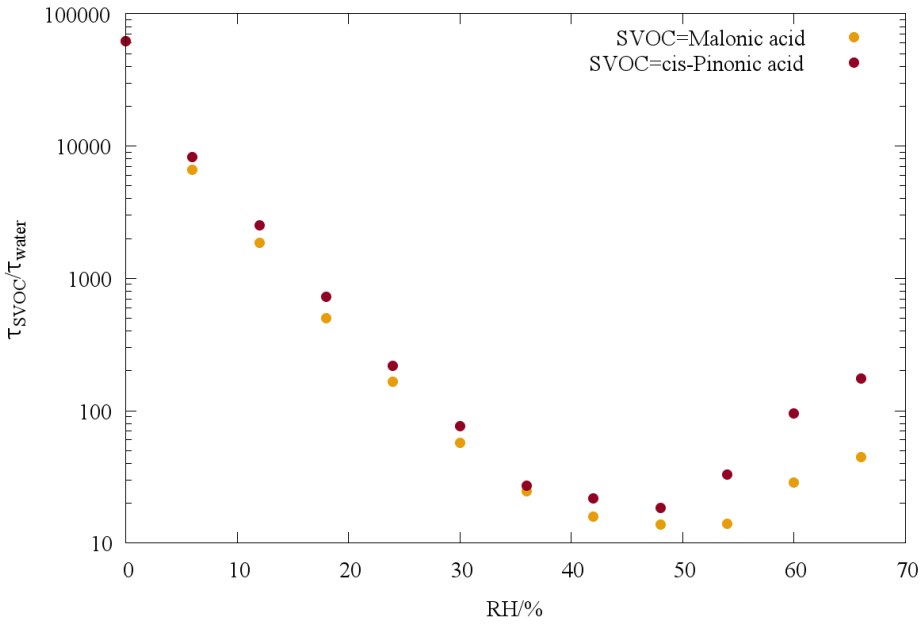

Figure 2.2.4: The ratio of the uptake timescales for two organics to that of water, within a 5 μm radius particle experiencing RHs below ~60%. The figure has been produced assuming that D_{SVOC} follows the Stokes-Einstein relation whereas D_w varies sigmoidally with RH (see chapter text).

For the tweezer radius particle, the dependence is more complex than increasing monitonically. The timescales are most similar in the region $40\% < \mathrm{RH} < 50\%$, where the ratio approaches $\tau_{svcc} = 10\tau_{water}$. At higher humidities, gas diffusion limitations begin to manifest for both malonic and pinonic acid uptake, placing a lower limit on τ_{svoc}. Meanwhile water continues to mix faster within the particle, increasing the separation between τ_{water} and the other two timescales. The slightly larger ratio for cis-pinonic acid suggests that, at least within the analytical framework, small differences in the Stokes flow diameter can have a disproportionate effect on the predicted mixing timescale. At lower humidities, water diffusion reaches a plateau which the organics do not experience, placing an upper limit on τ_{water}.

Taken together, these results tell us that within the crossover region between the bulk and gas diffusion limits, the kinetics of gas particle exchange are highly sensitive, not only to slight changes in molecular properties, but also to the initial conditions the particle experiences.

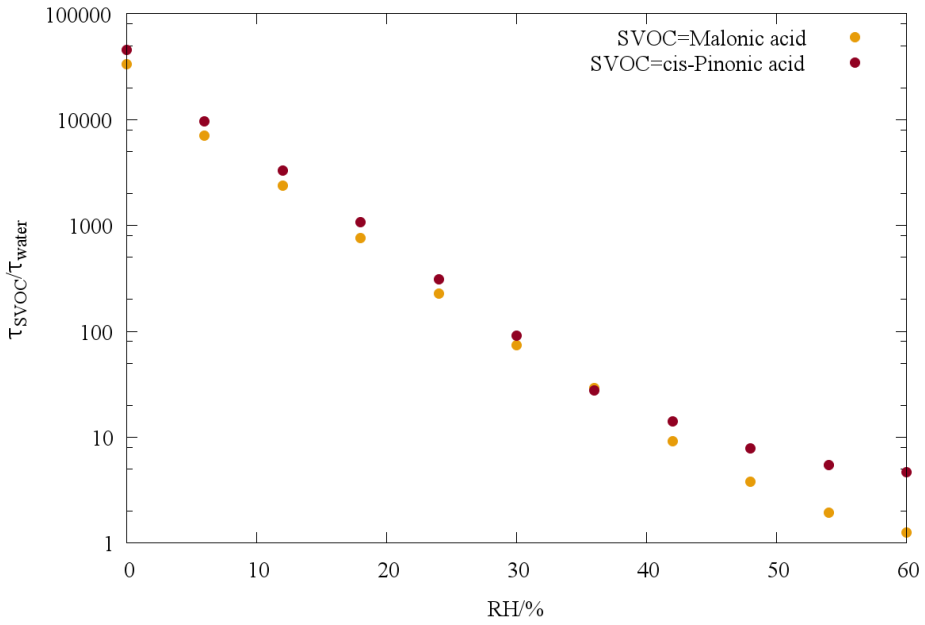

Figure 2.2.5: As in the previous figure, the ratio of the uptake timescales for two organics to that of water, within a 200 nm radius particle experiencing RHs below ~60%. The figure has been produced assuming that D_{SVOC} follows the Stokes-Einstein relation whereas D_w varies sigmoidally with RH (see chapter text).

For the SOA radius particle, the ratio is close to unity at 60% RH and does increase monotonically below that, for both organics (Figure 2.2.5). At the dry limit, the semivolatile uptake is a factor of 10^6 slower than water, which is very close to the ratio seen in the larger particle. We can therefore infer from these calculations that, to a first approximation, optically tweezed particles are a good proxy for the growth and evaporation of submicron SOA. The caveat is that all partitioning processes will be elongated by the extra mixing volume, scaling with the square of the radius difference as per equation 2.2.27.

2.3 Internal Particle Mixing in Two Component Aerosol

It has just been shown that condensing molecules can accumulate on the interface of an aerosol particle if there is a kinetic barrier to further diffusion. Similarly, evaporation of a volatile species can cause the outermost few nanometers of the particle to become enriched in less volatile

molecules which cannot diffuse away, if the initial viscosity is high enough.

2.3.1 Non-Ideality

When discussing the favourability of two liquids to mix, many chemistry textbooks will begin by discussing the vapour pressure above the solution. This seemingly unrelated quantity can actually be used as an indication of the strength of the intermolecular interactions. The experiment will be familiar to the reader: As a function of its mole fraction, we expect a liquid solute to behave according to Henry's Law[3]:

$$p_{svoc} = x_{svoc} H_{svoc} \tag{2.3.1}$$

at the dilute limit where $x_{svoc} \to 0$. Conversely, as the concentration increases and the solution more closely resembles that of a pure liquid solute, Raoult's law can be used to describe the volatilisation:

$$p_{svoc} = x_{svoc} p^{\bigcirc}_{svoc}. \tag{2.3.2}$$

The above equation means that the ratio of the observed partial pressure to the reference state, $p_{svoc}/p^{\bigcirc}_{svoc}$, is exactly equal to the molar proportion of the interface occupied by the solute.

Generally, $H > p^{\bigcirc}_{svoc}$, meaning that more molecules are liberated when the two components are nearly equal in composition than in either pure liquid. This suggests that bonds between solute and solvent tend to be weaker than either with themselves. In other words, vapour pressure above a mixture will be higher if that system requires requires heat to be input to mix, than one which releases energy when it is mixed.

Several aspects of this phenomenon are pertinent to the experiments described in this thesis. Firstly, aerosol are capable of accessing solute concentrations significantly in excess of the bulk solution phase, in effect allowing them to traverse the entirety of the x axis in the schematic figure 2.3.1. Note that this applies even if the solute exists as a solid under standard conditions.

[3]For the sake of argument, and consistency of notation, let us assume it is a semivolatile organic species

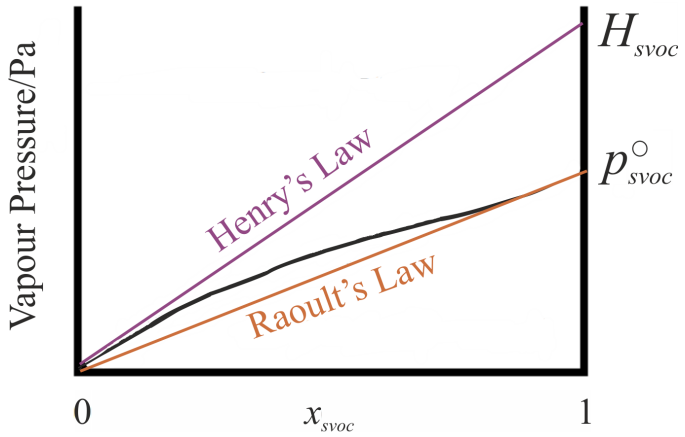

Figure 2.3.1: Schematic figure showing the influence of non-ideal mixing on the volatility of an organic solute above a binary mixture. Adapted from Chemistry Libretexts, under the Creative Commons Non Commercial - ShareAlike license.

Secondly, as per section 2.1, vapour pressure can be easily inferred from the dynamic loss of droplet surface area, and indeed will be. We must be able to differentiate between low vapour pressures caused by slow diffusion and low vapour pressures caused by non-ideal mixing within the data analysis. It therefore becomes useful to consider more complex diffusion models, and how ideality fits into the microphysics assumed.

2.4 A Comparison of Two Models of Fickian Diffusion

The proof described in section 2.2 and the associated implementation are a useful starting point in the assessment of the regimes of gas particle partitioning. Nevertheless, it is not a wholly rigorous description of the physical processes involved:

Firstly, it does not allow the particle volume to increase as a consequence of the condensation. Secondly, it considers gas phase transport to be mediated by molecules with uniform velocity, that only travel perpendicular to the particle interface. A more accurate treatment would take into account variances in speed, and the mean free path between collisions. Related to this, it may not be correct to assume that the time and space dependences of concentration are wholly separable (equation 2.2.7). Finally, a Henry's Law coefficient is a somewhat simplistic amalgamation of

different molecular parameters such as mass loading, solubility and vapour pressure.

It would therefore not be desirable to use this treatment to interpret experimental data. Instead what is needed is a model of particle phase dynamics that can be used to predict changes in radius as a result of gas-particle partitioning events.

As such, two differing models of internal particle dynamics have been utilised in this thesis for the analysis of different experiments. Both rely on solving equation 2.2.2 for a sequence of time points, in a spherically symmetric way. One is the Fickian Partial Differential model (Fi-PaD), described by O'Meara et al.[198] and the other is KM-GAP, which stands for Kinetic Model - Gas and Particles. KM-GAP was originally developed by Shiraiwa et al.[205] and has been applied to understand several ways since[206].

There are several differences between these models which are worth noting, and which inform the experiments they will be employed to interpret in later chapters. Perhaps most crucial is the way in which diffusion coefficients are represented.

The Fi-PaD Model

Fi-Pad assumes that the particle contains only one solute and one solvent, and treats their diffusion as symmetric. That is to say, both molecules will diffuse at the same rate in an equal and opposite manner.

The authors assume that any difference in the diffusion rate of the solute and the solvent will be thermodynamic in nature, rather than kinetic. They argue that these differences should not be included in the definition of the Fickian diffusion constant, but instead added as a correction factor. In a two component system, the symmetric diffusion coefficients can be deconstructed into the form

$$D_{12} = B_{12}\Gamma \tag{2.4.1}$$

Where B is the Maxwell Stefan diffusivity and D is the Fickian diffusivity. Physically B corresponds to the mean net diffusive motion that is possible due to drag effects on the molecule,

i, in question. Γ is the correction factor into which all effects of non-ideal interactions and solubility are 'moved'. It is related to the gradient of the activity as a function of composition:

$$\Gamma_{ij} = \delta_{ij} + x_i \frac{\partial \ln \gamma_i}{\partial x_j} \tag{2.4.2}$$

where δ_{ij} is the Kronecker delta, x_i and γ_i are the mole fraction and activity coefficient of component i respectively. The presence of the natural logarithm in the relation arises from the fact that it is the gradient in chemical potential, not activity, that is the driving force within the model. The two are related via

$$\mu_i = RT \ln(a_i) = RT \ln(x_i \gamma_i) \tag{2.4.3}$$

which is a common equation that arises in different areas of chemistry.

In plain language, these equations express that if there is little change in solute activity, a_i, as a function of concentration x_i, then the solute will diffuse much slower than the symmetric Fick diffusion constant would imply. Conversely, the *solvent* (j) diffusion must increase by an equal and opposite degree, such that the mean value of D remains the same. If $\partial \ln \gamma_i / \partial x_j < 0$, diffusion becomes *negative*, which suggests molecules will move towards regions of higher concentration.

This may seem counterintuitive, but is physically possible and corresponds to demixing: Due to solubility or unfavourable molecular interactions, the system splits into two phases predominantly made up of each component. Sometimes this is referred to as Liquid-Liquid Phase Separation (LLPS), as it was in the Introduction.

In an n component system with multiple solutes, equation 2.4.1 becomes an $(n-1) \times (n-1)$ matrix multiplication problem:

$$\begin{bmatrix} D_{11} & D_{12} \\ D_{21} & D_{22} \end{bmatrix} = \begin{bmatrix} B_{11} & B_{12} \\ B_{21} & B_{22} \end{bmatrix}^{-1} \begin{bmatrix} \Gamma_{11} & \Gamma_{12} \\ \Gamma_{21} & \Gamma_{22} \end{bmatrix} \tag{2.4.4}$$

where the on-diagonal elements are not zero:

$$B_{ii} = \frac{x_i}{D_{in}} + \sum_{k}^{n} \frac{x_k}{D_{ik}} \tag{2.4.5}$$

Due to the curious properties of logarithms when they are differentiated, the gradient in μ_i (over which diffusion is occuring) can be expressed with respect to almost any combination of the variables, assuming it is normalised appropriately[207]. For instance:

$$\frac{1}{RT}\frac{d\mu_i}{dr} = \frac{d\ln(a_w)}{dr} = \frac{d\ln(x\gamma_i)}{d\gamma_i}\frac{d\gamma}{dr} = \frac{1}{\gamma_i}\frac{d\gamma_i}{dr} \tag{2.4.6}$$

However, none of these equalities are particularly useful for interrogating the current problem. What we ideally want is an expression in terms of $\frac{dx}{dr}$, which is linearly related to $\frac{dC}{dr}$ and therefore is differentiable within Fick's Second Law (PDE 2.2.2). Therefore, using the chain rule, we will define the following identity:

$$\frac{x_i}{RT}\frac{d\mu_i}{dr} = \frac{x_i}{\gamma_i}\frac{d\gamma_i}{dx_j}\frac{dx_j}{dr} = \sum_{j}^{m} x_i \frac{\partial \ln \gamma_i}{\partial x_j}\frac{dx_j}{dr} \tag{2.4.7}$$

in order to separate out Γ. Crucially, the terms between the sum and $\frac{dx_j}{dr}$ on the right hand side are independent of r. Therefore, noting that Γ must not to be a function of distance, it may be equated to the right hand side, and equation 2.4.3 is recovered.

Further theoretical considerations, including examples where uphill or 'backwards' diffusion becomes crucial to the evolving properties of a system, can be found in the review of Krishna[207]. The specific formalism in equations 2.4.5-8 goes beyond the systems to which that Fi-PaD has been applied within this thesis, but is introduced to provide a flavour of the distinction between Fickian and Maxwell-Stefan diffusion.

The original corrections 2.4.1-3 were introduced into the model in order to maintain an assumption that the droplet behaves as an ideal solution. It may not be accurate, however, to assume that any asymmetry in the diffusion rate will be wholly due to solubility effects. For example, the motion of polymeric molecules is hindered by their size and the extent of the nonbonded contacts they have with their environment[208], in other words how 'tangled' they are. Such a suppression of diffusion is not strictly due to solubility, nor is it experienced by the solvent molecules

diffusing through them[209]. As we will see in later chapters, the mechanism of water diffusion through viscous organic aerosol has several similarities with that of solvent through a polymer lattice.

Beyond the corrections, the model allows for several different functional forms of the Fickian coefficient $D(x_w)$ to be investigated, as described in the initial publication[198]. Two will be discussed presently: the first dependence is logarithmic

$$D(x_w) = D_{wat}^{x_w} \cdot D_{solute}^{(1-x_w)} \tag{2.4.8}$$

Where $D_{wat} = 2 \cdot 10^{-9}$ m^2s^{-1} and D_{solute} is the *self diffusion* coefficient of the solute. As the molar fraction of water approaches zero, D tends to D_{solute}. Due to the symmetry assumption derscribed earlier, D_{solute} can also be interpretted as the diffusion coefficient of a single water molecule in an infinite matrix of solute molecules, or $D_{w,sol}$.

The second dependence is sigmoidal, which takes a very similar form:

$$D(x_w, \alpha) = D_{wat}^{\alpha(x_w) \cdot x_w} \cdot D_{solute}^{(1-\alpha(x_w) \cdot x_w)} \tag{2.4.9}$$

Except that it now incorporates a separate function, $\alpha(x_w)$, which controls the curvature of the function near the two limits. This is sometimes referred to as the Vignes function[210],

It has been suggested that since α modifies the mole fraction in the exponent of D_{wat} then it may be related to, or perhaps is,[180, 181] the activity coefficient of water. More specifically, using the notation of the Maxwell-Stefan corrections above, it may be that

$$\frac{\partial \ln \alpha}{\partial x_w} \sim \frac{\partial \ln \gamma_w}{\partial x_w} \tag{2.4.10}$$

Unfortunately there is no consensus on what functional form $\ln \alpha$ may take, and whether it is general to different chemical systems or not. These considerations are beyond the scope of the current section, but will be returned to at an appropriate point in Chapter 6. The more general purpose of equation 2.4.10 is to, in conjunction with Fick's Second Law (equation 2.2.2), allow the value of D_{solute} to be adjusted, such that the evaporation of a viscous aerosol droplet can be predicted.

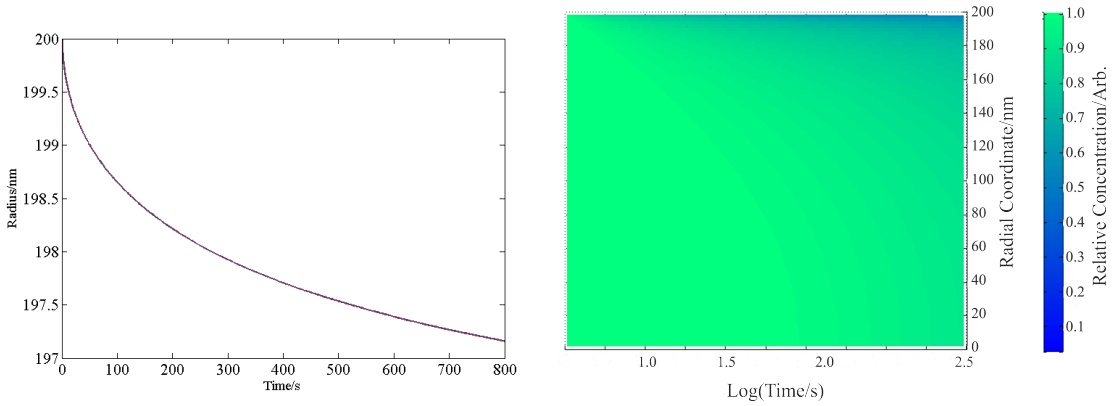

Figure 2.4.1: (a) The radius response of a 200nm SOA-type droplet to an RH change of 50-30%, as simulated by Fi-PaD (b) The internal dynamics of the simulated droplet. Model parameters are as follows: Molecular mass of the nonvolatile component = 150 Da, D_{solute} = 10^{-17} m^2s^{-1}, initial timestep = 0.01 s

An example of a model predicted radius change, and corresponding internal concentration profiles, are shown for the bulk phase limited evaporation of water in figure 2.4.1. Each vertical pixel in panel (b) corresponds to one concentric shell, and each horizontal pixel to one timestep. Note that the model time increases at a rate faster than linear but slower than logarithmic. This is because it dynamically adjusts the timestep on the basis of the size of $\frac{dC}{dt}$.

The KM-GAP Model

In contrast to the binary solute and solvent system treated by Fi-PaD, KM-GAP can simulate a theoretically indefinite number of components whose diffusion rates can be wholly decoupled from one another. As alluded to in section 2.3, a model constructed in this way should be used if there is a possibility that non ideal mixing may be influencing the experimentally determined volatilisation rate. In any case, the authors of the model intended it to be used to investigate a much wider scope of processes, and to interpret a wider number of experiments than water transport. These variously include particle formation and growth, bulk phase chemistry, and heat transfer to and from the gas phase. However, as applied to this thesis, we have been a little more prescriptive; limiting the scope of the analysis to the problem of coupled diffusion and

evaporation in three component aerosol systems.

When it was intially published, three examples showcasing the utility of the model were presented, involving the accurate reproduction of radically different experimental data. Each example was achieved through the variation of bulk, interfactial or gas phase parameters of the partitioning molecules. Employing a procedure that involves such finely tuned changes to the 'dials' of the microphysics is a matter of personal preference. It is difficult to say with objectivity which is the *better* approach, or even if that word has concrete meaning in this context. It is clear, however, that the methodology of the KM-GAP model contrasts with the more rigid parametrisations described earlier.

The general operation of the model is broadly similar to Fi-PaD: a particle is constructed of concentric shells, and a disequilibrium is set up between the gas and particle phases that drives the solution to the diffusion equation 2.2.2 between adjacent shells, over a defined timescale. Where the models are used to interpret measurements later in this thesis, the timescale will be defined according to each individual experiment.

Firstly, there are differences between the models in terms of how the shell compositions and densities are calculated. In KM-GAP, each component has a characteristic molecular length scale, which is defined by

$$\sigma_i = \sqrt[3]{\frac{M_{r,i}}{N_A \rho_i}} \tag{2.4.11}$$

Where ρ_{svoc} is the pure component density of component i. σ_i^2 and σ_i^3 are the effective molecular cross section and volume, respectively, which are used to determine the mole fractions of each component in each shell.

There are also several types of bulk phase shell considered in KM-GAP. The outer edge of the particle is comprised of two shells, the sorption and the quasi static surface layers. If only one compound i is partitioning, then both of these shells are defined to have a thickness equal to σ_i, which is not allowed to vary. One feature of note within the context of the works presented here is that the initial conditions of an evaporation process are constructed in starkly

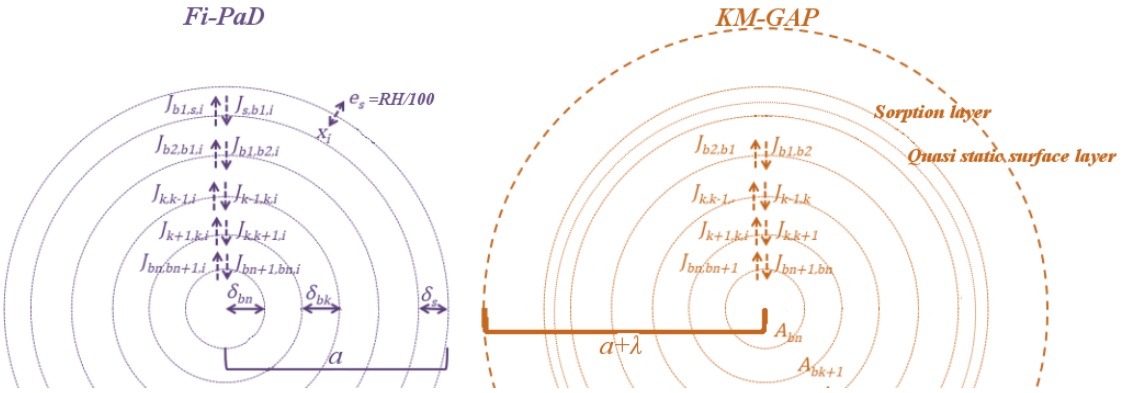

Figure 2.4.2: A representation of the concentric shell representations of modelled particles in the two Fickian models employed in this thesis.

different ways between the two models: In Fi-PaD, the outer shell is presumed to instantaneously reach equilibrium with the gas phase as soon as the simulation begins, whereas in KM-GAP the sorption shell begins in equilibrium with the *particle* phase. The mass fluxes into and out of the sorption shell are then calculated, and depend on the Knudsen number of the semivolatile species:

$$Kn = \frac{\lambda}{a} = \frac{3D_g}{va} \tag{2.4.12}$$

Where λ is the mean free path of the molecule, and all other terms are as defined in previous subsections. λ has another significance in KM-GAP, as the interface between the two gas phase shells that exist is defined at a radial coordinate of $a + \lambda$. Physically, this corresponds to the transition between laminar and tubulent flow within an evaporating vapour. In both models, the internal shell compositions are determined according to the initial gas phase saturation.

Once the chemical composition of the outer layers has adjusted due to gas-particle exchange, the adjacent shells will respond by solvent, nonvolatile or semivolatile molecules diffusing between them, or by the shells themselves changing shape. Figure 2.4.3 presents the internal concentration gradient formed in the kinetically limited cases, by analogy with panel (c) of Figure 2.2.2. The earliest time at which the semivolatile in the centre of the droplet begins to deplete depends on whether the modelled system is gas or particle diffusion limited. Of course, KM-GAP

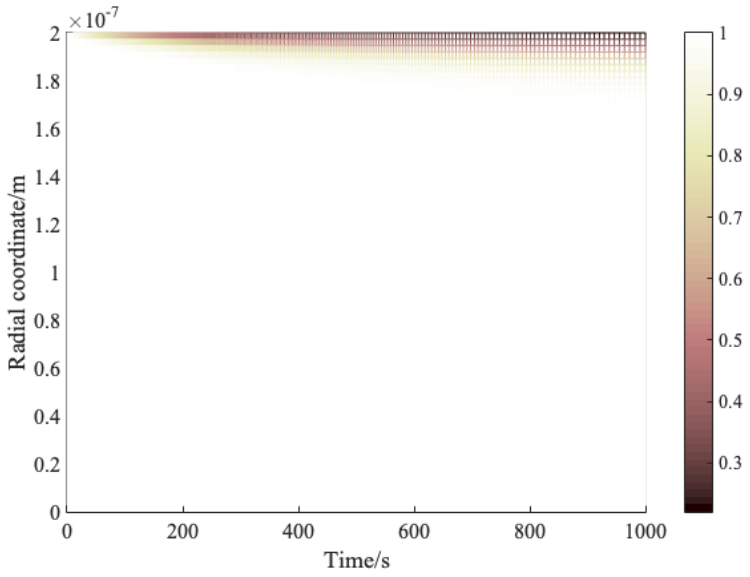

Figure 2.4.3: KM-GAP simulation of 1000s of water evaporation from a 200nm particle at 30% RH, showing the formation of a strong concentration gradient. Colour indicates concentration relative to the initial value in each shell. The viscosity of the particle is assumed to be that of Toluene SOA.[211]

is more complex and powerful than the model used in that study. For further details, including the definitions of the fluxes and concentrations, readers are directed to the appendix of the original publication[205], and the kinetic treatment of Poschl et al.[212]

With regards to the representation of diffusion coefficients, different parametrisations have been used across different publications in the literature when employing the model[213]. Frequently, the Monte-Carlo-Genetic-Algorithm procedure is used[214], whereby the same diffusion constant is varied across multiple experiments in an unbiased way, in order to optimize the output to the data. At no point in this thesis will that approach be used.

2.4.1 Outlook

The ability of the KM-GAP model to simulate multiple volatile components within a particle (in addition to water) makes it an appropriate candidate for interpretting the evaporation of organics. The fact that individual compounds can be defined with separate D values from one another may

not be wholly justifiable from the perspective of Maxwell-Stefan diffusion, but is crucial to capturing the physics of water coevaporation. In addition, KM-GAPs more detailed representation of the gas phase allows for the modelled particles to begin from a position of surface equilibrium, rather than surface disequilibrium. The driving force, at the interface, for each volatile to partition is then an emergent property from the pressures and saturations that are present in the gas. In some of the experiments that will be interpretted later in this thesis, this will be a more accurate assumption. Conversely, the Fi-PaD model contains no gas phase as such. Instead, a sequence of instantaneous saturation changes are pre-programmed into the outermost shell, and this is taken to be a proxy for the gas phase dynamics.

What we can say in favour of the Fi-PaD model is that its diffusion constants have a superior radial resolution. By this I mean that each shell has an independently varying diffusion coefficient from all the others, that depends on its local composition. Therefore, in systems where second order diffusional effects are important, such as when the rate at which D itself changes determines the flux, Fi-PaD is the more appropriate choice. In KM-GAP, each compound has a fixed D_{i} that is not influenced by either its position in the particle. Highly viscous systems, or systems with steep concentration gradients cannot be well simulated by such a scheme.

It should now be apparent that the two models complement each other rather well: each is strong in the areas where the other falls short. The above can be seen as developing a justification of the choice of the models for specific purposes, later on in this thesis.

Chapter 3

Experimental Methods

"I thought, I found a way to enter,

It's just a reflektor,

I thought, I found the connector,

It's just a reflektor" - Arcade Fire, *Reflektor*

The studies that will be presented in this thesis involve data collected using both laboratory experiments and computational models. Some insights will arise from both methods individually, and some from the combination. For clarity, discussion of the two methods will be separated into different chapters. Here, the single particle methods that are employed will be described. The objective of this chapter is to introduce both the aerosol optical tweezers technique, as well as the Raman effect from which spectroscopic information can be extracted. Both of these will be introduced from first principles, but care will be taken to describe them in such a way as to maximise the reproduceability of the experiments that will be presented in later chapters. As such, the presentation is not indended to be exhaustive, and the reader is directed to literature reviews or seminal publications at the appropriate time.

Raman spectra are the primary data recorded from the aerosol. Usually, each spectrum contains a form of scattering 'fingerprint' whereby the droplet itself acts as an optical cavity. The droplet properties at the moment each spectrum is collected define the wavelengths of stimulated peaks within this fingerprint. Using an algorithm that solves Mie scattering equations within certain bounds, it is possible to 'work backwards' and estimate the particle radius and refractive index that would have produced each observed scattering pattern. Because both homogeneous and core shell particles are studied herein, an explanation of differences in the stimulated scattering pattern of the two is provided. On some occasions in this thesis, the broad, spontaneous Raman bands will contain information of relevance to the experiment, but these cases are relatively few in comparison.

3.1 Aerosol Optical Tweezers

The Bristol Aerosol Research Center has been at the forefront of developing the optical tweezers technology for new applications for some time[215, 216, 153]. Improvements to the apparatus have also been the subject of various publications from the Reid group, among others[217, 218, 134]. The earliest research showcasing the ability of optical tweezers to levitate small particles will be discussed later, but for the time being a description will be provided of the apparatus that has been used in Chapters 6, 7 and 8 of this thesis.

The optical trap is formed using a 532 nm YAG laser (Laser Quantum, Opus 2W), which is redirected such that it propagates vertically upwards. Several mirrors are used to achieve this, and at least one lens is present between each mirror to recollimate the light as it is redirected, avoiding any dispersion of the beam. and is then tightly focused though a microscope objective, forming a focal point of high intensity. The choice of green light is motivated by the fact that light of that wavelength falls in a minimum of the absorption spectrum of water[203]. Hence, the effects of droplet heating by the optical trap can be discounted, to a first approximation.

The procedure when conducting an experiment using optical tweezers is generally similar for the studies discussed in Chapters 6-8. Some physical or chemical quantity is investigated, with

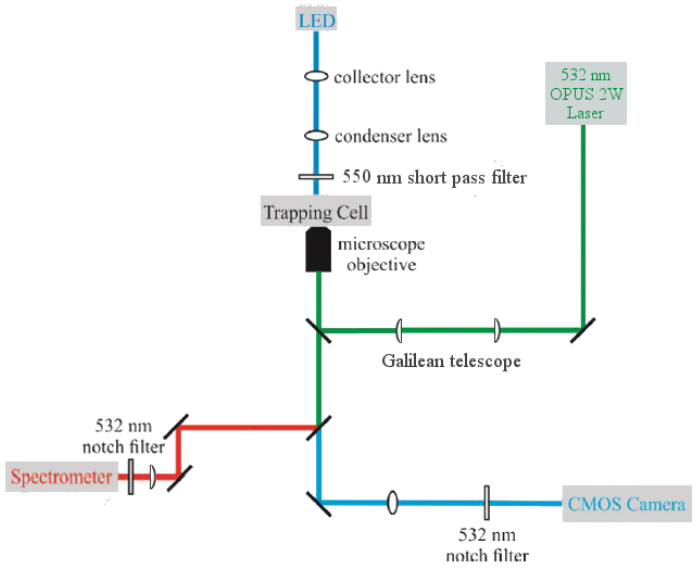

Figure 3.1.1: Schematic view of the aerosol optical tweezers arrangement used in this thesis, with (right). Red represents the droplet Raman Spectrum (see section 3.2), while green represents the trapping laser and blue represents broadband optical wavelengths from a blue LED.

reference to the evolving behaviour of a single droplet. We assume that the variance in these behaviours is sufficiently low that only a few repeats are required at each set of experimental conditions.

A glass coverslip (35 mm diameter, Chance Glass Ltd.), stored in a decon90 surfactant solution, is prepared by briefly washing both sides with deionised water. The coverslip is then placed onto the bottom of a plastic trapping cell, itself freshly washed, allowing the capillary forces around the edge of the glass to hold it to the plastic. A drop of immersion oil is added to the *outer face* of the coverslip, which then becomes the underside of the casing upon inverting it upside down. The oil used is fluorinated, meaning that no contamination is observed of the Raman spectra by the C-H bands of its constituent hydrocarbons, since none are present. The combined plastic and glass components are then inserted into a metal casing that is mounted several centimeters above the microscope objective. Using adjustment tools, the metal casing is then translated vertically down, until the immersion oil droplet connects to the objective on the underside of the coverslip, fully bridging the gap between them. Next, a metal lid, containing a

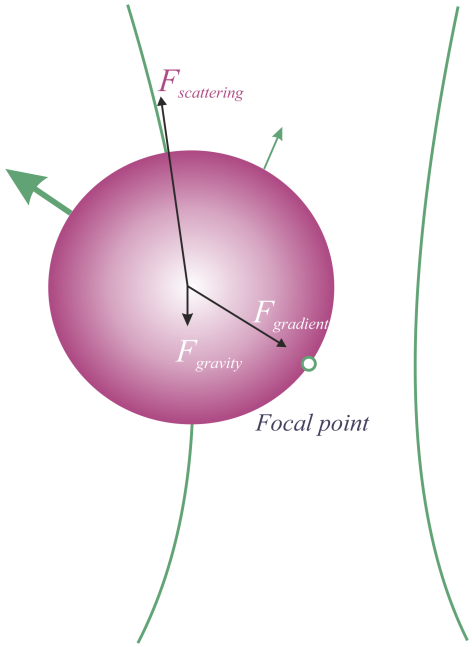

Figure 3.1.2: Schematic representation of the forces (black lines) experienced by a droplet in an optical trap. The direction of laser propagation is upwards. Line lengths are intended to indicate the approximate magnitude of the force but are not to scale (see main text for the relationships between each force and the particle size). The widths of the green lines indicate the strength of scattering both parallel and perpendicular to the vector connecting the droplet center and the focal point of the trap. For simplicity, the force caused by the gas flow has been neglected.

glass window, is affixed to the top of the apparatus. It is only at that point that the gas flow is established, and is maintained until the humidity reaches an equilibrium value within the tubing and cell.

A small volume of solution is prepared and loaded into an Omron U22 MicroAIR nebuliser. The aerosolised plume of solution is then produced by the nebuliser and drawn through the trapping cell until a single droplet strays close to the focal point. Typically, the trapping laser starts at 60% of its total power, and is then reduced accordingly as the droplet shrinks. The droplet is subject to several forces. These forces are, in order of (likely) decreasing magnitude: the gradient force, the scattering force, drag arising from the turbulence of the gas flow, and gravity[218].

The precise definition of the gradient force is:

$$F_{gradient} = \frac{\alpha}{2m\varepsilon_0 c}\nabla I \tag{3.1.1}$$

where α is the polarisability of the droplet, m is the refractive index, ε_0 is the permittivity of free space and c is the speed of light in the nitrogen atmosphere. The gradient force arises from the momentum transfer between the light beam and the droplet. It acts along a vector that connects the droplet center to the point of highest light intensity, I. As illustrated in Figure 3.1.2, if there is a gradient in intensity across the sphere, there will always be more refracted photons exiting the droplet in directions *away from* the higher intensity region. While photons are massless, they do possess momentum, which is redirected as the light is refracted. Therefore, the particle itself exerts a force on the light beam, and, due to Newton's Third Law, there must exist an equal and opposite force that 'pushes' the droplet towards regions of higher intensity. Conversely, if the droplet is in the center of the beam the refraction will be symmetric, and so no net force is imparted.[1] Sometimes this is referred to as a restoring force, suggesting that the focal point is a minimum in potential energy. The extent to which the beam is refracted by the droplet depends on the relative refractive indices of the droplet and surrounding medium (in this case, nitrogen gas).

The second force generated by the incident beam is the scattering force, which acts along the propagation direction. It is imparted by the energy transfer that occurs during the elastic and inelastic scattering (detailed in the next section). As with the gradient force, the magnitude is proportional to intensity, but crucially it also scales with the square of the volume ($\sim r^6$):

$$F_{scattering} = (m-n)^2 r^6 I \tag{3.1.2}$$

m remains the droplet refractive index and n is the refractive index of the suspeinding medium. For particles of sufficiently low radius (or mass), the gradient force far outweighs the scattering

[1] Strictly speaking, no force would be imparted in the plane perpendicular to the laser propagation. If the droplet is above or below the focal point, there will be a force *parallel or antiparallel*, respectively, to the propagation direction. The magnitude of this force will be proportional to the vertical component of the intensity gradient.

force. This is certainly the case for particles in the region $3\mu m < r < 7\mu m$, which constitute the entirety of aerosol studied by optical methods in this thesis. The mass of such droplets is of the order of picograms, making the gravitational force experienced insignificant in comparison. The schematic attempts to convey this through the lengths of the black lines.

The optical tweezers apparatus is an example of a gradient force trap, rather than one that achieves levitation by optical pressure. In the latter case, the scattering force is dominant and the beam is much wider. There is a slight dependence of $F_{scattering}$ on particle refractive index, but the relative change that m undergoes whilst they are trapped is lower than the change in r.

In order to observe when the droplet is stable, and when it is not, a blue LED illuminates the trapping cell from above, and the light then redirected into a CMOS camera (greyscale, 1024x1024 resolution, Thorlabs) such that a brightfield image can be inspected. In order to study the chemical composition, in addition to radius and optical properties of the particle, the backscattered light is redirected to a Raman spectrometer (see section 3.2). The short pass filter placed between the the LED and the trapping cell removes the small (but still present) amount of light emitted by the light in the wavelength range probed in the Raman spectra (625-660 nm). The purpose of the notch filter lenses is to remove the majority of the laser light from both the spectrograph and the brightfield camera. If the laser intensity is too high, the scattering force will outweigh the gradient force and the droplet will move vertically upwards, causing its outer edge to darken in the image and a bright white point to appear in the center. If the laser power is too low, the drag caused by gas flow becomes comparable to the gradient force. The droplet becomes 'buffeted', and begins to move horizontally in the plane of the image. Nebulisation is ceased, and the particle is then exposed to a reintroduced nitrogen gas flow of tuneable humidity. To avoid contamination of the interface by airborne hydrocarbons, oxidants, dust etc., it is vital to minimise the amount of time for which the droplet is exposed to laboratory air.

A photograph of the apparatus that was used primarily in this thesis is also shown in the next subsection.

Optical tweezing as a method for the immobilisation of microscopic objects in free air has

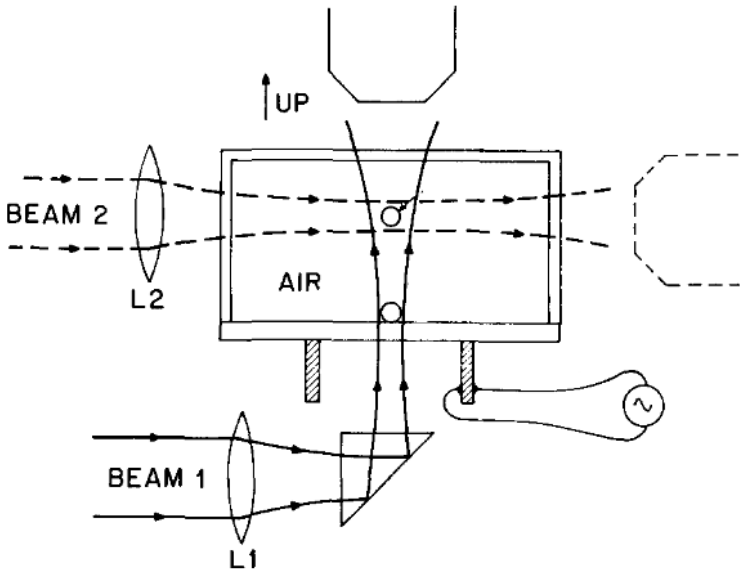

Figure 3.1.3: Schematic of the original optical tweezer used by Ashkin to levitate glass particles in 1971[219]

existed since at least 1971, when Ashkin and Dziedzic first descibed the levitation of 20 μm spherical glass particles by a 514.5 nm laser.[219] The paper itself was rather prescient, stating at the end that the technique 'will probably be useful in applications where the precise micromanipulation of small particles, free from any supports, is important, such as in [measuring] light scattering'. As we will see, that prediction has indeed come true.

Of course, since then the technique has been refined: the first publication describing a focused beam in which gradient force traps the droplet was published in 1986[220], paving the way for optical tweezing to occur in any direction, as well as in solvents. Spectroscopic methods used to probe the particles, the control over the gas phase conditions, and the range of experiments that can be conducted involving multiple particles have all improved markedly. Nonetheless, it is striking how similar the setup emloyed in this thesis is to Ashkin's original diagram. It is reproduced in Figure 3.1.3, to allow the reader to compare the two.

3.1.1 Control of Gas Phase Conditions

Humidity

A mixed flow of ultrapure (dry) and humidified (wet) nitrogen is directed into the trapping cell to control the RH by controlling the relative flow rates of both. Sometimes the flow rates necessarily vary during each experiment, but in all reported cases where RH is the independent variable, the levitated particles experienced a flow rate of 300 mL min^{-1}. Specifically, when the RH is changed, the ratio of wet and dry flows changes but the total remains constant. In such experiments, particles are sequentially dried or humidified. The RH is measured by a calibrated probe (HUMICAP HMT 330, Vaisala, error = $\pm$2% RH) placed several centimetres before the trapping cell. Sometimes, droplets are captured directly at the humidity under consideration, whereas others are dried consecutively and evaporated multiple times. In that case, the user must wait at least until the particle has completed equilibrating with the gas phase activity before changing the RH again, otherwise it can become unstable in the trap.

The volume surrounding the droplet within the trapping cell is small; several cubic centimeters at the most. One advantage of such a small volume is that the conditions can be altered on the order of tens of seconds, or sometimes seconds. In comparison to, for example, smog chamber studies, this timescale offers an enormous improvement in our ability to control and perturb the phase state of the trapped aerosol.

Oxidation of α-Pinene

In Chapter 8, several experiments will be described in which ozonolysis reactions are initiated in the gas phase, with the intention that the trapped droplet will act as a probe into which mass can be accreted. A brief explanation is provided as to how this was achieved, once again with the aim of maximising reproduceability. The current subsection is not intended to be an exhaustive discussion of the conditions that the trapped particles are subject to in each oxidation experiment, as there is some variation between them. A table detailing the differing conditions will be provided at the appropriate point in Chapter 8 and the reader is directed there. Instead, the following is

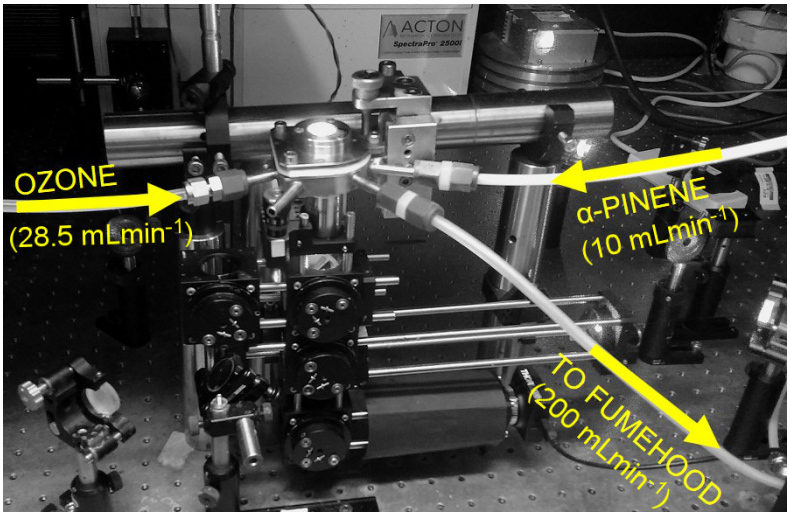

Figure 3.1.4: Gas flow configuration utilised in VOC oxidation experiments, promoting gas phase chemistry within the trapping cell. The spectrograph, laser and most optics can also be seen.

intended to generally introduce the instrumentation used, and the challenges that may be faced when attempting studies of this kind.

Several gas flow configurations were used in the preliminary experiments, involving different ways for the reactants to be mixed, either before the trapping cell, or within it. Since there were in theory four separate gas lines that needed to be employed, (dry, wet, VOC and ozone), and only two inlets into the cell, many permutations were possible for how to combine the flows.

The configuration used in the experiments described in Chapter 8 was chosen as it minimised the occurence of sudden increases in pressure during the experiment, which had a tendency to push the seed particle out of the trap. Procedurally, it involves the sequential exoposure of the particle to nitrogen saturated with water, followed by α-pinene, a reactive organic gas. Specifically, the humidity was slowly reduced to zero throughout the early stages of the experiment, at which point the contents of the water bubbler was replaced with α-pinene, allowing a small saturation to be introduced. 5% saturation (10 mLmin^{-1}gas flow, diluted to 200 mL min^{-1}with nitrogen and air) was used in all reported experiments, corresponding to between 210 and 290 ppm concentration, depending on the temperature[221].

Ozone production was achieved through the photochemical splitting of gaseous oxygen to

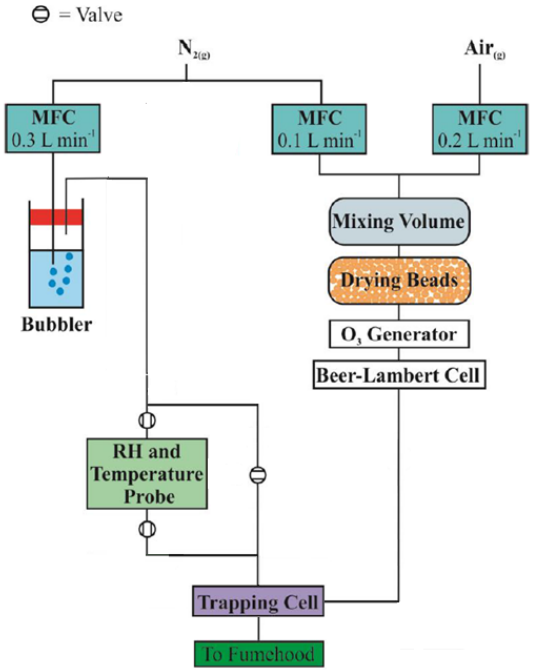

Figure 3.1.5: Schematic representation of the mass flow configuration, from a liquid boil off nitrogen supply (top), to the trapping cell (bottom), adapted from the thesis of F.H. Marshall[222]. If the bubbler contains deionised water, the ratio of the left and right flow rates regulate the RH. If it contains α-Pinene, it is possible to initiate ozonolysis, and then evacuate the resultant products out of the laboratory through airtight tubing.

form ozone when passed through a Mercury (emission $\lambda < 240$ nm) light source, placed before the trapping cell. It has been the subject of several previous publications, most recently to investigate the aerosol phase ozonolysis of maleic acid.[222] As shown in the schematic 3.1.5, the two right hand side mass flow controllers allow the concentration of ozone to be regulated through the relative proportions of dry nitrogen and 'air' ($N_2 + O_2$) entering the light source. The requirement for dilution meant that it was not possible to control both the RH and the gas phase chemistry conducted within the immediate atmosphere of the trapped droplet. In all reported experiments, a 15% air fraction (28.5 mL min^{-1} out of the remaining 190 mL min^{-1}) was used.

UV photometry can be used to measure the concentration of ozone[223]. Here, it was estimated using the Beer Lambert law:

$$\ln(\frac{V}{V_0}) = -\sigma C l \tag{3.1.3}$$

throughout each experiment, by measuring the absorbance of the air in the range 240-395 nm as the ozone is produced. V is the voltage readout of a photodiode that measures absorbance in that wavelength range. Here the drop in V from its initial value V_0 reflects the change in transmitted intensity, as is usually expressed in Beer's Law, as the photodiode can be assumed to convert from one to the other in an approximately linear fashion. V_0 was acquired by waiting for the voltmeter to equilibrate to a stable output during the time when the 190 mL min^{-1} air + nitrogen flow was passing through the photodiode. σ is the absorption cross section of a single molecule, whose value is 1.134×10^{-17} $cm^2 molecule^{-1}$[224]. l is the path length of the Beer-Lambert cell, or the distance between the light source and the detector. In this case l was 10 cm. C is the concentration in molecule cm^{-3}. Conversion to parts per million volume (ppmv) is achieved by assuming that 1 ppmv is equal to 2.647×10^{13} molecule cm^{-3} .[2]

3.2 Raman Spectroscopy

3.2.1 Fundamental Principles

The Raman effect is a relatively recent discovery in the field of spectroscopy, in part due to its very low intensity, relative to Rayleigh scattering. In contrast to infrared spectroscopy, the vibrations that are probed are symmetric and so do not require a change in the dipole moment of the molecules contained in the sample. Instead, Raman spectroscopy involves detecting changes in frequency that arise from the interaction of the incident beam with the electron cloud of the sample. It requires a change in *polarisability,* α*,* of the molecular orbitals during vibration.

Current theories invoke a so-called 'virtual state' to describe the process by which the energy transfers: In most experiments, the frequency of the incident photon (usually an optical or

[2]This number can be calculated in two ways. Firstly, one can use the ideal gas law, setting P equal to 1×10^{-6} atm, T equal to 295 K and calculating n/V. Secondly, by converting ground level air density, 1225 g m^{-3}, to molecules per cubic centimeter and then dividing the value by 10^6.

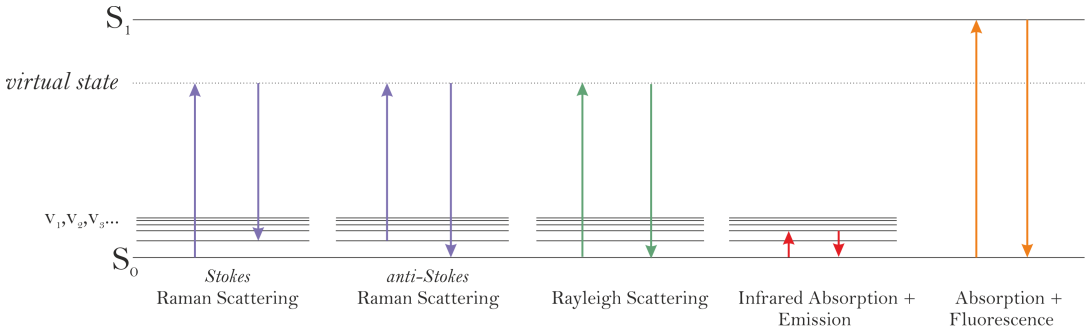

Figure 3.2.1: Simplified representation of different scattering and absorbance phenomena. S_0 and S_1 represent electronic energy levels (HOMO and LUMO) of the the sample molecule. $v_{1,2,3}$ etc. are vibrational energy levels of the ground state.

infrared wavelength) does not correspond to the energy difference between the ground and any excited states of the probed molecule. Therefore, instead of being an explicit absorption-emission process, the profile of the vibrational energy levels within the sample is somehow imparted onto the inelastically scattered photons, as they move across the electron cloud of the molecule. The observable outcome is that energy is transferred to, or from, the photon. Either the molecule is excited to a higher vibrational state within the ground electronic state, or, if it is initially vibrationally hot, it will lose energy. As such, Raman peaks are observed at both higher and lower energies than the incident light, by equidistant amounts. The peaks that occur at higher energies and lower wavelengths are called *anti-Stokes* peaks, and the complement are called *Stokes* peaks. A so-called Jablonski diagram is presented in Figure 3.2.1, that aims to distinguish the effects from one another, as well as from Rayleigh scattering and other absorption-emission phenomena.

The advantages of Raman over Infrared spectroscopy differ, depending on the chemical system, but some can be generally stated: Any incident wavelength can be used.[3] Signal contamination, or bleaching, from solvent is significantly reduced as common solvents tend not to be Raman active. The scattering is instantaneous, and so can be recorded in conjunction with flourescence or luminescence if the experiment is conducted in a sufficiently time resolved way. However, these other spectroscopic techniques cannot be employed here since the experiments, especially

[3] although it should be noted that the intensity of the resultant scattering is proportional to the fourth power of the light frequency.

those regarding evaporation, must be conducted in such a way that allows droplet properties to be determined in a *non-intrusive* way. Hence, the trapping laser must avoid heating the droplet or electronically exciting the sample within the droplet during the experiment. One somewhat obvious reason as to why Raman spectroscopy is employed here is that Raman scattering is occurring *anyway*, due to the interaction of the trapping laser with the aerosol.

As the Raman effect can occur, in theory, from any incident wavelength, the vibrational energy of the sample is expressed by the *red or blue shift* of the scattered light relative to the incident:

$$h\triangle\bar{\nu} = h[\frac{1}{\lambda_{incident}} - \frac{1}{\lambda_{scattered}}] \tag{3.2.1}$$

Where h is Planck's constant and $\triangle\bar{\nu}$ is the frequency change expressed in units of wavenumbers, cm^{-1}. Therefore both sides of the above equation are strictly equal to the (infrared) photon energy that would directly excite, through absorption, the molecule to the vibrational level that was populated by the Raman scattering. [4]

It is also possible to greatly reduce the detection limits for certain compounds by Raman based methods, in some cases to the single molecule limit. Such an analytical feat may seem counterintuitive, given the low intensity of the Raman effect, but can be achieved by a variety of enhacement methods. These methods include *surface enhanced-*,[225] *tip enhanced-*[226], *cavity enhanced-* etc. Raman spectroscopy. These techniques rely on increasing either the local intensity of the scattering beam passing through the sample, or the strength of the interaction between the sample and the photon. As we will see, the former is possible in this work, as an optically tweezed droplet will itself act as a resonance cavity[215]. This effect can be understood from the solutions to the Mie scattering equations for levitated spherical particles, which will be discussed presently.

[4]The inverse is also true: if $\lambda_{scattered} < \lambda_{incident}$, multiplying by h produces the energy of the photon that would need to be *emitted* to reduce a vibrationally hot molecule to the ground state.

3.2.2 Mie Scattering of a Homogeneous Sphere

By way of a caveat before the beginning of this subsection, it should be made clear that Mie scattering is a phenomenon that is elastic in nature. It does not derive from the Raman effect, or in any sense require Raman scattering to occur first, in order to be promoted. The connection to Raman spectroscopy in the context of this thesis is that Mie scattering is observed within the Raman spectra of single particles, and so the incident photons were first scattered inelastically. In theory, there is no reason that the mathematics presently described cannot be used to size particles from their so-called 'Mie fingerprint' in infrared spectra. However, as we will see, the incident light that stimulates the observed Mie scattering is not from the trapping laser *per se,* but inelastically scattered laser light arising from the Raman active bending and stretching modes of the molecules within the particle.

Rather, Mie theory concerns the interaction of incident light with particles of a similar diameter to the wavelength. In this description we will strictly consider spherical particles. However, even in this case it is substantially more complex to predict the scattering pattern than in the regimes where diameter and wavelength are highly dissimilar.

Here we are concerned with the intensity leaving the droplet as a function of angle or wavelength. If we can construct a consistent and reproduceable treatment then it becomes possible to 'go backwards', so to speak, and assign droplet properties to observed scattering patterns. For the purposes of concision, the angular dependence of these quantities will be ignored, and we will focus solely on backscattering, where the intensity of scattered photons is at a local maximum.

The intensity pattern around the droplet centre can be approximated as a sum of so-called *sombrero*, or Bessel, functions.

$$j_n(\chi) = (-\chi)^n \left(\frac{1}{\chi}\frac{d}{d\chi}\right)^n \frac{\sin\chi}{\chi} \tag{3.2.2}$$

$$h_n(\chi) = -(-\chi)^n \left(\frac{1}{\chi}\frac{d}{d\chi}\right)^n \frac{\cos\chi}{\chi} \tag{3.2.3}$$

χ is a dimensionless parameter equal to the particle radius, *r,* multiplied by the wave vector, $k = \frac{2\pi}{\lambda}$, of the scattered wave. λ is the wavelength of the incident beam, and so $\chi = {}^{2\pi r}/_{\lambda}$. As the sin and cos terms of equation 3.2.2 - 3 suggest, the functions j_n and h_n appear as sinusodal waves whose magnitude decays radially outwards. The scattered electic field depends on large sums of two functions, ψ and ζ, called *Riccati-Bessel* functions, which are defined as such:

$$\psi_n(\chi) = \chi j_n(\chi) \tag{3.2.4}$$

$$\zeta_n(\chi) = \chi h_n(\chi) \tag{3.2.5}$$

Given the relationship between sine and cosine functions, 3.2.4 and 3.2.5 are themselves interrelated to each other via a set of differential equations:

$$\psi_n(m\chi)c_n + m\zeta_n(\chi)b_n = m\psi_n(\chi) \tag{3.2.6}$$

$$\psi_n'(m\chi)c_n + m\zeta_n'(\chi)b_n = \psi_n'(\chi) \tag{3.2.7}$$

$$\psi_n(m\chi)d_n + m\zeta_n(\chi)a_n = \psi_n(\chi) \tag{3.2.8}$$

$$\psi_n'(m\chi)d_n + m\zeta_n'(\chi)a_n = m\psi_n'(\chi) \tag{3.2.9}$$

As we can see, ψ is sometimes a function of the refractive index, m, but always takes the argument of the size parameter. Of the four coefficients a_n, b_n, c_n, d_n, we are only concerned with a_n and b_n. c_n and d_n relate specifically to the waves *within* the particle and so are not relevant to the spectroscopic studies conducted in this thesis. Rearranging the differential equations to make a_{n} and b_{n} the subject, the above can be expressed as follows:

$$a_n = \frac{m\psi_n(m\chi)\psi_n'(\chi) - \psi_n(\chi)\psi_n'(m\chi)}{m\psi_n(m\chi)\zeta_n'(\chi) - \zeta_n(\chi)\psi_n'(m\chi)} \tag{3.2.10}$$

$$b_n = \frac{\psi_n(m\chi)\psi_n'(\chi) - m\psi_n(\chi)\psi_n'(m\chi)}{\psi_n(m\chi)\zeta_n'(\chi) - m\zeta_n(\chi)\psi_n'(m\chi)} \tag{3.2.11}$$

Whispering Gallery Modes (WGMs, sometimes called Morphology Dependent Resonances in the optics literature[227, 228]) occur when scattered photons are totally internally reflected by the inside surface of the droplet. This creates a cascade effect whereby each photon itself repeatedly stimulates further scattering of photons of the same wavelength, and the intensity rapidly increases.

With reference to the above equation, this can be approximated as a standing wave where $a_n = b_n \to \infty$. That is to say, the amplitude of scattering at those wavelengths approaches a singularity. Therefore, if we set the denominators of the above equations to 0, we can define:

$$m\psi_n(m\chi)\zeta_n'(\chi) = \zeta_n(\chi)\psi_n'(m\chi) \tag{3.2.12}$$

$$\psi_n(m\chi)\zeta_n'(\chi) = m\zeta_n(\chi)\psi_n'(m\chi) \tag{3.2.13}$$

It is possible to solve for the values of χ and m, assuming a large enough set of ψ_n and ζ_n can be calculated. Since λ for each observed WGM is known, the solutions to the above correspond physically to size and refractive index. In the context of an observed single droplet Raman spectrum, each observed whispering gallery mode must be identified by three attributes:

- The first is mode number, n. While the total scattered field leaving the droplet can be expressed as sums up to $n \to \infty$, each individual mode corresponds to the resonant wavelengths, i.e. waves that can fit an integer n times around the circumference of the sphere. Most of the whispering gallery modes that are possible will not be stimulated within an aerosol optical tweezers experiment, as there are no incident beams of those wavelengths

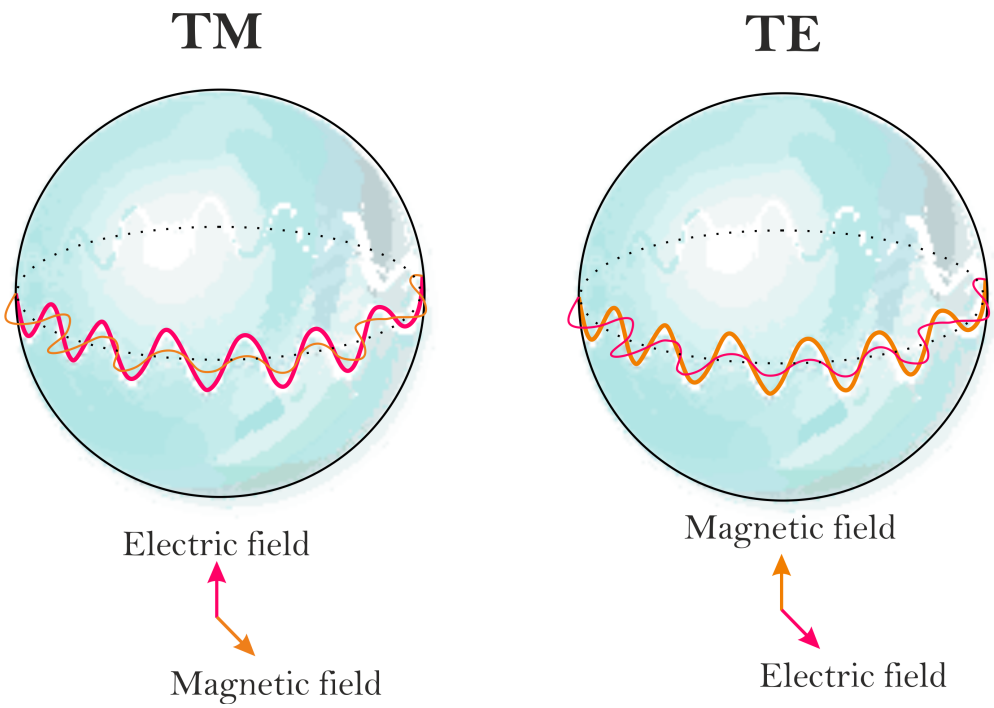

Figure 3.2.2: Schematic showing the distinction between Transverse Electric and Transverse Magnetic Whispering Gallery Modes.

to be intensified. Only those that occur at wavelengths that fall within the spontaneous Raman signal are observed.

- The second piece of information is whether the wave is transverse electric (TE) or transverse magnetic (TM). Physically speaking, the difference between the two is which waveform of the electromagnetic wave actually traverses across the surface of the particle. A schematic is presented in Figure 3.2.2, which attempts to capture the difference. While the wavelengths of the two waves are equal by definition, the wave that precesses into and out of the circumference is the one that is able to 'bend', or refract, as it traces the inside of the optical cavity. The wave that sits 'across', or in the plane of, the curved suface does not interact. Mathematically speaking, TM modes correspond to the solution to equation 3.2.12, and the TE to 3.2.13.[229, 230]

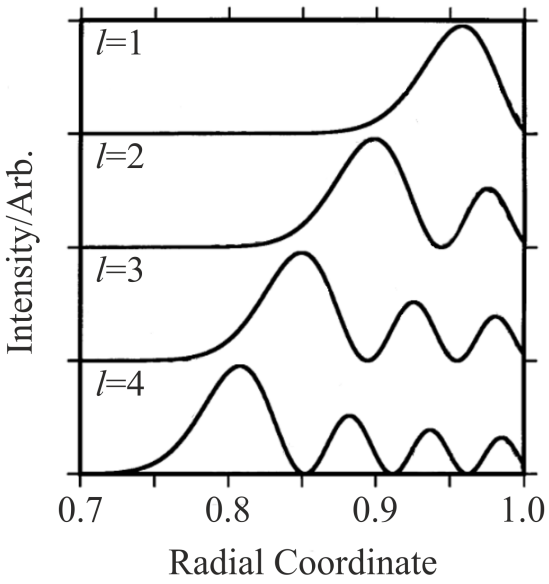

Figure 3.2.3: Intensity profiles of Whispering Gallery Modes of increasing mode order, *l*.

- The third piece of information which can be used to differentiate each whispering gallery mode is the mode *order*, *l*. The order is equal to the number of standing waves that are stimulated radially inside the droplet, counting from the interface backwards towards the centre. First order modes do not penetrate very far from the surface, whereas the photons from higher order modes are scattered from deeper within the optical cavity.

As a direct result of the third point, it is sometimes not beneficial to include higher order modes in a refractive index fitting process, since large concentration gradients present near the surface of a particle will lead to a large gradient in *m*. The extracted value will therefore be a weighted average of the refractive indices across the volume of the droplet that is probed. It is for this reason that WGM sizing is strictly only accurate for droplets of homogeneous composition[231]. Within the instrument, these calculations are done by the proprietary LARA (Live Aerosol Raman Analysis) software on each droplet spectrum.

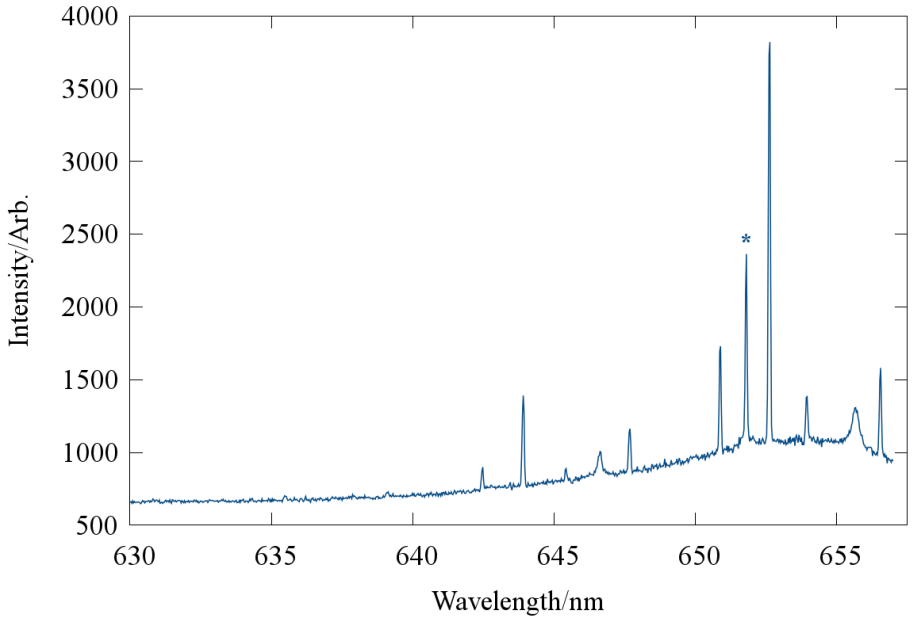

Wavelength/nm	Mode number/n	Mode order	Polarisation
642.41	72	1	TE
643.91	66	2	TE
645.43	71	1	TM
646.63	61	3	TE
647.68	65	2	TM
650.89	71	1	TE
652.62	65	2	TE
653.95	70	1	TM
655.69	60	3	TE
656.56	64	2	TM

Figure 3.2.4: Example of WGMs observed in the spectrum of a sodium nitrate droplet. Broad peaks observed are of mode order 3, as detailed in the table. The peak with accompanying asterisk at approximately 652 nm is not a WGM, it is a phantom peak arising within the spectrograph.

3.2.3 Mie Scattering of a Core-Shell Particle

Necessarily, the scattering pattern of a spherical core-shell particle will be more complex than a single sphere, as any light ray travelling through the droplet will interact with two new surfaces. Equations 3.2.12 and 3.2.13 must therefore be modified to include the influence of the new internal surface within the droplet on χ, a_n and b_n[232]:

$$m_s\zeta_n'(\chi)[\psi_n(m_s\chi)-a_n\xi_n(m_s\chi)]=\zeta_n(\chi)[\psi_n'(m_s\chi)-a_n\xi_n'(m_s\chi)] \tag{3.2.14}$$

$$\zeta_n'(\chi)[\psi_n(m_s\chi)-b_n\xi_n(m_s\chi)]=m_s\zeta_n(\chi)[\psi_n'(m_s\chi)-b_n\xi_n'(m_s\chi)] \tag{3.2.15}$$

Where m_s is now the refractive index of the shell, rather than the entire particle. Note that the Riccati Bessel function of the *third* kind, ξ_n, has been introduced. The coefficients a_n and b_n become extremely unwieldy in this scheme, and can be expressed in many different ways. For instance, one must either introduce a new characteristic length scale to define the radial fraction of the core, relative to the shell, f_c, or split the Mie parameter χ into kr_s and kr_c. In both cases the outcome is the same: The resonances between the derivatives of the first two Bessel functions, that defined the solution to the homogeneous particle[230], are broken.[5]

$$m_s\frac{\zeta_n'(kr_s)}{\zeta_n(kr_s)}\neq\frac{\psi_n'(m_skr_c)}{\psi_n(m_skr_c)} \tag{3.2.16}$$

$$\frac{\zeta_n'(kr_c)}{\zeta_n(kr_c)}\neq m_c\frac{\psi_n'(m_skr_s)}{\psi_n(m_skr_s)} \tag{3.2.17}$$

Instead, one must consider the beams emanating from the core and the shell separately, as well as the interaction of the two on the lengthscale r_c+r_s. Mathematically, the outcome of the broken resonance is that a large number of terms reappear in the denominators of the scattering coefficients, that previously cancelled one another. It is getting beyond the scope of this Chapter

[5]This is not a complete set: there are *at least* six more permutations of these inequalities that can be constructed, by substituting m_c, m_s, r_c and r_s for one another.

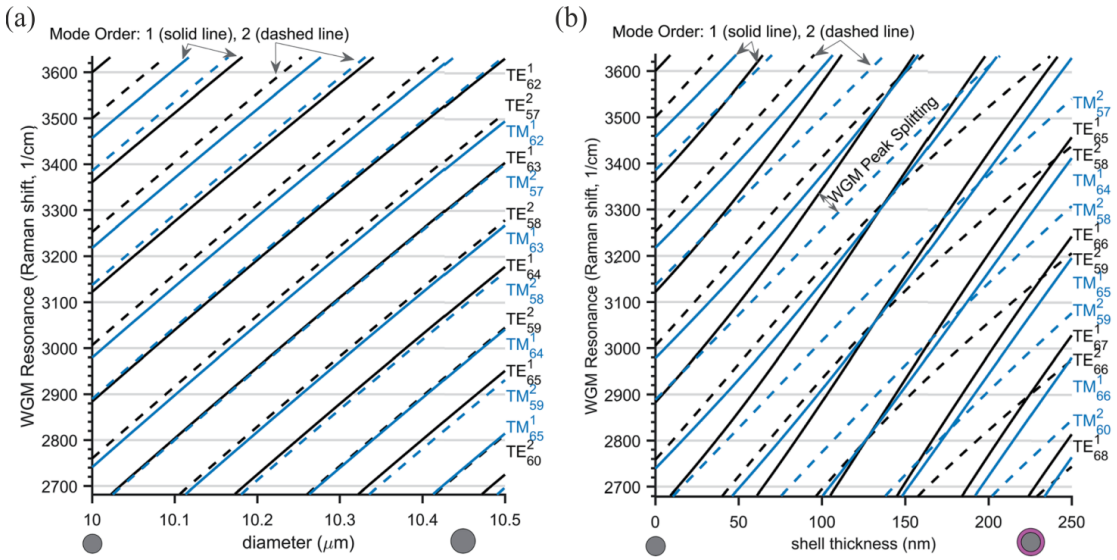

Figure 3.2.5: Changes in Raman shift $\triangle\nu$ of the Whispering Gallery Modes calculated for a 10 μm droplet. Panel (a) presents homogeneous growth, increasing particle radius by 500 nm. (b) is core shell growth: wavelength shifts were calculated as a shell of up to 250 nm width condenses. Reproduced with permission from Gorkowski et al. 2018[232]. Modes with TE (black) and TM (blue) polarisation, of mode order 1 (solid lines) and 2 (dashed lines) are presented, and are found to move in a non-concerted manner.

to present the coefficients in full here, and so the reader is suggested to inspect equations 2-11 in Toon and Ackerman[233] and 2-15 in Ray and Nandkumar[234]. The practical utility of the above, from the perspective of interpreting Raman spectra produced by single particles, is that, for a sufficiently different m_c and m_s, the wavelengths of the WGMs become sensitive to the differences in properties between the two phases. While more mathematically complex, and computationally expensive to evaluate, the effect will actually be of considerable benefit in Chapter 8, as it allows the two refractive indices to be determined as part of the fitting process.

Perhaps unsurprisingly, the singularities in these equations will not coincide with those of a homogeneous sphere (3.2.12-13). Instead, the extent of deviation will vary depending on the attributes of each WGM, as described in bullet points in the previous section. Some calculated solutions[232] to the equations are presented above, in Figure 3.2.5. In this example r_c = 10 μm, m_c= 1.37, m_s= 1.45, and r_s is scanned between r_c and 10.5 μm.

Firstly, TE modes change their wavelengths more for a given shell width than TM; Secondly, standing waves with mode order 1 will be more sensitive to the shell properties, as the intensity profile of lower order modes is concentrated nearer to the surface. There does not appear to be any obvious relationship to n: in the figure, all lines of one type (for example, blue dashed) are parallel to one another,[6] despite all posessing different mode numbers.

Implementation

The mathematics of core-shell scattering is of course an outgrowth of the Mie theory whose simple case was described in the previous section. The equations themselves appear to have first been formalised in 1981[233], and refined by Ray in 1995[234] to aid in the inverse problem of fitting m and r to experimental data. Both publications also extensively discuss the angular dependence of scattering (the 'phase function') which is beyond the scope of the spectroscopy done here.

In recent years, increasingly efficient methods to predict or calculate explicitly the WGM wavelengths of core shell particles have been presented by Stewart[235], Gorkowski[236, 237], and Moridnejad[228]. I have recieved the original source code of the model used in these publications, which will be the basis of the core-shell fits conducted and presented in Chapter 8. It was written by Thomas C. Preston in `fortran 90` and was compiled and run by myself on the Bluecrystal 3 supercomputer.

Unlike the LARA algorithm, the input it requires is not spectra, nor does it operate in real time on an instrument. Instead, a single table is read in that contains the center wavelengths of every WGM (columns) against time (rows), allowing the user the ability to 'clean' unwanted false positives from the online peak detection first. It is for this reason that some of the homogeneous radii presented in this thesis were actually fit with this model. It was converted to operate in a homogeneous 'mode' by setting either $r_c = r_s$ or $r_c = 0$. In those cases, initial estimates of radius and m were usually available from LARA for the experiment, but the spectra recorded expressed

[6] or at least, their motion is indistinguishable from parallel on the scale chosen.

low signal:noise and the data was high variance.

3.2.4 Single Droplet Spectrum Collection and Analysis

First, the backscattered light from the levitated particle is diverted to a spectrograph (Acton SpectraPro 2500i, 0.5 m focal length) coupled to a CCD (both a Princeton Instruments Pixis 256 and Pixis X were used to record spectra). To be specific, the experiments described in Chapters 6 and 7 were probed at a time resolution of 1 s, and those in Chapter 8 with a 2 s resolution. The wavelength resolution was 0.05 nm/pixel. The values of the wavelengths associated to each pixel of the CCD were regularly calibrated between experiments, as advised in the spectrograph manual, to avoid slow drift. The procedure involved placing an emission lamp containing either mercury or both helium and neon in the path of the the spectrograph grating. The deviation between the observed and known emission wavelengths was then assumed to be linear in the interval captured in the spectrum, and a correction equation $\lambda_{actual} = k\lambda_{observed} + c$ was produced via linear regression.

Once confidence in the recorded spectra has been established, it is possible to apply Mie theory fitting methods, based on the mathematics described above, to the resonances that are observed. The first objective of any data analysis method proceeding along these lines is to separate the stimulated peaks from the spontaneous: namely, to detect the enhanced resonances coincident with whispering gallery modes within the broad peaks arising from Raman scattering. If that can be achieved with a low number of false positives and false negatives, it becomes possible to extract droplet properties from the Raman signal.

Figure 3.2.6 presents an example that showcases the function of the online fitting algorithm (LARA) employed for homogeneous particles. The input is the wavelengths of the WGMs, presented in panel c, and the objective is to approach a self consistent solution to r (panel a) and m (panel b) within intervals preset by the user. In this example, the particle consists of a sodium nitrate solute coming into equilibrium with a relative humidity of approximately 57%. Initially, the fit radii and refractive indices have a high variation. As the number of spectra increases and

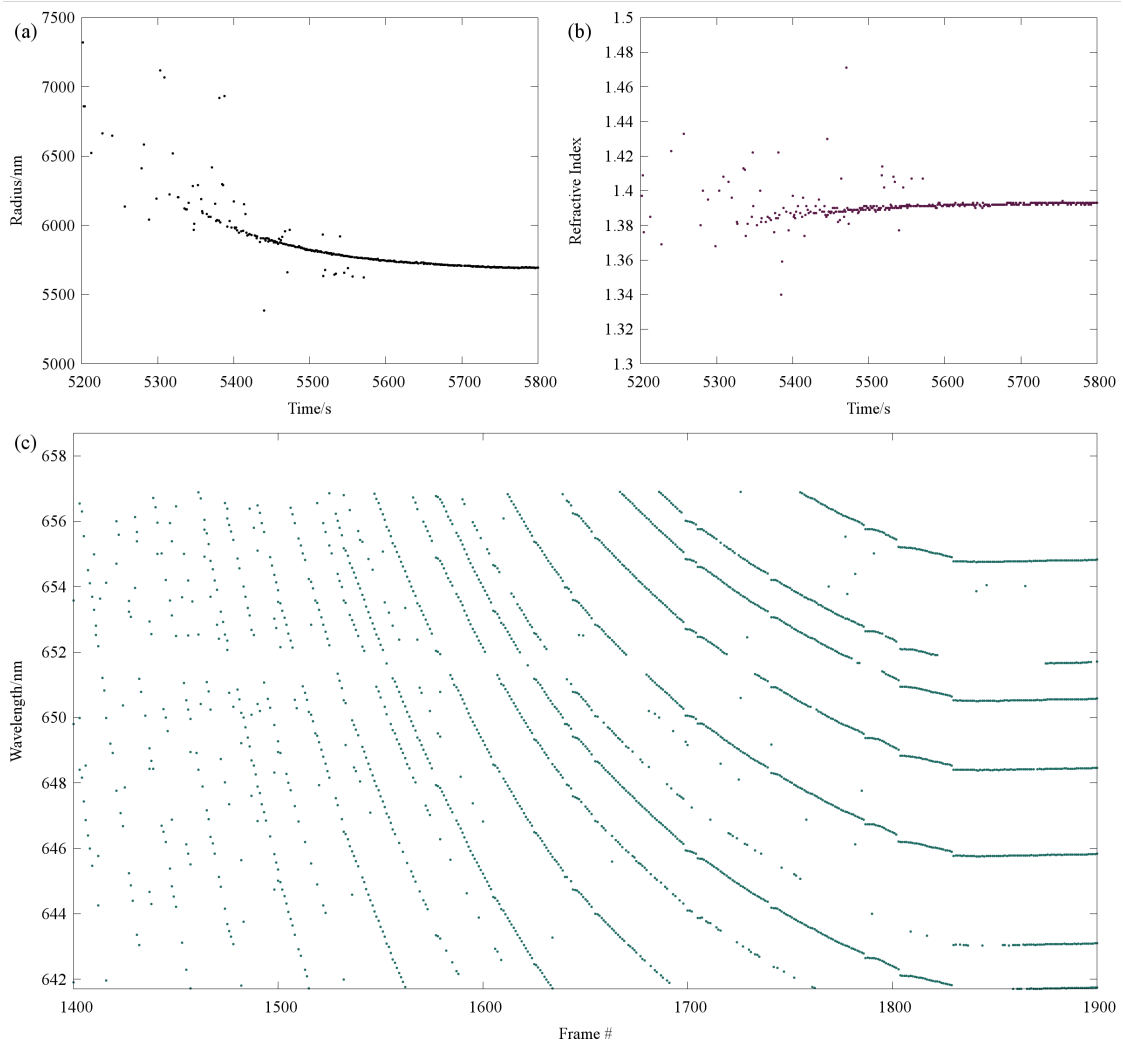

Figure 3.2.6: An example of the decreasing uncertainty in a Mie fit as a recently trapped sodiun nitrate particle comes into equilibrium with the trapping cell conditions. The variance in the predicted (a) radius and (b) refractive index slowly reduces as signal to noise ratio of the Whispering Gallery Modes (c) improves. By about 5700 s, a single solution has been found by the algorithm.

the peak detection becomes more consistent (occuring around frame 1600 in panel c, after which almost every whispering gallery mode is detected), the error reduces substantially and the signal to noise ratio in the fit points becomes almost zero.

The user should usually reduce the fitting interval once a consistent solution has been found to avoid erroneous solutions being found. These windows of r, m, mode number and dispersion should also be expanded or moved whenever the droplet is perturbed during the experiment. For instance, any time the humidity or laser power is changed, the particle may grow and its refractive index decrease due to the increased water content. If the true values leave the upper and lower bounds of the intervals respectively, then the resultant data will become untrustworthy. Different considerations one may employ when adjusting the bounds will be presented in Chapter 6.

3.2.5 Refractive Index Correction

The refractive index m is not constant as a function of the frequency of the incident light. This is because the path length the beam takes through an object, in units of wavelengths, λ, changes. Indeed, if multiple wavelengths are incident on the object simultaneously, they will be refracted to different extents and be separated as they leave. This effect is shown strikingly by the iconic cover of the Pink Floyd album '*The Dark Side of the Moon',* reproduced in Figure 3.2.7.

Higher energy, shorter wavelength beams experience a larger refractive index and so blue and purple light exhibit the sharpest exit angles from the prism. More specifically, one can construct a mathematical representation of the correction.

$$m(\lambda) = m(\lambda_0) + m_1(\frac{1}{\lambda} - \frac{1}{\lambda_0}) + m_2(\frac{1}{\lambda} - \frac{1}{\lambda_0}). \tag{3.2.18}$$

m_1 and m_2 represent the dispersion of the material contained within the sample, or in this case, the droplet. In the experiments described in Chapter 8, $\lambda = 589$ nm and $\lambda_0 = 645$ nm, meaning that $m(\lambda_0)$ is the refractive index arrived at through solving the Mie theory equations 3.2.12-13.

Figure 3.2.7: An example of wavelength dependent refractive index. © Storm Thorgerson

3.3 Summary

Optical tweezing is becoming an established method of studying single particles in a variety of research groups and universities, as there are now commercially available versions of the setup described herein. Indeed, Arthur Ashkin himself was jointly awarded the 2018 Nobel Prize in Physics for his invention of an apparatus for immobilising and manipulating small objects in three dimensions using optical forces. The origin of the forces has been introduced briefly. The apparatus used, as well the experimental procedure that was followed throughout the lab work conducted herein was also described.

The ability to investigate droplets that are levitating overcomes a significant drawback of deposition based methods. For instance, surface tension, vapour pressure and crystal nucleation can be altered significantly by the presence of an interface where the droplet touches a solid

surface. The rate of heat transferred through this interface is also distinctly faster than in free air. The Leidenfrost effect, where droplets are heated so much that they levitate on their own vapour, is a good example of the kind of undue influence this can have[238].

The spectroscopic techniques used here allow continuous determination of the droplet size and optical properties, by using the trapping laser as a scattering souce. This capability is achieved through a mathematical understanding of the Mie scattering phenomenon: As the droplets studied are too close in size to the wavelength of the laser to be approximated either as spherical lenses or point particles, we must understand the influence of resonance effects. These occur where waves can travese the droplet surface in an efficient manner, and correspond to incident wavelengths that divide neatly into the circumference of the sphere, to a first approximation. The requirement of total internal reflection within the interior also means that a dependence on refractive index is observed.

Core-Shell particles comprised of concentric spheres with different indices of refraction can also be sized, but the parameter space of the equations is enormous, and so the analysis becomes less efficient. Nonetheless, an initial description of the problem has been outlined.

Single particle methods may not be fully atmospherically relevant in the context of the emergent properties of a large plume, as separate from an isolated aerosol droplet (see Chapter 8 for a more detailed exploration of that subject). Nonetheless they offer a unique ability to perturb the environment a droplet experiences and observe the resultant effects. Specifically, two methods have been described that allow the control of the gas conditions directly around the tweezed droplet, which will be used as the independent variable in the majority of experiments: the first is the ambient humidity, which can change the composition, viscosity and crystallinity of the particles. The second is a method to initiate the oxidation of a VOC, which will hopefully prompt Criegee intermediate chemistry of the type described in Section 1.2.3 of this thesis.

Chapter 4

Computational Methods

"I know now why you cry, though it is something I can never do." - The Terminator, *Terminator 2: Judgement Day*

4.1 Introduction to Molecular Dynamics

Understanding the structure, bonding, dynamical properties of matter on molecular scales requires a model system of some kind. While it is true that single molecule spectroscopy methods have recently made it possible to investigate these properties experimentally, molecular dynamics has been a more crucial tool in the development of physical science, especially since the invention of computing.

Briefly, the model systems constructed seek to represent the atomic nuclei of a chemical system as spherical particles with defined mass and charge. The system is then propagated in time, either via Newtonian or Quantum Mechanics. In this thesis, only Newtonian (sometimes called Molecular) Mechanics will be used.

Two groundbreaking studies were conducted in the 1970s that first used Molecular Dynamics (MD) to construct a time evolving trajectory of many atoms: Stillinger and Rahman simulated small phases of liquid water at multiple temperatures in 1974[239]. They calculated both radial distribution functions and diffusion coefficients from the simulation to interpret what they were seeing, and to relate the computational model to the experimental literature.[1] Then, McCammon, Gelin and Karplus simulated the motion of the first organic molecule in 1977[240], the protein Bovine pancreatic trypsin inhibitor.

Since then, the capabilities of different MD packages have grown enormously[241], and currently the field of MD is much larger than can be introduced in the available space. In a similar way to the start of Chapter 3, it must be stated here that what follows is not intended to be a comprehensive account of the state of the literature. Instead, this Chapter attempts to explain the key concepts that underpin the simulations that were conducted as part of my work, as well as the techniques that will be used subsequently.

To begin with, we shall consider the equations of motion that the system is subject to, and how these are implemented using the Verlet algorithm. Secondly, the construction of thermodynamic ensembles will be discussed, specifically with reference to the use of periodic boundary conditions, as well as the coupling of temperature and pressure to an external bath.

The configurations that the atoms may adopt during the dynamics are usually constrained according to a number of different potential energy functions, which together are referred to as a 'force field'. The implicit parameters they contain, as well as a small number of tunable parameters that can be chosen by the user, are introduced. They relate to the bonds and angles between atoms, the influence of temperature on atomic velocities through changes in kinetic energy, the introduction of pressure, the electrostatic interactions between non-bonded atoms, and so on. Each of these will be explored in further detail.

Next, the precise details of the simulations that will form the basis of Chapter 5 will be stated, once again with an aim to enhancing the reproduceability of this work. As the extraction

[1] Both of these calculations will be performed by myself in Chapter 5, for exactly the same purpose, 45 years later.

of diffusion coefficients from both experiments and modelling is a central tenet of this thesis, an introduction to the procedure one can use to estimate diffusion rates from an MD trajectory will also be presented in Section 4.2. Focus will be afforded to the transition of molecular motion from the ballistic to the diffusive regime as it decorrelates from its initial state.

Finally, non-equilibrium methods will be described. The 'rare event problem' will also be introduced, justifying the benefits of simulation methods that can overcome limitations in the sampling of free energy landscapes.

4.1.1 Newton's Laws of Motion

The first objective of a model where individual atoms and molecules are represented separately is to determine the forces acting on each one, as a result of work being done *on* or *by* the system. The lay scientist will be familiar with the scalar form of Newton's Second Law:

$$F = ma \tag{4.1.1}$$

where a body of mass *m,* subject to a force *F,* will experience an acceleration a. For a many body atomic system, this expression can be expanded, becoming a matrix multiplication problem

$$\overrightarrow{a}(t) = M^{-1}\overrightarrow{f}(t). \tag{4.1.2}$$

Note that a and f are now vectors of dimension $(3N)$, where N is the number of atoms in the system. M is a diagonal matrix containing the masses of each atom. With reference to the atomic *positions*, *q(t)* it follows from these relations that

$$v(t) = \frac{d}{dt}q(t) \tag{4.1.3}$$

$$\overrightarrow{a}(t) = \frac{d}{dt}\vec{v}(t) = \frac{d^2}{dt^2}\vec{q}(t) \tag{4.1.4}$$

where *v(t)* is a vector of the atomic velocities. On the right hand side of equation 4.1.2, the force on the system, f, is defined as

$$\overrightarrow{f}(t) = -\frac{d}{dq}V(q(t)) \tag{4.1.5}$$

Which is to say, the force arises from a gradient in the potential energy, V, which also depends on the nuclear coordinates q. The above arises from the definition of work, W, in a closed system,

$$W = V(q(t_0)) - V(q(t_1)) = \int f(t) \cdot dr \tag{4.1.6}$$

and is also closely related to Hamilton's equations in classical mechanics.[2] If we take V to be the potential energy of the electron cloud surrounding the nuclei, then a model force field should aim to capture as much of the attractive and repulsive intractions within this cloud as is feasible. In this context, it should also be noted that equation 4.1.5 is valid only in systems when the Born-Oppenheimer approximation can be assumed to hold[242]. The assumption states that the electron density in a molecular system reacts instantaneously with respect to its nuclear motion. Strictly, it is only in this case that there is a one-to-one mapping between V and q. ab initio methods of extracting *V(q)* from the Schrodinger equation are increasingly commonplace, for example using Density Functional Theory, but these techniques are beyond the scope of this thesis. Instead, approximations can be made within a classical mechanics framework. As we will see in section 4.1.4, the molecules are considered to be non-reacting, and constructed from charged spheres bonded by spring like bonds. One of the most important approximations in MD is that the system Hamiltonian is simply the sum of potential and kinetic energy, K:

$$H(v,q) = K(v(t)) + V(q(t)) \tag{4.1.7}$$

4.1.2 The Verlet Algorithm

With the above axioms defined, it is possible to construct analogues to the so called *'suvat'* equations in classical mechanics. These equations interrelate the positions, velocities and accel-

[2] which relate the spatial derivative of a system's Hamiltonian to the temporal derivative of its momentum

erations of the atoms. In the Velocity Verlet algorithm[243], their purpose is to propagate the dynamics forward in time, from one configuration to the next:

$$q(t+\delta t) = q(t) + \delta t \cdot v(t) + \frac{1}{2}\delta t^2 \cdot a(t) \tag{4.1.8}$$

$$v(t+\delta t) = v(t) + \frac{1}{2}\delta t(a(t) + a(t+\delta t)) \tag{4.1.9}$$

In this way the time dimension is discrete rather than continuous. It *integrates* forward in steps of length δt.

A common variant of the Verlet algorithm is the Leapfrog algorithm. It differs from normal Verlet integration in that the positions and velocities of the atoms are decoupled from one another, and calculated in a staggered manner. The position component of the system can be replaced by the following:

$$q(t+\delta t) = q(t) + \delta t \cdot v(t + {}^{\delta t}/_{2}) \tag{4.1.10}$$

where

$$v(t + {}^{\delta t}/_{2}) = v(t) + a(t)\frac{1}{2}\delta t \tag{4.1.11}$$

Therefore, as the name alludes, each time one of the above is evaluated it 'leaps over' the other by half a timestep. Additionally, as *q(t)* is differentiable numerically, the original velocities defined by equation 4.1.8 can also be evaluated at each 'full' timestep if required.

At different points in this chapter and the next, the concepts of configuration space and phase space will be used. For the avoidance of confusion, the configuration space of a chemical system is the set of all possible coordinates q where the constituent atoms can reside. Phase space, by constrast, is a much larger set that contains the configuration space, as well as every permutation of atomic velocities associated with each configuration. The objective of any integration scheme is to construct a physically realistic trajectory through the phase space of the system, from which

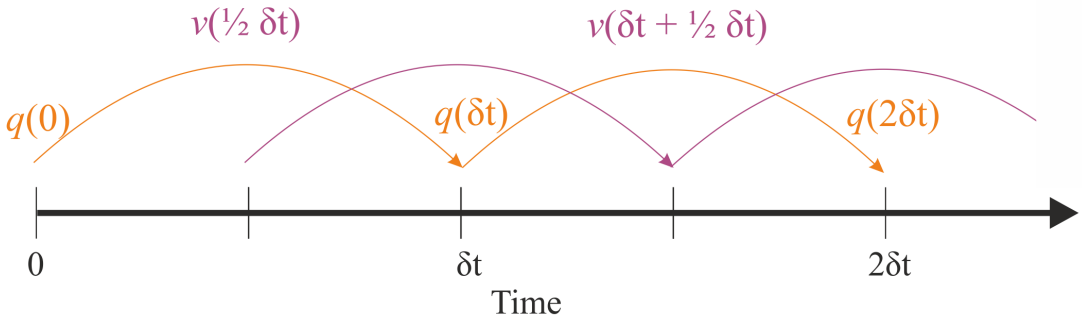

Figure 4.1.1: Schematic representation of the leapfrog algorithm (equations 4.1.10-11). While the intervals between the evaluations of atomic positions and velocities are the same, they are offset from one another by half a timestep.

an event can be observed, or a thermodynamic quantity estimated. To achieve that the user must constrain the geometric relationships betwen atoms in space, as well as the range of possible velocities those atoms can adopt. As we will see, the choice of molecular force fields is what achieves the former, whereas pressure and temperature coupling achieve the latter.

4.1.3 Temperature Coupling

If the observations made or quantities extracted from a trajectory are to be meaningfully interpretted, it is necessary for the system to be subject to a thermodynamic ensemble. The construction of an ensemble is depedent on thermodynamic degrees of freedom being constrained. For instance, it is usually the case that the number of atoms present in an MD simulation, N, is constant. That is certainly true for all simulations conducted in Chapter 5. Therefore, one can choose between running dynamics in the NVE, NpT, or NVT ensembles, and within each choose different methods of maintaining the ensemble.

Generally speaking, the purpose of specifying a variable is to mimic the influence of the surrounding phase outside of the simulation box, be it crystal, liquid or glass. The size, or mass, of the hypothetical external phase can be considered large enough to damp any instantaneous fluctuations in V, T, or E etc. such that those quantities are *constrained*. In this way a connection

can be established between microscopic and macroscopic observables[244].

To avoid confusion, it is appropriate here to more precisely define the relationships between the quantities of *temperature*, *molecular velocity* and *kinetic energy*. As stated in Chapter 2, the Maxwell-Boltzmann distribution defines how the speeds of molecules, v, are distributed as a function of temperature. The precise dependence is:

$$f(v,T) = 4\pi v^2 \left(\frac{M_r}{2\pi k_B T}\right)^{3/2} \exp\left(\frac{-M_r v^2}{2k_B T}\right) \tag{4.1.12}$$

Where f is the probability of a given molecule possessing a speed equal to v, and M_r is the molecular mass. There is a strong influence of the temperature, T, on the shape of the distribution: hotter systems exhibit more broad distributions than colder systems, and the mean velocity is higher. Therefore temperature can be considered a collective variable: a single value prescribes the relationships between many particles, through equation 4.1.12.

Strictly, the above equation was only formalised to describe the velocity distribution of an ideal gas. Despite this, it is often used to generate and to update the velocities assigned to each atom in molecular simulations of solids or liquids. It is beyond the scope of this introduction to discuss whether such a choice is physically realistic. It is certainly accurate in the limit of very short timescales, where molecules have a sufficiently long mean free path then they can travel ballistically at their intial velocity, as if they were in a gas. Then, as the density of the system increases, the ballistic regime will shorten and each molecule will collide with its nearest neighbours after a decreasing number of timesteps. Once the ballistic regime has been overcome and the decorrelated motion becomes important, the shape of the distribution f will change (See section 4.2.3 for a more in depth discussion of decorrelation from the initial state). Finally, it should also be noted that translational motion is not the only way for heat to manifest itself on a molecular scale: any solid object with a temperature above 0 K possesses thermal energy, but its constituent molecules cannot diffuse within their local environment. Therefore, rotational and vibrational degrees of freedom will also be populated by thermal energy in a molecular system. This is the crucial distinction between thermal and kinetic energy: kinetic energy is the subset of

thermal energy that acts through translational degrees of freedom.

In the latter two ensembles stated above, the isothermal-isobaric (NpT) and canonical (NVT) ensembles, the thermal energy generated (or experienced) by the system is continuously exchanged with a hypothetical heat bath. It is also exchanged between molecules of different types within the simulation box. Unless otherwise stated, the NpT ensemble will be used for most simulations reported in this thesis, including all relating to extracting diffusion coefficients. The bath acts to counter the effects of slow drift in temperature, as defined by the inverse of equation 4.1.12, and damp any oscillations that may arise. The strength of the coupling between the system and the 'surroundings' is determined by the rate of decay of these oscillations. In GROMACS, which is the MD package used for all simulations, the user may set the rate by defining a time constant τ_T in advance. Two schemes are currently available, namely the *Berendsen* and *velocity rescaling[245]* thermostats. In this thesis only the velocity rescaling thermostat will be used as it is known to more effectively replicate the thermodynamic ensemble when N is comparatively low. As they only differ by the addition of one term to the thermal energy a brief introduction will be given to both.

Berendsen operates by forcing an exponential decay of temperature towards the bath temperature, T_0:

$$\frac{dT}{dt} = \frac{T_0 - T}{\tau} \tag{4.1.13}$$

Where $\tau \geq \tau_T$.[3] In this thesis it has been set to 0.01 ps. T is interrelated to the kinetic energy of the system and the momenta of each particle by

$$K = \sum_i^N |\frac{1}{2} m_i v_i^2| = \frac{k_B T}{2}(3N - N_C) \tag{4.1.14}$$

as well as the set of velocities v_i by the distribution 4.1.11. Therefore any fluctuation in either K or T that occurs will be damped by the Berendsen algorithm, and will return to the bath values.

[3]The precise ratio of the two varies depending on the heat capacity and the constrants the system experiences: $\tau = 2C_V \tau_T / (N - N_C) k_B$. The GROMACS manual provides a number of rules of thumb for the magnitude τ_T should take in different simulations.

N_C is the number of constraints applied to the system, which in most cases will be defined by the force fields applied.[4]

For now it is useful to differentiate the velocity rescaling components that may be included in the coupling scheme. Additionally, since their inclusion will incur a computational expense, the advantages that might justify using the *velocity-rescale* thermostat will also be described. Firstly, since only T is time dependent on the right hand side of equation 4.1.14, both K and T should decay at the same rate:

$$dK = \frac{K_0 - K}{\tau_T} dt. \tag{4.1.15}$$

The velocity rescaling thermostat begins with this assumption and then adds a second term to the evolving kinetic energy:

$$dK = \frac{K_0 - K}{\tau_T} dt + dW \cdot 2\sqrt{\frac{KK_0}{\tau_T(3N - N_C)}} \tag{4.1.16}$$

dW is a stochastically varying interval of energy that keeps changing in size according to a random walk: in other words, in a memoryless way, meaning that a time series of dW would appear as noise. The key difference between the stochastic formalism and the Berendsen thermostat is that the latter is deterministic; this is not. In the context of the sum over i that is present in equation 4.1.14, the velocities of each atom are also selected randomly within dW. In the GROMACS implementation, a numerical seed is taken to produce the chain, and in the simulations described in Chapter 5 the $RANDOM variable in the bash shell is used, being changed continually.

If the right hand side of 4.1.14 is substituted into the rescaling term in 4.1.16, one obtains

$$dW \cdot k_B \sqrt{\frac{TT_0(3N - N_C)}{\tau_T}} \tag{4.1.17}$$

Which shows that the rescaling term is less strongly dependent on T than the decay term.

[4]The nature of the functions that constrain atomic motion will be introduced in subsection 4.1.5 and the precise force fields used are described in Section 4.2.

4.1.4 Pressure Coupling

All simulations described herein will be subject to so-called periodic boundary conditions in three dimensions. The boundary refers to the commonly used procedure that each face of the simulation box is placed in contact with the face immediately 'opposite' it, creating an infinite recursion in all three dimensions. The atoms and molecules near the box edge will then experience attractions and repulsions with nearest neighbours, or indeed diffuse across the boundary and reappear on the other side.

When operating in the NpT ensemble, the simulation box must be allowed to grow and shrink. If the total pressure the molecules exert on the outer surface of the box changes from some user defined P_{ref}, it suggests the density is fluctuating from its equilibrium value, and so a rescaling of the volume is applied to damp the fluctuation. When the Berendsen barostat is employed a rescaling function is applied to the matrix of the box vectors, and depends on the isothermal compressibility β_{ij} and to some damping timescale τ_P. A precise definition of the function can be found in the GROMACS manual and is deemed outside the scope of this thesis. In all described simulations the time constant is set as 2.5 ps for all molecules. The isothermal compressibility of water and all organic molecules was defined as $5{\cdot}10^{-5}$ bar^{-1}.

What is of crucial importance is the effect is has on the box pressure, which is expected to decay in much the same way as temperature under the Berendsen thermostat.

$$\frac{dP}{dt} = \frac{P_{ref} - P}{\tau_P} \tag{4.1.18}$$

An example of the influence Berendsen coupling has on the box vector length over a 500 ps equilibration trajectory is shown in Figure 4.1.2.

During equilibration simulations the Berendsen barostat was used and during 'data collection', the long time dynamics simulations intended to estimate diffusion coefficients, the Parrinello-Rahman barostat was employed. It has been suggested that the NpT ensemble is approximated better by this scheme in systems where N is small[246]. Instead of the pressure itself being coupled to a reference value, the second derivative of the box vectors is:

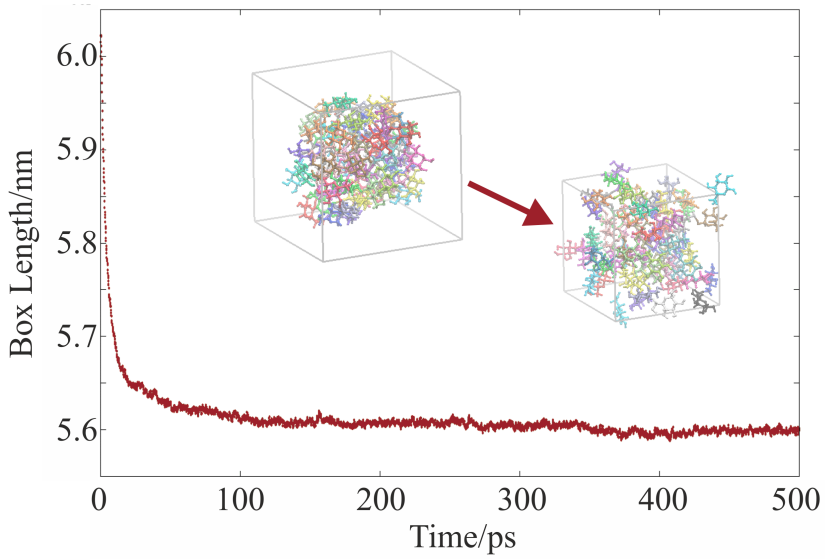

Figure 4.1.2: An example of changes in simulation box length as Berendsen pressure coupling is turned on in an equilibration trajectory. Inset are snapshots of a box containing 60 glucose molecules (individually coloured) before and after pressure coupling has converged it to a steady state. Note that individual molecules cross the periodic boundary in the rightmost image, which is indicative of a uniform density.

$$\frac{d^2\mathbf{b}}{dt^2} = V\mathbf{W}^{-1}\mathbf{b}'^{-1}(P - P_{ref}) \tag{4.1.19}$$

Where **b** is a diagonal matrix containing the lengths of the x, y, and z dimensions of the box.[5] V is the scalar volume of the box, ' denotes the trace of **b**, and

$$\mathbf{W^{-1}}_{ij} = \frac{4\pi^2\beta_{ij}}{3\tau_P max(\mathbf{b})} \tag{4.1.20}$$

wherer *max(***b***)* indicates the largest box element of the matrix **b**.

4.1.5 Interaction functions

As established in section 4.1.1, there are many force fields available for molecular simulation, and there is ample debate as to which may be the most appropriate or accurate to study a given

[5] $x = y = z$ for all simulations conducted here. Nonetheless it is entirely possible to have cuboid boxes, or crystallographic unit cell boxes with angles that are not $90^{\bigcirc}$, at which point a matrix is required to express the vectors.

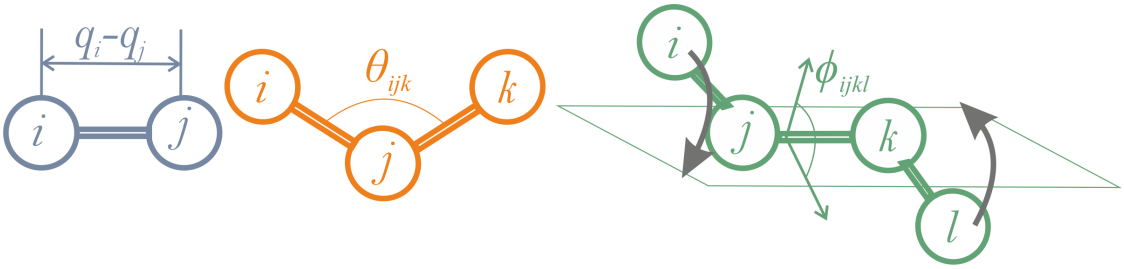

Figure 4.1.3: Molecular degrees of freedom which are subject to potential energy constraints in common MD force fields. See main text for the functional form of the potential energy function. From left to right: Bond, angle, and dihedral.

system. Nonetheless, all force fields and simulation packages contain similar terms within their potential functions, that describe certain processes or phenomena. These terms usually take the form of mathematical functions that penalise the system when it seeks to move outside of some 'chemically reasonable' state.

Classical potential energy functions are divided into specific terms. In some cases or model systems extra terms can be added to the system Hamiltonian, but usually a general set of terms can be stated. Bonding interactions are often the strongest, and relate to interactions between sets of atoms in pairs, groups of three and groups of four:

$$V_{bonding}(q) = \sum_{i \neq j} k_r(|q_i - q_j| - q_0)^2 + \sum_{i \neq j \neq k} k_\theta(\theta(q)_{ijk} - \theta(q)^{\ominus}_{ijk})^2 + \sum_{i \neq j \neq k \neq l} k_\phi(1 + \cos(n\phi_{ijkl} - \phi^{\ominus}_{ijkl})) \quad (4.1.21)$$

Where the parameters are as follows: q_i is the position of atom i, q_0 is the equilibrium bond distance between i and j, θ_{ijk} is the angle suspended between the vectors ij and jk, and ϕ_{ijkl} is the dihedral angle between the planes ijk and jkl.[6] $\theta^{\ominus}_{ijk}$ and $\phi^{\ominus}_{ijkl}$ are the set of equilibrium angles which minimise the potential energy of a given molecule. $\phi_{ijkl} = 0$ is defined as the configuration where atoms i and l adopt a *cis-* alignment with respect to one another. All three are schematically shown in Figure 4.1.3.

It is possible, and in fact common, to replace the first Hooke's Law type term with a linear

[6] or, alternatively, between the vectors ij and kl when viewed along the jk axis.

constraint (LINCS) algorithm, that reproduces bond oscillations but with improved computational efficiency[247]. The algorithm is called every timestep to compute forces on the atoms using both their masses and a matrix of gradients, $\boldsymbol{B}$, whose elements are defined by

$$B_{ij} = \frac{\delta}{\delta q_i}[|q_i - q_j| - q_0] \tag{4.1.22}$$

The full algorithm is beyond the scope of the current subsection, but it is crucial to note that it involves expanding a constraint coupling matrix, that arises from the transformation of $\boldsymbol{B}$. The number of terms evaluated increased the accuracy of the predicted force, and the subsequent bond oscillations.

The terms containing non-bonding influences on V can be defined in a larger variety of ways. But they tend to involve electrostatic attractions at long distances and hard repulsions at short distances:

$$V_{non-bonding}(q) = \sum_{i \neq j} 4\varepsilon_{LJ}\left(\frac{\sigma_{ij}^{12}}{q_{ij}^{12}} - \frac{\sigma_{ij}^{6}}{q_{ij}^{6}}\right) + \sum_{i \neq j} \frac{C_i C_j}{4\pi\varepsilon_c q_{ij}} \tag{4.1.23}$$

The first term is a Lennard-Jones (LJ) potential and the second describes the Coulombic interactions of the partial charges on each atom. ε_{LJ} and ε_c are the potential energy minimum in the LJ potential (well depth) and the relative dielectric constant of the system respectively. Their values, as well as the set of partical charges C_{i} and LJ constants σ_{ij} for all atom types are parametrised within each force field. 'Atom types' refer not only to the element but contain some information relating to different hybridisations that are possible: a vinylic carbon atom requires a different set of parameters to a carbon atom present within an alkane chain, or a carbonyl.

There are different approaches to deciding which pairwise interactions to consider important and which to truncate, how to sum them throughout the simulation box, and how to a deal with interactions across the periodic boundary. These have been considered beyond the scope of this thesis. The original publication detailing the particle mesh Ewald method[248] provides a good introduction to constructing such a simulation from first principles.

At several points in Chapter 5 the concept of atoms or molecules posessing a Van der Waals radius will be utilised. Generally speaking, this is the maximum distance away from some chemical moiety under consideration at which repulsion is first experienced. In the context of the above equation we can say that the Van der Waals radius of atom i can be approximated by the mean value of the interaction parameter $r_{VdW} = \bar{\sigma_{ij}}$, averaged over all atoms j that are present in the simulation box. Each individual σ_{ij} is one of the roots of the Lennard-Jones potential: specifically, the root where attractive and repulsive forces balance. For a more in depth overview of the connection between the Lennard Jones function and the Van der Waals equation of state, see Allen and Tildesley[244], as well as the publication of Oostenbrik et al.[249]

4.2 Simulation Procedure

What has been described here thus far refers mostly to the underlying mathematics of an MD simulation. Care has been taken to explain the essential concepts, as well as more complex factors any user should be aware of if they wish to have confidence in the resultant trajectory. Throughout, my focus has been on presenting information which will be relevant to the contents of Chapter 5, and so it is not intended to be exhaustive. What will follow is related specifically to the models, inputs and construction of the simulations discussed in the next Chapter.

All simulations were run using GROMACS, version 5.0.6, running on the Blue Crystal 3 high performance computing cluster at the Univeristy of Bristol. In most of the reported simulations GPU acceleration was implemented using Plumed[250]. They contained both water and a series of organic saccharides, of different molecular mass and chain length.

4.2.1 Equilibration

Water was represented by the TIP4P/2005[251] potential, due to its accuracy in reproducing the experimental phase and self diffusion characteristics. Sucrose, Glucose and Raffinose were each represented by a modified version of the GROMOS 54a7 force field[249], with an expanded range of atom types. Both the force field and the initial all-atom coordinates were acquired

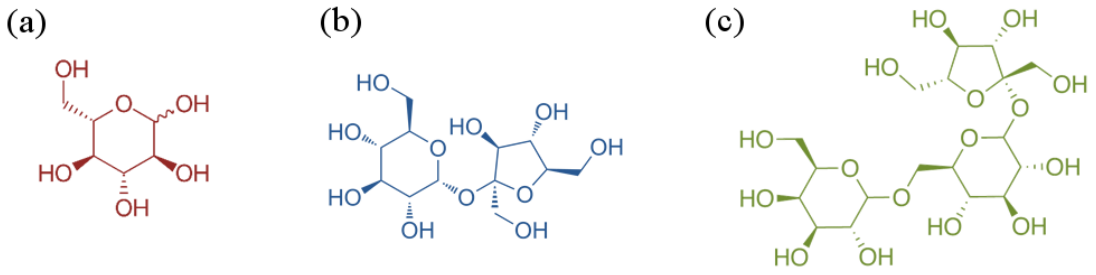

Figure 4.2.1: Structural formulae of the organic molecules investigated in this thesis by both experimental and computational methods: (a) Glucose, (b) Sucrose, (c) Raffinose

from the automated topology builder (ATB) database[252] (further details on the generation[253] and validation[254] of coordinates, partial charges and force fields by ATB has been detailed extensively in the literature).

Initial coordinates were generated using the packmol program[255], which randomly places set numbers of molecules into three dimensional space, allowing tight control over the solute mole fractions in the generated simulation boxes, whilst not biasing the simulations to one area of configuration space. Constraints were inserted such that no two molecules were placed within 3Å of each other, and the input random seed was continuously replaced (again using the $RANDOM global variable in the bash shell). In experiments where the mole fraction of organics was relatively low, $x_{org} < 0.9$, the GROMACS solvate command was used to insert water molecules. In the more dehydrated simulations packmol was used to insert the few water molecules required.

The Lincs algorithm[247] was used to constrain all bonds, to an order of four in the constraint coupling matrix, with seven iterations in the final step. Electrostatic forces were calculated using the particle mesh Ewald summation[248], and Van der Waals interactions were provided by the twin range cut-offs method, both of which were truncated at 8Å. The update frequency was every 5 timesteps. The Verlet scheme[256] was used for neighbour searching across the periodic boundary conditions in three dimensions. Velocities were generated using a Maxwell-Boltzmann distribution at 300 K (See section 4.1.3), with the random seed continuously changed.

The starting coordinates produced by packmol are not suitable for MD simulations immediately. The configuration must be energy minimised using the steepest descent method to allow

bonds and angles to satisfy the constraints of the topology file. The minimisation was conducted with an initial step size of 0.001 nm until the maximum force was below 50 kJ mol^{-1} nm^{-1}. After this, approximately 500 ps of equilibration was conducted with the standard GROMACS md integrator, Berendsen pressure coupling and the velocity-rescaling thermostat to produce the desired thermodynamic ensemble. Therefore the NpT ensemble was generated in all described trajectories. In what we can describe as 'data collection' simulations of section 5.1, the run parameters were the all same, except that the barostat used was Parrinello-Rahman[246], in recognition of the small number of atoms being simulated. τ_P was concomitantly increased from 0.5 to 2.5 ps. The input coordinates were taken as the output frame of the equilibration trajectory, but the atomic velocities were rerandomised rather than read in.

4.2.2 Convergence (to the Diffusive Regime)

It is not always possible to extract diffusion coefficients from a short trajectory, or indeed short intervals of longer trajectories, as there are two regimes of motion that the molecules must transition between for diffusion to manifest. In the initial timesteps, molecular motion proceeds in a purely ballistic way until the atoms collide with their nearest neighbours.[7] Ballistic motion is a consequence of the fact that most atoms will not be colliding with any others[8] in a given frame, and so they will act as if in a vacuum for at least a few timesteps after the displacement calculation has been begun. Once the solvent cage is encountered, the system slowly begins to decorrelate from ('forget') its initial state. In this sense diffusion is an emergent property, and requires the motion of the molecules under consideration to arrive at a steady state.

The initial coordinates were taken from the output frame of the equilibration trajectory, within the regime where the total energy was stable. Simulation parameters were identical to those detailed above, with the addition of GPU acceleration via PLUMED. Coordinates and energies were both written out at a frequency of 100 timesteps. Mean squared displacements were calcu-

[7] In the literature the set of surrounding atoms is sometimes referred to as the 'solvent cage' of the atom or molecule under consideration.

[8] A good metric for what constitutes a collision could be that the magnitude of the repulsive terms in the Lennard-Jones potential becomes comparable to the bonded potential: $V_{non\text{-}bonded} \sim V_{bonded}$

lated both using the GROMACS g_msd program, and on the three cartesian coordinates of the centers of mass, looping through all possible values of t-t_0. This was achieved using the `mdtraj` module in python.

Mathematically, we can begin by rearranging equation 4.1.3:

$$q(t) - q(0) = \int_0^t v(t')dt' \tag{4.2.1}$$

Recall that q is the configuration of all molecules present. The calculation relating to the displacement of a single molecule is slightly different, but that will be introduced at the appropriate time in Chapter 5. Instead, the displacement of a given molecule type, averaged over all of the individuals in the simulation, must become an expectation value. The *mean squared* displacement (MSD) can therefore be defined in terms of the velocity-velocity autocorrelation function:

$$< |q(t) - q(0)|^2 > = < \int_0^t v(t')dt' \int_0^{t'} v(t")dt" > \tag{4.2.2}$$

Where *t'* and *t"* are dummy variables which are integrated up to the simulation time *t*. The right hand side can be restated as a so-called *Green-Kubo* relation, wherein the temportal coordinate system is slightly translated and the integrals are taken outside of the evaluated expectation value:

$$< |q(t) - q(0)|^2 > = 2 \int_0^t \int_0^{t'} < v(t" - t')v(0) > dt"dt'. \tag{4.2.3}$$

The factor of 2 arises from integrand symmetry[9]. D is defined as the constant of integration appearing upon evaluation of the outer integral. When the inner variable, *t"*, is integrated out we get:

[9]This is a slightly subtle effect to convey. In Eq. 4.2.2 both the velocity functions are integrated over separately. In Eq. 4.2.3 both integrals operate on the same (even) function, which is multiplied by a scalar ($v(0)$). As the domain of the second integral is always less than or equal to the first ($t" \leq t'$), the 'area under the curve' increases at half the rate.

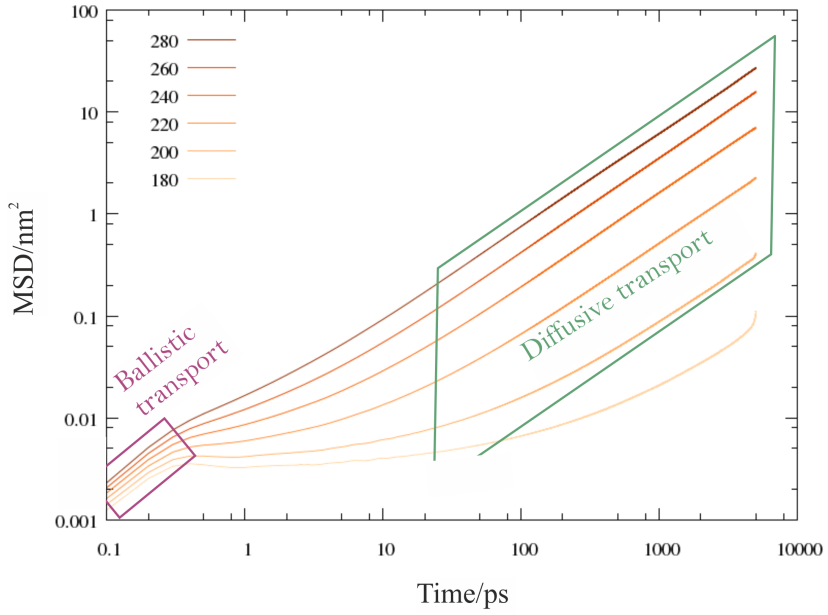

Figure 4.2.2: Systematic series of $< |q(t) - q(0)|^2 >$ mean squared displacement curves calculated from water simulations, as a function of temperature over a 100 K window.

$$< |q(t) - q(0)|^2 >= 2t \int_0^t < v(t')v(0) > dt' \equiv 2t \cdot D \tag{4.2.4}$$

in one dimension. In three dimensions the right hand side would be equal to $6tD$. These relationships are usually sufficient to extract the value of D from the calculated MSD. If we assume that the velocities of the atoms decorrelate in an approximately exponential manner from their initial values,

$$< v(t)v(0) >=< v(0) >^2 \exp(-t/\tau_D) \tag{4.2.5}$$

Then a more explicit formula can be stated by substitution:

$$< |q(t) - q(0)|^2 >= 2 < v(0) >^2 \int \exp(-t'/\tau_D)dt' = 2\tau < v(0) >^2 (1 - \exp(-t/\tau_D)) \tag{4.2.6}$$

where τ_D is the relaxation time of the transition from ballistic to diffusive behaviour.

Diffusion coefficients should therefore only be fit within the range of timesteps after the velocities have fully decorrelated and the evolving motion of the molecule under consideration

converges to a t^1 diffusive dependence, which can be determined by fitting the value of τ_D in equation 4.2.6. It is difficult to identify the ballistic regime except on a logarithmic scale. An example is shown in Figure 4.2.1: With reference to the Maxwell-Boltzmann equation 4.2.6, as well as the thermostat equations 4.1.12 - 14, the lower temperatures reduce the initial <v(0)> and increase τ_D , shifting the lines downwards and constraining the available displacement.

4.3 Non-Equilibrium Methods

In the discussion of molecular dynamics methods thus far in this chapter, there has been an inherent assumption: that any process or phenomenon under study has a high probability of occuring within the time window probed by the simulation. This is not always, or perhaps even usually, the case. When the window is too short, or the underlying probability too low, different approaches must be used to explore phase space in order to 'find' or 'catalyse' the desired event. There are many methods available to do this, although only one was employed in this thesis. Broadly speaking, non-equilibrium methods introduce some form of energy (enthalpy) into the system, on top of that supplied by the temperature coupling. The conceit is that this will expand the region of the potential energy surface that can be explored enough to include the desired event. In other words, we hope that the excess energy will dissipate through degrees of freedom that are likely to bring about rare events.

4.3.1 The Rare Event Problem

It is useful to consider why the model time accessible in an MD simulation is limited. Most crucially, the computational power, and CPU time available, are finite. Together, these two factors define the total number of floating point operations that can be performed, which sets an upper limit on the number of timesteps that can be evaluated by the integrator. The choice of timestep length is also important. Pragmatically, the user wants to chose the longest value possible, that is still capable of capturing the fastest oscillation in the system. When organic molecules

are present, as is the case in this thesis, the vibraion of aliphatic C-H bonds is likely to be the limiting frequency.

Given these constraints, it is not feasible to employ equilibrium molecular dynamics to probe certain kinds of events: only those that occur after a large activation barrier has been overcome, or those that require strange configurations to be adopted that are unlike the initial conditions. The 'problem' with both kinds of events is one of ergodicity. To say anything confidently about the event, it is usually the case that the user wishes to measure a quantity related to it and extract a time average. For that to be the case it must be known with some confidence that the phase space of the system has been sampled effectively. Only then can the ensemble average of the quantity be equated to the time average of the quantity:

$$\langle A \rangle_t = \frac{\int A(q(t)) \exp(-\frac{V(q)}{kT}) dQ}{\int \exp(-\frac{V(q)}{kT}) dQ}. \tag{4.3.1}$$

dQ represents an infinitesimal element of the atomic coordinates and momenta of the system, as stated in section 4.1.2. In this sense the right hand side can be considered analogous to an observation in a physical laboratory experiment. *In silico*, it is rarely possible for t to be long enough to converge the left and right hand sides stably to the same value, and so most MD simulations are not ergodic. However, it does not necessarily follow from this limitation that the hypothesised event will not occur, simply that statistically significant information cannot be extracted about it. It therefore becomes desirable to 'enhance' the sampling of the system by the molecular mechanics integration, in order to create a non-equilibrium trajectory such that the *event* is sampled effectively.

How one may produce and sustain a non equilibrium state within a trajectory is a non-trivial problem, and many procedures have been discussed or devised in the literature. Some methods, such as Boxed Dynamics (BXD) or Umbrella Sampling (US)[257], involve allowing the system to gain a certain amount of potential energy, and then constraining its motion through phase space to stop that energy being dissipated. Sometimes non-equilibrium MD methods will disrupt the sampling of the *thermodynamic ensemble*, and the resultant trajectory will be unphysical. Other

methods can supply energy to the system in a way that the degrees of freedom still fluctuate in a realistic manner. Monte Carlo (MC) methods[258] forego any kind of time integration and simply construct a sequence of frames that are intended to stochastically sample configuration space.

4.3.2 Hybrid Monte Carlo

Monte Carlo is a common method of unbiased searching that may be applied to many mathematical or physical problems. In the context of molecular simulation, it actually predates molecular dynamics[258] as a method of sampling configurations of atoms. It can be applied to explore the potential energy surface more fully than standard MD integration, as it generates constrained or unfavourable configurations that may not be reached in a reasonable timescale otherwise. Unlike the Newtonian mechanics based methods described in section 4.1, it does not directly simulate the time evolution of a system.

Instead, Monte Carlo integration generates a random distribution of input configurations, which are then either accepted into, or rejected from, the sequence of frames, on the basis of whether certain conditions are satisfied. The conditions are defined by the so called metropolis criterion, and the output sequence is, if assembled correctly, referred to as a Markov chain. This can aid in the discovery of rare events.

Enhanced sampling was provided by the Hybrid Monte Carlo/Umbrella Sampling (HMC/US) scheme[259]. It is a recent development of the HMC scheme and has been used successfully to probe classical nucleation theory by driving the growth of sodium chloride crystals[259], and has repeatedly shown utility in accelerating non-equilibrium rare events. Broadly, the procedure works by repeatedly[10] supplying the system with randomised kinetic energies, that are 'pre-screened'. The Metropolis Criterion is used in the screening process:

[10] every 50 MD timesteps.

$$P(acc(old \rightarrow new)) = \begin{cases} 1 & \triangle U + \triangle K < 0 \\ \exp(-\triangle U/k_B T)\exp(-\triangle K/k_B T) & \triangle U + \triangle K > 0 \end{cases} \quad (4.3.2)$$

Where *P(acc)* is the probability of accepting a new set of momenta onto the atomic coordinates, and $\triangle$ refers to the difference in energy between the old and new (proposed) states. One of the benefits of using the Metropolis criterion is that the resultant energy distribution is physically realistic, approximating somewhat the Maxwell-Boltzmann distribution.

4.3.3 Calculating the Potential of Mean Force

While one can estimate the potential energy that an *atom* experiences on the basis of the force field and interaction parameters (section 4.1.5), determining the potential energy of an event is a non trivial process. To begin with, we can consider the ensemble average equation 4.3.1. If the values of an obervable quantity are a function of the atomic coordinates, then the mean value of the variable $\langle A \rangle$ must be calculated by weighting each observation according to the changes in potential that occur at that configuration. Therefore, it stands to reason that the equation can be inverted: That is to say, the way in which a quantity is distributed about its mean contains all the information necessary to determine how the potential fluctuates as a function of atomic coordinates, or cartesian space.

Mathematically, if the integral over $A \cdot dQ$ is replaced with a discrete sum over *timesteps*, *t'*, then it is possible to create an expression for the Botzmann weight of a normalised distribution of *A*.

$$\frac{A(Q)}{\sum_{t'} A(q(t'))} = \exp(-\frac{V(Q)}{k_B T}) \quad (4.3.3)$$

When implemented in code, Q can be either a single configuration, a sequence of configurations in time, or a matrix of configurations where two or more coordinates are changed independently. Q can be considered the input coordinates of a potential energy surface. *q(t)* is the configuration adopted in one frame. If the sequence is constructed along a one dimensional

reaction coordinate, for instance by Umbrella Sampling, then this is the approximate basis upon which the Weighted Histogram Analysis Method operates[260, 261]. However, as we will see in Chapter 5, other methods of effectively probing coordinates of interest can be achieved using the tools of constraints and temperature coupling.

One condition that must apply no matter the simulation method is that the user needs confidence in the system having been able to effectively sample the important area of phase space. It is only in that case that the left hand side of equation 4.3.3 will be equal to the *probability* that *A(Q)* is adopted. Therefore, we can rearrange the equation to make *V(Q)* the subject:

$$V(Q) = -k_B T \ln(P(A(Q))) \tag{4.3.4}$$

In this way a dynamic trajectory can be converted into a static representation of a property of the system. When implementing such an approach in code, certain decisions may need to be made where there is no objectively correct solution. I will try to introduce them, explaining the factors that one should consider before arriving at a solution, before finally describing the implementation that was used in this work.

- Firstly, it is usually the case that Q represents a hyperdimensional surface over which the system traverses, which is difficult to render or interpret. Therefore, either the important dimensions should be chosen, or a *dimensionality reduction* must be performed. Both procedures are open to interpretation, but the intended result is the same: A representation of the potential energy surface in a drastically smaller set of coordinate axes, usually two or three. It is the objective of the reduction scheme that they will capture the majority of the variance in the observed trajectory. If the rare event being probed is a conformational change of a small molecule, one can select bond angles and lengths (recall section 4.1.5) which are known to change as the molecule rearranges. In that case one must rely on 'chemical intuition', so to speak, to decide which parameters most strongly affected. Conversely, the secondary or tertiary structure of a large protein depends on the collective motion of many subunits, some of which are not directly bonded, and may not even be

close to one another. In this thesis one potential energy surface has been created (in section 5.1.3) as a function of cartesian coordinates, which means that dimensionality reduction is not required, since there are already a low number of orthogonal dimensions.

- Secondly, the resolution at which the histogram *P(A(Q))* is created will influence the 'output' value of *V(Q)*. If there are too few bins, then the histogram will be unable to resolve each separate state which the system can adopt. The resultant potential energy surface will therefore be a too simplistic a representation, as barriers or wells may disappear. Consequently, kinetic information (eg. rate constants) calculated from V could be inaccurate. If the resolution is too high (ie. the number of bins is comparable to the number of timesteps), the probabilities will be artificially small as the frequency of observations in each bin will be very close to zero. When this happens the extracted potential energy will be wrong, and the entire surface will appear to be more unstable than it is. Hence, the choice of resolution and interval width is difficult to make, especially when one does not know in advance what to expect. The histograms of occupancy over cartesian space shown in section 5.1.3 are two dimensional projections of a 2.5 nm^3 cubic volume onto a matrix of size 150×150. Several other sizes were attempted, and were not found to change the well depths significantly. That resolution maximised the information extracted whilst minimising the number of artefacts.

4.3.4 Restraints and Constraints

In GROMACS[262] (and indeed in other MD packages) it is possible to impose a number of forces onto atoms in addition to those defined within the force field[263, 264]. The purpose of doing this is generally to hold the system in a high potential energy, or rare, configuration and to sample around it using the other molecular degrees of freedom. Harmonic potentials are used in Umbrella Sampling to produce the histograms from which the PMF may be extracted. A drawback of this method is that it requires the coordinate across which the restraint is imposed to be one dimensional. It is also difficult to implement reaction coordinates which are not related

to the atomic coordinates either through linear combinations or derivatives.

Another way to restrict atomic motion is to freeze it. That is to say, to remove certain molecules from the Verlet algorithm altogether, such that their positions and velocities are not updated as the simulation progresses through time. In terms of the internal evaluation of the velocities, freezing necessarily requires equation 4.1.11 to be replaced. Instead the following is evaluated:

$$\overrightarrow{v}(t+\delta t/2) = \begin{bmatrix} x \\ y \\ z \end{bmatrix} \times \lambda \times \left[\overrightarrow{v}(t-\delta t/2) + \frac{\overrightarrow{f}(t)\cdot\delta t}{m} + \overrightarrow{a}(t)\delta t \right] \tag{4.3.5}$$

where x, y, and z are either zero or one, depending on which axes the user would like to freeze the motion. $0 < \lambda < 1$, and acts as a scaling constant that allows degrees of slowing to be imparted on the selected molecules.

4.4 Outlook

Throughout this chapter a number of mathematical formulations of physical laws or processes have been described, that were first published and implemented by many different authors over decades. Together they can create a 'state of the science' approximation of the Hamiltonian of a system at the nanoscale, and propagate it in time. Our intention is to control for fluctuations in the dynamics with which we are not interested, by choosing an appropriate thermodynamic ensemble, constructing it through short equilibration trajectories, and maintaining it for as long as is computationally feasible.

It is not believed to be an exagerration to state that Computational Chemistry has become so advanced that researchers now commonly treat simulations in a manner akin to how Physical Chemists treat laboratory experiments. Once a hypothesis has been chosen and a set of initial conditions constructed, the evolving behaviour, while deterministic, is highly chaotic: Very slight changes to the input will substantially affect the outcome, and which trajectory is taken to get

there. As a result, many observable thermodynamic quantities are effectively unpredictable to the researcher, and must be interrogated after the simulation has finished. Another reason one may want to analyse an MD simulation as if it were a physical system being perturbed is that the construction of MD programs tends to induces emergent phenomena: each of the algorithms that have been described in this chapter tend to interact and feed back with each other in complex ways as time progresses.

Chapter 5

The Microscopic Mixing State of Organic Aerosol and its Impact on Mechanisms of Diffusion

'Frozen in pose,

Locked up in amber eternally.' - Queens of the Stone Age, *Un-Reborn Again*

To date, there have been relatively few attempts to apply molecular mechanics methods to the task of understanding mass transport in aerosol, either of organic or inorganic composition. The few publications that can be found in the literature usually contain very low concentrations of solute[202, 122, 193, 265] in comparison to the supersaturated structures that can exist stably in the aerosol phase. Other studies have focused on the nucleation of particles from the gas phase[266] and the deliquescence of sodium chloride nanoparticles[267]. By contrast, water diffusion in the kinds of highly concentrated, highly viscous, and amorphous lattices that are believed to form at lower relative humidities have received comparatively little investigation.

Here a large number of simulations are presented that can be placed broadly into two different MD studies. The first, presented in section 5.1, is an examination of the diffusion of water in an organic aerosol close to the limit of zero water activity. We consider the structure of such a system to be a single water molecule surrounded indefinitely by amorphously packed organic molecules. As the simulations probe a volume much smaller than could contain the mean size of an SOA particle in the atmosphere (see Figure 1.2.2), these studies are intended to represent processes occuring close to the surface of a dry particle.

Much of the text of section 5.1 appears in the publication *Transient Cavity Dynamics and Divergence from the Stokes-Einstein Equation in Organic Aerosol,* currently under review, and of which I am the second author. The first half of the paper pertains to viscosity and diffusion measurements conducted by Young Chul-Song. A large number of independent diffusion and viscosity measurements were collated as part of his work. Viscosity measurements were conducted using the coalescence methodology described in Section 1.4.2, and the methodology of the diffusion measurement was developed by myself and will be the subject of Chpater 6, although the specifics are not important for the analysis conducted here. The crucial result that these studies were intending to understand was that the two phenomena become decoupled, as measured by the inability of the Stokes-Einstein relation (Equation 1.5.1) to interconvert between them in highly viscous organic particles. Crucially, the extent of the decoupling was found to be dependent on the molecular weight, and volume, of the organic molecule present in the droplets.

The simulations were conducted separately to try to interpret the nanoscale phenomenon that might be influencing the single particle observations. However, it is believed that they constitute a standalone study, and the results are applicable outside of the scope of the paper. Rob Arbon also collaborated on this work, using Markov model approaches to interpret some of the trajectories, finding key features and moments that deserved further investigation. His work contributed to Section 5.1.3: specifically, he calculated the time constants for water motion within its enclosing matrix, from which barrier heights were estimated and discussed.

Secondly, diffusion coefficients have been extracted from the dynamics of water in sucrose at

different mole fractions, which is representative of the molecules present in the SOA. The initial coordinates are generated with ratios of the two compounds concentrations that span a range of water activities. The values are fit using a more conventional mean squared displacement procedure and compared with several literature studies, showing good agreement. The structure and dynamical pathways that the constituent water molecules adopt are investigated both by inspection and by calculation of pair distribution functions.

5.1 Molecular Dynamics of Caged Water

In order to better understand the mechanism of water transport on a molecular level, atomistic simulations of water-sucrose mixtures have been conducted at several mass fractions, corresponding to varying water activities. One advantage Molecular simulation posesses in this context is that any composition can be investigated. Unlike bulk experimental methods, we are not constrained by the solubility limit: the range concentrations of solute that can exist stably in a solution without condensing or crystallising out. It is very easy to create metastable or non-equilibrium microstructures and investigate their dynamics. Indeed, that is the focus of this entire chapter. Firstly, this section will investigate the mechanism of water diffusion at a composition very close to the dehydrated limit. The limit represents an asymptote of the internal structures that can be formed within organic aerosol, and so is a useful starting point for the study. Additionally, full dehydration is usually difficult to achieve experimentally[268], making this an interesting example of a computational measurement that exceeds the scope of laboratory measurements.

5.1.1 Motivation

It is now generally understood that atmospheric processes such as drying[139], cooling[130, 160] and oxidation[137] can induce glass transitions in organic aerosol, an effect which is especially prevalent in *secondary* particles[19] (see Chapter 1). Given the viscosities which both biogenic and anthropogenic SOA are known to adopt when confronted with such conditions, it is highly unlikely that a homogeneous concentration of water will be maintained between the center and

the edge of any particle (see Chapter 2). Instead, a morphology is adopted where a gradient in hydration exists between the droplet core and the interface. Residual water trapped within the droplet will need to diffuse through the dry outer surface in order to escape.

The water content of a plume of aerosol influences its size distribution, refractive index[269, 270], photochemical reactivity[91] et cetera. It is therefore of considerable interest to the broader aerosol science community to be able to predict accurately the evolving amount of water within a droplet. To achieve this, we must understand the flux of small amounts of water diffuse through otherwise dehydrated organic material.

Perhaps the most famous definition of diffusion is the Stokes-Einstein equation:

$$D = \frac{k_B T}{6\pi\eta a} \tag{5.1.1}$$

Where all parameters are as defined in Chapter 1. The dry limit was found to generate the largest deviation between the predicted diffusion rate and the observed viscosity.

One of the crucial outcomes of my coworker Dr. Young Chul-Song's experiments was that the inapplicability of the Stokes-Einstein equation to organic aerosol increases with the disparity in size between water and the organic molecule which constitutes the remainder of the particle. We believed this is intricately linked to the fact that no reference is made to the size of the medium through which the species under consideration is diffusing in equation 5.1.1; the solvent molecules are assumed to be significantly smaller, meaning that that can be approximated as a continuum. When this is not the case, and the molecule whose diffusion we are interested in is in fact smaller than the molecules through which it is diffusing, the dynamics of the system can no longer be described by Stokes flow.

Several attempts at modifying the equation, to bring it in line with experimental data, have been suggested in the literature. A very recent, at the time of writing, paper by Zaragoza et al.[271] proposed that the effect of confinement into pores and channels on the diffusion of water can be accounted for by introducing a second term:

$$D_w = \frac{k_B T}{3\pi\eta a}[1 + \frac{3a}{8d}\ln(\frac{2d}{a})] \tag{5.1.2}$$

where a remains the hydrodynamic radius, and d is the the mean pore width, which in their simulations was on the order of tens of nanometers. In one limiting case, if $a = d$, the increase in diffusion rate is constant. Then, as confinement becomes less severe, the size of the pore increases relative to the diffusing species and the second term collapses in magnitude, and the original relationship is recovered. Other examples of Stokes-Einstein variants include modifying the exponent of viscosity such that D does not vary so severely with it[126, 128, 185] ($D \sim \eta^{-\alpha}$, also known as the 'fractional' S-E relation), replacing the viscosity with the structural relaxation time of diffusing the molecule[272](which may not be as easy to determine experimentally), or changing the the constant by which ηa is multiplied in the denominator[273].

But these modifications are akin to 'papering over the cracks', so to speak. Something is clearly occurring in many chemical systems that violates the assumptions of Stokes' Law, and so the molecules are experiencing less frictional drag than the equation requires them to in order for them to obey it. Indeed, some authors have even suggested replacing equation 5.1.1 entirely with other treatments that do not prescribe the the relationship between the diffusing object and its surroundings[274].

More examples of systems exhibiting non S-E physics, and their surprising applicability to aerosol, will be introduced in Chapter 7. For now, we shall focus our attention at a smaller scale, namely the diffusion process of a single water molecule experiencing close to infinite dilution.

5.1.2 Representing the Amorphous State at the Nanoscale

Unlike in common molecular dynamics studies, where diffusion coefficients are calculated by averaging across every molecule present in the simulation, here there is only one molecule to chart, by definition. Instead, we must average over trajectories initialised from different starting coordinates.

Nine trajectories containing one water molecule randomly placed within an amorphous lattice of sucrose were run for 1 μs. The simulation box used in each case was a cubic unit cell of side length 2.5-3.5 nm, periodic in all three dimensions. The 'placement' of the organic molecules is intended to replicate the amorphous packing structure that is expected to occur near the surface of a glassy sucrose droplet[135]. Packmol was used to generate the initial configuration, by placing sucrose molecules into a large box with uncorrelated positions and orientations. The 'concentrations' involved (35 sucrose molecules to one water) imply these simulations replicate a macroscopic water activity very close to zero. Equilibration and pressure coupling were then conducted as described in Chapter 4.

5.1.3 Random Walks Through Sucrose

A snapshot of the initial coordinates of one of the nine trajectories can be seen in Figure 5.1.1. Due to the extremely kinetically limited state of the aqueous-sucrose system, it is necessary to simulate dynamics for very long periods of time, relative to, for example, the timescale of molecular vibration or rotation. This maximises the probability that the initial conditions are overcome, and that the constituent molecules decorrelated from their initial conditions as the simulation proceeds. In each of the trajectories of caged water, dynamics were computed for 1 μs, and it was found that, when averaged over all nine trajectories, the mean squared displacements of the water molecules converged to a diffusive dependence on simulation time, t:

$$< r^2 > \sim 6D_w t \tag{5.1.3}$$

or, more specifically:

$$< r^2 > = 6D_w t + \varepsilon. \tag{5.1.4}$$

Where ε is a small offset related to a localisation uncertainty which arises when tracking single particles[275]. As a position write-out frequency of once per 100 MD timesteps has been

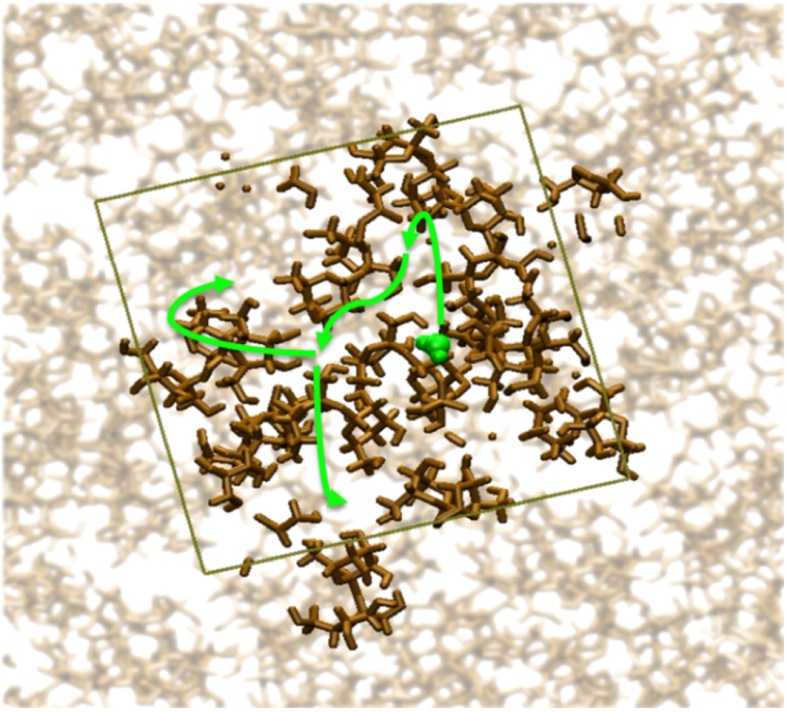

Figure 5.1.1: The initial coordinates of a trajectory of a single water molecule (lime), produced by taking a slice across the simulation box. This representation clearly shows stable, empty cavities within the sucrose lattice (brown bonds). Some of the possible pathways available to the water molecule are also shown via the green arrows. In the background the periodic images in two dimensions are produced in light brown to give a rough indication of the lattice density.

used in this study, the water molecule's position should be considered to accrue a variance associated with its motion in the MD steps we do not see[276].

Inspection of the resultant trajectories reveals that the motion of the water molecule is highly intricate, and appears to be influenced by several factors, acting on different timescales. On the timescale of hundreds of picoseconds, the motion proceeds by discrete movements between cavities within the sucrose structure. Between each of these events, the water spends extended periods confined within a new region until either (1) it is able to deform the local environment and escape, or (2) the collective motion of the sucrose opens a pathway that allows further displacement within the lattice (see supplementary movies). The word region was used as the cavities are stochastically distributed throughout the nanostructure, meaning that in some cases the water molecule may be surrounded by one, two, or three states that are separated by cages comprised

of the functional groups of sucrose. As such, each of these 'jumps' can be considered as an independent rare event process with an activation barrier (the energy distribution throughout all nine trajectories will be discussed later). It is found that the cavities do not appear to close or shrink significantly upon the water hopping away, and in fact 'return trips' are a common feature of the observed trajectories.

The net displacement achieved by a random walk in three dimensions will be less than the path length taken between the initial and final positions, a consequence of the fact that the total translational motion of water through such a lattice is not Brownian: Firstly, because only discrete positions in the matrix can be occupied; Secondly, because all nine trajectories contain segments during which the water is travelling perpendicularly, or even backwards, relative to its net displacement. It is also the case that the decorrelation of the water velocity is limited by the rearrangement of the sucrose, as well as how close its initial location is to the nearest available cavity, rather than the dynamics of a more typical solvation shell in an aqueous environment (recall Section 4.2.2). Therefore, it is desirable to calculate the magnitude of the displacement to the current position, $|< r^2 >|$, at every timestep, rather than cumulatively sum the path length that takes into account every intermediate 'jump'. Additionally, removal from the calculation of the centre of mass motion of the simulation box ensures that any rapid motion whilst trapped, which does not contribute to the net displacement, does not count towards the calculation of net displacement.[1]

The mean value for $D_{w,org}$ that was calculated given these criteria was 4.64×10^{-17} m^2s^{-1}. The mean of the errors computed from fits to each of the nine trajectories individually was 9.09×10^{-17} m^2s^{-1}, suggesting an upper limit of approximately $1.37\times10^{-16}$and lower limit of *negative* 4.54×10^{-17} m^2s^{-1}, leading to an infinitely large lower error bar on a log scale.[2] As the water clearly is achieving a net displacement, it is more realistic to take the smallest value of D_w recorded from a single trajectory as the lower bound of the error: that being 1.004×10^{-18} m^2s^{-1}.

[1]The calculation including the center of mass motion was performed initially and produced an inflated value.

[2]Recalling Chapter 2, we can say that Maxwell-Stefan diffusion coefficients cannot be negative, although Fickian coefficients can.

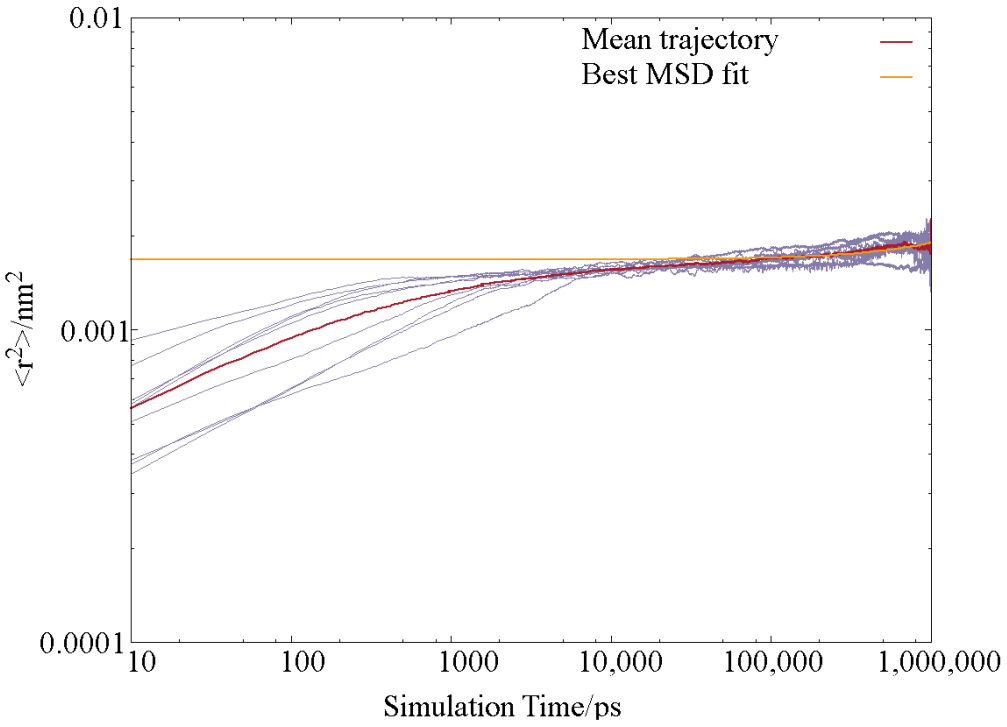

Figure 5.1.2: Single particle mean squared displacements of nine trajectories (purple lines), along with best fit of the mean path (red) to equation 5.1.4 (yellow, including constant at t=0).

Interpetation

A literature review was conducted, to investigate whether any corrections or different functional forms of mean squared displacement had been proposed in studies of similar molecular systems. For instance, it has been previously suggesting that water flux through large sugars occurs via a process posessing some characteristics of percolation[277, 278], although these studies are conducted on bulk systems that cannot access the concentrations probed here.

More interestingly, several investigations of diffusion which proceeds by executing discrete hops were found:

- A recent publication[279] by Alcazar-Cano and Delgado-Buscalioni has suggested that in systems where the diffusing particles are trapped in the manner that we have observed manner, and cannot freely move through channels, it may be more appropriate to fit to a

*sub*diffusive dependence, namely

$$< r^2 > \sim 6D_w t^{\alpha} \tag{5.1.5}$$

Where $\alpha \rightarrow 0$ as the proportion of particles that are trapped approaches 100%.

The standard deviation of the nine fit diffusion coefficient estimates was larger than the mean, leading to an infinitely large lower error bar on a log scale. Therefore, extracting values of D from fits to equation 5.1.5 whilst also floating the value of α, was considered as an alternative method of quantifying the error in the extracted values of D. While the functional form of the MSD data (Fig 5.1.2) is similar to that presented in the publication, the extracted values were too fast to be physically realistic at this composition: D_w = 3.22×10^{-11} $m^2 s^{-1}$ and $\alpha = 0.61$, which is faster than D values determined from systems containing more water in this work (See section 5.2.3).

- Perhaps attempting to capture the same effect, the work of Zwanzig in 1988[280] assessed jump diffusion in what he called a 'rough potential' where the particle under consideration must traverse a landscape of many nearly degenerate local minima. In that publication, he concluded that effective diffusion will be much lower than the value of D equation 5.1.1 would imply. Therefore, the effect on the mean squared displacement was incorporated into the mathematics by correcting D, rather than t. As the observed D is smaller than than any of the deviations observed in the companion study by Young Chul-Song.

It is unknown why these treatments cannot be reconciled with the experimental data by such a significant margin. It could be

- he effective D (ie. the trapped displacement exceeds the net displacement), a factor ε was introduced, that accounts for the 'roughness' of the free energy landscape:

$$D_{eff} = D_w \cdot \exp\left(-\varepsilon / k_B T\right)^2 \tag{5.1.6}$$

It is likely that, in the limit of long enough sampling, and a suitable definition of ε, the deviation from Stokes-Einstein should be the same as the correction term in the above equation.

If we take ε/k_BT to be the activation barrier (which is 6.42 k_BT; see the next subsection), as per the above section, the calculated value of the S-E deviation, $D_{eff}/D_{w,org}$ is 2.7×10^{-6}.[3] The value is much larger than any of the deviations observed in the companion study by Young Chul-Song.

It is unknown why these treatments cannot be reconciled with the experimental data by such a significant margin. It could be possible that the physics described in both publications only manifests with more full statistics than it was possible to acquire here, or that the probe particle was too constrained in its motion here. In any case, now that alternative treatments have been investigated, it is possible to say with confidence that Equation 5.1.4 produces the most accurate fits to the observed mean squared displacement.

Interestingly, nanoscale phenomena such as that described here are often observed in conjunction with, and are presumably coupled to, stretched exponential relaxation of different variables in sugar solutions[281, 282]. Relaxation dynamics of a such a functional form will be central to the investigations conducted in Chapter 6, and where they arise, will be interpretted with reference to this microscopic diffusion mechanism. There is a similar process which has been referred to as the 'micropore diffusion' mechanism, and was proposed (or perhaps rediscovered) whilst describing the uptake and transport of small molecules through porous Zeolite structures[283].

Potential of Mean Force

It is unclear to what extent the type of motion described above will lead to productive diffusion against a chemical potential gradient, which is what is induced and probed during the optical tweezers measurements reported in later chapters of this Thesis. Strictly speaking, it is also the only type of diffusion that will be described by a Fickian diffusion constant, as per Chapter 2 of this thesis. What we can say is that the cavities do not have a uniform free energy. Nor is there a uniform lifetime spent at each one.

Inspecting histograms of the coordinates visited by the nine water molecules reveals the kinds

[3] implying a particle viscosity of 3.5×10^{4} Pa s.

of clusters around specific places that one would expect from a hopping motion, most notably in simulations numbered 3 and 7. Those simulations are slightly more ambiguous, and suggest that the molecule is residing in one cavity for an extended period of time as it deforms. If this is true, then some component of the energy landscape that the water experiences will slowly change at the same timescale as the matrix readjustment. The autocorrelation of the position of a single sucrose molecule is one piece of evidence from which some insight can be gleaned. This has been calculated for trajectory three, and is presented in Appendix A. It shows that the timescale of the organic motion is significantly longer than the water hops, in part due to its smaller diffusion coefficient[185]. Indeed, the value only begins to decorrelate between 1 and 10 ns.

Therefore, in order to determine changes in the potential energy surface of the cavities, several shorter trajectories were initialised from three points within a 3 ns timeslice, where it was determined that water was repeatedly jumping between two distinct positions in the lattice. These points were chosen on the basis of their proximity either side of jumps between cavities. The sucrose molecules were frozen in place using constraints, and the water allowed to traverse the matrix, with its velocity initialised from the value it had at that frame in the original trajectory.

Each of these simulations was 50 ns in length. Other changes in MD parameters are as follows: SHAKE[284] was used to constrain bonds instead of LINCS, and the Parrinello-Rahman barostat was exchanged for Berendsen. The temperature was also increased to 400 K, which allows the water molecule to become a 'probe' of sorts, to chart the frozen cavities within the lattice.[4]

Figure 5.1.3 presents four frames from the early timesteps of the trajectory, showing free movement between cavities on very small timescales. If we assume the motion is ergodic, then the frequency that each cavity is visited should be proportional to its stability, and to the stability of the water molecule when it resides there. In the limit where the sampling is effective, the potential of mean force of each cavity can be determined by Boltzmann weighting of the resultant

[4]These aspects having been stated, it is unclear whether the concepts of pressure and temperature have any physical significance when applied a situation where only one molecule is capable of motion, and its immediate landscape is fixed in place. Suffice to say that these are not intended to be simulations from which physically realistic trajectories can be inferred.

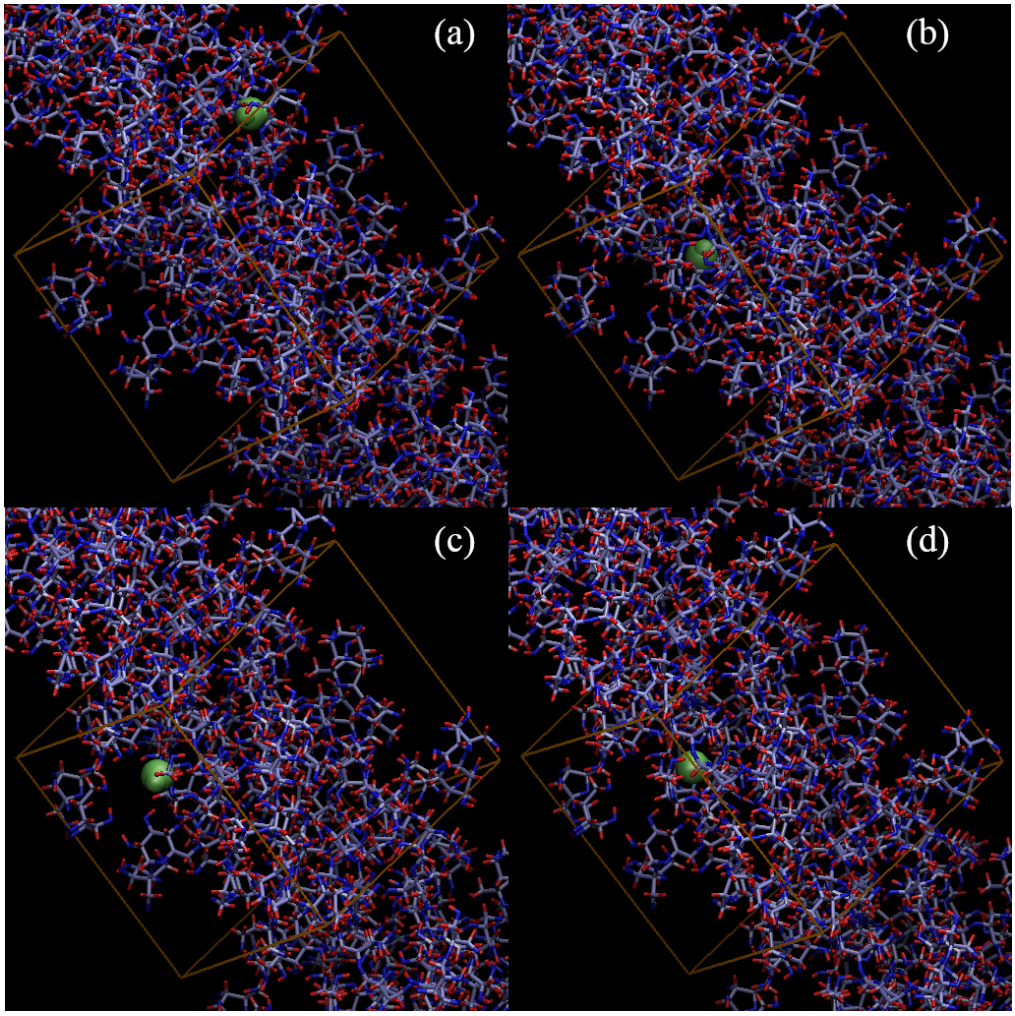

Figure 5.1.3: Snapshots from a simulation in which sucrose has been frozen and water (green atoms) has been given 400 K of kinetic energy, showing extremely rapid motion throughout the lattice (see supplementary movie). Time stamps are (a) initial frame (b) 1 ps (c) 3 ps (d) 4 ps. Periodic boundaries are shown in bronze, and one periodic image is shown in the y dimension only.

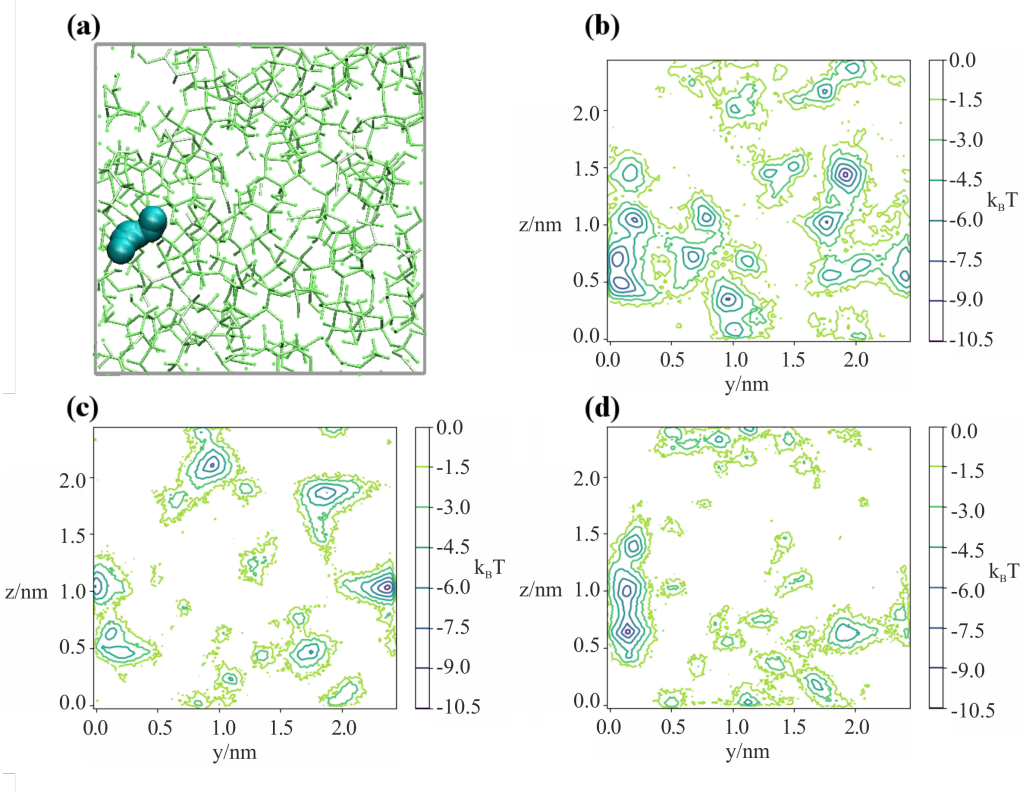

Figure 5.1.4: (a) Snapshots of the trajectory of a water molecule 'jumping' between interstices in an amorphous sucrose lattice, crossing the periodic box (in grey) in the process. An example potential energy surface that a water experiences in the *xz* plane in shown in panels (b) to (d).

probability distribution, P:

$$PMF(x,y,z) = -k_B T \ln P(x,y,z) \tag{5.1.7}$$

Where P is the normalised frequency of the water occupying any given cartesian position, and PMF is a matrix whose elements represent the associated free energy, excluding the entropy of the sucrose lattice. As such, we can infer the influence of sucrose dynamics from the change in width and depth of each of the local minimum between frames. Projections of the calculated matrix onto the *yz* plane of PMF from three trajectories are shown in Figure 5.1.4, panels b-d. The initial sucrose coordinates roughly correspond to before (b), during (c) and after (d) a cavity jump. The colour of the contours indicates the PMF value in units of $k_B T$ (left hand scales). There is a small but noticeable change in the local energy landscape around the water molecule

(the region around y = 0.1 nm, z = 0.5-1 nm) as the sucrose reorients. Nonetheless, defined cavities are observed, rather than a continuous channel. Other cavities appear and disappear within the probed window, approximately 8.7 k_BT below the free energy of the occupied sucrose volume,[5] and separated from one another by higher potential pores in the lattice. Panel (a) shows overlaid frames from the trajectory in this period as the water transitions from one cavity to another.

As cavity stability can only be assessed when the sucrose motion is dynamic (unconstrained), we return to the analysis of the 1 μs trajectories. Identifying the local minima in the *PMF* surface within constrained lattice is a very useful tool, as it gives an indication of the absolute stability of a water molecule at that site. However it does not provide any indication of the barrier heights between cavities.

Markov State Modelling

The cartesian positions of the waters in the nine trajectories have been analysed and a Bayesian Hidden Markov Model has been constructed by Robert Arbon. Briefly, consecutive 1 ns slices are analysed separately and the states accessible to the water molecule are determined, and clustered into discrete cavities. The MSM allows the relative population of a cavity to be found as a function of simulation time, as well as both the conditional probability of hopping in each available direction, and the rate constants associated to each hop. Extended periods of 'two-state' behaviour are found in several of the unfrozen 1μs trajectories, whereby the water repeatedly moves back and forth between adjacent cavities. The cavities do not collapse once they are vacated, even when the sucrose has not been frozen. We can therefore surmise that the water is not so constrained that is fails to sample its environment in the time available. It is also likely that 'return trips' may be a common feature of water transport in these matrices, if the free energy of adjacent pores is approximately equal.

The probabilities which were analysed previously to determine the potential of mean force

[5]This value was estimated by sorting the values of *PMF* along one dimension, finding local minima by inspection, and taking their mean. It is not intended to be statistically significant.

can only give an enthalpic, and not entropic, picture. The two results provide complementary information: the time constants and barrier heights are the more atmospherically relevant quantities, as they should directly relate to water transport as it is manifests in organic aerosol. The well depth relates to cavity stability, and the barrier height describes the energy required to deform the sucrose matrix and escape the current cavity. Taken together, the analysis of all nine trajectories reveals that the cavities do not have a uniform set of free energies, meaning that there will be a distribution of lifetimes spent in different cavities.

One way to connect the time constants associated with each hop and the free energy barrier that must be overcome is to assume that the jumps obey Transition State Theory. which is to say that the reciprocal of the mean time constant, $\langle\tau\rangle$, defines a frequency that a transition state between the cavities will be crossed:

$$\frac{1}{\langle\tau\rangle} = \frac{k_B T}{h} \exp(^{-\triangle G^{TS}}/_{RT}) \tag{5.1.8}$$

Where h is Planck's constant and $\triangle G^{TS}$ is the barrier height in kJ mol^{-1} between the initial cavity and the local maximum. Note that the equation contains both the Boltzman (k_B) and Gas (R) constants, meaning that it connects microscopic to macroscopic (molar) quantities. If it is rearranged to make $\triangle G^{TS}$ the subject, we obtain:

$$\triangle G^{TS} = -RT \cdot \log(\frac{h}{k_B T \langle\tau\rangle}). \tag{5.1.9}$$

A number of requirements must be satisfied by the system under consideration for transition state theory to be strictly applicable to it: Namely, that the 'reactants' (in this case the water molecule occupying its initial cavity before hopping) are in possession of thermal energies that satisfy the Maxwell-Boltzmann distribution, and that a molecule at the transition state has a 100% probability of falling into the product cavity. The velocity rescaling thermostat ensures that the first condition is satisfied, although the extent to which the second can be assumed is unclear.

The calculation was performed by myself on a histogram of $\langle\tau\rangle$ provided by Rob Arbon. The median value of $\triangle G^{TS}$ was found to be 11.6 kJ mol^{-1}, or 6.42 $k_B T$. The uncertainty, as defined by

half the difference between the 25th and 75th percentiles of the distribution, was determined to be 2.33 kJ mol^{-1} or 1.29 k_BT. The distribution across all trajectories corresponds to a hop frequency of between 1 and 50 per nanosecond per water molecule.

5.1.4 Relationship with Packing Efficiency

One interesting consequence of the transport mechanism reported here is that the magnitude of the Stokes-Einstein deviation should be coupled to the packing efficiency of the organic molecules under dry conditions. For instance, raffinose (or any large and highly oxidised molecule) may self-diffuse slower than sucrose (hence why the observed particle viscosity is higher), but if the average volume of free space around the raffinose molecules is larger, and also more highly connected, then net flux of water through the raffinose matrix should be higher at low humidities.

Unfortunately, fully integrating the mean-squared displacement of a single water molecule through a matrix of each of the saccharides whose viscosity has been investigated would be prohibitively computationally expensive and is beyond the scope of this work. Figure 5.1.5 presents calculated values of the free volume for a mono-, di- and trisaccharide, namely glucose, sucrose and raffinose. Snapshots of the output coordinates of the three matrices are also presented in panels *(a)*, *(c)*, and *(e)*, showing decreasing occupancy of the box by the organic's Van der Waals (VdW) surface. The right hand panels *(b)*, *(d)*, and *(f)* are the mean free volume over two 10 ns simulations in each case. The much shorter timescales (10^4 vs 10^6 ps) show that it is far more straightforward to converge to a steady state the total cavity volume within a given saccharide using an MD trajectory. The free volume is calculated using the GROMACS 'free-volume' program, which attempts to insert probe particles into the box. A successful insertions is defined as anywhere the probe is at least the VdW radius away from any sucrose atom present.

We have chosen to express this quantity as a fraction of the simulation volume, given that the box dimensions and molar volumes differ for each system. Three repeat trajectories of 10 ns length were conducted for glucose and raffinose, once again generated with randomly placed and oriented molecules, and containing a single water. To determine the sucrose packing effi-

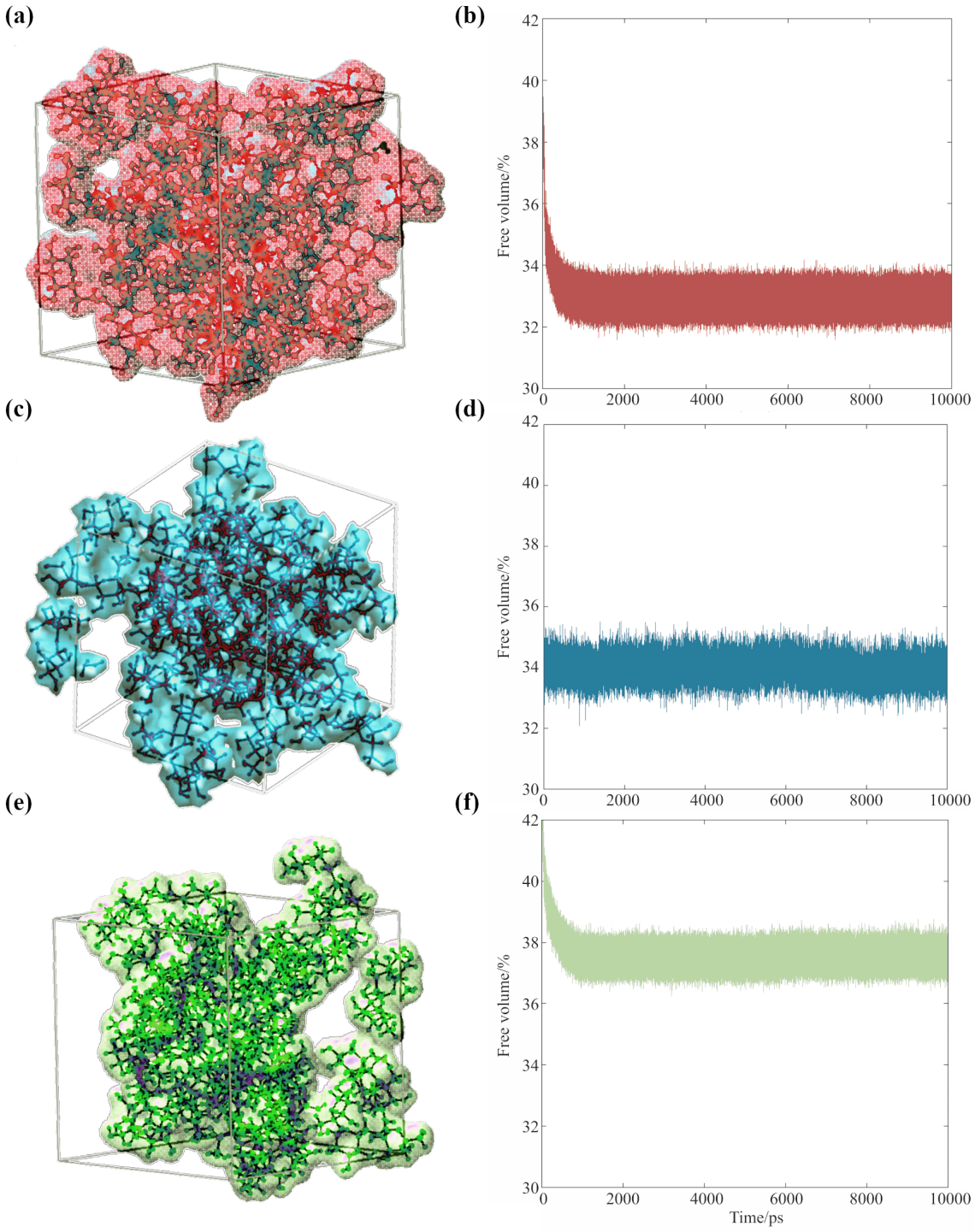

Figure 5.1.5: Occupied volumes of (a) glucose, (c) sucrose and (e) raffinose matrices, showing the outer surface formed by the Van der Waals radii of the saccharides within the final equilibrated frame of NpT trajectories. The free volume of each matrix throughout 10 ns trajectories are shown in the adjacent panels (b), (d) and (f) respectively.

ciency, truncated trajectories of length 10 ns were extracted from the microsecond trajectories and subject to the same analysis. Hence, the early picoseconds of panel *(d)* do not show a collapse during pressure coupling as first frames were extracted from 50 ns through two of the nine equilibration trajectories. By constrast, the data in panels *(b)* and *(f)* were recorded immediately after equilibration.

It is observed that the fraction of the matrix taken up by cavities increases with the molecular weight, or chain length, of the organic. This corroborates the interpretation of the viscosity and diffusion data described earlier, which showed increasing deviation from Stokes-Einstein physics across the same series, from mono-, to di-, to trisaccharide. It also correlates with the experimentally determined amorphous melt densities[285], if expressed in *moles* per cubic centimeter.[6]

Taken together, these results suggest that the 'hopping' mechanism of water transport will become more efficient as the size of the organic constituent increases. Thus, the frictional forces experienced by water molecules will be further from those assumed by Stoke's law, and equation (5.1.1) will under-predict the observed D_w to a greater extent for larger organics. Put another way, out of a set of particles *exhibiting the same viscosity*, those containing the largest organic molecules will also exhibit the fastest water transport. At a constant RH, water diffusion in raffinose will still be slower than in sucrose, but the ratio of the rates will be smaller than S-E predicts.

With reference to atmospheric organic aerosol, this effect may be significant in particles containing large number of 'humic like' molecules. Such constituents are frequently found in aerosol formed under low RH[77, 59], low temperature[286] or high precursor concentration[75] conditions.

[6]Glucose = 7.8 mmol cm^{-3}, sucrose = 4.3 mmol cm^{-3}, raffinose = 3.0 mmol cm^{-3}. The trend in mass per unit volume is the opposite, although this is consistent with diffusion in raffinose being lower at a given humidity than sucrose etc. What we are interested in is diffusion at a given *viscosity*, which is a different quantity that doesn't correlate exactly with composition.

5.2 The Mean Squared Displacement of Water at Varying Water Activities

Now that the mechanism of diffusion of a single water molecule has been observed and investigated, it is useful also to consider its occurrence in different aerosol matrices with higher water content. It may be, for instance, that slow drying processes allow water molecules to organise themselves into coherent channels to the surface. Were that to be the case, the concentration of water would no longer be uniform but would vary depending on local conditions.

5.2.1 Motivation

There is compelling evidence that nanostructure will affect the dynamical properties of macroscopic objects. In their review of the Maxwell-Stefan model of diffusion through a porous network, Krishna and Wesselingh[283] noted that diffusion is not a single process, but instead can usually be decomposed into several distinct mechanisms that contribute to the measured flux:

- Surface diffusion, where the majority of molecules are absorbed onto the wall of a pore. The cavity hopping mechanism can be considered a close approximation to surface diffusion, as the dynamic timescales of the encasing matrix must be taken into account in both cases.

- Knudsen diffusion, when the pore diameter is comparable to the mean free path of the diffusing molecule.

- Bulk diffusion, where molecules are assembled into sufficiently large clusters, or phases, that they experience self diffusion.

We would like some way to quantify the relative importance of these different mechanisms as a function of composition. It would also be interesting to determine whether each mechanism has unique diffusion coefficients associated to it. Were that to be the case then we could say that

changes in intraparticle diffusion rate are in fact due to changes in the *dominant mechanism* of diffusion, and the proportions of each of the others, rather than the molecular diffusivity in total.

There is also an emerging field of research in physics and materials science which concerns itself with the properties of small amounts of organic species confined within pores of size 1-10 nm, at or below their glass transition temperature. The reviews of Jackson and McKenna[287] and Alcoutlabi and McKenna[288] provide a thorough introduction to the field, its discoveries and current challenges.

For our purposes, the most interesting result is that changes in pore size are found to both increase and decrease the glass transition temperature depending on the substance confined. Theory does not adequately explain the observations as yet, although it is again proposed that the surface area to volume ratio of the pores is likely to be important[208, 129].

Aspects of these research questions apply directly to viscous organic aerosol: The heterogeneity in *water content* within a particle, where regions of almost pure water are formed and enclosed within organic matter, or vice versa, may induce the same effects as the zeolite matrices Krishna and Wesselingh[283] studied. Molecular rotor studies[140, 141, 142] suggest that regions of high and low viscosity do form, and remain stable for extended periods of time, in organic aerosol (Figure 5.2.1). These studies found that the size and frequency of the regions[7] increases as the humidity is lowered. Porosity of this type could have pronounced impacts on the ability of a droplet to equilibrate with changes in the ambient air, as well as to internally equilibrate its composition.[8]

It is possible to place a theoretical upper limit on the size of a viscous domain, as a droplet containing very large organic rich clusters (circa 1-10% of the droplet radius) should behave like a droplet containing solid inclusions. Various literature studies support that droplets containing nanoparticles (a good model system for inclusions) evaporate in manner that is distinct from

[7] A note on nomenclature: the regions will be variously referred to as regions, domains, clusters and aggregates. I have consciously not referred to them as phases as binary organic aerosol does not phase separate as it dries. It is also more complex than the structure consisting pure organic and pure water clusters.

[8] I am slightly uncomfortable describing this as 'porosity': usually it refers to networks of voids, or gas, within a solid material. Interestingly, there is some evidence atmospheric aerosol can form such structures if they are conditioned in a specific way during ice nucleation[289, 290]. However this is probably not a common occurrence.

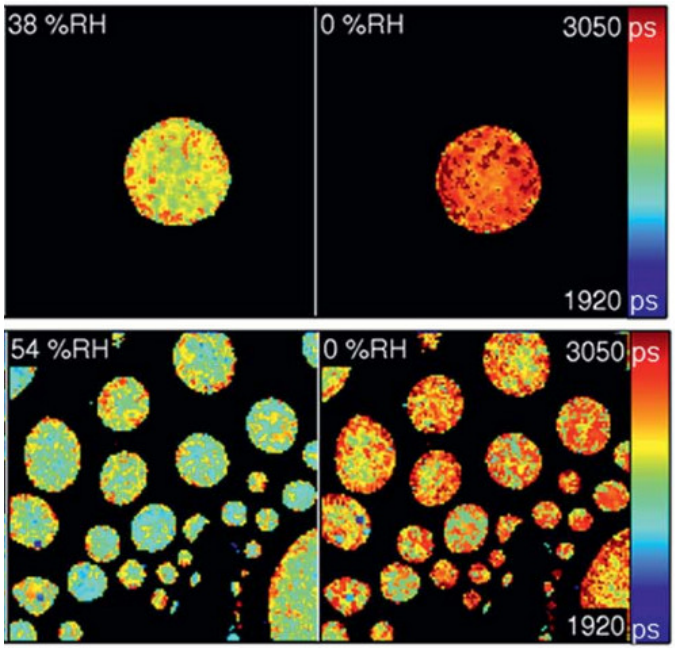

Figure 5.2.1: An example of dynamic heterogeneity in organic aerosol, in this case myrcene SOA, using flourescence lifetime as a proxy for relaxation time. Reproduced from Hosny et al.[142] under Creative Commons Attribution 3.0 Unported license.

viscous aerosol[291, 292, 230]: the evaporative flux of water changes in a stepwise manner as the surface becomes saturated with inclusions and water must travel between the solid nanoparticles to escape. By contrast, in viscous aerosol the evaporative flux changes in a smooth way as the droplet is dried, suggesting that the organic aggregates are not many orders of magnitude larger than the water rich regions. However, at present there is little investigation into which aggregate sizes are likely to be more stable, and so computational evidence is preferrable.

Variations in the relaxation behaviour across local regions is an example of *dynamical heterogeneity* (DH). It is characterised by mobility remaining low, when averaged over the all molecules in the system, but both diffusion and relaxation time varying substantially at the nanoscale. DH has been observed in chemical systems where the Stokes-Einsten relation (equation 5.1.1) fails to predict translational[273, 293] and rotational diffusion from the viscosity, as well as in systems that exhibit stretched exponential relaxation[294]. As we will see in detail in Chapters 6 and 7, water transport in viscous aerosol is observed to proceed in a stretched exponential manner, at a

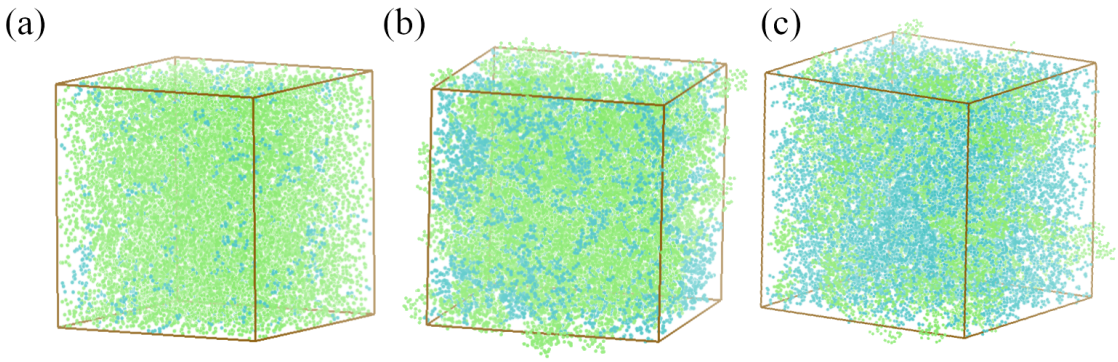

Figure 5.2.2: Differences in the nanostructure of sucrose (green) and water (blue) in equilibrated simulation boxes. Mole fractions of sucrose are (a) 95%, (b) 72% and (c) 47%.

rate that is faster than Stokes-Einstein predictions. It would therefore be entirely constistant with the observations if DH were found to manifest on the nanoscale.

While it is still unclear if this equation is valid across a range of chemical systems or enclosing matrices, the changes in dynamics it desribes are very similar to water transport through aerosol. It is therefore important to understand how pore size and connectivity changes as a function of humidity; i.e. at water activities above zero.

Here simulations have been conducted investigating sucrose matrices in larger simulation boxes (~5×5×5 nm), coexisting with water at a variety of volume fractions, such that the structure and dynamics of the water can be probed. Three such examples are shown in in Figure 5.2.2 which correspond to significant changes in the structure as the water content increases: (a) contains very few water molecules, most of which are isolated in cavities that are stochastically distributed. (b) shows a composition where the volume fractions of the water and organic are comparable, and (c) shows an almost bulk solution where sucrose is solvated near its saturation. It is believed that molecular dynamics studies are a useful computational tool here: given the number of atoms that must be simulated in order to capture multiple clusters of high and low water content, and the mechanisms of diffusion found in each, it would be impractical[9] to employ ab initio density functional theory based methods.

[9] with the high performance computing facilities currently available.

5.2.2 Procedure

The Packmol program was once again used to initially place the molecules in the simulation box, followed by multiple steps of equilibration as described in the chapter 4. The equilibrated simulation boxes were about a factor of 2 larger on each face (6×6×6 nm i.e. an 8-fold increase in volume). The plasticising effect of the water meant that less simulation time was required to converge the mean squared displacement to the diffusive regime than the single molecule simulations. Usually the length of the trajectories was 100 ns.

The *molecule* fraction was chosen to approximate the *mole* fractions sucrose aerosol will adopt at equidistant water activities from ~0.45 to 0.95. Here the Norrish equation[134]

$$a_w = x_w e^{-6.47(1-x_w)^2} \tag{5.2.1}$$

was used to relate the the activity and composition. It was chosen as it is known to accurately replicate experimental data between $a_w = 0.3$ and $a_w = 1.0$[295]. Additionally, it contains only one fitted parameter, and so is unlikely to suffer from overfitting. Many other parametrsations have been published in the literature for sucrose aerosol. As we will see in the next chapter, the choice can have a substantial effect on steepness of the descent that diffusion coefficients undergo as a function of RH.

The fitting of diffusion coefficients is itself much easier than in the simulations containing the single water molecule: No repeat trajectories need to be run as, in the simulation, the mean squared displacement value is sampled over the different molecules in the box rather than over different starting configurations of the same molecule.

5.2.3 Results and Discussion

Figure 5.2.3 presents the calculated mean squared displacement at each water mole fraction, averaged over every molecule in the simulation. Each of the systems had successfully equilibrated, as judged by the decay of the system potential enegry, before the MSD was calculated. The box

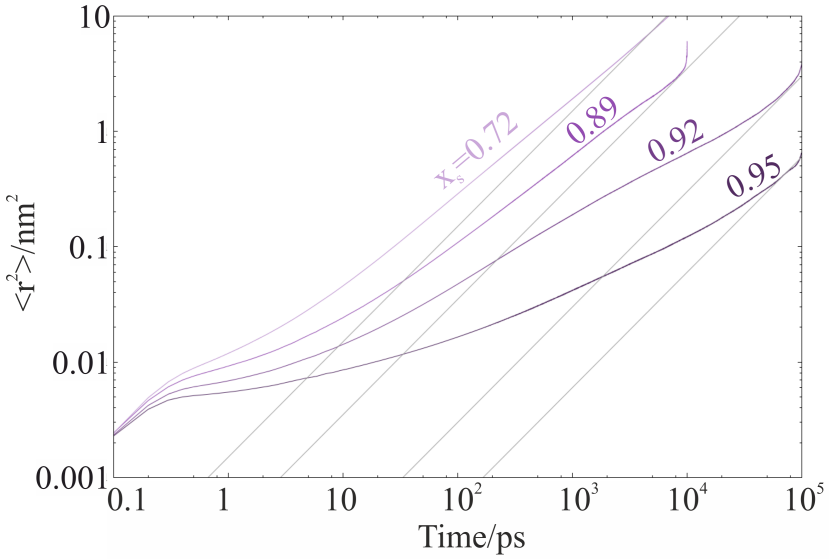

Figure 5.2.3: Composition dependent mean squared displacement for water in sucrose, as calculated by GROMACS. Ballistic transport manifests in the early timesteps (0.1:1 ps) of all four simulations, which then collapses to diffusive (grey asymptotes) as the water molecules overcome their original initial conditions and decorrelate. See main text and section 4.2.3 for additional information.

volume also showed no signs of oscillation, suggesting a consistent NpT ensemble was being experienced.

Mean Squared Displacement

The trend is clear in that dehydration slows the dynamics and reduces the final displacement (at either 10 or 100 ns). Grey lines representing diffusive $< r^2 > \sim 6D_w t^1$ dependences for varying values of D_{wat} are also presented in the figure, into which the atomistic dynamics should collapse as the system decorrelates from its initial state (section 4.2.3). On a log-log scale, any reduction in the value D_{wat} has the effect of translating each line vertically downwards. Once the onset of the diffusive regime has been identified by inspection, the time interval in which the displacement aligns with the gray lines can be used to calculate D_{wat}.

Plotting the fit values against the mole fraction of water in each simulation, the diffusion coefficients show an approximately loglinear decline with the level of dehydration (Figure 5.2.4).

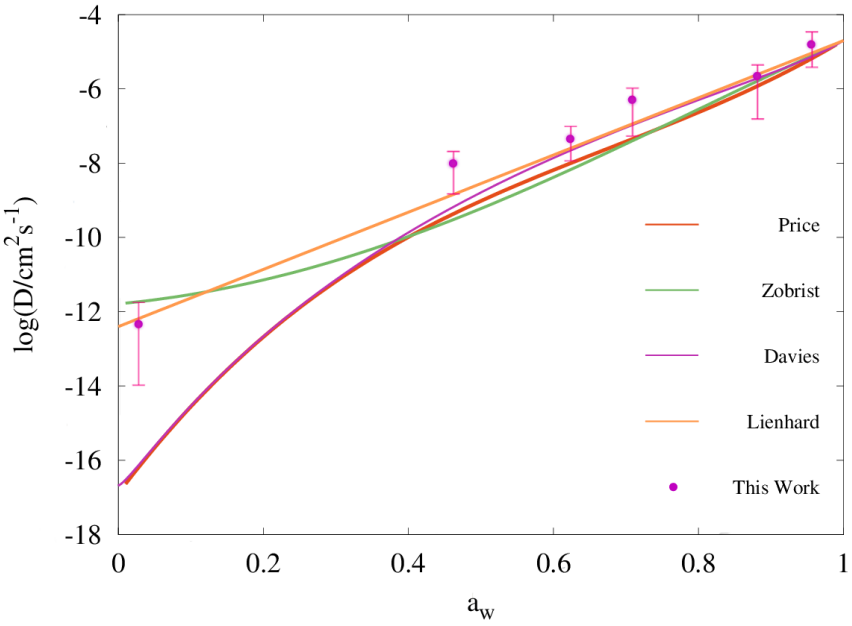

Figure 5.2.4: A comparison of the Diffusion coefficients fit from the mean squared displacement of water in the MD trajectories in comparison to a variety of literature parametrisations of aerosol data, including Price[181], Zobrist[132], Davies[182] and Lienhard[180].

A selection of recent literature values extracted from single particle measurements are also presented for comparison (see figure caption for references). It was found that the simulations agreed well with all literature in the region above a_w= 0.4. Below that value, there is a deviation between the different literature values. Within the 95 weight percent organic simulation box (a_w = 0.465), it was observed that the majority of the water molecules were isolated from each other within cavities, in contrast to the other compositions. That this was the randomised amorphous structure adopted suggests that the cavity hopping mechanism may continue to have a substantial effect on particle phase water transport well above zero water activity, assuming that these microstructures are representative of a viscous SOA droplet at 40% RH.

The method by which the water activity was related to the mole fraction of water was found to be unique to each publication which contributed the lines in Figure 5.2.4, which will be discussed in greater detail in Chapter 6. The deviation between the predicted diffusion rates below a_w= 0.4

in each publication will also be interrogated. For now we can be confident that the intermolecular forces being experienced by the water molecules are physically realistic.

Microstructure

In order to gain an understanding of the changing interactions of water with sucrose as the hydration level increases, a number of analysis techniques have been employed. Firstly, individual water molecules have been selected randomly and their motion inspected. We shall consider the most water rich simulation box. By plotting and overlaying the atoms which the water approaches at a distance of $1.5\mathring{A}$ or less in each frame, the mean environment experienced can be represented. Usually in molecular simulation, solvent molecules are considered to be interchangeable except when they are in the first solvation shell of a solute molecule of interest. It is at this point that changes in orientation and bonding begin to be observed. In the structures investigated here, the accessible surface area of organics is enormous, so we should expect a significant influence of such effects on the motion, as well as the bonding, of the water. Movie 2 in the supplementary materials shows an example of the effective self-diffusion that one of the water molecules experiences.

If motion such as this is commonplace at higher water activities, it is of interest to understand the implications for water transport in general: When water collides with the sucrose it is unable to continue its translational motion and is almost always repelled back into the pore (or cluster) that it began in. The apparent immobility of the sucrose is a manifestation of the slow decorrelation (presented in Appendix A), which results in sucrose possessing a self-diffusion coefficient around two orders of magnitude smaller than water[185]. Occasionally, the sucrose reorients, or is slowly moved aside by the accumulated pressure of many collisions, and the water is able to access a new channel or pore, in a similar way to the single molecule traversing the interstices.

Secondly, a more rigorous method of quantifying local correlations is to calculate a radial distribution function.[10] It is a time independent correlation function expressing the probability

[10]Sometimes referred to as a pair distribution function.

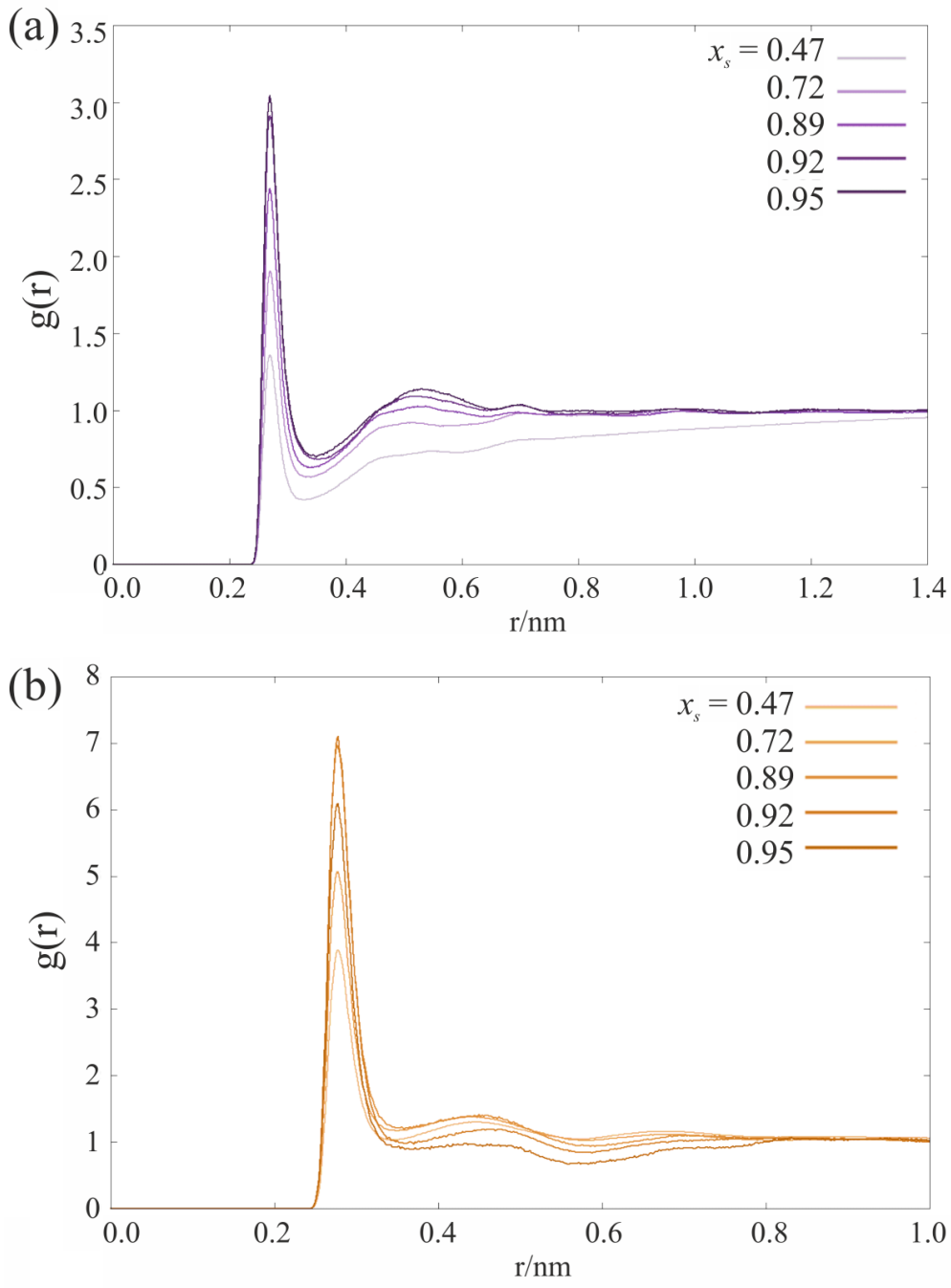

Figure 5.2.5: Oxygen - Oxygen pair correlation functions for water in sucrose. (a) Water oxygen with sucrose hydroxyl (mean over all oxygens); (b) Self correlation of water oxygen.

of finding two atoms at a given distance from one another, averaged over all such atoms present. The function is unitless and so is referred to as the probability relative to a uniformly distributed liquid. Evaluated numerically, the RDF is equal to:

$$g(r) = \frac{V}{N^2} \left\langle \sum_i \sum_{i \neq j} \delta(r - r_{ij}) \right\rangle \tag{5.2.2}$$

Where $\delta()$ is the Dirac delta function. In liquids a very sharp peak is observed close to the Van der Waals radius of the atom under consideration, followed by progressively less intense peaks that decay to unity as the distance increases. Each peak can be thought of as a representation of a consecutive solvation shell. Two such distributions are plotted in Figure 5.2.6. They were calculated over a 500 ps interval within each data collection trajectory, where the densites had stabilised as a result of the pressure coupling. Panel (a) shows the *g(r)* of water oxygen with all of the hydroxyl oxygens present in sucrose, and panel (b) shows the self-correlation of water oxygen. As the water activity is decreased, the long range order of water is disrupted, whilst the correlation with organic hydroxyls increases. Simultaneously with the area under the first peak increasing, a second peak grows in at around $r_{O\text{-}O}$ = 0.55$\mathring{A}$. The probabilities are qualitatively consistent with the results of the inspected trajectories, suggesting that nanoconfinement of individual water molecules is prevalent at humidities above zero. The extent to which it increases as the volume fraction of organics increases will influence which mechanisms of diffusion will dominate.

5.3 Summary and Outlook

As an organic aerosol droplet usually does not crystallise or phase separate as it is dried, then the microstructure formed is characterised by the amorphous packing of large organic molecules. Here we have investigated the mechanism of water diffusion in precisely such an amorphous envirnoment, formed by the viscous saccharide sucrose. When a single water molecule is isolated from any others, as in a particle within a completely dry atmosphere, transport is observed to proceed by discrete hops between interstices. These ‘cavities’ are surrounded by relatively high

(~6 kT) free energy barriers, and reorganise on a timescale limited by the diffusion rate of the organics (i.e. substantially slower than the interstitial water motion).

It is proposed that there is a direct connection between this hopping mechanism and recent atmospheric observations showing that water transport occurs significantly faster in organic aerosol than is predicted by the Stokes-Einstein equation. We propose that the assumptions of Stokes' Law no longer hold when a significant fraction of the water content of a droplet diffuses in this manner.

The trend in diffusion coefficients as a function of dehydration was calculated, and found to be consistent with the results of several literature studies. The mean squared displacements of the single molecule simulations were also calculated, accounting for the lack of displacement during residency in a cavity. The mean, averaged over nine trajectories, was found to agree with that the experiment to within an order of magnitude, albeit with a high standard deviation because the statistics are inevitably poor.

Dynamic trajectories within more hydrated matrices have found that confinement within cavities is a relatively common fate for water molecules doping sucrose, even at water activites as high as 0.4. In combination with calculated pair distribution functions, the findings of these two studies show that the arrest of water diffusion close to the glass transition is correlated with increasing association between water and hydrophilic groups on the encasing organic species, and a decreasing probability of water-water bonding.

It was hypothesised that larger molecules will pack less efficiently, facilitating more frequent hops through a porous network of a given viscosity. The equilibrium structures of two other saccharide matrices have been determined at 300K and 1 atm and compared with sucrose, confirming this hypothesis. We have therefore concluded that the decoupling of diffusion from viscosity in organic aerosol is defined by the available free-volume (vacuum) between the organic molecules through which water must diffuse. With reference to atmospheric aerosol, we believe that this effect may be significant in oxidised particles, or particles containing oligomeric and 'humic-like' molecules.

Several phenomena that seem to have been known for some time in the glass physics community have been independently rediscovered as part of this work. Of most immediate interest to our understanding of the behaviour of droplets are dynamic heterogeneity, and activated diffusion in a so-called 'rough' potential energy surface. Additionally, while such molecules have not been investigated here, it may also be the case that polymer science can offer insights into the dynamics of SOA, as oligomeric species are known to be present in the particle phase. It is certainly the case that atmospheric aerosol scientists and members of these fields have a lot to learn from one another, and should find scope to expand collaborations in the future, specifically in the area of SOA and its climate impacts. If that were to happen then existing knowledge would be shared more effectively and fewer cases of 'reinventing the wheel', would likely occur.

Chapter 6

Characterising Diffusive Limitations to Water Transport Through Viscous Aerosol

"The number ten, raised almost literally to the power of infinity!" - Dr. Morbius, *Forbidden Planet*

6.1 Motivation

Dehydration can cause drastic changes in the phase state of particulate matter, especially organic aerosol. Due to the viscoelastic properties of the molecules involved, it is rare for organic droplets to crystallise in the way inorganic droplets are observed to: i.e. through a first order phase transition once a critical concentration of the solute is reached. Instead, the low water content in the surrounding atmosphere drives an increase in surface viscosity. Vitrification slows molecular motion within the droplet and the centre ceases to be in equilibrium with the interface. This may

in turn lower the probability of the organics to crystallise, as the reorientation of molecules will take a prohibitively long time.

Recent studies have investigated the influence of ultraviscous and glassy aerosol on concentrations of highly reactive species in the atmosphere[296, 206], and on cloud/ice nucleation[112]. It is expected that both of these processes would also be limited by, or at least coupled to, the rate of intraparticle water transport. As it stands in the literature, studies have shown that water diffusion in SOA progresses faster than would be expected from the S-E relationship, given the high viscosity of the aerosol[176]. Numerous other studies have shown that the diffusional transport of large organic molecules is hindered and follows much more closely to the expected trend from the S-E equation[222, 179]. The range of atmospheric conditions over which these phenomena may lead to a slowing of particle phase mixing have begun to be investigated[297, 298].As altitude increases, temperature and pressure fall, and it is unclear whether there is a general trend in humidity. Indeed, there may be a connection between the porosity of a particle and the ability of water to diffuse through it faster than the Stokes-Einstein equation would predict[290]. From a more fundamental perspective there is considerable interest in the relationship between diffusion on the molecular scale and viscosity on the mesoscale of particles[137].

It is clear from the simulations in the previous chapter that a highly concentrated lattice of organic molecules significantly impedes water transport, even to the point of altering the diffusion mechanism itself. What is required now is an understanding of the connection between the water flux crossing a droplet interface and the dynamic behaviour of the droplet. In other words, is it possible to deduce what's occuring within a particle by observing its growth and shrinkage? The purpose of this Chapter is to separate and quantify the competing kinetic and themodynamic effects on evaporative mass transport of water. Here, the Fickian model Fi-PaD is applied to this problem: firstly, to predict the timescale over which radius changes occur, in response to step changes of humidity; and secondly, to provide information about any concentration gradients that may form near the surface of the particles. Both drying and humidifying steps are analysed and interpretted in this manner. As was the case with cavity diffusion mechanism described in

Chapter 5, the physics revealed by the experiments conducted here has been known for some time within the glass physics community[299], but has yet to considered within the context of glassy or semisolid aerosol. Special attention is paid to the fact that the collapse of particle radii towards a smaller asymtote follows a stretched exponential relationship with time. This is interpretted with reference to heterogeneities within the internal structure of the particles.

Additionally, aerosol systems are investigated that contain multiple solutes. It was discovered that until recently, single particle studies tended to either focus on the diffusional mixing of water and a single non-volatile solute[112, 132], or on highly complex particles produced in smog chamber studies[300, 301, 302, 167]. Less attention has been paid to the interplay with other solutes. In both cases, evaporation timescales increase as droplets are dehydrated, using this to infer diffusivity.

If one of these solutes is volatile or semivolatile, our analysis must account for the fact that this species will continuously evaporate in addition to water. This process is slightly, though not significantly, accelerated by the unsaturated gas flow passed over the droplets within the optical tweezers aparatus. Therefore, the differing contributions of these processes to the observed size behaviour must first be decoupled, such that they can be interpreted separately. An in-depth study of the process of SVOC evaporation from the captured particles is outside the scope of this chapter and will be discussed subsequently in this thesis. What is of interest for the current context is the influence of the presence of SVOCs on the water transport characteristics. What we will see is that they exert a plasticising effect on the organic mass within the particles, both lowering the viscosity and raising the diffusion coefficients relative to systems containing two involatile organic solutes.

This chapter presents methods to determine the water diffusivity from the evolving radius of levitated aerosol particles containing either one or two solutes, with special focus on the latter. It is based on the publication *'Characterising the evaporation kinetics of water and semi-volatile organic compounds from viscous multicomponent organic aerosol particles'* published in *Phys. Chem. Chem. Phys.[303]* The capture, dehydration and radius determination of Sucrose and

Glucose droplets presented in that work was conducted by myself, Young Chul-Song and Chen Cai, with the majority done by Cai. However, the results presented in Figures 6.3.4-5 contain my contribution only. Viscosity measurements were performed by Chul-Song. All experiments relating to droplets containing malonic acid were performed by myself. The coding of the stretched exponential fitting, and the software development which allowed the Fickan model extract diffusion coefficients was performed by myself, however the model itself was initially coded by O'Meara et al., as introduced in Chapter 2.[198]

6.2 Experimental Procedure

Production and Trapping

Saccharide solutions have been prepared and transferred into a medical nebuliser prior to any experiment. The method of optical trapping proceeded as described in Section 3.1. The only caveat that should be added to the procedure description is that some consideration must be made for the viscosity of the bulk solution, as this can interfere with the normal operation of the nebuliser. If the starting solution was too concentrated it can simply cease to aerosolise. Conversely, if the solution is too dilute then the dry mass of the particle will be too low to accurately trap or size. It was found that 15-17.5% by weight Sucrose was an acceptable compromise that minimised both issues.

Since a bulk phase solution cannot access the same range of water activity that an aerosol particle can, there is often a significant amount of water loss that occurs upon aerosolisation. Once a levitated droplet loses sufficient water that it equilibrates with the cell conditions and the radius is (mostly) stable, a series of step changes of RH can be conducted. A flux of water into or out of the particle is then induced. The kinetic responses to changes in RH are examined either by considering the change in particle radius or the change in wavelength of a selected WGM as described earlier in the thesis of Rickards[268]. The time intervals between RH steps are programmed in advance and were generally chosen to increase as the particles became more

kinetically arrested (i.e. longer periods of RH stability at lower RH).

Employing Fickian modelling, we extract the compositional dependence of the diffusion constant of water and compare the results to recently published parametrisations in binary aerosol particles. The treatment of ideality and activity in each case is discussed, with reference to use in multicomponent core shell models.

6.3 Multiexponential Relaxation of Saccharaide Particle Radii

6.3.1 Radius Retrieval and Analysis

Throughout each measurement, the droplet size and refractive index were determined from the whispering gallery mode 'fingerprint' appearing on top of the hydroxyl and aliphatic C-H bands in the recorded Raman spectra.[231, 304, 216] The droplet size should be roughly stable prior to a step in RH. The Mie theory differential equations were solved online via the proprietary LARA software at intervals of either 1 or 2 s. Subsequent offline analysis was occasionally required, if the signal to noise ratio of the whispering gallery modes within the spontaneous peaks was too low to fit radii reproduceably. Some typical spectra are reproduced in Figure 6.3.1, showing the range of possible WGM intensities that can be observed, and still fit adequately. Re-fitting was usually achieved using a modified version of the LARA software, which can combine adjacent spectra to improve the noise and reduce the error in extracted droplet properties.

The user must set the ranges of possible radii, refractive indices, mode orders and dispersion within which the algorithm may search. If the returned fit errors are too large to trust the resultant radii,[1] a decision must be made to narrow or move the range. Additionally, if multiple solutions are found by the algorithm, all but one must be discounted. Such a procedure is open to subjective interpretation, and relies on a certain level of intuition on the part of the user. Nonetheless, there are several factors that are worth considering, which I have attempted to describe below:

[1] Any point where the mean deviation between the predicted and observed WGM positions was larger than 0.01 nm^2 was considered untrustworthy.

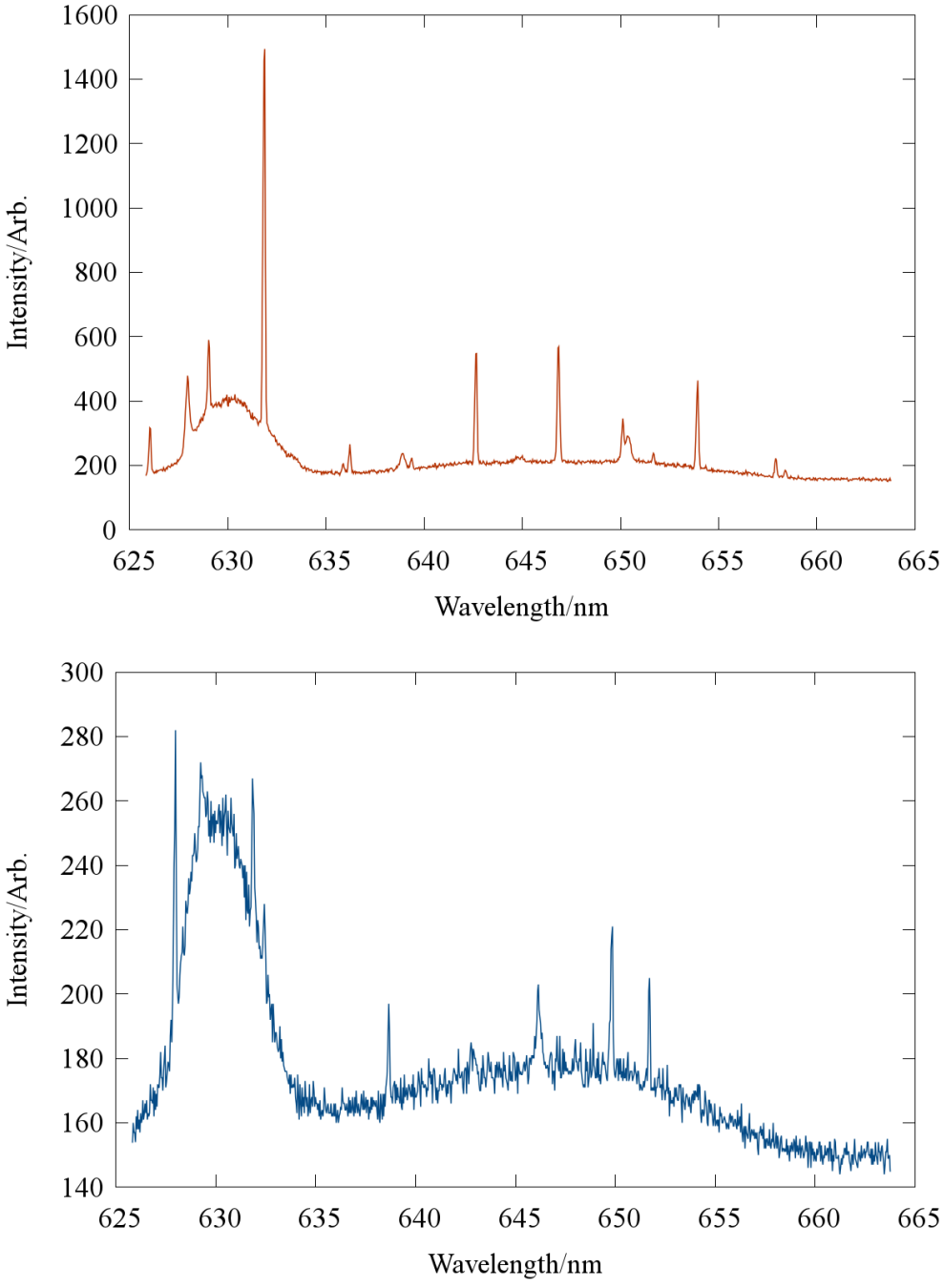

Figure 6.3.1: Examples of (a) high and (b) low signal to noise ratio (SNR) spectra recorded for the same aerosol droplet. The software determines a baseline through the C-H (625-635 nm) and O-H (637-660 nm) bands and places a threshold intensity that a WGM must achieve above this to be detected.

- What are the mean values of fit error returned for the different solutions relative to each other?

- Has the refractive index of this solute mixture in the aerosol been published as a function of water activity? If so, what would we expect the refractive index to be? The fit window should be centered around that value.

- Is the solution consistent with basic first approximations that can be made to Mie theory ie. is the radius what one would expect given the mode spacing?

- Are the relative changes in radius and WGM wavelengths $\Delta\lambda$ approximately the same, in that they satisfy this relationship[270]:

$$r(t) = \frac{(\lambda(0) + \Delta\lambda(t)) \cdot r(0)}{\lambda(0)}. \tag{6.3.1}$$

It is for this reason that in some experiments Mie fitting was foregone totally and wavelength was used to infer changes in radius.

Once a series of extracted radii with low enough error as to be trusted has been arrived at, it is possible to fit the radius data to approximate functions, and to interpret the fit variables accordingly. Secondly, from the dataset, a smaller number of experiments is selected, containing radius curves which are deemed most likely to provide statistically significant D parametrisations from the Fi-PaD code. The criterion for this selection is to find experimental data where the change in radius is appreciably slower than the timescale of the RH change in the local gas flow of the trapping cell. Experiments which induce water loss close to the gas phase change are difficult to fit because the model assumes an instantaneous change in surface activity of the particle, which would no longer be the case.

Figure 6.3.2 illustrates the separations in timescales between humidity and radius responses when high viscosity is exhibited, by inlaying the radius changes within the evolving RH data of a set of three transitions. In this particular example the gas flow is twice dried fully, and in

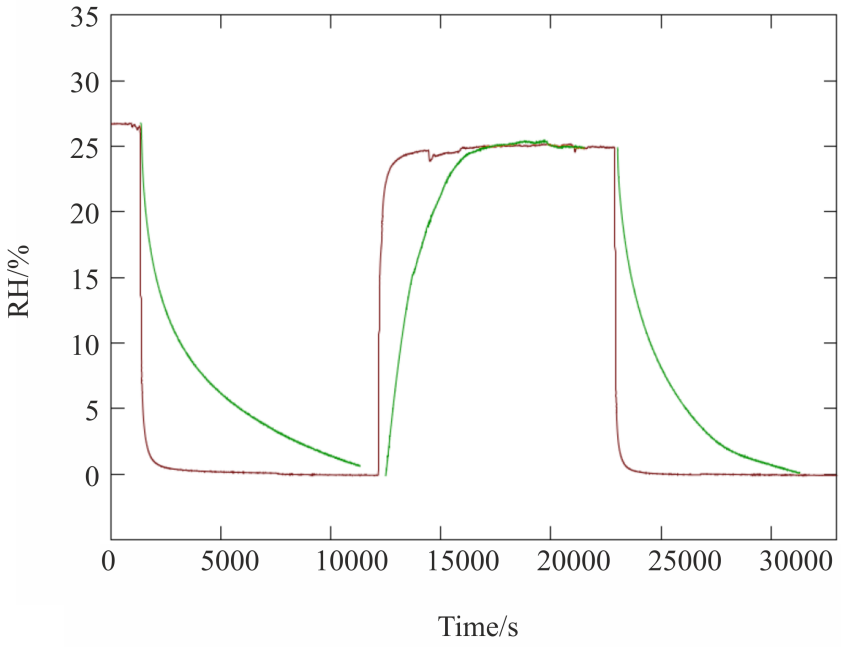

Figure 6.3.2: A prototypical RH profile showing sequential drying and humidifying events in the lifetime of a trapped droplet (red). Inset are the concurrent radius dynamics (green), in this case inferred from single WGM traces, which have been appropriately rescaled such that the beginning and end points are coincident with one another.

between humidified to approximately 27% RH. The organic component of the droplet contains sucrose and glucose in a 1:1 mass ratio, meaning that each step should cross the glass transition humidity. As can be seen from the red line, the RH within the trapping cell takes of the order of hundreds of seconds to equilibrate to the new value. Conversely, the tweezed droplet never fully equilibrates, although the 'folding' of the radius curves takes at least 1 hr (3600 s) during each step. Therefore, relatively speaking, the water loss and uptake in the particle phase is at least a factor of ten slower than changes in the gas environment. Coincidentally, Maclean et al.[147] defined a timescale of 1 hr as the threshold for 'slow' particle mixing within their atmospheric modelling, as it is a commonly used timestep in global climate models.

In any case, a more robust way to quantify these timescales is needed. It is known that the radial responses are not monoexponential in nature, and as a result fit functions of the form

$$\Phi(t) = S \cdot \exp(-t/\tau) \tag{6.3.2}$$

do not accurately capture the decay throughout the experiment.

Here, the time-dependent wavelength shifts of individual WGMs extracted from the Raman spectra are used to infer the relaxation timescale in particle size following a step change in RH. Such data can be represented as a response function $F(\lambda(t))$, where $\lambda(t)$ is the time dependent wavelength in nanometers. The response function is then fit to a modified stretched exponential function similar in form to the Kohlrausch-Williams-Watts equation:

$$\Phi(t) = s \cdot \exp(-t/\tau)^{\beta} + a \tag{6.3.3}$$

When compared with our previous fitting procedure, two new parameters have been introduced, s and a. a accounts for the deviation between the final recorded data point and the true end point of the transition. It follows that the proportion of the full transition to thermodynamic equilibrium captured in the experiment is equal to

$$\frac{1}{(1+|a|)} \tag{6.3.4}$$

The pre-exponential factor, s, then scales the data such that the fit and response functions both begin at unity. Here the e-folding timescale, τ, represents the kinetic limitation to the evaporation of water within the droplet. For binary systems studied in previous publications, the value of τ increases as the initial and final RH are lowered.

6.3.2 Origins of Stretched Exponential Relaxation

Previous studies by Rickards et al. have shown that fixed values of β between 0.4 and 0.6 represent the relaxation of binary sucrose aerosol close to its glass transition[268]. A multi-exponential description of ternary systems is also believed to be appropriate (β<1) in this case. The main difference between that publication and the studies conducted here are that we have unconstrained the value of β during the fitting process (Figure 6.3.3). The chemical significance of

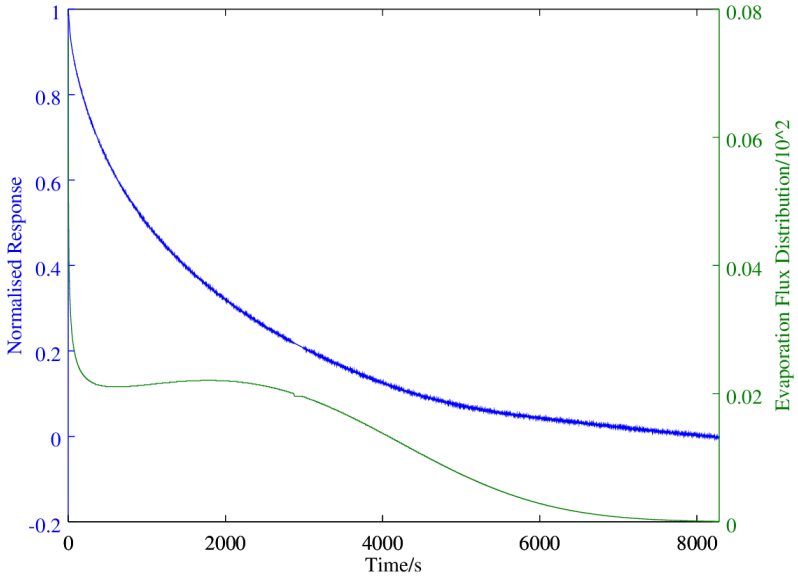

Figure 6.3.3: Example distribution $\rho(\tau)$ of monoexponential time constants (green) that reproduce the stretched exponential decay of particle radius (blue) across the same timescale.

this parameter is somewhat unclear: in the field of glass physics, stretched exponential relaxation of macroscopic variables is commonplace, and indeed may even be an intrinsic consequence of the system being in a glassy state. There is some consensus[305, 306, 307] that β is representative of the dynamic heterogeneity of the system, i.e. that there is an underlying distribution of mono-exponential events whose width becomes larger as β approaches zero. This is often expressed [308, 309] in the form

$$\exp(-\frac{t}{\tau})^{\beta} = \int_0^{\infty} \rho(\tau)\exp(-\frac{t}{\tau})d\tau \tag{6.3.5}$$

Where $\rho(\tau)$ represents the distribution of time constants. An example of the distribution is shown in Figure 6.3.3, calculated using the treatment of Trzmiel et al.[310] and overlaid with the concomitant radius relaxation for a 52-18% RH change. This description is appealing when applied in the context of organic aerosol as it correlates with the findings of recent fluorescence imaging studies,[141, 140] and may in fact be an emergent property of heterogeneities in concentration. Specifically, if there is a strong dependence of composition on diffusivity then much

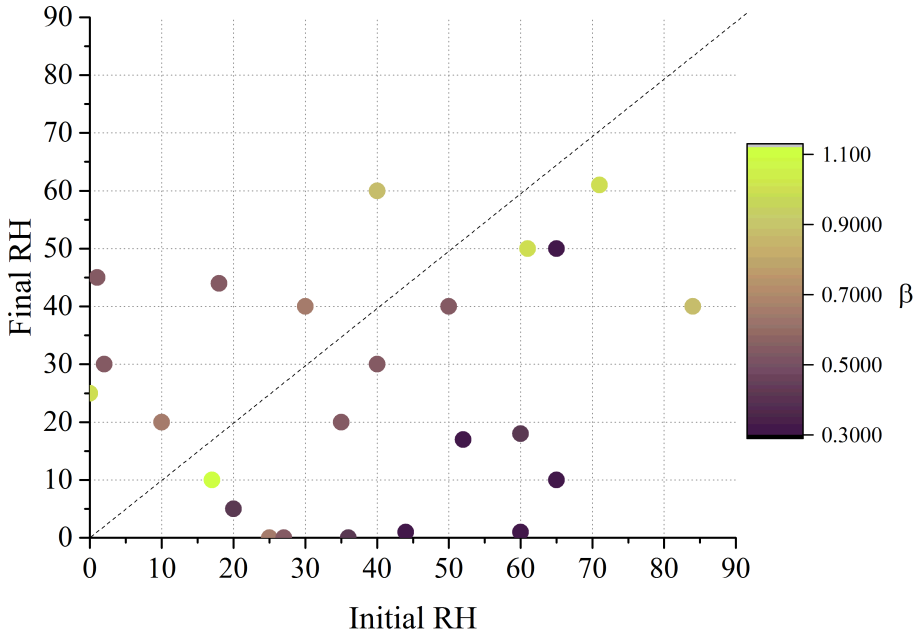

Figure 6.3.4: The stretched exponential parameter, β, extracted from equation 6.3.3 from best fits to ternary sucrose/glucose particles (1:1 mass ratio).

slower water dynamics will occur within the regions of low water content. Expressed mathematically, the tail of $\rho(\tau)$ must extend to longer timescales to account for the increased proportion of 'trapped' water molecules, leading to β values closer to zero.

6.3.3 Quantifying the Folding Time and Stretch Factor of Water Evaporation

Twenty five RH transitions have been conducted in the atmosphere surrounding ternary component aerosol particles consisting of water, sucrose and glucose. It should be noted that water is the only volatile component in these measurements; sucrose and glucose can be considered involatile. By capturing the non-exponential nature of relaxation in size (i.e. water partitioned to particle) following the RH step[311] using equation (6.3.3), the complex multi-exponential time-dependence in droplet radius has been converted into a simple estimate of the timescale of internal water transport.[268] Time-constant values for all changes in RHs may be found in

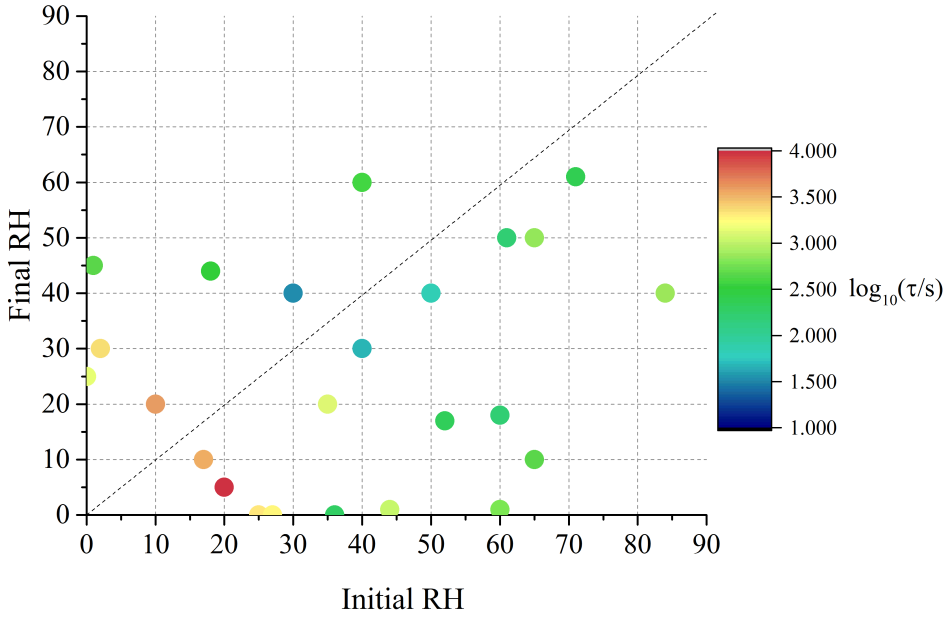

Figure 6.3.5: Exponential folding time, τ, of particle radius responses of ternary sucrose/glucose particles (1:1 mass ratio), mapped over initial and final values.

Figure 6.3.5.

In evaporation experiments, the time constant broadly increases as the final state of dehydration of the particle increases (i.e. as the RH change moves towards the bottom left of the figure), unless the particle begins in a very low viscosity state at high RH. In addition, the slow release of water over long time is consistent with a value of β <1. It may be that this is due to the larger variance in molecular evaporation timescales that together make up the observed radius response. However, we must be careful: stretched exponential behaviour is observed in every transition, including those that take place for liquid aerosol above the moisture driven glass transition RH of the organic components. This suggests that we are using the stretched exponential to represent a fundamentally different physical process to that usually just ascribed to glasses.

6.3.4 Quantifying the Folding Time and Stretch Factor of Water Condensation

The condensation experiments are somewhat more complex to characterise, involving the condensation of a pure water layer on the dehydrated particle surface[173]. Induction behaviour is observed in the first several hundred seconds of condensation for many of the measurements. By this it is meant that a thin water layer is likely to have formed on, but not yet been absorbed by, the dehydrated particle. This process seems to occur on a longer timescale than condensation followed by absorbtion. Therefore the combination of the two leads to the initial decay being elongated, rather than the final. The stronger the effect, the larger the increase in β above 1[268]. Conversely, for purely gas-diffusion limited condensation, the size response should be independent of the internal composition[312]. The independence means that both the probability of accommodating each water molecule to the surface, and the net flux from the gas phase is uniform, which corresponds to monoexponential decay.[2] Therefore, at high humidities, condensation events should be well represented by a value of β close to unity.

6.4 Diffusion Kinetics in Viscous Saccharide Aerosol

6.4.1 Parametrising Symmetric Diffusion

A comparison of the reported water activity dependencies of the diffusion constant of water inferred from isotope exchange and RH step experiments suggests that they are incompatible with qualitatively different shapes.[182] Recently, it has been common to adopt the Vignes parametrisation, introduced in chapter 2, to express the diffusion constant of water $D_w(x_w)$ in the mixture. Given the limiting diffusion constants of water in pure water, $D_{w,w}$, and at infinite dilution in pure solute, $D_{w,org}$, the parametrisation as a function of mole fraction, x_w, is[112, 181, 206, 182]:

$$D_w(x_w, \alpha) = D_{w,w}^{x_w \cdot \alpha} D_{w,org}^{(1-x_w \cdot \alpha)} \tag{6.4.1}$$

[2]Here 'decay' refers simply to the shape of the change in radius, rather than implying a *decrease* in radius. See equation 6.4.5 below for a method of converting condensation data to achieve like-with-like comparisons.

Each of these studies involves fitting equation (6.4.1) to datasets of D values inferred from two different techniques. One involves measurements at steady gas-phase RHs (i.e. constant water activities) in isotope exchange measurements[181, 182], and the second from least squares regression fits to D values inferred for a single particle during the transition in particle size and heterogeneity in water activity following a step change in gas phase RH[112]. Here, we explicitly include the Vignes dependence within a Fickian diffusion model to reproduce experimental data in which the water activity is changing within a particle following a step change in gas phase RH.

When defining the dependence of the diffusion constant on composition, as in equation (6.4.1), some assumptions must be made regarding the dimensionless constant α. As alluded to in section 2.4, it appears[180, 181] that the natural logarithm of α is coupled to, or in some sense represents, the activity coefficients of the diffusing components. Here, its primary mathematical purpose is to modify the curvature of equation 6.4.1. We have chosen to define $\ln\alpha$ using a cubic compositional dependence upon mole fraction,

$$\ln\alpha = C(1-x_w)^3 \tag{6.4.2}$$

The above parametrisation was recently introduced by Davies and Wilson[182] as a modification of the temperature dependent Margules type[313] binomial expansion of activity:

$$\ln\alpha = (1-x_w)^2 \cdot (C(T) + 3D(T) - 4D(T) \cdot (1-x_w)) \tag{6.4.3}$$

C and D are fit coefficients for the different terms in the expansion. Although equation (6.4.2) is a formulation that was intended for use in treating binary solutions[314], and its initial use in the parametrisation of aqueous sucrose activity[313], it has shown some applicability for representing water diffusion in organic aerosol by accurately fitting water diffusion in citric acid[180] and highly complex secondary organic material[181].

Compared to the binomial expansion, the cubic parametrisation of α produces an almost identical shape for $D_w(x_w)$, but with a much less pronounced plateau at the bulk water value

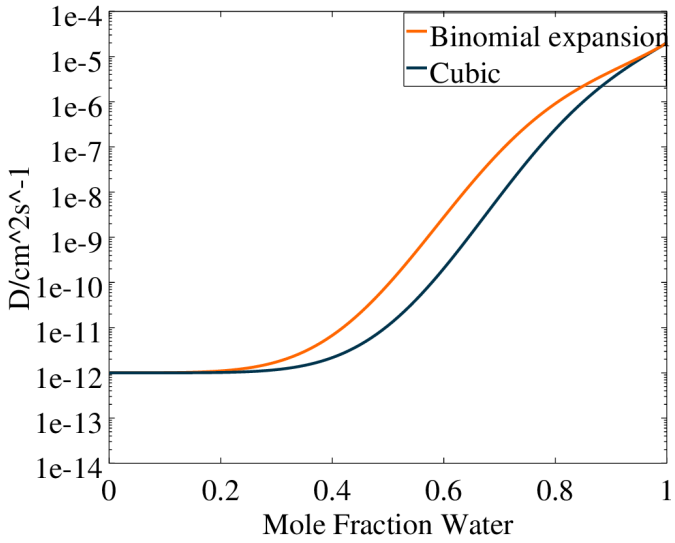

Figure 6.4.1: Comparison of the curvature of equation 6.4.1 using different functions of $\alpha(x_w)$.

of D_w at high water activity. Many techniques, including aerosol optical tweezers experiments, are insensitive to transitions within this region of activity, as the timescale for water transport is comparable to the timescale for the instrumentally limited change of RH. As such, it cannot be said with any confidence which of these parametrisations, (6.4.2) or (6.4.3), is a more realistic approximation to the binary diffusion coefficients in such particles. Instead, we are seeking the most accurate method to represent data recorded for highly dehydrated droplets that experience large kinetic limitations, and access compositions governed by the shape of the curve at much lower water mole fractions.

Incidentally, a review of the literature found that diffusion coefficients of chloride ions through cellulose membranes has been investigated[277], and exhibited a dependence on composition that appears very similar to the sigmoidal function. At first reading these results seemed fortuitous but not immediately relevant to the study at hand as, instead of mole fraction, D was observed to decay as the porosity of the membrane approached zero. However, in light of the

results presented in the previous chapter, where diffusional hopping between interstices was observed at very low water activity, it is believed that the water content and the porosity may not be such different parameters from one another.

The utility, drawbacks, and recent uses of Fickian modelling for characterising diffusional transport in binary viscous aerosol have been discussed in previous publications.[268] We have chosen to use the recently developed partial differential model, Fi-PaD, described by O'Meara et al.[198] and a brief description is provided below.

Fi-PaD represents the particle by a vector containing compositional information, with each element describing a radial shell within the particle bulk; here 400 shells are used, corresponding to a shell resolution of around 10 nm for typical particle radii in our single-particle measurements, 4 μm. The model assumes an initial homogeneous concentration profile at equilibrium with a user specified gas phase RH, which can then undergo an immediate transition to another (or several consecutive) humidities. After initialisation, the model begins to simulate the immediate aftermath of the first such activity change, where only the concentration of water in the outermost shell has equilibrated with the gas phase RH. The concentrations in every shell are then evaluated iteratively as time progresses by solving Fick's second law in spherical coordinates with the diffusion coefficient varying across the shells (i.e. dependent on local composition of each shell). Time dependent radius data may then be generated, covering the precise residence time of the droplet being modelled. Further details of the operation and implementation of Fi-PaD may be found in the initial publication[198].

The simplified treatment of α described above greatly decreases the computational expense of the data analysis as it removes one dimension from the fitting space when compared with fitting to the more complex dependence of equation (6.4.3). By iteratively varying $\log(D_{w,org})$ and C it is possible to improve the overlay between the simulated radius responses and the data. This was achieved using the Matlab interior-point algorithm, within the `fmincon` function, starting from four randomly selected starting points in ($D_{w,org}$, C) space. The extent of agreement between each simulation and the experiment is quantified by calculation of the residual between the two

response functions at each simulated timestep:

$$\frac{\sum_{t=0} F(r_{exp}(t)) - F(r_{sim}(t))}{length(t)} \tag{6.4.4}$$

where the radial response function

$$F(r(t)) = \frac{(r(t) - r(\infty))}{(r(0) - r(\infty))} \tag{6.4.5}$$

is used, as discussed in the publication of Rickards et al.[268] ∞ represents the final recorded spectrum (or model radius) under consideration. *length(t)* is the number of elements in the output vector of radii, and its inclusion converts the residual to a per timestep value, allowing experiments of different length to be compared. As stated in section 6.3.1, it was sometimes desirable to use the changing wavelength of a single stimulated peak in the spectrum instead of *r(t)*. In that case only the initial radius was required, so as to initiate the model. Equation 6.4.5 was then applied to both the model and experiment before comparison.

Running on a single Intel i7-4790 core, simulation of a typical experimental RH step change (8,000-10,000 s in length) was found to take approximately 500 s, with typically around one hundred simulations required to converge the fit parameters and reproduce the measured response in size. The model was considered to have fit when all four independent fitting runs had found the nearest minimum in the parameter space to their starting positions. The goodness of fit was calculated as the mean deviation, across all calculated radii, from the closest experimental data point. A solution was considered optimal if the deviation was less than 3% of the magnitude of the experimental radius curve. An example of the trajectories that independent fitters take across the ($D_{w,org}$, C) space can be found in Appendix B. As the value of $D_{w,org}$ is the limiting value of the diffusion coefficient of water in a fully dry particle, the importance of the value diminishes as the final humidity is raised.

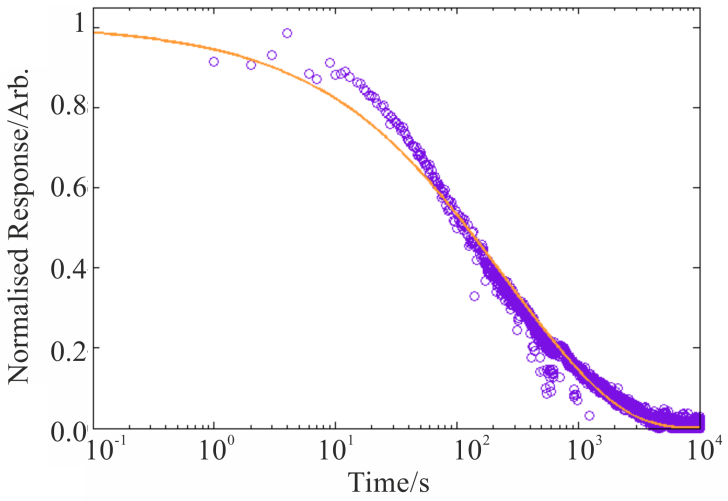

Figure 6.4.2: Example Fi-PaD fit to the response in size of a viscous droplet following a change in gas phase RH, monitored through the shift in a single WGM. The droplet is composed of a ternary aqueous solution of glucose and sucrose (solutes with mass ratio 1:1) following a step decrease in RH from 52 to 18 %. Model parameters are $\log(D_{w,org}/\mathrm{cm^2 s^{-1}})$ = -11.14, C = -5.44, initial radius = 5205 nm.

The associated change in internal structure from a forward simulation with the lowest error between predicted and observed radius is also shown. It can be inspected in panel (b) of the above figure, and shows a sharp decrease in near surface water at around 100 s. The matlab software developed to achieve this fitting can be seen as a method to vary the microphysical parameters and reduce the likelihood of becoming trapped in a local minimum. In that sense, it is a similar procedure to the Monte Carlo Genetic Algorithm employed in a number of publications in conjunction with the KM-GAP model[214]. Nonetheless, by restricting the number of dimensions to two, much of the internal physics within the model is kept.

6.4.2 Water Diffusion in Binary Sucrose Aerosol

As we will see in later chapters, care must be taken in interpreting kinetic measurements from radially inhomogeneous particles: the radial inhomogeneity at any moment in time is a complex function of the processing history of the particle and therefore very rarely even starts in a uniform

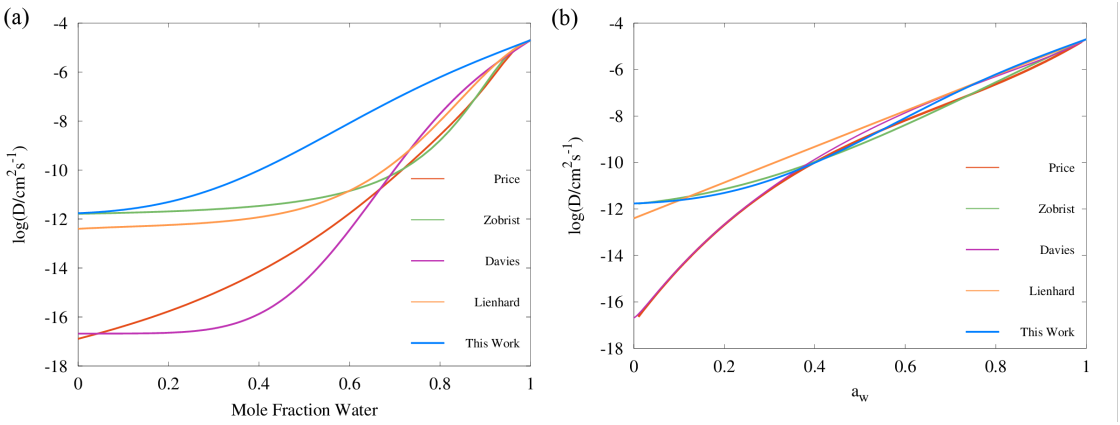

Figure 6.4.3: Comparison of diffusion coefficient parameterisations for sucrose aerosol plotted in (a) mole fraction space, and (b) water activity space: mean trend of Vignes functions (ideality assumed, with cubic treatment of α coefficients) simulated with Fi_PaD; Third order polynomial parametrisation of $D_w(a_w)$ in log space by Price et al.[181], converted to mole fraction using the AIOMFAC model (red); Vogel-Fulcher-Tammann (VFT) parameterisation by Zobrist et al.[132] to RH step experiments in an Electrodynamic Balance (green); Temperature dependent Vignes functions (with binomial expansion of α coefficients) fit to RH step experiments in an Electrodynamic Balance by Lienhard et al.[180] (orange); Temperature independent Vignes functions (with cubic treatment of α coefficients) fit to isotope exchange experiments by Davies et al.[182](purple).

homogeneous form[315]. To the best of our knowledge, most studies that assess the impact of internal microphysics on the composition of atmospheric aerosol do not account for this effect: The gas phase environment at which the experiment is conducted tends to be specifically prepared for the measurement. In any case this level of complexity would be too expensive to include in the models of air quality that are tasked with predicting the evolution of organic aerosol.

Instead, individual RH transitions were modelled assuming that the particle begins in a homogeneous state. Once it was determined that enough repeats had been made, the extracted values of $D_{w,org}$ and C were averaged and used to construct a general trend of equation 6.4.1 for the water sucrose system.

Comparison with Literature Parameterisations

A comprehensive comparison of our results applying this method to binary sucrose aerosol with previous optical tweezers and isotope exchange parameterisations is also shown in Figure 6.4.3, showing the same literature as in Figure 5.2.4. Diffusion coefficients are plotted against mole fraction in addition to gas phase activity, as previously reported, in recognition of the fact that this is the composition parameter implicitly used internally to evaluate D within Fi-PaD and within any Fickian based framework. Additionally, it is noted that activity does not appear anywhere in Eq. 6.4.1, and so a choice of thermodynamic model has been used in each publication to implicitly relate particle phase mole fractions, x_w, to water activity, in order to connect the model output to the experimental data.

The alternative is to assume ideality, treat activity coefficients as unity and define

$$x_w \equiv a_w \tag{6.4.6}$$

for the entirety of the study. This is consistent theoretically with Fickian diffusion in a two component system, and also has the advantage that the independent variable in the experiment is the same as that evaluated within the model.

Following on from this, it must be stressed that representing the diffusion coefficient as a function of relative humidity, as previously reported[182], is less rigorous and necessarily requires an assumption that the thermodynamic models of particle phase activity are consistent with the rest of the literature. It just so happens in this case that mole fraction and particle phase activity are considered equal by definition, as above, but the relationship between a_w and RH can be less trivial. Inspection of panel (a) in Figure 6.4.3 reveals how different these assumed relationships can be: the shape of every line substantially changes, as do the relative trends. Therefore, the choice of activity coefficients can have a hidden influence on the shape of D_w if RH is chosen as the x axis. In other words, the relationship between activity and composition seems to be more uncertain than the relationship between activity and diffusion.

One feature that contrasts these data with the other studies is that the Fi-PaD does assume ideality, and so there is no influence of axis choice on the blue curves. As for the other publi-

cations, the divergence in curvature between the isotope exchange (purple and red) and RH step (blue, green and orange) parametrisations is much less in the x_w panel; in mole fraction space, the shape of all five curves become roughly similar, albeit with large deviations in the $D_{w,org}$ intercepts.

With regards to the dry limit, there are several reasons why the isotope exchange technique would produce results that are incompatible with the RH step technique. Firstly, none of the experiments that are perfomed fully dry the particles. The water activities probed are rarely below 0.2, as there is an assumption that there is no concentration gradient between the surface and the centre of the droplet. As a result the parametrisation must be extrapolated to zero, rather than generated from data recorded at zero. The choice of the activity coefficient function α may exacerbate this problem, as the curvature of such a function increases as it approaches zero. The underlying data may not corroborate such a deceleration.

Secondly, and as a result of the homogeneous nature of the particles, the diffusion probed is not diffusion against a chemical potential gradient, but rather an exchange process. The difference may be significant at the dry limit, as the greater the thermodynamic driving force, the greater the mass flux.[3]

Finally, the organic species present in the particles often contain large numbers of hydroxyl groups, or other functional groups that may accept protons (or, in this case, deuterium nuclei). As it is the case that organics diffuse slower than water, any deuteration of them will bias the extracted diffusion rate in the direction of slower diffusion.

6.4.3 Water Diffusion in Ternary Organic Aerosol

In order to successfully determine diffusion coefficients of water in the ternary mixture using the Fi_PaD model it is essential that an accurate radius response is inferred. The fully equilibrated droplet size and refractive index are determined by fitting the WGM fingerprint at a high initial RH (typically 70 – 80 %) at which the droplet can be assumed to be in equilibrium with the gas

[3] see the derivation of equation 2.1.7 for proof: the physics of intraparticle flux are the same as evaporative flux, other than ρ now signifiying liquid rather than gas phase density

Organic Component(s)	RH Change/%	τ/s	C/Arb.	Log($D_{w,org}$/cm^{2}s^{-1})	$D_{w,org}$ range/cm^{2}s^{-1}
Sucrose	30-5	3794	-2.02	-11.74	$1.60 - 2.40 \cdot 10^{-12}$
	30-10	2277	-2.10	-11.76	$1.49 - 2.59 \cdot 10^{-12}$
	50-10	1076	-2.49	-11.79	$1.06 - 2.30 \cdot 10^{-12}$
	50-20	244	-2.05	-11.64	$1.96 - 4.71 \cdot 10^{-12}$
1:1 Mixture	20-5	2542	-9.71	-11.39	$3.10 - 4.17 \cdot 10^{-12}$
	27-0	1702	-2.51	-11.39	$3.20 - 4.99 \cdot 10^{-12}$
	0-25	1387	-5.81	-11.16	$5.86 - 8.17 \cdot 10^{-12}$
Glucose	50-20	37	-2.16	-10.73	$1.41 - 3.69 \cdot 10^{-11}$

Table 6.1: RH transitions recorded for binary and ternary component saccharide aerosol, alongside fit values for $D_{w,org}$, C (equation 6.4.1-2), the uncertainty in the $D_{w,org}$ estimate (see section 6.4.5) and the stretched exponential time constant τ (equation 6.3.3).

phase and to be homogeneous in refractive index. Then, the droplet radius response following an RH change is inferred from the relative change in wavelength of a WGM; in such a kinetically limited system, it is inappropriate to rely on radius data produced by Mie theory fitting to a radially homogeneous sphere[231]. Instead, we must assume that the refractive index of the outer micron or so of the droplet is approximately constant throughout the transition and use the approach of Krieger and coworkers, who estimate radius changes from experimental wavelength shifts[270].

We consider, as an example, the diffusion constants of water in ternary particles containing two non volatile solutes: Glucose and sucrose at a 1:1 mass ratio, along with RH transitions in pure sucrose and pure glucose. Each transition (see Table 6.1) has been simulated with the Fi_PaD model to produce diffusion dependences, modelling the droplet as a two component system with the non-volatile component molecular mass taken as the weighted average of glucose and sucrose. As Fickian diffusion coefficients are assumed symmetrical (the same for all components at any given composition), no extra information may be gained by explicitly modelling the separate movements of the two organic components. The constants ($D_{w,org}$, C) within equations 6.4.1-2 were floated within the model as described earlier, until simulated radius responses agreed with experiment. The sigmoidal dependencies of D_w on mole fraction resulting from these eight optimal fits, for both binary and ternary aerosol, are shown in Figure 6.4.4.

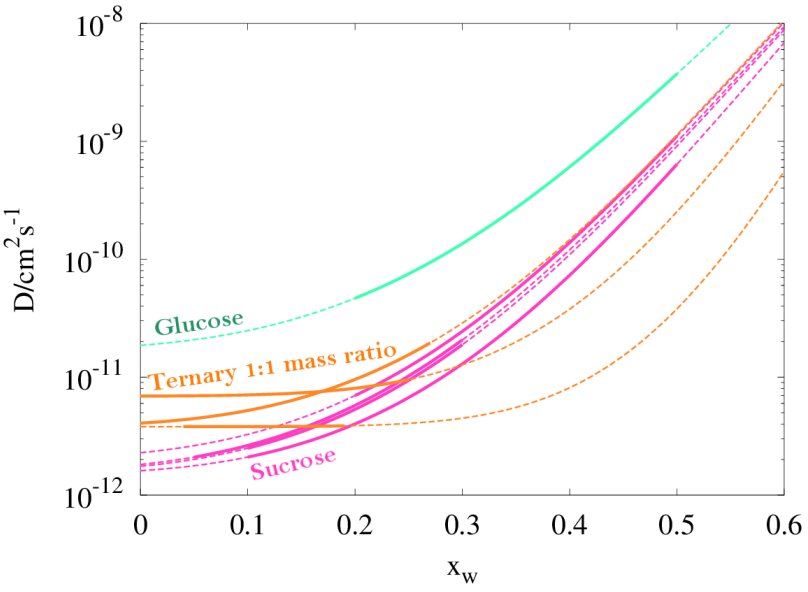

Figure 6.4.4: Dataset of composition dependent diffusion coefficient parametrisations for binary (green and purple) and ternary (orange) saccharide aerosol. Each curve is produced from a sigmoid function according to fit $D_{w,org}$ and C values for a single RH transition, corresponding to the bolded region of x_w in each case.

It is possible to determine that the trend in intercepts confirms the initial hypothesis, with an increase in average molecular weight suppressing diffusion. The four sucrose dependencies exhibit a low degree of spread in the ($D_{w,org}$, C) coefficients and as such are highly consistent as a function of RH. Only one binary glucose water transition was considered slow enough to accurately model, so it remains unclear to what extent the teal line is emblematic of the true 'statistical' dependence of diffusion on mole fraction. An alternate way to interpret this is that an aerosol droplet whose viscosity is close to that of glucose will act in a liquid, and therefore gas diffusion limited, manner, equilibrating very quickly to changes in ambient humidity. Unfortunately the spread in the ternary parametrisations in the region $x_w > 0.2$ complicates the picture somewhat, making unambiguous statements about the microsphysics difficult. Within the range that is actually evaluated within the model (bold sections), two of the particles seem to exhibit D values that are flat, or invariant, with RH, while the third retains a large gradient across the same

space. Indeed, two of the parametrisations intersect at approximately x_w= 0.17, a phenomenon that does not occur with any of the binary sucrose curves.

When extrapolated above the RH range of the experiment, i.e. to the region $x_w > 0.3$, two of the ternary curves generate values of D which are lower than the pure sucrose parameterisations. Such extrapolations are not believed to be physically meaningful, as this is inconsistent with both the trend of $D_{w,org}$, and what one would expect considering the pure component viscosities of glucose and sucrose. In section 6.4.5, a method will be introduced to quantify the level of error in a parametrisation outside of the window probed in an experiment. It is discussed mostly within the context of the error envelope at the limit of low activity, and the concomitant uncertainty in $D_{w,org}$, but precisely the same argument applies to the limit of high activity.

The meaning of the two parameterisations crossing over is difficult to interpret. It may be that mole fractions evaluated in the shells (and especially the surface shells) is biased towards the final composition. If that were the case, the value of D(x_w) at the crossing point would have less overall influence on the predicted radius dynamics, as it is closer to the mole fraction present at the initial RH.[4] But we must be careful here: it may be less legitimate to assume ideality (Eq. 6.4.6) in ternary aerosol than binary. That would constitute a drawback of the methodology, and in section 6.4.5 we will discuss ways to quantify the variance that can be expected outside of the x_w range evaluated (dotted lines). If we assume that the two dependences are both accurate representations of the two droplets, the crossover could physically correspond to each particle having different distributions of the two sugars: A particle with a more sucrose rich outer shell will be more kinetically suppressed, whereas a more glucose rich interface will elevate the water diffusion rate. The effect cannot be resolved with the Fi-PaD model as it is currently written, but will be a consideration in Chapter 7 with the KM-GAP model. It would not (and does not) influence the previous modelling of binary systems.

[4]Strictly, it is only in droplet drying steps that the final composition is lower than the initial. The opposite will be true for a humidification step.

6.4.4 Coupled Evaporation of Water and Organics

Here we increase the complexity of the chemical system probed, to more closely represent the dynamics of SOA evaporation. The particles still contain only two solutes, but the viscous saccharide was doped with a semi-volatile organic molecule, rather than another involatile organic molecule. Aside from the compositional change, the experiments are conducted as described in Section 6.2.

A complicating factor in assessing the time dependent size response when semi-volatiles species are present is the exact deconvolution of the evaporation rates of competing volatiles from the droplet, water and the SVOC. In the limiting case in which the vapour pressure of the SVOC differs from that of water by a factor of 10^6 and when there is no kinetic impairment of water loss from the aerosol particle, rapid water evaporation will dominate the first several tends of seconds, after which an underlying linear time-dependent loss in r^2 becomes apparent[316].

By simply fitting the stretched exponential function (equation 6.3.3) to the radius data, a first estimate of the water loss timescale τ can be determined. Normalising the data to the initial and final radii, the long tail can be assumed to have a constant gradient in r^2 with time once the water evaporation has ceased. This causes the r^2 loss to appear exactly in the residual between the data and the best fit, from which the gradient can easily be determined. If we assume that the SVOC loss begins immediately at the RH transition, and is masked by the water evaporation, a new function

$$r^2 = r(\infty)^2 + A \cdot \exp(^{-t}/_{\tau})^{\beta} - \frac{dr^2}{dt} \tag{6.4.7}$$

can be defined that takes into account the linear combination of the two contributions. The rate at which the radius recedes, $\frac{dr^2}{dt}$, is kept constant at the value fit to the residual in the previous step, and A, $r(\infty)$, τ and β are allowed to vary. $r(\infty)$ is the final particle size containing the involatile solute and solvating water at equilibrium with the gas phase. The deviation between this function and the experimental data is found to decrease by several orders of magnitude when compared to fits carried out using a standard stretched exponential on the same dataset (Equation

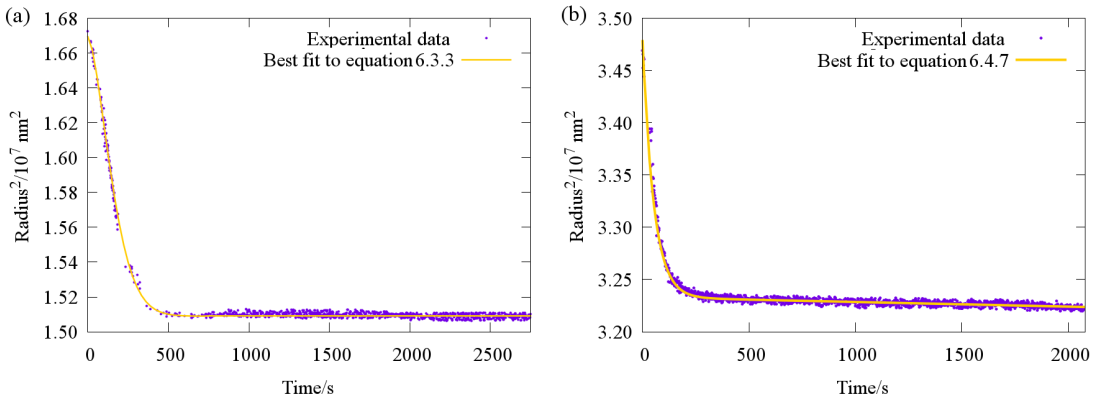

Figure 6.4.5: Typical evaporative profile (purple points) for ternary aerosol containing (a) sucrose and glucose (as per Chapter 6), and (b) sucrose and malonic acid (a semivolatile component). Comparison with fit functions (yellow lines) based on the stretched exponential equations for the different evaporative dynamics are also shown.

6.3.3).

A comparison of the two functions is shown in Figure 6.4.5, with both fit to typical optical tweezers data for ternary aerosol particles, with one or two volatile components.

The accuracy with which the new function reproduces radius responses for particles containing SVOCs can be seen in panel (b) of Fig 6.4.6. There are two features to note here. The first is that the underlying r^2 gradient is assumed constant throughout the entire experiment, including between 0 s and τ. This suggests that transitions between differing semi-volatile loss rates occur rapidly after relative humidity changes. The second is that squaring the data does not seem to double the value of β for the same experiment. In fact, it continues to vary between 0 and 1. It is difficult to speculate as to why this is the case, given that there is still some debate about the precise physical origin of β.

It is possible to probe the water loss response occurring simultaneously with the SVOC loss in the early stages of the particle response by simply subtracting the known r^2 profile from the experimental data. This produces a hypothetical 'water loss only' radius response. We believe the success of the above treatment to be a consequence of the typical disparities in the time constants for SVOC and water loss illustrated in Chapter 2 (typically more than a factor of 10),

effectively allowing the two processes to be decoupled. After the conversion, these data may then be modelled using Fi-PaD, making this the first instance of precise water diffusion coefficients being extracted from a ternary system with this distribution of volatilities.[5] From a dataset of seventeen sucrose : malonic acid transitions, prepared at a 5:2 molar ratio, four were deemed to not be limited by the timescale of RH changes within the trapping cell ($\tau > 200s$), and therefore ideal candidates for this analysis. The assumed involatile molecular mass was once again the weighted average of the two organic components, with the composition assumed to be constant at its initial value throughout the experiment.

The compositional dependence of the diffusion constant (Figure 6.4.6, panel (a)) indicate a substantial plasticising effect of malonic acid – just under a 30% molar component within the organic matter enhances $D_{w,org}$ by the same amount (relative to pure sucrose) as a one to one mass ratio of glucose (cf. Figure 6.4.4). This is also borne out by presenting the diffusion dependences against viscosity data, collected by Young Chul-Song using the particle coalescence methods described in Chapter 3. Nine coalescence events were conducted between 13% and 93% RH, which we have chosen to represent with a loglinear trend line constrained to the water viscosity (8.9×10^{-4} Pa s) at 100% RH (Figure 6.4.6b). In comparison with pure sucrose, a nearly six order of magnitude suppression of the extrapolated viscosity at 0% RH (η_{org}= 2.58×10^6 Pa s) is observed by the presence of a mole fraction of 0.3 of malonic acid. In panel (c), we present the diffusion constant parameterisations in terms of viscosity instead of RH based on these viscosity measurements. As observed in our previous work[176, 222], the diffusion constants of water have values at least one order of magnitude larger than expected from the Stokes-Einstein equation when the viscosity is ~10^5 Pa s.

One note of caution when interpreting these results is that this is a deliberately simplistic model of the internal dynamics of the particle, where all three components are assumed to diffuse at an identical rate, and the mean molecular mass of the organic species does not change as a function of the depletion of the diacid. As discussed in Section 2.4, these assumptions have been

[5]Malonic acid is considered to be an involatile species for the purposes of this Chapter. In Chapter 7 it will be considered volatile and its depletion from particles will be central to the analysis performed there.

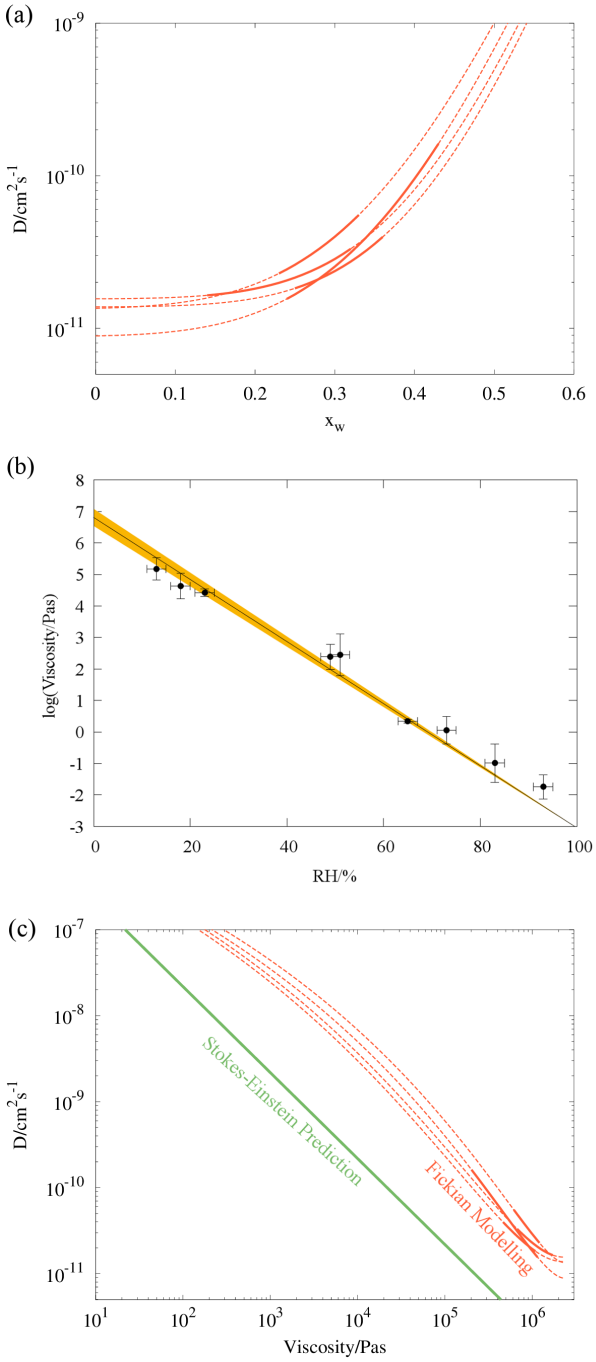

Figure 6.4.6: (a) Composition dependent diffusion coefficients fit to four radius responses of sucrose + malonic acid particles using Fi-PaD. (b) Single particle viscosity measurements, with a loglinear parametrisation (black line, yellow envelope). (c) Combination plot of data from (a) and (b) showing correlation between D and η. A comparison of the Stokes-Einstein predicted diffusivity for malonic acid (green) is also provided in panels (b) and (c).

made in order to preserve the definition of ideality within the model. It would therefore be unwise to infer anything specifically about the diffusion of malonic acid (or, indeed, sucrose) from this treatment. That will be addressed in detail in the next chapter, using a different diffusion model, that will allow the underlying dependences of each species to be revealed.

For now, however, it is clear both from the time constants of particle evaporation, and from the mean D_{org} of the constituents that the presence of multiple organic solutes in a particle will alter the microphysical environment in such a way that it approaches some form of weighted average between the binary particle properties.

6.4.5 Error Analysis and Extrapolating to Zero Activity

It is necessary for the experiments to cover as much of the humidity range as possible in order to have confidence in the parametrisation of equation 6.4.1 produced for each chemical system. Ideally, every activity will be probed by more than one experiment. However, that does not mean there can be equal confidence in the $D_{w,org}$ values fit to each step change:

The diffusion constants evaluated within the model will become progressively less sensitive to the correct value the higher the humidity range gets from 0%. This is because less of the curve is being evaluated within the model, and the values that are are closer to the water-in-water self diffusion coefficient. Clearly, the level of the uncertainty in $D_{w,org}$ varies, and so some method of calculating or measuring it is required.

Usually the droplets are not dehydrated totally. One must therefore consider the deviations that are possible in the 'shape' of equation 6.4.1 down to zero water content, that could still maintain the fit diffusion coefficients at higher water mole fractions. As discussed in section 6.4.1, not all physically realistic dependences of D on $x_w$will be describable by the Vignes equation. Nevertheless, if we are to assume some degree of curvature then it becomes possible to define a 'kinetic parameter space', bounded by differing values of $D_{w,org}$ and C, that describes any fully analysed experiment. An example of this is shown graphically in Figure 6.4.7, panel (b). The red lines accurately reproduce the range of $D_w(a_w)$ within the activity region probed in the ex-

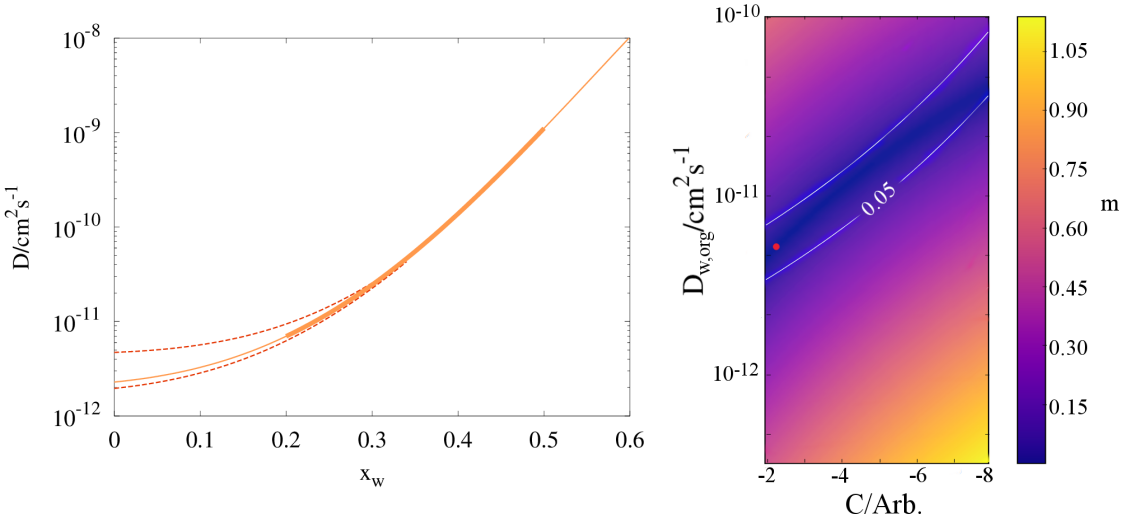

Figure 6.4.7: (a) Isolation of the 50-20% RH transition showing the error envelope in the region $0 < x_w < 0.35$. The envelope was determined by Equation 6.4.8. (b) The values of equation 6.4.8 mapped for the 50-20% RH transition as a function of $D_{w,org}$ or C.

periment, yet their extrapolated $D_{w,org}$ values vary by a factor of 2 or so. The extent to which the dotted line deviates within the bold region is critically important to the goodness of the fit.

An estimate of the deviation can be calculated using the following function

$$m(D_{w,org}, C) = \frac{|\log(D_w(x_w, \alpha)) - \log(D_w^{fit})|}{100 \cdot (x_{w,fin} - x_{w,init})} \tag{6.4.8}$$

which produces a measure of the overlap of two functions in the region important to the experiment, and avoids the need for forward simulating at every point of the ($D_{w,org}$, C) space.

m is a measure of the mean deviation, in log space, between two Vignes equations: the experimentally retrieved dependence D_w^{fit} and an arbitrary function iteratively varying over ranges in physically meaningful values of $D_{w,org}$ and C. RH_{init} and RH_{fin} are the initial and final relative humidities over which the particle transitions, respectively. x_w is the ith element of the mole fraction vector at each intermediate RH, over intervals of 1%. $\alpha(C)$ refers to equation 6.4.2. The division by $x_{w,fin} - x_{w,init}$, the mole fraction range over which the particle transitions, converts m into a deviation per unit mole fraction, so that measurements with differing ranges RH_{fin} - RH_{init} may be analysed in a consistent way. Panel (b) of the above Figure shows how the value of the

merit function varies across a wide range of possible ($D_{w,org}$, C) combinations for a single RH step for a binary water sucrose droplet. The values of $D_{w,org}$ are considered consistent with the fitted parameterisation to the experimental data within error over the limited range in water activity if the merit function value is less than 0.05. The red point in Figure 6.4.7(a) represents the original Fickian solution. The upper and low bound parametrisations are also generated from the Vignes equation and represent the maximum possible deviation in the compositional dependence of D_w while still adequately representing the experimental fit within a merit function value of 0.05.

6.5 Summary and Oulook

Water is in many ways a unique molecule, and this certainly extends to its behaviour in the atmosphere. Presented in this chapter are a variety of experiments on optically levitated droplets that reveal the strong influence water content has on on the phase state of organic aerosol.

The experiments conducted involve inducing rapid changes in the surrounding RH of single aerosol particles containing large organics. All of the compounds investigated are soluble in, or miscible with, water. Step changes of this form are a perturbation which has some atmospheric relevance, for example to updraft events. It is also a procedure that can rapidly probe the full range of water activities from zero to unity.

In the immediate aftermath of a drying step, the optically tweezed droplets begin to vitrify from the interface inwards, impeding the dynamics of their constituent molecules. Consequently, no first order crystal nucleation of any kind is observed, as the rearrangement of the surface molecules becomes prohibitively slow. Instead, the viscosity increases continuously in a more or less exponential fashion as the droplets are dried, and the dehydration works its way 'back' towards the centre. Simultaneously with this, the radius of the particles shrinks in a *stretched exponential* fashion, a phenomenon that requires careful consideration. A literature survey of the glass physics field revealed that the origin of this behaviour is not entirely understood, but that dynamic heterogeneity on the molecular scale is the current leading hypothesis.

The inverse process to drying was also probed, by inducing humidifying events. During these experiments, a close to pure water phase condenses onto the particle surface. Using Fickian diffusion modelling, we have observed and quantified these concentration gradients forming. If one assumes that the diffusion coefficients of the constituents are equal to one another, but determined by their local composition, it is possible to accurately describe the timescale of the water transport phenomena across a wide range of internal structures. This methodology has been successfully applied to understand water loss, and gain, in viscous matrices of one and two saccharides, as well as sucrose mixed with a volatile organic.

To contextualise the diffusion coefficients arrived at in this work, the mean dependence for water in sucrose was compared to recent literature produced across the aerosol science community. The comparison reveals that there are considerable differences in how humidity is assumed to affect concentration in different research groups and model frameworks. Additionally, the limiting value of the diffusion coefficient within an otherwise effectively dry particle, $D_{w,org}$, is found to deviate in an irreconcilable way between different types of experiments. Several arguments were presented as to why this is the case in section 6.4.2, which it is hoped may form the basis of future experiments, that could go some way towards resolving the discrepancy.

The next two chapters will expand on the methods developed here, in order to probe changes in the volatility of organics in increasingly complex systems. Chapter 7 will adopt a 'bottom-up' approach, using multicomponent aerosol with well-defined starting compositions. The mean of the diffusion parametrisations presented in Figure 6.4.6(a) will be incorporated into the modelling, but will be assumed to describe *water only*. In other words, from this point onwards in this thesis, symmetric diffusion is no longer assumed to apply. The Fickian models utilised will consequently become more complex in nature, no longer treating the system as ideal, instead decoupling the kinetic representation of each solute.

Chapter 8 will be closer to a 'top-down' study of the dynamic evaporative behaviour of secondary organic matter produced via chamber oxidation of a common VOC. The methodology used to isolate and remove the contribution of that volatilisation from the particle radius be-

haviour across long time scales (~10,000s) will be immediately useful to both of these studies, as it allows determination of the vapour pressure directly above the droplet's surface.

Chapter 7

Understanding the Evaporation of Semi-Volatile Organic Compounds from Optically Trapped Particles

"If you tell the truth, you don't have to remember anything." - Mark Twain

---

7.1 Motivation

The key difference between the experiments described herein and those in the previous Chapter is that semivolatile organic components (SVOCs) continuously disrupt the equilibrium between the external humidity and the particle phase water activity. As was proven analytically in Chapter 2, the characteristic time of their volatilisation will be at least a factor of ten slower than water in a particle of radius 5μm. The water content of the particle must therefore adjust to the slowly changing organic mass and composition. The assumed 'binary-like' evaporation profiles invoked in the previous chapter to fit the diffusion coefficients of water are therefore not an adequate

representation of the particles investigated. A more thorough and physically realistic model must be used. For that reason I have employed KM-GAP to quantify the different kinetic influences on organic evaporation in viscous particles.

Diffusion in ternary mixtures is a novel chemical physics problem that has been little explored in the current literature, wholly separate even from its utility in understanding the evaporation of SOA[207]. However, especially at the solute concentrations accessed in organic aerosol, molecular diffusion becomes complex and highly sensitive to slight changes in solubility or intermolecular interactions. An initial investigation into the latter has already been presented in Chapter 5 and in any case is beyond the capability of currently available Fickian models. In this chapter the water diffusion dependence on activity is once again assumed to be sigmoidal in nature, and fixed to the values discovered in sucrose and malonic acid particles (see Figure 6.4.7). Focus is instead afforded to the semivolatiles and their internal mixing as they evaporate, as this will be the 'bottleneck' to size and composition changes.

It was recently discovered by Bastelberger et al.[175] that when rapidly drying and then humidifying droplets containing a large fraction of SVOCs, the rapid decrease in viscosity can liberate so much of the semivolatile content that the droplet will lose more mass and volume than is gained from the condensing water. These kinds of counterintuitive effects are prevalent in more complex chemical systems such as those investigated herein. It is important to disentangle whether the evaporation of small organic molecules must be considered a path function, rather than a state function, if we wish to accurately predict the rate at which it proceeds. If path function behaviour is observed, it would allow a number of general assumptions to be made about how changes in environmental conditions influence particle phase mixing, viscosity and saturation contentrations. Unfortunately, it would also require the conditioning histories of any aerosol plume to be known in substantially greater detail and resolution before any meaningful predictions could be made.

Much of this chapter was originally written as part of a manuscript that is currently titled '*Accurate Prediction of Organic Aerosol Evaporaion Using the Stokes-Einstein Equation*'. At

the time of writing it has not yet been submitted to a journal. The theory and implementation of the viscosity determinations presented in section 7.1.2 were conducted by Dr. Grazia Rovelli, and provided to me to aid in the modelling of electrodynamic balance experiments of glycerol evaporation, also conducted by her. The underlying viscosity data was collected both by her and Young Chul-Song. All experiments involving the evaporation of malonic acid were conducted by myself. Some of the experiments involving sucrose as the nonvolatile component are the same as those discussed in the previous chapter. However, as alluded to in section 6.5, the purpose of the analysis employed here is different, and complimentary.

The KM-GAP model is utilised to aid in the the analysis. KM-GAP was first published by Shiraiwa et al.[205] but has since been modified and adapted in numerous ways, including in the publications of Julin[317], Berkemeier[214], Yli-Juuti[301] and Vander Wall[213]. The changes made to the version employed here were all introduced by myself, and the majority of the coding took place during a four week research visit I made to the group of Prof. Shiraiwa at the Univeristy of California Irvine.

7.1.1 Deviations from the Stokes-Einstein Equation

The extent to which molecular diffusion is slowed by a given increase in viscosity is the subject of some debate: As discussed previously, different experimental techniques disagree about the limiting value diffusion coefficients collapse to as a particle approaches a glassy state. Such a disagreement will, if different parametrisations are incorporated into atmospheric models, lead to a divergence in the predicted rate of secondary aerosol evaporation. Other complicating factors are the strong influences of moisture[144, 211, 318] and temperature[155, 286], in addition to environmental processing, on viscosity.

It has been known for some time that the Stokes Einstein relationship (equation 5.1.1) is not universal, i.e. under certain conditions it fails, and the macroscopic viscosity η no longer predicts the microscopic diffusion D. This 'breakdown' has been observed to occur in various chemical systems, such as those containing a high degree of hydrogen bonding[128], polymeric

substances[319], supercooling[320, 321, 322], confinement of small molecules within porous networks[323, 324], or in systems which are close to undergoing a glass transition[126, 325, 326], Strikingly, the internal structure of a tropospheric organic droplet contains, or is thought likely to contain, every one of these features[71, 130, 173, 290].

It is therefore not surprising that the equation routinely fails to predict the observed viscoelastic properties of different types of SOA. Indeed, in Chapter 5 I proposed to directly link the nanoconfinement of water to the failure of Stokes' Law, by invoking a new mechanism of water transport, that proceeds via hopping between discrete sites.

Most other publications on the topic within the aerosol science field exclusively study the failure of the S-E equation to describe water. It remains an open question, however, whether organic species may behave in a way which more closely satisfies the assumptions upon which Stokes-Einstein is based: On a molecular level, they tend to be larger than the solvent through which they move. This promotes Brownian trajectories which are broadly consistent with the derivation of Stokes' Law .

On the other hand, fluorescence imaging studies[141, 142] have observed significant heterogeneities in the concentration and rotational motion of organics in particles over a wide range of humidities. Such 'dynamic heterogeneity' may be significant enough to influence the mean diffusion rate, averaged over the droplet. More generally, it is a common feature of molecular glasses[299, 327], whose dynamics are known to be inconsistent with Stokes' Law.

The relative importance of these factors on a given droplet in a given atmospheric scenario is unclear. Making more precise measurements of organic diffusion are therefore crucial in determining the applicability of Equation 5.1.1 to SOA.

In this Chapter it is investigated whether the evaporation rate, and hence diffusion rate, of organic compounds from SOA can be predicted accurately using Equation 5.1.1, without any of the modifications[272] or fractional terms[126, 328] that are occasionally discussed in the literature[185], and some of which were introduced in Section 5.1. As we will see, this appears a general trend i.e. it holds for each of the semi-volatile compounds investigated, and is not de-

pendent on the initial volatility of the evaporating species. This result suggests that it is possible to simplify the prediction of phenomena where diffusion of semivolatile organics is important, such as particle growth rates[97] or surface chemistry[210].

7.1.2 The Viscosity of Multicomponent Systems

While it is possible to determine the viscosity of simple, one solute systems in the aerosol phase[139, 152], or of SOA particles[144, 148], systems of intermediate complexity represent a challenge. In the case of of SOA viscosity, it is not possible to apportion the contribution to the viscosity of any one constituent, as there are potentially tens of thousands of them[329]. It is also difficult to predict with certainty the time evolution of viscosity as an SOA particle evaporated, even if the 'equilibrium' value at a given RH is known.[301]

Yli-Juuti et al. utilised a flow reactor to study the early evaporation of freshly produced α-pinene SOA into dry air recently[301], and encountered precisely this limitation. The radius response, acquired with a scanning mobility particle sizer (SMPS) at frequent intervals from the otherwise sealed reactor, was compared with forward predictions from the KM-GAP model[205]. It was found that particle viscosity must be assumed to rapidly increase, by four orders of magnitude over a period of minutes, in order to reproduce experimental observations. Unfortunately their conclusions were constrained by the coupling between viscosity and volatility in the model: they could not determine with confidence whether the SOM present in the later stages of the experiment was (1) volatile yet kinetically limited from partitioning back into the gas phase by the viscosity they experienced, or (2) non volatile. Additionally, the flow into the SMPS was not truly continuous, and so the curvature of the particle sizes was not recorded in a highly time resolved way.

In the final sentence of the article, the authors state their belief that, to quote, 'higher scientific priority for future investigations is to decrease uncertainties in the [volatility basis set] representation of the organic compounds contributing to SOA production.'[301] That is to say, what are the evaporative properties of these molecules and how are they influenced by the par-

ticle phase state? The data analysis methods described in Chapter 6 can be modified to extract vapour pressure information from multicomponent organic aerosol. They were therefore seen as an ideal starting point to resolve these effects.

Ternary aerosol represents a stepping stone between binary systems, the viscosity of which is now a reliable and reproduceable measurement[153, 139], and the incredibly complex task of probing atmospheric aerosol in field campaigns.

We discuss methods to predict particle viscosity in situations where the ratio of non-volatile to semi-volatile components is changing. We would like to produce a methodology that can accurately determine the viscosity of a mixture if the majority by molar ratio of its constituent parts are known, and then predict the changes that may occur as one of those organic molecules evaporates from the particle.

Mixing rules

It is found that humidity dependent viscosity is most accurately predicted when the species in the particle are weighted according to their hygroscopic growth. Conversely, when considering how viscosity changes as semivolatile species deplete from the particle, a simpler mole fraction mixing rule is found to be a sufficient level of detail. Both kinds of dependence can be considered types of the Bosse mixing rule, after Dennis Bosse[330], whose PhD thesis first proposed it in detail. The procedure involves a sum over the logarithms of the pure component viscosities of each component i:

$$\ln(\eta_{mixture}) = \sum_{i}^{n} x_i \ln(\eta_i) \tag{7.1.1}$$

or, more specificaly,

$$\log_{10}(\eta_{mixture}(a_w)) = \sum_{i}^{n} x_i \log_{10}(\eta_i(a_w)) \tag{7.1.2}$$

where each compound is weighted by its mole fraction x_i.

Physically speaking, it may seem peculiar that the average should be taken logarithmically rather than linearly, given that other aerosol properties like density and refractive index are found to replicate experimental data well when linear mixing rules are applied[331, 285]. However, plasticisation effects in viscous matrices do not seem to scale linearly with concentration: a relatively small molar proportion of a plasticising compound will disproportionately reduce the viscosity of a particle as a whole. This may be because viscosity is a collective property arising from the coupled motion of molecules that are not directly bonded. Such disruption of the long distance ordering will have a much stronger than linear effect, as has been observed with both water and semivolatile species in organic aerosol.

Returning to the mathematics of the mixing rule, multiple methods of calculating $\eta_i(a_w)$ can be employed that capture differing levels of detail about the particle. Here we employ a method that was recently described by Rovelli et al.[332] The hygroscopic growth of each solute is considered separately, allowing the water mass present to be divided between the two. Each pure component viscosity is replaced with the binary mixture viscosity of *i* and water, at a recalulated water activity:

$$\eta_i(\kappa(a_{w,i})) \tag{7.1.3}$$

Meaning that the presence of other solutes is assumed not to influence the association of water to the first. component *i*, from which an associated mass fraction $m_{H_2O,i}$ can be determined. Here, $\kappa(a_{w,i})$ is the κ-Kohler equation (1.3.2) defined in Chapter 1, solved separately for each solute in the droplet. The total water mass within the ternary mixture is then divided into two 'hypothetical' water masses for the two binary solutions,

$$m_{H_2O} = m_{H_2O,1} + m_{H_2O,2} \tag{7.1.4}$$

distributed according to the mass fractions of the solutes, ε_i:

$$m_{H_2O,i} = \varepsilon_i \cdot m_{H_2O}. \tag{7.1.5}$$

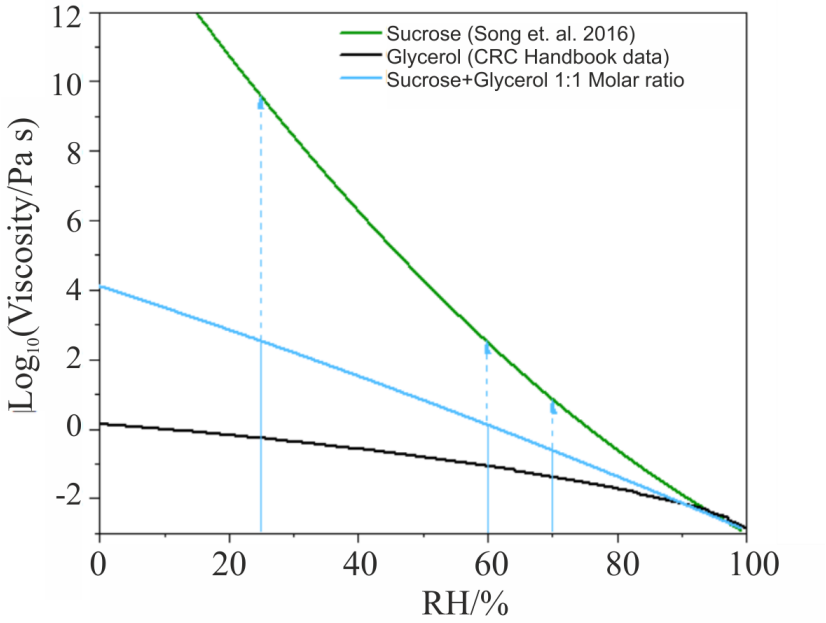

Figure 7.1.1: Calculated humidity dependent viscosity for the glycerol + sucrose system (blue) at its initial molar mixing ratio of 1:1. Data acquired by Dr. Youn Chul-Song[139]; calculation performed by Dr. Grazia Rovelli.

The purpose of this approach is to introduce a degree of non ideality into the way the model represents the particle phase. While the treatment assumes that the two solutes do not interact with 'each other's solvent', the hygroscopic growth factors of the binary solutions are taken from aerosol phase measurements, and as such constitute the most accurate information available.

Data

One example of the Bosse mixing rule is shown in Figure 7.1.1, alongside two viscosity parametrisations for the constituent solutes. Glutaric acid, a small semivolatile, does not achieve a glassy state under dry conditions, in contrast to raffinose. This parametrisation will be used later in the chapter to estimate diffusion coefficients of raffinose and Malonic acid, a diacid with a similar molecular weight, and O:C ratio, to that of glutaric.

Secondly, the mixing rule approach in equations 7.1.1-5 can be made time dependent. Viscosities can be estimated in situations where the evolving solute concentrations are known accu-

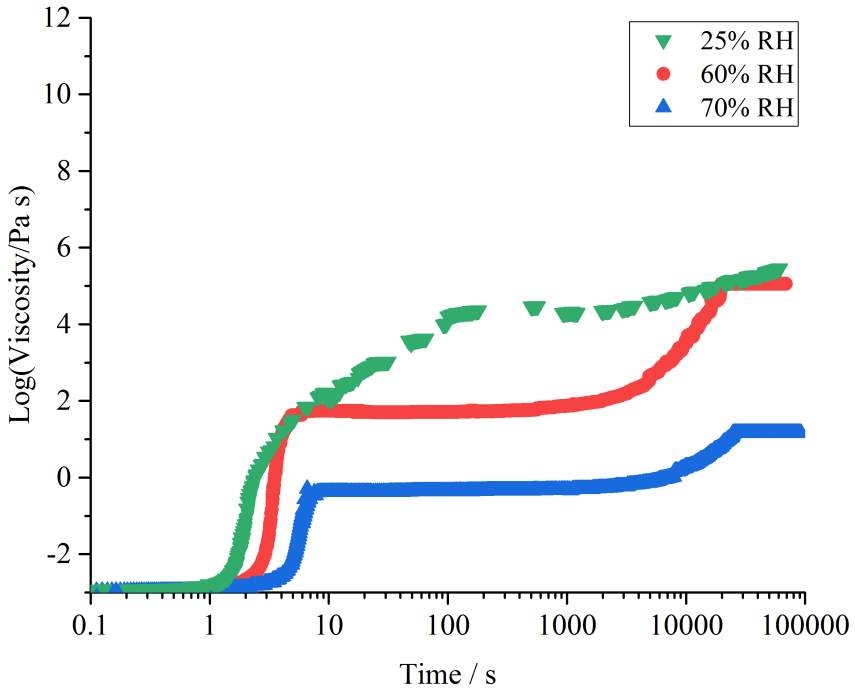

Figure 7.1.2: Three time dependent viscosity parametrisations of ternary particles containing sucrose and glycerol, taking into account the differing hygroscopic properties of the two compounds, as described in the text.

rately, or can be estimated. For instance, the mass flux can be inferred from the literature vapour pressure of the volatile solute to a first approximation. More accurately, the concentration can be determined from the refractive index, by using a molar refraction treatment, which will be described in detail in section 7.3.1.

Figure 7.1.2 presents the calculated viscosity of a sucrose + glycerol mixture at three RHs, over a time frame of 100,000 s. At 25% RH, which is close to the glass transition humidity of sucrose, the solution vitrifies rapidly as glycerol evaporates. It does not manage to achieve the glassy state (10^{12} Pa s), but exhibits the highest viscosity during the glycerol evaporation (100-100,000 s). By contrast, the particles evaporating into higher humities (60 and 70%) exhibit progressively lower viscosities, and also both reach constant values at the limit of long time. It may be hypothesised that the regime of plateaued viscosity is only reached once the semivolatile

is totally lost from the organic matrix, allowing the saccharide to fully equilibrate with the gas phase conditions. At which point, the viscosity returns to its thermodynamically controlled value and so loses any time dependence.

Interestingly, the droplets with the slowest assumed organic evaporation vitrify the fastest in the time interval 1 - 10 s (green vs red vs blue). One explanation is that when the driving force in water activity between the starting solution and the equilibrium gas phase is larger, the initial flux will increase. Hence, the water evaporation that takes place in the early seconds is faster, as per Fick's first law. It is only when the organic constituents begin to dominate in terms of mole fraction (after 1000 s) that the viscosities begin increasing substantially. Additionally, the gradient of the viscosity parametrisations tend to accelerate as they approach the dry limit of $x_w \rightarrow 0$ (as shown in fig. 7.1.1).

7.2 Experimental Description

The objective of these studies is to treat the SOA mass as a non-reacting mixture of semivolatile and involatile organic species. Hence, the droplets contained a viscous sugar in addition to a small organic molecule, either a diacid or an alcohol. The sugars are intended to replicate the physical and molecular properties of highly oxidised[48, 333] or oligomeric[71, 76] constituents of SOA.

At each humidity, the water activity in the particle was allowed to equilibrate with the gas phase, after which point the dominant process controlling mass loss is the diacid or alcohol evaporating[334, 303]. Here, radius loss rather than mass loss is recorded, as in the previous chapter.

Electrodynamic trapping was also used to levitate particles in this study. The data was acquired by Dr. Grazia Rovelli. The electrodynamic balance apparatus is used in numerous research groups and has aided in many discoveries in the aerosol science field. It has been found that the technique provides a comparable level of droplet stability over long periods of time to optical trapping methods.

It is beyond the scope of this thesis to describe the construction of theoretical framework behind the device. Howevever, a brief introduction is appropriate, such that the important differences with respect to optical trapping are communicated. An Electrodynamic Balance is constructed of two cylindrical electrodes, into which a charged organic droplet is dispensed. The gas phase conditions are set using gas flows and liquid cooling (if necessary), and can be changed rapidly (of the order of 0.1 s) by replacing one vertically propagating gas flow with a counter-propagating one. Flow rates are 50 mL min^{-1}. Particle sizing is similarly conducted at a much faster frequency than methods based on droplet Raman spectra, and is achieved by collecting the *elastically* scattered light across a range of angles at once.

7.3 Considerations when Analysing Evaporation

Experimental data generated through different techniques was collated as part of this work, either for inclusion ('hard coding') within the KM-GAP model, or to validate its results. Not all of it was suitable for comparison in its original form. Therefore, the purpose of this section is to describe any transformations that were made, and justify them, such that the reader can reproduce this study.

7.3.1 Correcting Vapour Pressure for Surface Concentration Changes

Semivolatile species are not evaporated in isolation in these studies. As mentioned above, a dry mass of an involatile species is present, in addition to water in the droplets captured. Therefore, the pressure above the droplet surface will be lower than above a pure liquid phase of the semivolatile species. The ratio of the observed to the pure reference state pressures will therefore be equal to the proportion of the surface that is covered by the evaporating species. This proportion can, in turn, be assumed to be equal to the molar proportion of semivolatile x_{svoc} near the surface of the droplet. Raoult's law encapsulates this effect and relates the pure component vapour pressure $p^{\bigcirc}_{svoc}$ to the observed p_{svoc} via

$$p_{svoc} = x_{svoc} \cdot \gamma_{svoc} \cdot p^{\bigcirc}_{svoc}. \tag{7.3.1}$$

Substituting this into equation 2.16 results in

$$p^{\circ}_{svoc}(a) = \frac{da^2}{dt} \cdot \frac{RT\rho_{droplet}F_{svoc}}{2x_{svoc}\gamma_{svoc}M_{svoc}D_g}, \tag{7.3.2}$$

where a is the time evolving particle radius. All other parameters are as defined in Chapter 2.

Were there to be no effect of viscosity on the rate of evaporation, the value of p_{svoc} would increase linearly with the surface coverage of solute as the droplet dries. It therefore follows that, if the mole fractions x_{svoc} and activity coefficients γ_{svoc} are accurately known across the RH range of the experiments, $p^{\bigcirc}_{svoc}$ can be calculated for each particle at each RH. The humidity at which a reduction in the value is observed will indicate the onset of the bulk diffusion limited regime.

7.3.2 Correcting Vapour Pressure for a Moving Gas Environment

The velocity of the nitrogen gas passing over the tweezed droplets in this study is substantially higher than air would move past a droplet falling at its settling velocity. Additionally, the larger radius of the droplets studied here, in comparison to SOA particles, may alter the gas flow characteristics. To be precise, the relative importance of the air viscosity to the inertial force imparted by the gas may reverse. Under those circumstances the relationship between the aerosol and N_2 flow would transition from laminar to turbulent, with serious consequences for the evaporation process in the near surface gas phase.

Clearly we require some way to quantify these effects, so that if evaporation is observed at a rate that is unrepresentative of atmospheric conditions, the value can be understood in context, and corrected accordingly. Fortunately, a number of dimensionless quantities exist that can capture aspects of the physics involved. The quantity that comes closest is the Reynolds number:

$$Re = \frac{2a\rho_{gas}v}{\eta_{gas}} \tag{7.3.3}$$

where a is the particle radius and v is the gas velocity, and η_{gas} is the viscosity of the (in this case) nitrogen flow. If Re is low, this suggests a large demoninator, meaning that viscous forces are more important than inertial forces. Therefore, the less perturbation there is to the near surface gas, and the greater extent of laminar flow around the droplet. With reference to water droplets falling through the atmosphere, Kinzer and Gunn[335] proposed that any droplet in an environement from which one calculates $Re < 7$ would be surrounded by an essentially stationary parcel of gas, and so would 'experience' a stationary environment. Higher Reynolds numbers would lead to turbulent flow which would continuously replace the atmosphere above the interface, artificially increasing the evaporation rate.[1]

A related quantity is the Sherwood number:

$$Sh = 2 + \sqrt{Re}\sqrt[3]{\frac{\eta_{gas}}{\rho_{gas} D_{gas}}} \tag{7.3.4}$$

Due to the square and cubic roots present, it increases much less strongly with the level of turbulence than Re. The importance of the Sherwood number is that a vapour pressure may be multiplied by *Sh/2* to obtain a value more accurate to that adopted in a given aerosol system. Taking prototypical values of the flow rates, densities and particle radii used in this work we have calculated that, for optically tweezed particles, Sh = 2.0427, or, an increase in the evaporation rate of just over 2%. Therefore, the partial pressure around the droplet of an evaporating gas is effectively invariant, and will build up as if the air in the entire trapping cell were stationary. Given the small magnitude of the change, it was decided to forego the correction. As we will see, the values of vapour pressure extracted here vary by *orders of magnitude* across the humidity ranges probed. Finally, Sh is only indirectly dependent on RH, through the weak dependence on a (drier particles are generally smaller, but the variance in starting size is large enough to obscure that here). Therefore, the qualitative effect, on a logarithmic axis, would be to shift all of the data points by approximately the same distance.

[1] Of course, what is being described here is a natural phenomenon, by definition. The word 'artificial' is meant to imply that the evaporation rate ceases to be a function just of what is being investigating, and fluid dynamic forces begin to play a role.

7.4 Kinetic Modelling

Here we employed a modified version of the KM-GAP model, first described by Shiraiwa et al.[205], and discussed in Chapter 2, to forward simulate the portion of the experiment where organic evaporation dominates. It has been observed in numerous studies[199, 301], and indeed in the previous Chapter, that the microphysical treatment of particle phase diffusion employed is crucially important to the accurate modelling of evaporation data. In contrast to the Monte-Carlo-Genetic-Algorithm procedure[214], where multiple diffusion constants are varied in order to optimize the model output to fit the observed data. we have fixed their values according to independent viscosity measurements. The organics have been assumed to follow the Stokes-Einstein relation, with η determined through coalescence measurements across the range of relative humidities for single solute systems.

The viscosity of two solute systems was parametrised from the constituent solutes using mixing rules that was the subject of subsection 7.1.2. Once a parametrisation of η has been produced, we can convert it to a diffusion constant for the organic compounds via equation 7.1.1. Meanwhile, water motion was represented by the mean of the four sigmoidal dependences determined in Chapter 6 for water in sucrose + malonic acid particles using the Fi-PaD model[303]. The trends of all three diffusion coefficients across the RH range for a system of measured viscosity are shown in Appendix B.

When comparing predicted to observed radius data, several other model details are required. The particle density has been calculated from the experimental RH using polynomial dependences published previously[285] for the relevant solutes. Where available, the starting mole fractions of the various organic species and water have been determined by employing the statistical thermodynamic treatment of Dutcher et al.[336, 337], implemented as a lookup table in the model whose rows are unique water activities. Such a table was not available for the sucrose + glycerol system, and so the the hygroscopicity treatment (equations 7.1.3-5) was used initially to determined the starting water content of the droplet. This was, paradoxically, found to be *too accurate*: The microphysics within KM-GAP does not adequately represent non-ideal molecu-

lar interactions, and so a significant degree of evaporation or condensation occured in the early timesteps to revert the particle to the ideal composition. This changed the starting radius.

Another modification is the introduction of Raoult's law (Equation 7.3.1) to correct the vapour pressure of both the semi-volatile component and water emanating from the particle, according to the surface mole fraction *within the model*. This is updated at every time step that the model is evaluated, and so captures the time evolving nature of the volatilisation. Water's vapour pressure above the droplet surface is defined by the Köhler equation[205, 338] and the pure component (gas phase) value defined by the RH (Equation 1.3.1). The majority of the particles are modelled as if they are made up of 75 shells which can grow and shrink as the densities and radial concentrations change. The glycerol + sucrose experiment modelled in section 7.5.3 is modelled as 60 shells. The initial concentrations are determined via a charateristic molecular volume that is calculated for each component. It is defined as:

$$V_i = \frac{M_{r,i}}{N_A \rho_i} \tag{7.4.1}$$

where N_A is Avogadro's number, and $M_{r,i}$ and ρ_i are the molecular mass and pure component density of component i, respectively. The number of molecules present within each bulk shell is then calculated from the shell volumes divided by the V_i values, which are then adjusted to account for the starting mole fraction of the solution. As in the Fi-PaD model, when shells shrink or are removed, concentrations are redistributed to maintain mass balance within the particle. Surface shell concentrations are calculated in a similay way, which involves dividing the surface area by the effective molecular cross sections of each component.

The concentrations, vapour pressures and gas conditions are then converted into a single thermodynamic driving force for the evaporation of each component during the simulation. A set of differential equations, arising from Fick's second law, can then be solved for the initial shell concentrations and time steps, to determine the final output. The length of the input timesteps vary: the solution to the differential equations governing diffusion is calculated for a 1000 element time vector that increases logarithmically from 0.1 s to the length of the experiment.

7.5 Study of Small Molecule Evaporation from Viscous Saccharide Particles

7.5.1 Experiment Length and Statistical Significance

In the previous chapter, a method of deconvoluting the contributions of water and SVOC to observed radius dynamics was described (section 6.4.4). The phenomenon is a coevaporative process and so there is no precise radius point before which only water evaporates and after which only organics. Instead, a method was designed to identify, in a reproduceable way, the timescale over which the radius response can be considered dominated by water or SVOC loss. Then, the purpose was to analyse the former while removing (or at least minimising) the influence of the latter. Here, I would like to do the opposite. Moving beyond a binary representation of the internal composition of the particles is now appropriate if we wish to more fully interstand the internal dynamics of these particles.

Assuming that there is no kinetic impairment to diffusion, rapid water evaporation will take place during the first several tens or hundreds of seconds. In the limiting case of an organic with low volatility, for example one that has a vapour pressure ca. 10^{-5} Pa, it can be assumed that effectively no depletion occurs during this time. As the ambient air becomes drier, intraparticle diffusion of water slows and the two regimes begin to 'bleed into one'. Indeed, the analytical modelling of condensation described in Chapter 2 provides an approximate prediction of how similar or different these timescales can become, as a function of the different particle phase diffusion coefficients.

Precisely which points the fit should be conducted over is a non-trivial matter. A sequence of da^2/dt values calculated using the modified stretched exponential equation 6.4.7 is shown in Figure 7.5.1, alongside the input experimental data. During the fitting process, a guess value of da^2/dt is fit from the residual of the Mie fit radii and a stretched exponential function. The assumed length of the water loss regime is increased, as a proportion of the total experimental length. Systematically removing the early residual data between the folding time τ and 50% of

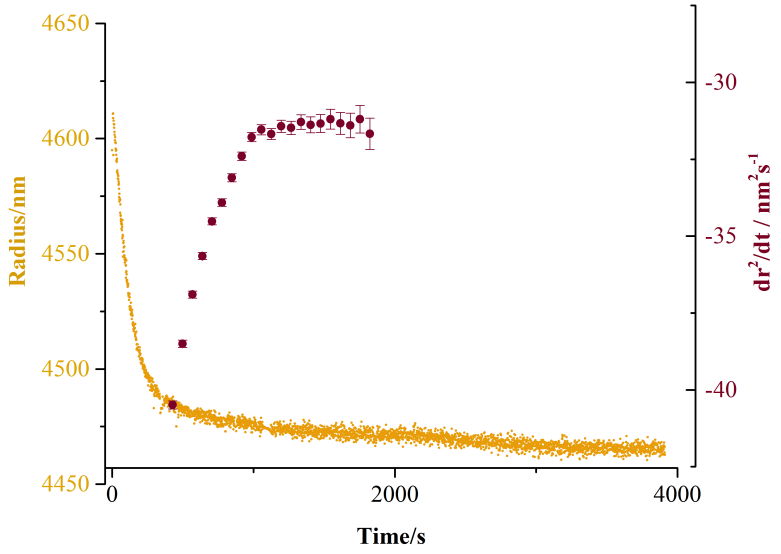

Figure 7.5.1: Retrieved gradient values da^2/dt (dark red points)from equation 7.3.2 determined from a typical sucrose/malonic acid/water radius curve (yellow points). Each point is plotted at the time at which the water loss regime is assumed to end, i.e. it is the gradient of the yellow data remaining after that time.

the way through a single experiment (approx. 2000 s) shows the uncertainties at the two limits.

The fit values were found to converge to a value of approximately -32 nm^2s^{-1} at a cutoff of 1000 s. After that, a plateau in the value of da^2/dt is reached, and the fit error increases each time the residual dataset is shortened. This suggests a compromise exists between fitting the largest number of points, and ensuring that the error associated with the returned value is small. Depending on the scale used, that value occurs at either 25% removed, or $\sim 2\tau$ in the above case.

Since compounds with varying p_{svoc} values are investigated at varying humidities, τ will vary in a non-trivial way as a proportion of the experiment. It is not believed that it would make a good unit for the determination and so the 25% value was used in all experiments reported in this chapter. Once that value was decided, it became possible to calculate the length of experiment *that would have to be conducted* to capture a size change of at least a given magnitude. Figure

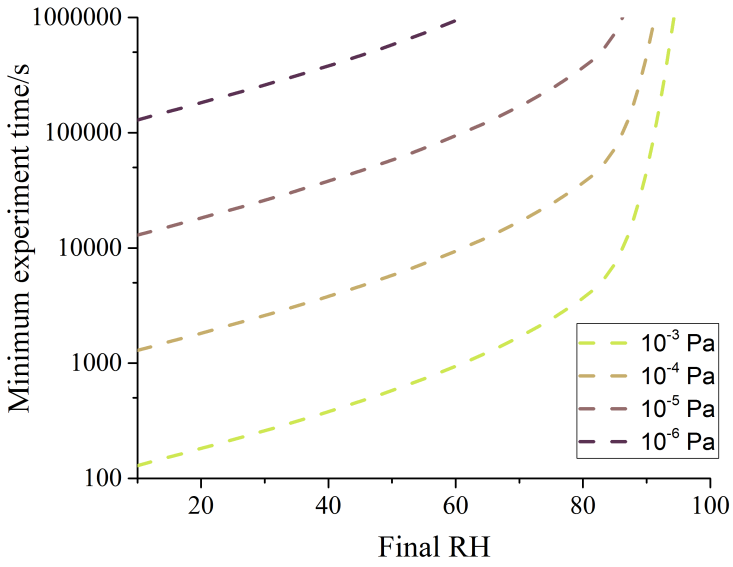

Figure 7.5.2: Examples of the experiment length required to observe a statistically significant radius change, calculated assuming there is no kinetic limitation to evaporation. Four different vapour pressures are shown.

7.5.2 is a visual representation of of this phenomenon, with a number of assumptions made. Firstly, if the Mie fit radii have a variance, σ, around the true value, then for an experiment to be statistically significant, the radius loss $\triangle a^2$ should be much larger. Here we have assumed at least a factor of five. Stated mathematically:

$$\frac{\triangle a^2}{\triangle t} = \frac{da^2}{dt}(p_{svoc}) \tag{7.5.1}$$

$$\triangle t \geq \frac{5\sigma}{da^2/dt(p_{svoc})} \tag{7.5.2}$$

where da^2/dt is calculated from equation 7.3.2. The mass and mole fractions were taken from the Dutcher et al. thermodynamic model of malonic acid in sucrose. The semovilatile was assumed to be 40% by molar ratio of the organic mass. Particle density was assumed to vary by a third order polynomial as a function of mass fraction, using published coefficients for sucrose[285]. p_{svoc} was varied logarithmically from 10^{-3} Pa down, to represent suppressions

in *effective* pure component pressures, rather than the pure component vapour pressure of the compound. σ was assumed to be 10^4 nm^2 .[2] $\triangle t$ was also multiplied by $4/3$ to account for the removal of water loss at the beginning of the experiment.

It can be seen that an order of magnitude decrease in pressure approximately leads to an order of magnitude increase in the minimum timescale. There is only a weak dependence on RH below 80%: da^2/dt increases slightly as the humidity is reduced, as it is proportional to the increasing organic content of the droplet as water is driven out. As the RH approaches 100%, the surface concentration of organics becomes very close to zero, creating a singularity like effect on da^2/dt .

Despite the fact that simplistic treatment described above does not assume any kinetic limitations to evaporation, it is still instructive. Most of the experiments described herein will be of the order of hours (6000 - 9000 s), and at RHs of below 80%, meaning that 10^{-4}Pa is approximately the smallest observable vapour pressure via this method.

7.5.2 Predicting Kinetic Limitations Under Dry Conditions

In Chapter 2 the existence of a moisture driven transition was introduced, below which organic aerosol does not internally mix while it evaporates but above which they can: In humid environments, semi-volatile molecules are capable of diffusing from the centre to the surface of the droplet without impediment. As the molecule evaporates, the concentration within the particle remains uniform, regardless of the distance from the interface. Vapour then begins to accumulate directly above the surface, and it is then the diffusion of this vapour into the ambient air that becomes rate limiting. In more dehydrated environments, the mechanism inverts and the resupply of organics from *below* the interface becomes the slowest step in the evaporation process.

Transitioning between these two regimes of partitioning may alter the meteorological properties of atmospheric aerosol, as kinetically limited evaporation will artificially keep volatile mass high in the condensed phase when it should not be. To illustrate this, the evaporation of a 200 nm radius particle was simulated with KM-GAP. It was hypothesised that the transition would cause

[2] this may actually be a conservative estimate - see the variance in fit radii in Figure 6.4.5, panel (b)

an abrupt change in the predicted evaporation rate, as a function of RH. The modelled particle contained water and two organic solutes. The starting composition defined such that the organic matter was 25% by volume semivolatile, and the remaining 75% nonvolatile. The density of the organic components have been fixed at 1.5 g cm^{-3} and the viscosity of the particle assumed to be the same as SOA formed from the oxidation of Toluene[211]. Three different volatilities were assumed for the semivolatile species, in addition to two hygroscopic growth factors, making six datasets that should cover the range of tropospherically relevant particle compositions.

The mean evaporation rate, da^2/dt, was then calculated from the radius responses across the humidity range from 100-0%, in increments of 4%. Instead of converting this rate directly to a vapour pressure, we have instead substituted the definition of mass concentration of the compound (Equation 2.1.1), producing:

$$fC = \frac{da^2}{dt} \cdot \frac{\rho_{droplet} F_{svoc} \gamma_{svoc}}{2D_{gas}}. \tag{7.5.3}$$

Where *fC* is the *fractional* C* that is linearly related to the vapour pressure at the surface. It is a conversion of p_{svoc} into the units of mass concentration and so the above equation is analagous to the vapour pressure equation, 7.3.2.

Hygroscopicity has been represented by κ-Kohler theory[101], which is to say that the changing volume of water within the droplet, V_{water}, can be represented by the equation

$$\kappa = \frac{V_{water}}{V_{dry}}(\frac{1}{a_w} - 1) \tag{7.5.4}$$

where a_w is the particle phase water activity, and the other terms are as defined in Chapter 1. κ values of 0.1 and 0.25 were chosen for this study, which is consistent with the range of calculated values for various types of SOA[339]. Larger values were investigated, but were found to disrupt the equilibrium between the model RH and particle phase a_w, artificially increasing the water evaporation rate. These values are consistent with a recent parametrisation of toluene SOA viscosity by DeRieux et al.[340], which found that $0.2 < \kappa < 0.25$ needed to be assumed.

Water evaporation did not seem to follow this mechanism within the model framework, as it was assumed that water diffuses more quickly than organic molecules in both the gas and particle phases. More specifically, the Vignes dependence for ternary sucrose + malonic acid aerosol arrived at in the previous chapter was used. If this was shown to hold in a more complex model system, it would disentangle some of the complexities that arise in our understanding of organic aerosol. For example, one could confidently say that bulk diffusional limitations should manifest for organics even at viscosities below the glassy state, and therefore at humidities higher than RH_g. In this way, the switch from thermodynamic to kinetic control can be determined quantitatively, as a function of the surface mass concentration of multiple different organic components. This is shown in Figure 7.5.3.

The absolute value of the fractional fC(RH) is an estimate of the mass loading established directly above the droplets surface as it recedes. If there is some saturation of the semi-volatile in the distant gas phase, C_∞, the equation 7.5.3 needs to be modified, to account for the different thermodynamic end point:

$$(fC - C_\infty) = \frac{da^2}{dt} \cdot \frac{\rho_{droplet} F_{svoc} \gamma_{svoc}}{2D_{gas}} \tag{7.5.5}$$

Once the particle phase activity of the semi-volatile approaches that of the distant gas phase, the outward evaporation rate will not change substantially. Instead there will be an equal and opposite condensation occurring that keeps the activities in dynamic equilibrium, meaning that the net evaporation rate collapses, and $\frac{da^2}{dt} \rightarrow 0$ as $fC - C_\infty \rightarrow 0$.

The predicted fC(RH) value divided by the saturation value (the intercept at RH=100%) indicates the extent of the kinetic limitation the organic experiences. In this case the initial mass loadings were set to 100, 10, and 1 μg m^{-3}. Every compound is found to be kinetically limited in its evaporation below an RH of approximately 50%. Those with a higher saturation C^* become limited in the evaporation in more humid environments.

Unexpectedly, the trend in mass loading of all compounds at a given κ value collapses onto one dependence at around 30% RH. This suggests that, once an SOA particle achieves a certain

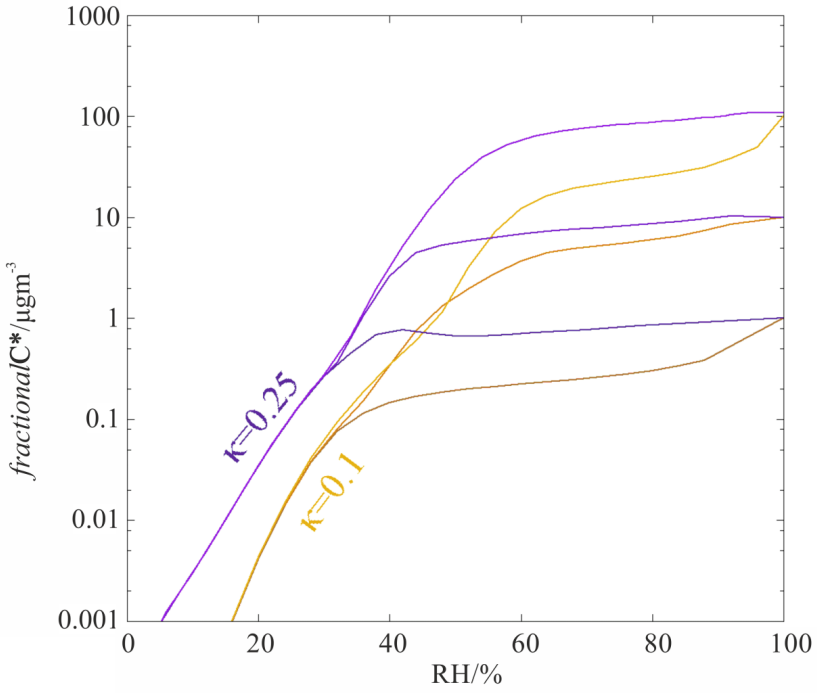

Figure 7.5.3: The modelled impact of humidity on mass loading of SVOC molecules evaporating from a 200 nm droplet. Viscosity is taken from a loglinear representation of toluene SOA from Song et al.[211] The pure component vapour pressures were defined to correspond to mass loadings of 100, 10, and 1 μg m^{-3}.

viscosity, its evaporation rate ceases to be strongly dependent on the inherent volatility of the organics evaporating. It should be noted that we have not accounted for changes in the density and molecular cross section of different volatility species, which may also influence the diffusional flux in a way that separates out the different curves.

A second set of simulations was done over a more extensive range of fC values, a slightly higher value of κ (0.3, towards the upper end of SOA hygroscopicity[339]), and a radius of 5μm. Otherwise, all model parameters were as above. The fit values of $\frac{da^2}{dt}$ are shown as a contour plot of RH against fC. The bulk limited regime was found to manifest at around 35% RH and was independent of the volatilities of the evaporating compounds, similar to the lower κ values in Figure 7.5.3. Conversely, at higher RH the gradients were highly dependent on volatility and surface concentration.

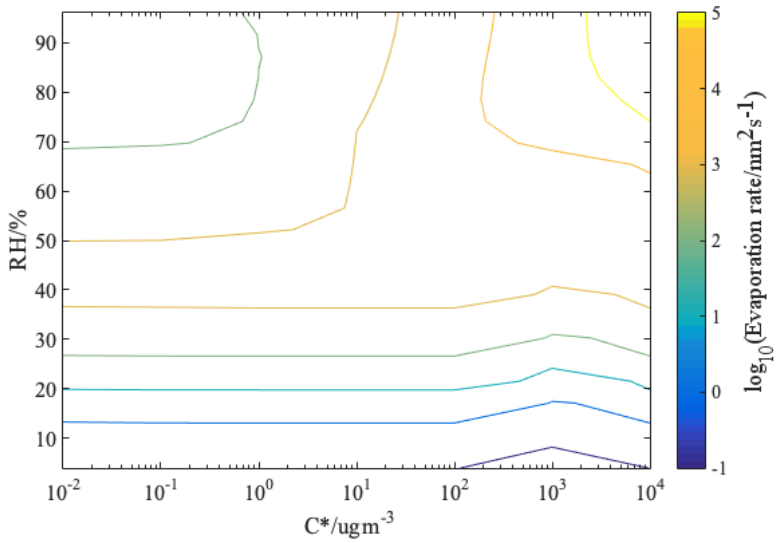

Figure 7.5.4: Evaporation rates of a 5μm SOA droplet, as predicted by KM-GAP.

In the top right corner, high volatlility and fast diffusion combine to produce the steepest gradient in surface area recession (~10^5 nm^2s^{-1}) and the time to reach equilibrium is of the order of seconds. In the top left corner, the gradient decreases slightly with increasing RH. It was determined that the effect can be accounted for by invoking Raoult's law: the initial radius remains constant at 5 μm and so the amount of SVOC in the particle decreases as the water activity increases (moving vertically). Similarly, the amount of the SVOC that wants to be in the gas phase at equilibrium decreases as one moves horizontally left (lower saturation). Combining the two effects in the gas diffusion limited state, we can say that the evaporation of a $C^* = 10^{-2}$ $\mu g\ m^{-3}$ compound will contribute less to the radius change in the 1000 s simulation at a high RH than at a more moderate RH, hence the decrease in rate in that corner.

The 'no man's land' where the volatility, water content and viscosity all balance can be found at C^* values of approximately 10^2-10^3 $\mu g\ m^{-3}$ and RH = 40 - 60%.

7.5.3 Observation of Kinetic Limitations Under Dry Conditions

What we wish to investigate is the path function type behaviour observed in the evaporation of viscous organic droplets in this regime. That is to say, the humidity that a particle currently experiences does not fully determine the rate of evaporation. In fact, the entire processing history of a particle since its emission (or formation) must be considered to fully understand the viscosity and particle phase concentration of semi-volatile species. If there is an influence of semi-volatile depletion on the observed evaporation rate, then comparisons of particles experiencing the same RH, but with different drying trajectories, will reveal it.

As a result of the resupply of the gas flow within the trapping cell in our laboratory experiments, there is no saturation of semi-volatiles within the immediate atmosphere of the levitated droplets. This maintains a continuous thermodynamic driving force for evaporation and the concentration of semi-volatiles monotonically decreases over time. The depletion is not an insignificant effect, especially when the particle viscosity is low. An upper limit of the rate of volatilisation can be determined as a function of a compounds vapour pressure using one of the equations from Chapter 2:

$$\frac{dm}{dt} = \frac{4\pi r M_{svoc} D_g}{RT}(p_{svoc}(r) - p_\infty) \tag{7.5.6}$$

where a is the droplet radius, M_{svoc} is the molecular mass and D_g is the gas diffusion constant. Assuming a 4.5μm droplet composed entirely of a single semi-volatile species whose properties are p_{svoc} = 10^{-3} Pa and M_{svoc}= 100 g mol^{-1}, the above equation predicts that approximately 14% of the droplet mass will be lost per hour.

In reality, viscosity increases by many orders of magnitude as the concentration of water approaches zero. This has the effect of limiting the resupply of semi-volatiles to the surface and quenching the mass loss. We have shown this by comparing radius data extracted from the Raman signals of optically levitated raffinose + malonic acid particles in different RH environments, in Figure 7.5.5. As the humidity decreases, the rate of evaporation also decreases.

While the surface concentration of organics is higher at 45% compared to 68% RH, in both

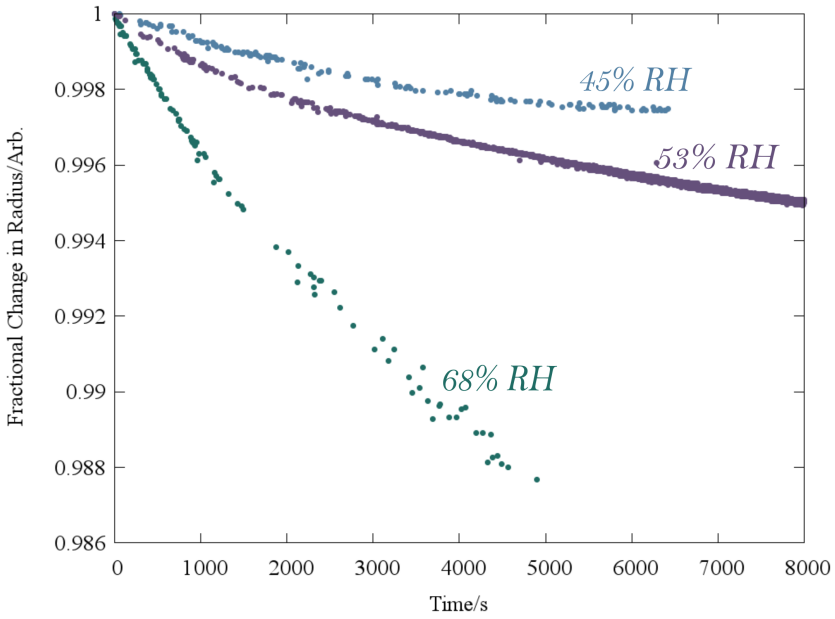

Figure 7.5.5: Normalised radius change profiles for malonic acid evaporating from increasingly kinetically limited raffinose particles.

cases this layer will be enriched in involatile species after a few minutes of exposure to the N_2 flow. If the initial viscosity is high enough, then once the outermost few nanometers of the particle are depleted of malonic acid, the surface becomes a 'crust' of sorts that increasingly traps the remaining SVOC molecules in the particle bulk.

The dataset from which these three radius curves originate contains experiments conducted in an aerosol optical tweezer at 14 RHs, between 75 and 38%, the latter of which is close to the glass transition humidity of the raffinose. Additionally, an experiment was conducted by Grazia Rovelli observing the evaporation of glycerol from sucrose particles levitated up to 10^5 s in an electrodynamic balance. Here our aim is to accurately predict the initial gradient and subsequent curvature of the particle radii during these evaporation events, and consequently to try to quantify the influence of varying the water content on the internal dynamics. The pure component vapour pressures of the semi-volatiles employed range from 10^{-2} to $4{\cdot}10^{-4}$ Pa, roughly corresponding to C^* values from 400 to 20 $\mu g m^{-3}$.

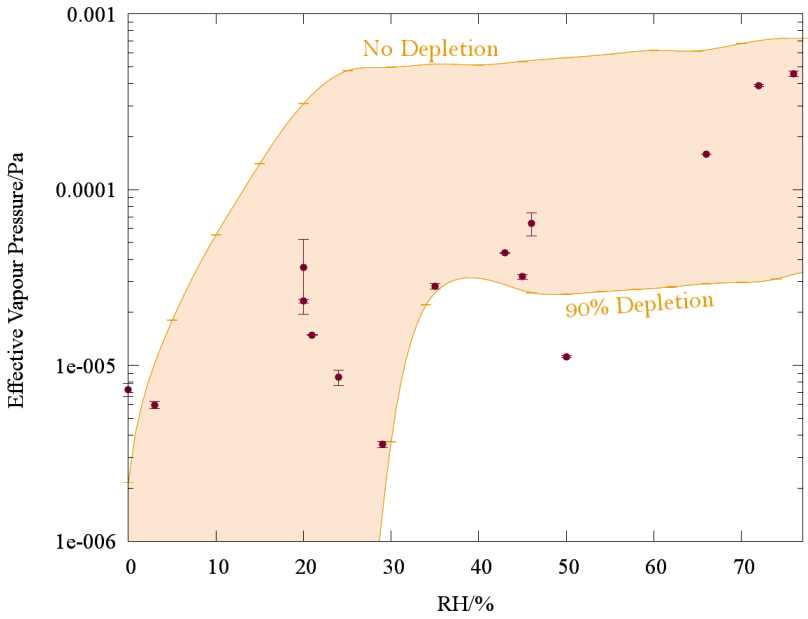

Figure 7.5.6: Comparison of observed (red) and predicted (yellow) humidity dependent vapour pressures of Malonic acid evaporation from sucrose droplets. The envelope is bounded by two KM-GAP simulations, beginning from extremes in starting composition.

Malonic acid evaporation from Sucrose

A gas flow removes evaporated SVOC from the trapping cell and maintains a background gas phase partial pressure that can be considered to be zero in the vicinity of the droplet. The gas velocity is sufficiently slow that no enhancement in evaporation rate from the droplet need be considered (i.e. the Sherwood number is ~2). Thus, in Figure 7.5.6 we report the RH dependence of the effective pure component vapour pressure, bounded by an envelope produced by the KM-GAP model for different limits of the starting concentration.. As the Raoult's law correction to the pure component value accounts for the unique mole fraction of malonic acid at each RH and after each transition, this normalising of the observed values allows meaningful comparisons to be made. Therefore, the ratio of the effective pure component to the pure component ($4.3 \cdot 10^{-4}$ Pa[341]) values can be used to quantify any kinetic suppression in the evaporation. Even though a pure component vapour pressure should remain independent of RH, the effective values for the vapour pressure show an approximate 2.5 decade suppression of the vapour pressure of MA as

the particle is dried. This is a broadly similar level of variance at low RHs to that reported in a previous publication from the group for the volatility suppression of maleic acid in aqueous maleic acid/sucrose particles and reflects the increasing kinetic limitation imposed on volatilisation as the particle becomes more viscous.[222]

One potential inaccuracy that may arise when examining inferred vapour pressures arises from the fact that particle composition, and hence viscosity, is continuously changing as volatilisation proceeds. Indeed, the magnitude of the diffusive limitation to volatilisation will change as the relative proportion of remaining SVOC changes. The degree of variance in the points between 20 and 30% RH in Figure 7.5.6 shows the magnitude of this effect: Each point is a unique single particle transition, with some droplets trapped and consecutively dried over multiple RH steps, while others were caught and rapidly dried just once. This necessarily produces a large degree of variation of both the pure component vapour pressure estimate and retrieved refractive index at any given RH. While the solution was prepared with a 5:1 molar ratio of the sugar to the acid, it was estimated using equation 7.5.6 that almost all of the malonic acid could evaporate within 3 hours of aerosolisation if the viscosity remained sufficiently low.

Therefore, the slow evaporation appears to be correlated with the conditioning history that the particle experiences, in addition to the composition of the starting solution and the ambient RH. With reference to thermodynamics, aerosol vapour pressure can therefore be considered a path function. One way to estimate droplet composition, and hence confirm this hypothesis, is to inspect the retrieved refractive indices. Calculated values can be found in Appendix C. When corrected for wavelength, they were found to mostly conform to the initial mole fraction, although some refract more strongly, which is indicative of an enhanced sucrose concentration. With that in mind, it could be hypothesised that particles in which less malonic acid has previously volatilised exhibit higher effective vapour pressures, due to a decreased diffusive limitation.[3] This trend leads to the spread in observed volatility for the five experiments with final RHs between 20 and 30%. The variance is also reflected by the KM-GAP modelling, with less malonic

[3] For reference, the refractive index pure sucrose in an amorphous lattice, n_{melt} = 1.5462[285]

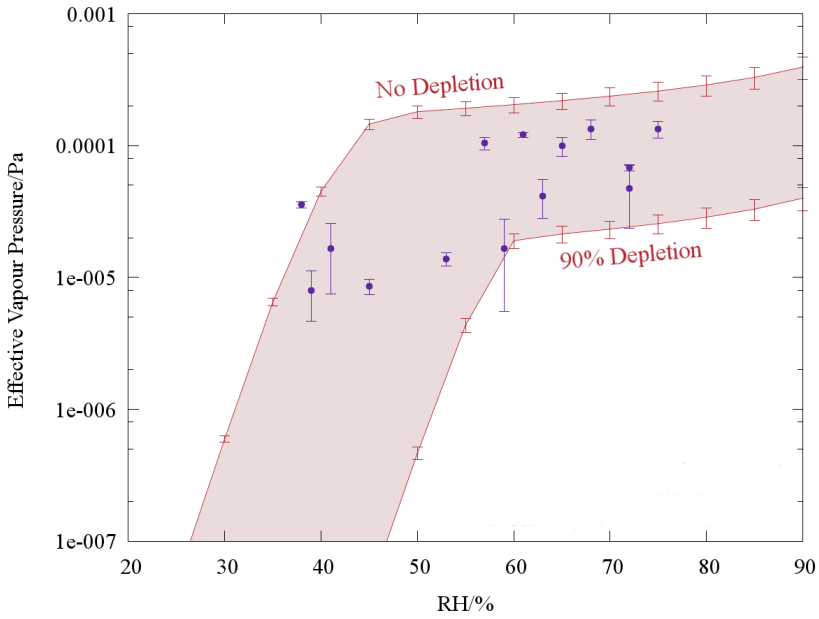

Figure 7.5.7: Comparison of observed (purple) and predicted (red) humidity dependent vapour pressures of Malonic acid evaporation from raffinose droplets. The envelope is bounded by two KM-GAP simulations, further details of which can be found in the main text.

acid present at the start leading to a slower change in particle radii, and hence a more suppressed vapour pressure at the droplet surface. It was found that a lower limit to the envelope of 90% depletion (25:1 sucrose:malonic acid) stretched over all but one of the experiments.

The non-monotonic change in predicted vapour pressure in the region of RH between 35 and 45% is an artefact of the interation between the viscosity mixing rule and the composition change in the model. In essence, the viscosity increase 'lags behind' the surface composition, leading to a small regime where the pure component evaporation slightly increases. Such behaviour is not physical.

Malonic acid evaporation from Raffinose

Figure 7.5.7 shows both the calculated and modelled malonic acid vapour pressure above raffinose particles, in much the same way as 7.5.6 above. Raffinose is a trisaccharide with a

larger molecular mass and as such raffinose particles should increase in viscosity more strongly, as a function of RH, than sucrose. The modelling confirms this more rigorously, with a steeper gradient of p_{svoc} versus RH predicted in the bulk diffusion limited regime. As was also the case for sucrose particles above, the 90% relative depletion bound (i.e. a 24:1 starting molar ratio) encapsulates the experimental data in the figure.

Returning to the experimental effective vapour pressures, they vary by just over a factor of ten between the highest and lowest humidities, which we can infer from the Bosse mixing rule corresponds to a change in viscosity of seven orders of magnitude. This six decade discrepancy between 'cause' and 'effect' may be due to a rapid surface enrichment of raffinose, leading to a surface viscosity increase that supresses the vapour pressure even at high RHs. This would not be detectable in the coalescence data as the viscosity determined is averaged over the entire volume of the particle.

Note that the pure component value of the malonic acid vapour pressure is $4.3 \cdot 10^{-4}$ Pa[341], which both the data and model converge to as the RH approaches 100%. The variance in observed values of p_{svoc} is also noticeable. In the previous chapter, and the methodology section of the accompanying paper[303], we proposed that increasingly saccharide rich (or in atmospheric terms, increasingly aged or oxidised) particles would be more viscous. Hence, they should evaporate more slowly at the same RH.

To assess the sensitivities of the model to these kinds of effects, intermediate contours were modelled for 30 and 60% depletion (Figure 7.5.8a). The lower starting concentrations tend to reduce the vapour pressures across all RHs simulated, as well as increase the RH range over which bulk diffusion limitations are observed. The influence of the uncertainty in viscosity on the predicted vapour pressure is also shown, in panel b. In contrast to the depletion study, the gas-to-bulk diffusion crossover seems to happen at approximately the same RH for both parametrisations, but

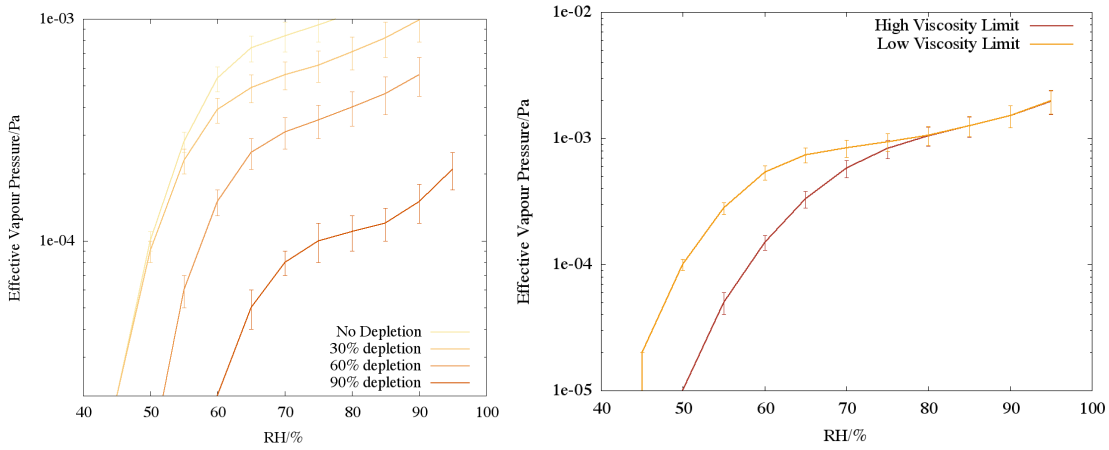

Figure 7.5.8: Predicted vapour pressures of malonic acid above raffinose particles under increasingly dry conditions. The sensitivity to (a) increasing levels of semi-volatile depletion from the initial droplet, and (b) the viscosity parametrisation are shown. All particles begin with a radius of 4.5 μm and a homogeneous starting composition. Error bars are propagated from uncertainties in droplet density.

is broader for the upper limit of viscosity. Predictably, the volatilisation is more strongly suppressed below the transition in the more viscous particle.

As discussed at several points in this thesis, water in viscous aerosol diffuses faster than the Stokes-Einstein relation predicts, sometimes by many orders of magnitude.[176, 184] The evaporative dynamics of the particles under consideration seem to reflect fast intraparticle diffusion of water in concert with slow diffusion of organics. Specifically, there is a range of intermediate humidities in which markedly different internal concentration profiles are observed for the two volatile species *during the same experiment*. The KM-GAP simulations of individual experiments where this occurs are found to reroduce the observed radius changes well. Figure 7.5.9 presents the clearest example of this phenomenon. A simulation was conducted of malonic acid loss from a raffinose particle at 53% RH, over nearly two hours.

Water loss was found to be limited by gas diffusion (i.e. it is rapid and occurs from everywhere in the particle at once), while a gradient is quickly established in the concentration of malonic acid (panels (b) and (c)). This is remarkable given that the water volatilisation is itself caused by the malonic acid loss – it is a co-evaporative process. The overlay of predicted and

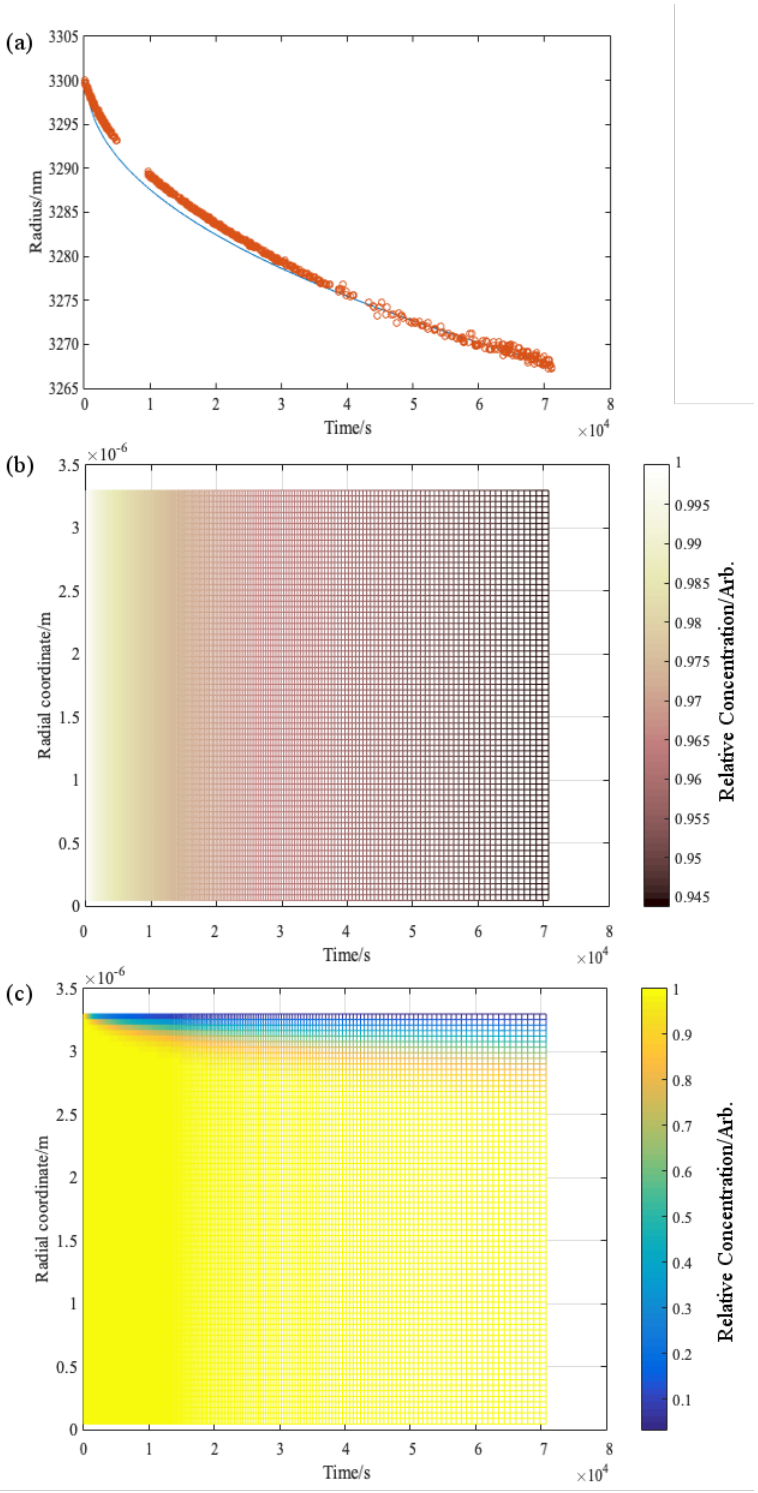

Figure 7.5.9: (a) KM-GAP prediction of the radius change (blue line) due to evaporation of malonic acid from raffinose particles at 53% RH. Bulk concentration gradients of (b) water and (c) malonic acid are also presented

observed radius is also shown, in panel (a), to prove that the model correctly predicts the experiment. This result is entirely consistent with a percolation theory type picture[277, 278] of internal water flux occuring along nanoscale channels that form between and around the larger sugar moieties as the particle dries. In such a situation, the water content can adjust very quickly to changes in the activity of the organics, even when the particle itself remains viscous.

Note that the colour scales for the latter panels are relative concentration in each shell, in molecules (or moles) per unit volume. Therefore the sucrose concentration concomitantly increases in the outer layers, as the acid evaporates, to conserve mass and volume. It is also worth noting that, even though the relative change is much smaller (5% versus 95%), the total amount of the two volatiles that leaves is similar.

A second example where this phenomenon was observed is at 45% RH, an experiment of shorter length (Figure 7.5.10). The initial ratio of the semivolatile to sugar was just over 10% depleted from the starting solution. This was determined by a simulating the ambient conditions experienced by the particle immediately before the experiment: 5000s at 77% RH.

In fact, similar improvements in the accuracy of the radius prediction are found when simulating multiple experiments consecutively. The approach is as follows: the mole fractions of the two organics are output at the final timestep of each simulation as a normalised ratio, excluding water (for example 0.65:0.35). A new viscosity is then calculated using the Bosse mixing rule (equation 7.1.2) for this ratio, which is multiplied by the parametrisations of raffinose and glutaric acid.[4] The volatilisation at the next humidity can then be simulated, using the previously determined organic composition and viscosity as the starting point. As before, the water content of the particle is determined from the model of Dutcher et al. at the new RH, and total organic content is scaled accordingly.

[4]Glutaric acid is a diacid of similar molecular weight to malonic, it only varies by the presence of two additional methylene (CH_2) groups. The viscosity profiles can be assumed to be very similar.

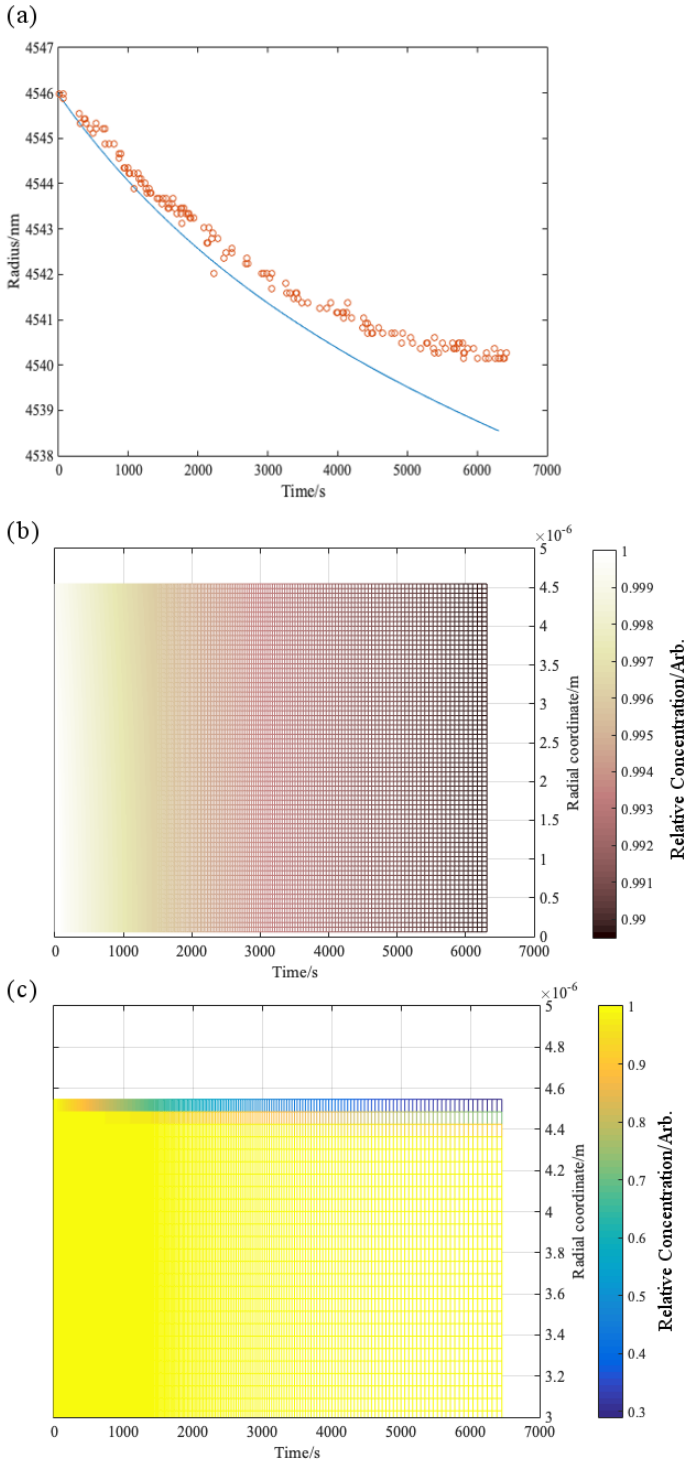

Figure 7.5.10: As in Figure 7.5.9, (a) KM-GAP prediction of the radius change (blue line) due to evaporation of malonic acid from raffinose particles at 45% RH. Bulk concentration gradients of (b) water and (c) malonic acid are also presented. Note that the y axis in panel (c) has been zoomed in, in contrast to 7.5.9c.

Glycerol evaporation from Sucrose

Glycerol is about 25 times as volatile as malonic acid, and the experiment conducted was substantially longer than previous, indicating that depletion of glycerol may play a more significant role here. This is illustrated in the radial profile of the evaporation of a droplet prepared at a molar ratio of 1:1 sucrose:glycerol (Figure 7.5.11), in which the interface recedes by several hundred nanometers over the course of the experiment. The data has a pronounced curvature, and appears exponential, or perhaps stretched exponential[315], in nature. This reflects a second order phenomenon whereby the flux itself changes in a time dependent manner. It was decided that a time dependent viscosity parametrisation was the most appropriate way to model the changes in composition throughout the experiment.

Unfortunately, the ternary viscosity prediction as presented in Figure 7.1.2 (green points) is not appropriate to insert directly into the kinetic modelling, using the Stokes-Einstein equation. It is not a smooth function of time, nor does it monotonically increase in every experiment. The region around 10^4 s in the 25% RH experiment (black triangles) provides an example of the latter: there are two strands that the solution rapidly exchages between as time proceeds. The true dependence is likely somewhere in between. The crucial drawback of using data in the 'raw' form is that there are many occasions where the magnitude of the predicted viscosity decreases instantly between two timesteps. Initially, the raw viscosity predictions were transformed using the equation (7.1.1) and inserted directly into the microphysics of KM-GAP, updating at every step to the nearest predicted value in time. Unfortunately, it was found that many step changes were being generated in $D_{glycerol}$ (t) and $D_{sucrose}$(t). This manifested itself in unphysical jumps in the predicted evaporation rates, and jagged regions in the concentration profiles. In addition, the ODE within KM-GAP became significantly stiffer and throughput was reduced whenever such an event was encountered.

It was decided that a lower resolution, smoothly varying function was required. A number of functional forms were tried, but it was found that a bi-exponential function reproduced the shape of the parametrisations most accurately. In each case the fit values corresponded to a rapid

increase offset by a slower decay.

$$\eta_{fit} = A \cdot \exp(t/\tau_1) + B \cdot \exp(-t/\tau_2) \tag{7.5.7}$$

The ratio of the two folding times was found to be 71.8, reflecting the fact that much of the increase in viscosity occurs early in the experiment, when the water loss still dominates. The radius data associated with much of this time period has been removed from the modelling but all viscosity data is included in the fitting process. The rationale for conducting the modelling in this way is that there may be residual influence of the early increase on the curvature of the later increase that persists throughout the experiment, and so fitting a monoexponential function would not accurately reproduce it. Additionally, the kinetic modelling can fail to evaluate the desired time series and stop early if too much water loss is experienced in the early timesteps.

The particles are also substantially larger than the tweezed particles described previously. Nonetheless, the KM-GAP simulation accurately reproduces both the initial gradient and the aforementioned 'folding' as the glycerol is depleted from the particle (panel (a)).

As in tweezers experiments, the 'raw' experimental data includes a regime where water is rapidly lost. A determination needed to be made of the crossover time point of the two regimes, after which it can be assumed that glycerol loss is the primary influence on the radius change. Due to the depletion effects, which themselves render the experiments an interesting modelling challenge, da^2/dt is no longer constant but instead changes through regimes. Some methods have been proposed to separate the regimes and identify when different compounds dominate the evaporation. A survey of recent literature revealed that Tikkanen et al.[342] solved a similar problem by defining a threshold for organic loss and excluding all data where the gradient was above its value: $\frac{da^2}{dt} < 0.1 \mu m^2 s^{-1}$. Here, the crossover was observed by plotting the full radius curve on a logarithmic time axis. The time scale was then rezeroed to that value and the model initiated there. The water evaporation can still be seen in the bottom left corner of the viscosity prediction (Figure 7.5.11, panel (b)), which also contains the smoothing function 7.5.7.

The KM-GAP radius change underpredicts and overpredicts the experimental data by tens

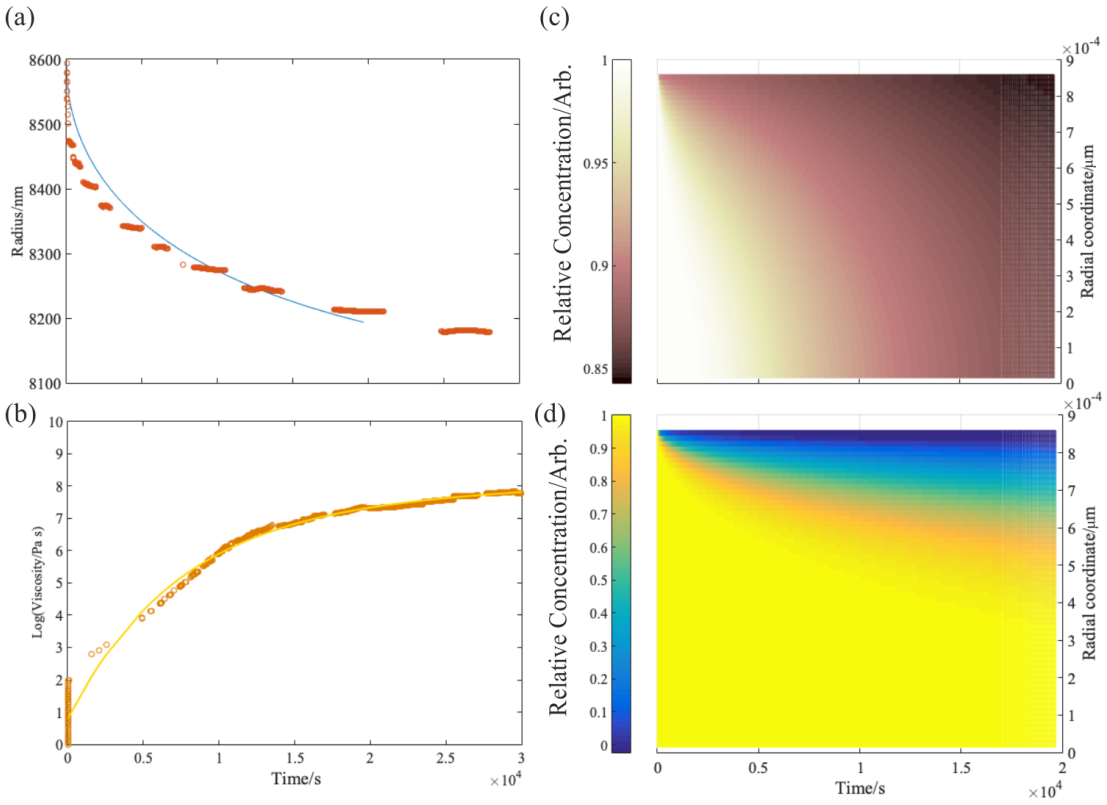

Figure 7.5.11: (a) KM-GAP prediction (blue line) of the radius change (orange points) due to evaporation of glycerol from sucrose particles at 25% RH. Electrodynamic balance data acquired from analysis of the phase function is shown in orange points. (b) Time dependent viscosity over the same interval: The Bosse treatment of sucrose and glutaric acid (orange points) was converted into a smooth function bi-exponential fit (yellow curve) before inclusion in the model simulation. Bulk concentration gradients of (c) water and (d) malonic acid are also presented.

of nanometers at different points in time (panel (a)), but generally captures the magnitude of the evaporation. It bears reiterating, however, that these simulations only rely on information that has been determined experimentally, namely the starting radius and the viscosity of the system. The success or failure of the approach, then, relies on the validity of the assumptions inherent to the model rather than the optimisation of the parameter space. We wish to understand the timescale over which evaporation takes place, rather than its precise thermodynamic end point. For this reason, in the previous chapter of this thesis, and in other publications within the group[303, 268], radii and predicted radii were converted into response functions (equation 6.4.5). The conversion

allows a comparison to be made between model and experiment without needing to represent the equilibrium state of the evaporation with complete accuracy, among other quantities.

The experimental data has regular gaps in time where no radii are presented, a result of the phase function fitting process in the electrodynamic balance[343], which causes perturbations in the extracted radius whenever the number of recorded peaks changes. This is not believed to impact the accuracy of the fit of any of the orange points in panel (a).

7.6 Conclusions and Outlook

The main conclusions from this study are that:

1. The diffusion kinetics of small organic components in SOA can be accurately described by the Stokes Einstein equation. The range of evaporation experiments that have been reproduced give us confidence in this statement. The particles vary significantly in the relative mole fraction of the semivolatile and its volatility. As a result the viscosity of the enclosing matrix, the absolute mass loss from the particles, and the timescale over which it occurs all vary over orders of magnitude. In this context, this Chapter and the previous compliment each others results. Indeed, the decreasing volatility of the compounds focused on in this chapter relative to Chapter 6 has helped the interpretation of the measurements I have taken: As the experiments became more complex, certain parametrisations, such as water diffusion in a ternary system containing a sugar and a small organic, had already been determined before the modelling was conducted. All that was needed was for the sigmoidal function to be 'slotted in' to the model microphysics and unnecessary fitting was avoided. Therefore the parameter space that needed to be explored was reduced.

In this sense, the methodology of optimising the model parameters to the data has been shown not be the only way to interpret the experiments: The fact that these results could be reproduced by the KM-GAP model with a small number of defensible assumptions also reveals that it is not always required to probe a multidimensional parameter space. Indeed, some aerosol transport models, and some implementations of KM-GAP, have become so complex that changes made to

the variables are coupled to one another in non-trivial ways. Unpredictability can then lead to unphysical solutions, or sets of contradictory solutions, that nevertheless reproduce experimental data (be it radius, concentration, or some other observable) to a high degree of precision. The remedy could be studies such as those conducted here, where parametrisations of existing aerosol data are incorporated into kinetic models with the purpose of constraining the freedom of any optimisation scheme.

2. Several of the results described above suggest there may be a set of atmospheric conditions in which the equilibration of SOA with ambient humidity will be thermodynamically controlled, yet the diffusion of organics within the same particles will be kinetically controlled. On the basis of the assumed viscosities of the particles, we predict that such a phenomenon will occur close to the transition region between the gas and bulk phase kinetic limitated states of the organics. In other words, the slowing of water transport, as modelled, is less severe as a function of humidity. Therefore the appearance of the kinetically limited regime lags behind that experienced by less volatile species.

Mathematically speaking, the lag in RH is a consequence of the curvature of the sigmoid function (equation 6.4.1), in that water diffusion eventually plateaus as the particle approaches a fully dry state, whereas the Stokes-Einstein equation is effectively log-linear with RH.[5]

Physically speaking, it is proposed that the above phenomenon is predictable, given the results already described in Chapters 2 and 5. Firstly, if the 'cavity hopping' type diffusion described in Chapter 5 is widespread, then it would be expected that the displacement that water molecules can achieve over a given time window will be significantly larger than the organics encasing them.[6] Observations by Price and Murray[185] lend further credence to the picture described above, in that they found the diffusion coefficient of sucrose to be several orders of magnitude smaller than that of water diffusing in the same droplets. Secondly, the fact that the rapid water adjustment was observed during a co-evaporation process also implies a diffusion

[5] depending on how viscosity is parametrised.

[6] The MD simulations described in this thesis corroborate a disconnect in the timescales of molecular motion between sucrose and water.

limited mechanism for the organic: The relative change in water activity as a function of the molar ratio of semivolatile to nonvolatile is quite small in comparison to the reduction in SVOC activity that occurs during the experiments. Therefore, only a small amount of water evaporation actually occurs (see Figures 7.5.9-11). With reference to the mixing times calculated in Chapter 2, the value of D_w probed in this chapter is faster than the largest probed in the modelling there, and hence could be content should always be able to keep up with the depletion.

3. Once the particles have achieved a sufficient level of drying, the range of observed evaporative fluxes can be explained quantitatively by a path function type dependence of viscosity on depletion. The KM-GAP predictions of sequential experiments have provided us with corroborating evidence, since the depletion predicted to occur in the previous 'conditioning' steps leads to more accurate simulation of the subsequent evaporation rate. Extrapolating into the atmosphere, such an effect would manifest most strongly in conditions where organic aerosol undergo glass transitions, namely low temperature and/or RH conditions[147]. However, what is beginning to be uncovered in this diffusion modelling is a more complex picture of the *evolving* viscosity. It may be that dynamical changes in size distributions, the intraparticle mixing times and eventually mass concentrations of SOA plumes will be altered by depletion effects throughout their lifetime.

It should be stressed that the complexity described here is not a function of whether the evaporation is thermodynamic or kinetic in nature. Rather, it seems as though there is not always a one-to-one mapping of external conditions to evaporation rate, and in fact the conditioning a particle has experienced throughout its lifetime is crucial to its properties in a given atmospheric situation.

Chapter 8

The Optical and Physical Properties of Laboratory Generated Secondary Organic Aerosol

"It is possible to commit no mistakes and still lose. That is not a weakness, that is life" - Jean-Luc Picard

---

8.1 Motivation

The study of how reversible vapour exchange processes are, and on what timescale, is thought to be a key uncertainty in our ability to predict the fate of organic aerosol mass[103]. In recent years, intense research has focused on the role of gas particle partitioning both in particle nucleation[52, 344, 54] and later in the lifetime of organic particles[345, 346]. Evaporative kinetics of this form can be considered as an interplay between viscosity and vapour pressure. The experiments described in previous chapters revealed that under the right conditions even relatively small,

water soluble organic molecules can become trapped almost indefinitely within droplets. The array of molecules produced by the oxidation of α-pinene, by contrast, is likely to be even less well behaved: Many species can be produced that are involatile, insoluble and highly reactive, and their yields appear to be sensitive to changes in humidity[223], nitrogen[347] or sulphur[348] concentration.

The early stages of the ozonolysis mechanism have been shown in the Introduction, stopping at the formation of the stabilised Criegee intermediate. A more full, but still incomplete, scheme is presented in Figure 8.1.1. Assuming no N, S or H_2O is present, as will be the case in these experiments, there is a competition between several reactions: the HO_2/RO_2 channel, the autoxidation (reaction with O_2) channel, and dimerisation through reaction with the parent VOC. Most of the compounds can decompose, by loss of a single oxygen into a hydroxyl radical. Depending on the residence time of the hydroxyl species in the trapping cell, a series of new hydroxyl reaction channels may open up for most of the species presented. The relative probability of autoxidation, compared with dimerisation and intermolecular rearrangement, will depend on the oxygen concentration. Dimerisation, and even oligomerisation, are thought to be likely reaction channels here as the VOC is in excess relative to ozone. It is also worth noting that only one product of the ozonide bond cleavage is shown here; a comparable scheme can be produced where the Criegee has formed on the other carbon (where the aldehyde resides in this scheme). Additionally, the green dimer species in the bottom left can decompose in the same way as the original ozonide, opening the possibility of further autoxidation.

Smog chamber studies have begun to investigate different conditions[146], or sequences of conditions that SOA may experience in the atmosphere[167], for instance updrafts that may cool and humidify the particles as they ascend[111]. Unfortunately, some chambers do not allow frequent determination of the particle radii during the experiment, as they operate in batch mode when sampling the evolving aerosol[301]. Optical tweezers do not suffer from this drawback, and so offer a unique opportunity to study a crucial phenomenon in a highly time resolved manner.

Here we have initiated the production of a large concentration of first generation oxidation

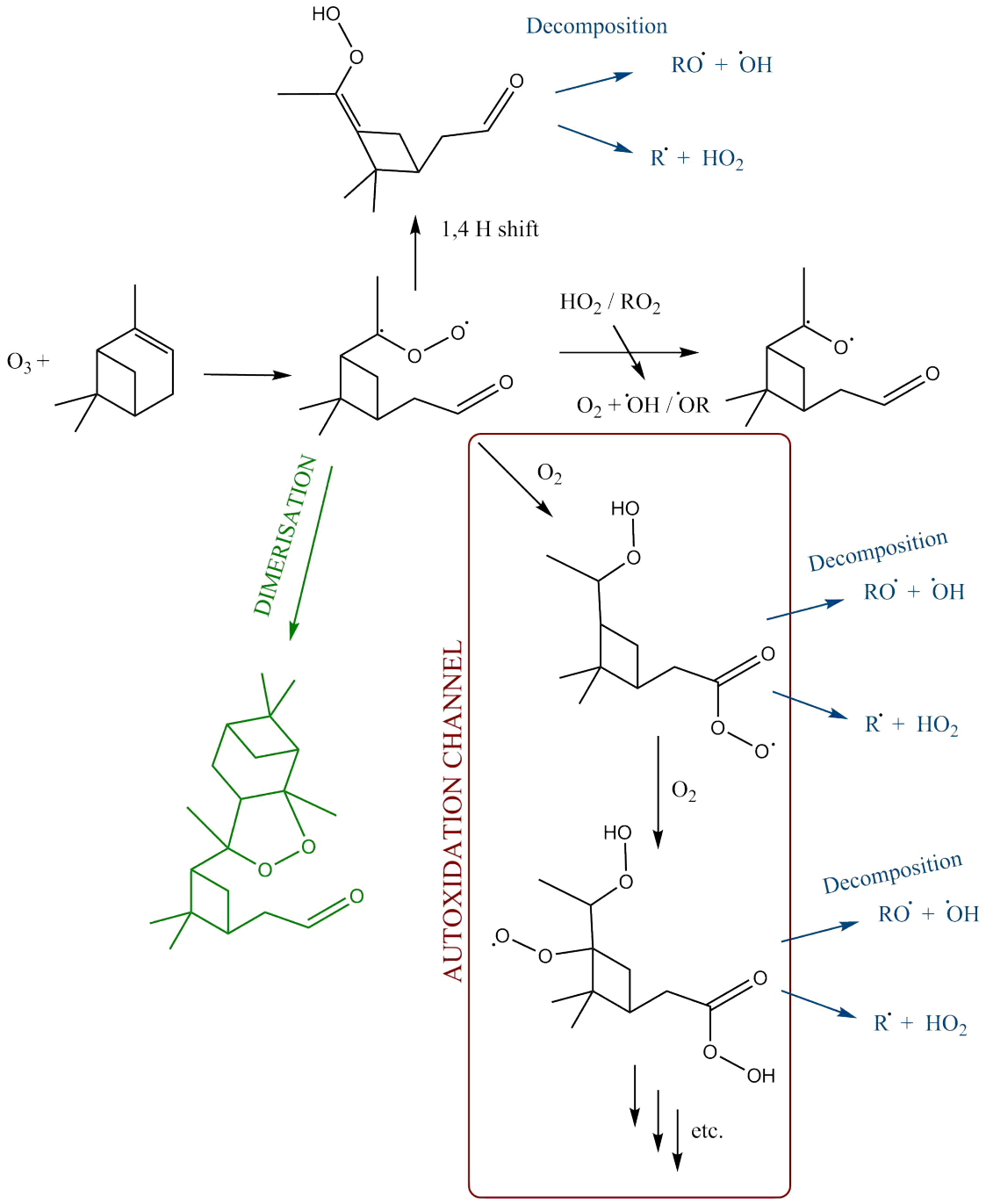

Figure 8.1.1: Simplified reaction map of the possible reaction pathways available during the ozonolysis of α-Pinene.

products of the monoterpene α-pinene *in situ* within an aerosol optical tweezer instrument. The products are likely to be a complex array of oxygenated organic molecules of varying volatility, which will be a much closer approximation to the 'true' dynamic behaviour of SOA than any of the experiments described thus far.

Every experiment described herein was conducted by myself, and the results have yet to be published elsewhere at the time of writing.

8.2 Development of Experimental Procedure

8.2.1 Gas Phase Chemistry

The intention of the experiments was to achieve consistent oxidition of α-pinene by ozonolysis over a period of several hours. Compounds from the product distribution can then condense onto the surface of a levitated seed droplet within the air mass. The procedure can be considered a model of a two-step mechanism of particle formation and growth in the atmosphere[349]: a small cluster of inorganic molecules nucleates, followed by rapid condensation of organics to grow the particles. It is also akin to injecting aqueous aerosol as a seed to initiate condensation, a common tactic in smog chamber measurements[166, 350]. Finally, the volatilisation will be assessed by determining the time evolving radius of the multiphase seed + SOA particle.

Whilst these experiments were being conducted, a bespoke optical trapping cell was described by Gorkowski et al.[236] in the literature. The design allows a very similar procedure to be carried out, forming multiphase particles by condensation. It was designed with specific attention paid to the fluid dynamics of the condensable vapours. Since then, preliminary experiments were conducted with the apparatus[237] investigating evaporation of organics through an SOA shell deposited on a trapped particle. Our setup differs in that it has a much smaller internal volume and operating flow rate, but the principles by which the reactant gases are mixed and the condensational growth is probed from the droplet Raman signal are nearly identical. The reader is therefore directed to the Gorkoswski publications if they wish to see a more refined version of

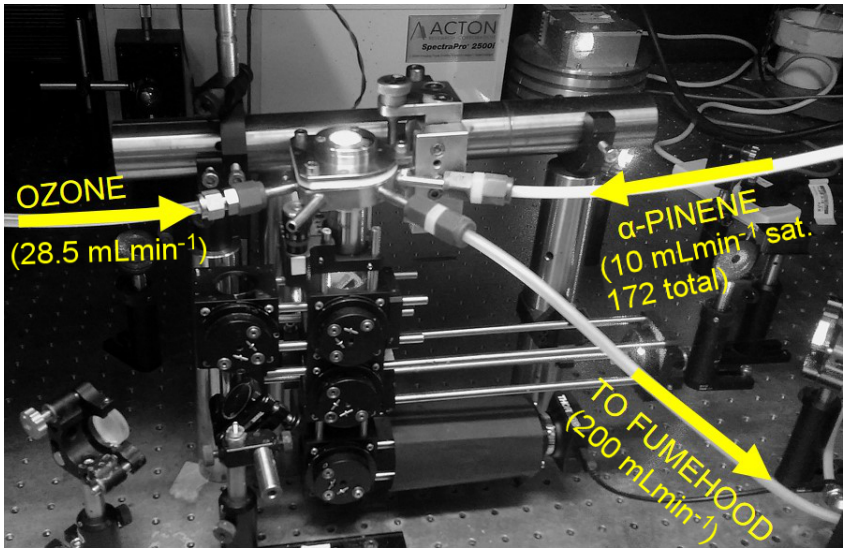

Figure 8.2.1: Gas flow configuration for α-pinene oxidation experiments. Note that the stated α-pinene flow is the saturated value, which is then diluted by dry N_2 to ensure an overall flow through the trapping cell of 200 $mLmin^{-1}$.

this type of experiment.

The precise control of gas phase conditions in our optical tweezer apparatus allows the ozonolysis reaction to be ceased on a timescale of seconds. The organic coating then experiences a nitrogen gas flow with a zero partial pressure of organics, driving the evaporation of volatile components. The effect of differing particle and vapour phase conditions on the remaining organic molecules is then observable in the evolving dynamics of particle radius. It is possible to perform oxidation reactions in and/or around the levitated particle.

Since water is not believed to be a reactant in the oxidation mechanism[51], or at least to not significantly change the product distribution[351], a decision was made to conduct these experiments in a dry gas flow. This was also convenient as there were insufficient inlets to the trapping cell to allow air, humidified nitrogen, ozone and α-pinene to all be mixed simultaneously. Therefore, the procedure relies on keeping the seed droplet trapped and completely dry before the reactants can be introduced.

It was decided that the initial ('trapping') RH should be as close to zero as possible: the faster the initial drying, the more time available for condensation and further analysis. However,

in practice low trapping humidities induce rapid evaporation, which can destabilise the droplets within the trap if the laser power is not adjusted fast enough. This is especially prominent in inorganic seed particles, which tend to evaporate in a gas diffusion limited manner. A compromise humidity that minimised drying time while keeping the droplets stable was found to be 55%. Seed particles were trapped at this RH as described in the experimental chapter, and then dried to 0% RH over in either one or two step changes. After each step, evaporation occurs and the particle surface is allowed to regain equilibrium with the trapping cell conditions, as determined from the motion of whispering gallery modes across the spectrum.

Once the outer surface of the droplet is dry, humidified nitrogen is exchanged for α-pinene saturated nitrogen (5%, corresponding to approximately 290 ppmv) by replacing the glass bubbler leading into the trapping cell. α-pinene was purchased from Sigma Aldrich ($\geq$99% purity), and ozone was generated photochemically as described in Section 3.1.1. During the experiments, the observed concentrations of ozone varied substantially between experiments (30 - 80 ppm), but were found to stay relatively constant within each experiment.

8.2.2 Droplet Raman Spectroscopy

If the seed particle was sufficiently viscous, the core and the condensing shell remain separate phases with a defined boundary in composition. As a result, the Raman scattering pattern produced by the seed particle as condensation occurs will reflect the relative radii of the two concentric spheres that are forming.[234] The positions of stimulated whispering gallery mode peaks within each droplet Raman spectrum are a unique signature of its internal structure[352]. This allows determination of the time dependent thickness of the organic shell: They are compared to Mie theory predictions to accurately extract the radii and refractive indices of the two phases, as described in section 3.2.3. In the limit where the outer shell width is significantly larger than the wavelength of the excitation source (532 nm), a levitated core-shell morphology particle may be treated as 'all shell' for the purposes of Mie fitting[229], i.e. a homogeneous sphere comprised entirely of the outer layer. Clearly, this assumption greatly simplifies the postprocessing

of recorded Raman spectra. In the intermediate regime, where the layer is thinner than the depth from which the observed whispering gallery modes are scattered, a more complex fitting algorithm is required. Here the model of T.C. Preston was utilised. Wherever figures are presented containing radii arrived at from both homogeneous and core-shell fitting methods, they will be coloured differently to aid in interpretation.

8.2.3 Choice of Seed Particle

In smog chamber studies, a high concentration of droplets is usually introduced at controlled intervals to catalyse the condensation process[148, 65, 353]. These aerosol are usually referred to as 'seed' droplets within the literature, however their function is somewhat dissimilar from that of the particle accepting SOA in this case. Aqueous ammonium sulphate is often used[302], given the important roles of both the anion and cation of that molecule in atmospheric chemistry and new particle formation.

The results described herein were conducted with both raffinose and sodium nitrate droplets. The two compounds have both been found to succesfully accept large amounts of condensing SOA molecules (and submicron particles) from the gas phase, whilst remaining stably trapped in otherwise dry nitrogen. However, the viscoelastic properties of the initial (dry) particles are substantially different, and worth comparing.

Raffinose: The main advantage raffinose aerosol posesses is its extraordinarily high viscosity under dry conditions, achieving a solid, glassy state at approximately 40% RH[139]. This gives us a very high level of confidence that any organic molecules colliding with the surface will not diffuse into the bulk and there will remain a sharp phase boundary between the seed and the shell. The intense bulk limitation to water diffusion up to the surface when drying the seed also means that the mass losses are slowed. From an experimentalist's standpoint this is useful as the laser power will not need to be adjusted rapidly or frequently to keep the droplet trapped.

The main drawback of the use of raffinose as a seed is that, under dry conditions, the spontaneous Raman signal scattered from the droplet core contains a broad, intense C-H band. This

makes it difficult to assess the extent of condensation, as the SOM C-H bonds will scatter in the same wavelength range (626 - 636 nm). A purely inorganic seed particle would remedy this, as by definition no C-H bonds will be present other than the condensing SOM.

Sodium nitrate: Aerosol containing metal nitrate salts were seen as an ideal candidate as they appear to be unique among inorganic aerosol in retaining their sphericity when dried; almost all other salts crystallise once the solute concentration exceeds its bulk saturation value[354]. Nitrate salts act more like organic compounds and form semi-viscous (10^3 Pa s) matrices upon drying. A lower viscosity implies a less defined phase boundary and the absorption of some of the condensing molecules into the bulk. It can be assumed that the growing SOM layer to have a dry viscosity of around 10^8 Pa s[144], and so some collective rearrangement of the two phases may take place on the timecale of the experiment. $NaNO_3$ scatters photons in a number of regions below 600nm in the Raman spectrum, allowing some crude estimates of the relative concentrations of water, organics and nitrate to be made, as there is a strict separation between the three.

8.3 Atmospheric Relevance

The use of single particle techniques to investigate atmospheric aerosol is, in general, difficult to rationalise if one's objective is to precisely replicate the conditions they experience in the atmosphere. Experiments designed to inform the literature on SOA are especially sensitive to these effects. Very soon after emission or formation, a plume of aerosol becomes a highly interconnected system where changes to one aspect very quickly have repurcussions on the others. Considering processes such as particle coagulation, or the complex gas phase chemistry that occur in the gas phase, it becomes clear that some of the the quantities measured need to be scaled to relate observations made on optically tweezed droplets to the Earth's atmosphere. It is also worth noting that the larger volume of the particles trapped in this thesis necessarily slows the intraparticle mixing times, which was first discussed during (and can be quantified using) the modelling studies described in Chapter 2.

Firstly, it should be stated that the experiments conducted here can be thought of as an extension of the ternary component work of Chapters 6 and 7, rather than the smog chamber works of (for instance) McFiggans[70] or Yli-Juuti[301]. It may therefore be that the pertinent question we should be asking is 'how does the evaporation rate of lab produced SOM compare to that of glycerol from sucrose?' rather than 'how does the evaporation of lab produced SOM compare to that of SOA in the atmosphere?'. However, since much of section 8.5 will address the former, it was deemed worthwhile to spend some time considering the latter.

This section will be divided into two parts. First, the reactant concentrations used will be discussed and justified, with reference to published rate constants for the reactions of α-pinene and its first generation Criegee intermediates. Secondly, other atmospherically abundant molecules will be discussed, along with the potential impact of their absence in this study.

8.3.1 Effect of High Mass Concentration

With regards to the absolute values of reactant concentrations used in this work, it should be noted that they are several orders of magnitude higher than would ever occur in the atmosphere. This is often the case in publications seeking to study α-pinene ozonolysis spectroscopically, or with other analytical methods.[48, 355] Additionally, the previously referenced studies also use an excess of α-pinene, in contrast to smog chamber studies, where the oxidant is the major reactant by volume fraction[356].

The high gas flow means that the reactants are continuously replenished, and the products are only present in the atmosphere of the droplet for a short time, before they are carried into the exhaust line. Therefore, novel chemistry, or molecules with anomalously high levels of oxidation, were unlikely to be accessed in the apparatus. As shown in Figure 8.1.1, the first reaction product of α-pinene and ozone will be a primary ozonide, each of which will decompose into a Criegee intermediate and an OH radical. They will then undergo either further ozonolysis, dimerisation, or autoxidation. If a mean residence time of 30 s within the trapping cell is assumed, it is possible to estimate the turnover of primary ozonides within this timeframe.

Current literature has observed the second order rate coefficient of the reaction to be approximately $8 \cdot 10^{-17}$ cm^3 $molecule^{-1}$ s^{-1}[357, 358]. Assuming that only 80 ppmv of the α-pinene reacts (ie. equal to the amount to the ozone in the chamber) at a temperature of 296 K, the turnover rate is calculated as ~0.159 s^{-1}, or a unitless yield of 4.76 in 30 s, before the reactants and products are completely replaced. This was compared to the same calculation made for some recent smog chamber studies, which have residence times on the order of hours: Bell et al.[359] reacted 200 ppbv of α-pinene at 298 K for 1.5 hr, generating a unitless yield of 2.156. Huang et al.[167] reacted 0.714 ppmv α-pinene at 223 K for 3.5 hr, or a relative yield of 9.873, which is significantly more. In this context, it can be claimed that the high gas flow mediates the high turnover somewhat. As judged from the change in ozone absorbance, a steady state is formed within the trapping cell soon after the reaction starts, after which product concentrations stay relatively stable.

Therefore, the condensing molecules are unlikely to be radically different from those generated in the referenced studies. If they were then buried by further condensing molecules, the growth mechanism would be very similar to that described by Perraud et al.[349], namely it would create a surface layer of similar density and refractive index to submicron α-pinene SOA. Additionally, discounting wall loss or loss onto the coverslip, the only available surface for the SOA generated to condense onto is one single seed droplet. The gas-particle equilibrium is therefore heavily shifted towards the gas phase, so much so that conducting this experiment closer to atmospheric concentrations would not be feasible: the time required to condense enough matter for any statistically significant results to be achieved would simply be too long.

8.3.2 Changes in Radical Chemistry

One aspect of the gas phase chemistry occurring that is uncertain in these studies is the role played the hydroxyl radical. As shown at the beginning of the current Chapter, the production of ·OH is a common decomposition pathway of a Criegee intermediate. The radical itself can then act as an oxidant, and as well as participate in radical chain reactions with other atmospheric

molecules, eventually forming even more radicals. While ozone exists at a higher concentration in the atmosphere than hydroxyl, it was expected that the production of the radical from the stabilised Criegee species[360] in the second step of the oxidation would probably influence with the product distribution. The absence of NO_x species, which can intercept Criegee species before hydroxyl formation and react competitively in the atmosphere, is also a contributing factor.

Quenchers, which are molecules that react readily with hydroxyl and form stable closed shell molecules, but leave the rest of the oxidation chemistry unperturbed, are often used in the literature to overcome this uncertainty. However, a review of smog chamber studies revealed that common quenchers, such as cyclohexane[361] and 2-butanol[356], need to be introduced significantly in excess of the monoterpene VOC if they are to be effective. Therefore, if they were to be used in this study, we run in to the same problem as the mass concentration: introducing cyclohexane in a similar reactant ratio would require a bubbler solution with a significantly lower α-pinene concentration. As before, this would reduce the turnover of SOM and slow the accretion rate into the probe droplet.

It is a difficult balance to strike: involatile molecules tend to form most efficiently by autoxidation. Autoxidation requires C-H bonds to be cleaved by the hydroperoxide radical on the Criegee (see Figure 8.1.1), which is the first step towards hydroxyl formation.[362, 45]

8.4 Optical Properties of SOM

A number of factors were considered early on regarding which spectroscopic information to record during the experiment, and which specific SOM properties to investigate. It was decided that a wider Raman spectrum than is usually recorded may able to provide some information on functional groups present in the condensing mass. It was also found that extraction of refractive indices of both the seed and coating during the radius determination remained possible, which was believed to be of use to the wider literature.

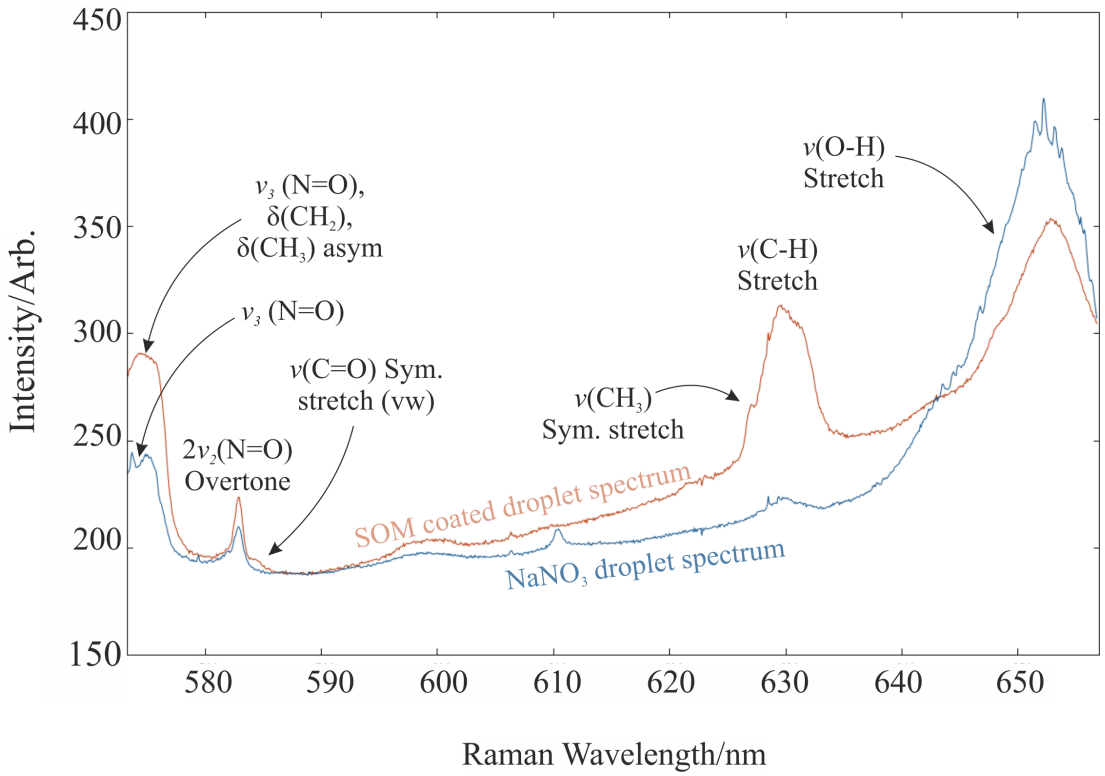

Figure 8.4.1: Comparison of wide grating Raman spectra of a sodium nitrate droplet with and without a coating of α-pinene SOA, alongside attributed Raman active modes and the associated functional groups.

8.4.1 The Raman Signature

The Raman spectrum of a sodium nitrate droplet is presented in Figure 8.4.1. A time interval of one hundred adjacent spectra, corresponding to two hundred seconds of spectrograph exposure, were averaged in order to remove the whispering gallery modes. The observed peaks have been assigned to the constituent moieties - water, nitrate ions and SOM molecules. Comparison of the seed and coated seed spectra reveals that a broad peak centered at 629 nm grows in, with at least one shoulder peak at a wavelength of 626 nm. Additionally there is a weak shoulder peak to the 583 nm nitrate peak at approximately 584.5 nm. It was initially hypothesised that this peak arose from the $\delta(H_2O)$ bending of a small amount of residual water in the particle, but the seed droplet spectra was recorded under dry conditions and so it should have either been present

in either both spectra or neither. It can therefore be said with some confidence that this peak is statistically significant as it appears in every experiment conducted using the wide spectrograph grating. A Raman shift of this value (~581-588 nm) corresponds to some form of carbonyl functional group, although its chemical identity is difficult to determine: It could be a saturated ketone, saturated carboxylic acid or an aliphatic aldehyde, as they all fall in that range.[1]

Another change in intensity that occured during the condensation, rather than appearance of a new peak, was the increase in the peak centered at ~574 nm. It was found that medium intensity peaks from the symmetric bending of methylene and the asymmetric bending of methyl groups resonate in this position[363]. Intuitively, it is unlikely that the methyl groups, or most of the methylene C-H bonds of α-pinene will be reactive with respect to ozone. So, we should expect their wavelengths to stay constant in both reactant and product, and that is exactly what is observed.

A fortuitous occurence provided an opportunity for additional information about the optical properties of the organic matter: During an otherwise unrelated condensation experiment, a sub-micron particle which had nucleated inside the trapping cell became caught in the laser beam whilst diffusing along the surface of a bulk water layer on the coverslip. Enough scattering was detected that the particles C-H band was observed as a shoulder to the intense O-H band of the aqueous solution. Figure 8.4.2 compares it with the α-pinene C-H peaks.

A pronounced red shift was observed in the product versus the reactant. This suggests the majority of the bonds experience a higher level of electron density in their immediate environment than in the parent monoterpene (for reference, the 634 nm peak is likely the hydrogen bonded to the alkene). From this we can conclude that the SOM has a greatly enhanced number of vinylic (sp^2 hybridised) bonds, alkyl (sp^3hybridised) groups, or simply a high degree of oxygenation of the backbone. This suggests a high degree of autoxidation is occuring in the trapping cell[364], perhaps leading to lower volatility molecules with multiple units of molecular oxygen added to them. The peak at 627 nm appears in both spectra and can be assigned as the methyl stretching

[1] Additionally, all three are only expected to be very weakly active in the Raman spectrum.

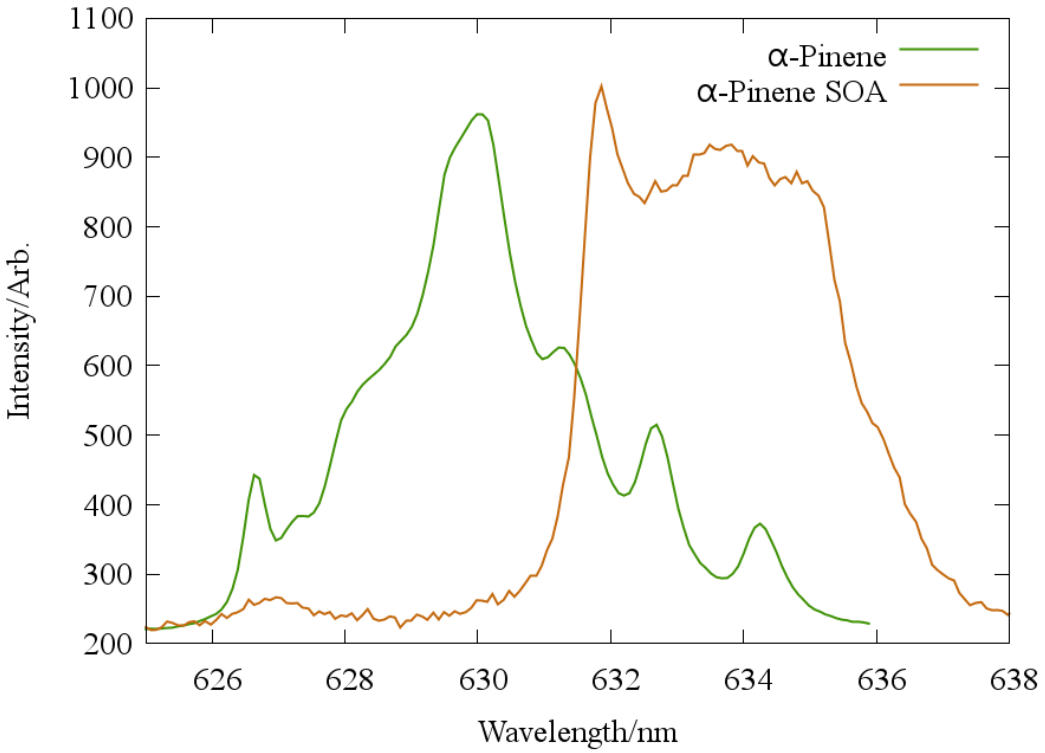

Figure 8.4.2: Comparison of scattering by C-H bonds observed with a Raman spectrometer. Green: bulk α-pinene deposited on a coverslip. Orange: a lab nucleated particle on the surface of deoinised water.

mode of the dimethylcyclobutane group[2], whose hydrogens are completely inert to reaction with ozone, and at least three bonds away from any site autoxidation could occur.

8.4.2 The Refractive Index

Very few measurements have been made of the refractive index of SOA thus far. The core-shell Mie theory algorithm returns the refractive indices of both phases with each fit spectrum, which offers a unique opportunity to augment the existing literature.

The scattering functions within the Core-Shell code estimate the refractive index of the shell at the center wavelength of each spectrum, and then use that to predict WGM positions. A combination of different spectrograph gratings have been employed in these experiments and the

[2] ν =2850 cm^{-1}

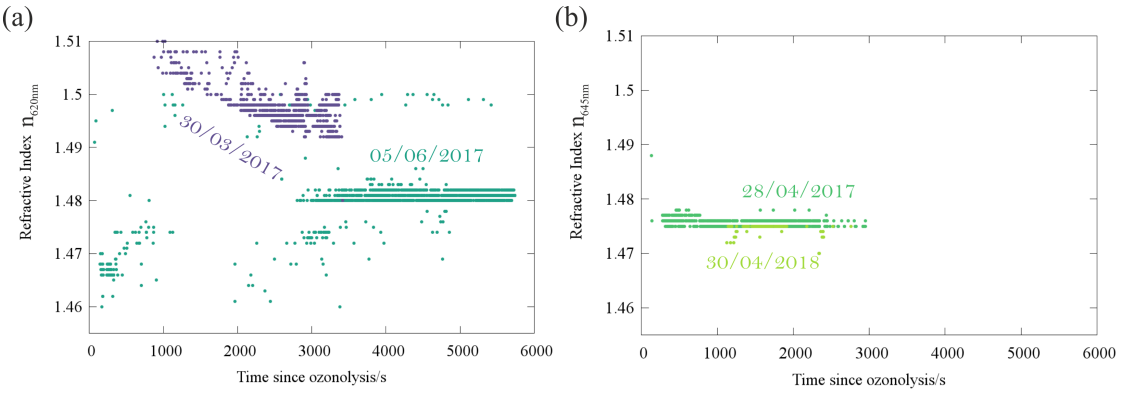

Figure 8.4.3: Retrieved refractive indices of α-pinene SOA in dry air, using core-shell Mie theory. (a) 620 nm midpoint spectra. (b) 645 nm midpoint spectra.

resultant spectra successfully analysed with Mie theory, allowing a determination of n for the organic coating at two wavelengths, 620 and 645 nm. Four sets of fit values are presented here, each from a different condensation and re-evaporation experiment under dry conditions (more on that in the next section). The time axis has been normalised to the moment the ozonolysis reaction was ceased. There are a few features to note here. Firstly, only in one of the experiments does n increase as the evaporation proceeds. Of the others, two remain effectively constant and the third decreases with evolving time. Such variability may be reflective of the fact that each experiment involved a slightly different gas concentration of ozone, as well as condensation time, meaning it is difficult to directly compare like with like. Secondly, note the discrete nature of the values of n adopted in some fits. Some resolution was sacrificed during the fitting process to increase throughput, as there is a much larger parameter space for a core-shell algorithm versus homogeneous Mie theory[234, 232]. Nonetheless, the range of the observed values is actually quite good in comparison to much of the existing literature[98](and Table 2 therein).

While there is some noise present, we can say from these data that $1.47 < n_{645nm} < 1.48$ and $1.48 < n_{620nm} < 1.50$, which is consistent with the behaviour of the dispersion Equation 3.2.18, namely that n should increase at lower wavelengths. To the best of my knowledge, this is the first measurement of the refractive index of α-pinene SOA at 620 nm. The stated range of n_{645nm} is consistent with the only other value that appears to have been calculated at this wavelength

which was 1.473±0.003[237]. The closest wavelength studied in the literature for the α-pinene ozone reaction was n_{670nm}, whose value was found to vary between 1.43 and 1.54, depending on particle radius[365].

8.5 Reversibility of Gas-Particle Partitioning

Different observations can be used to determine that the condensation was occurring in each experiment. Firstly, non concerted motion of whispering gallery modes to higher wavelengths is oberved, which suggests an increase in radius as a core-shell is forming. Underneath the stimulated peaks, it is possible to probe the rate of the condensation process using the integral under the *spontaneous* peaks. An example of changes in the aliphatic C-H resonance (625-635 nm) in a set of superimposed spectra is shown in panel (a) of Figure 8.5.1, overleaf. Assuming no C-H band is present in the seed droplet spectrum, the growth of the peak is indicative of the shell thickening. It can be determined that α-pinene was not itself condensing onto the droplet by inspecting the integrated area of the region 635-638 nm. Any scattering between these wavelengths would correspond to a vinylic (sp^2 hybridised) C-H bond, which would be present in the reactant but not the products.[3] Within the range of the fluctuations, there is no increase in intensity during the condensation process.

Finally, larger increases in the size of the trapped particles can be observed using the CMOS camera. A representative example of the rate of mass accretion is also provided below, showing two images of a particle before and after exposure to the ozonolysis reaction for approximately 1.75 hr (panels (b) and (c)).

Once it was determined that a significant amount of organic matter had condensed, the ozonolysis was discontinued, and the droplet exposed to a combined flow of air and dry nitrogen. The gas flow rate was high enough to remove any reactants from the atmosphere surrounding the resultant particle in one minute. It was hoped that the surface organic layer would then begin to

[3]It should be noted that the saturation vapour pressure of α-pinene, ~630 Pa, is sufficiently high that a negligible amount will condense unreacted[221].

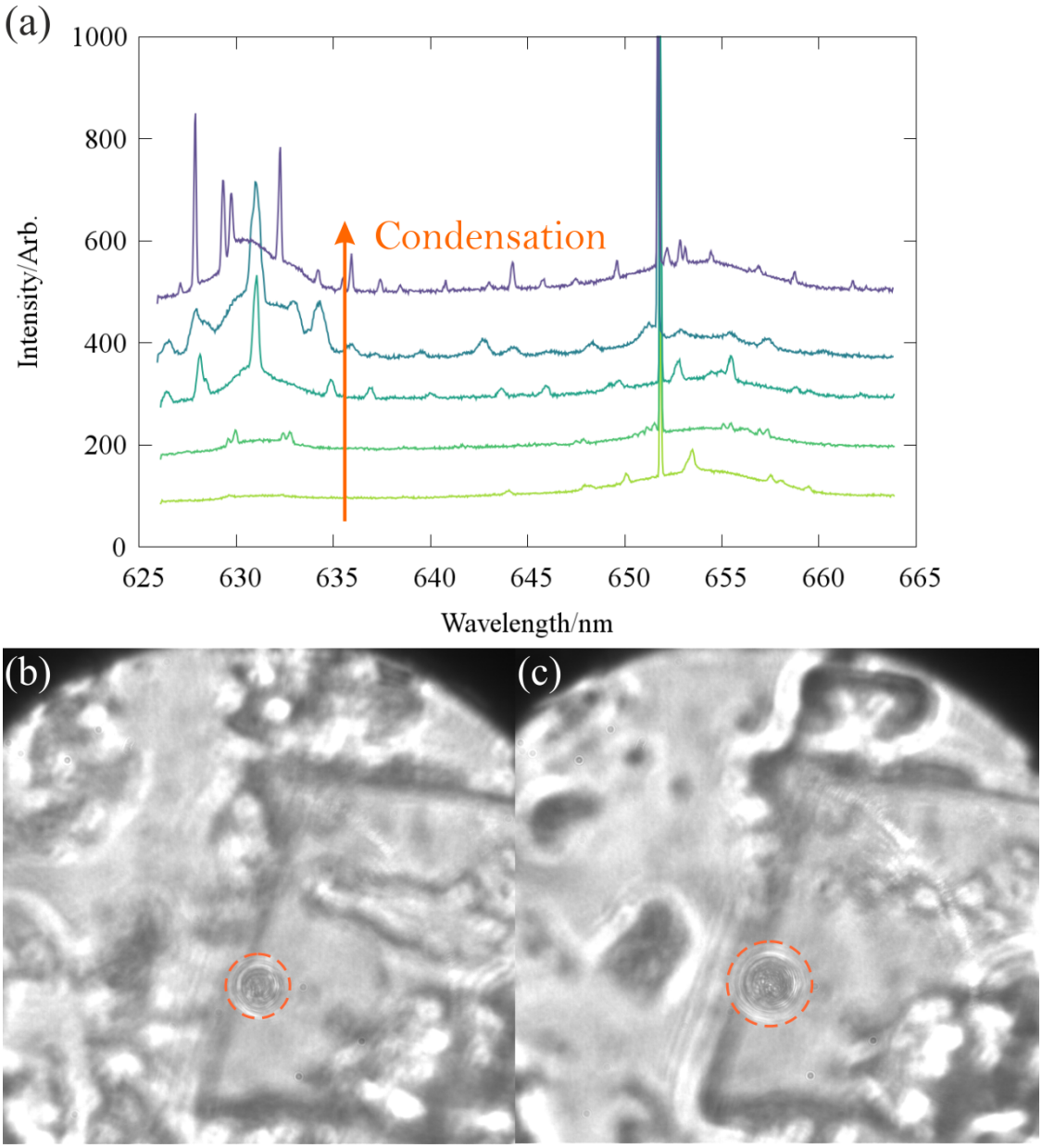

Figure 8.5.1: Different methods of observing the condensation of α-pinene secondary organic matter onto a seed particle. (a) Growth of a C-H band (626 - 635 nm) into the droplet spectrum. Each line is a composite of 20 adjacent spectra, corresponding to 40 s of exposure time. Spectra have been vertically offset for clarity. (b) and (c) show brightfield images of a sodium nitrate seed droplet increasing in diameter during a condensation experiment. Panel (a) was taken at 15:52 and panel (b) at 17:36. Ozone concentration fluctuated between 45 and 47 parts per million volume.

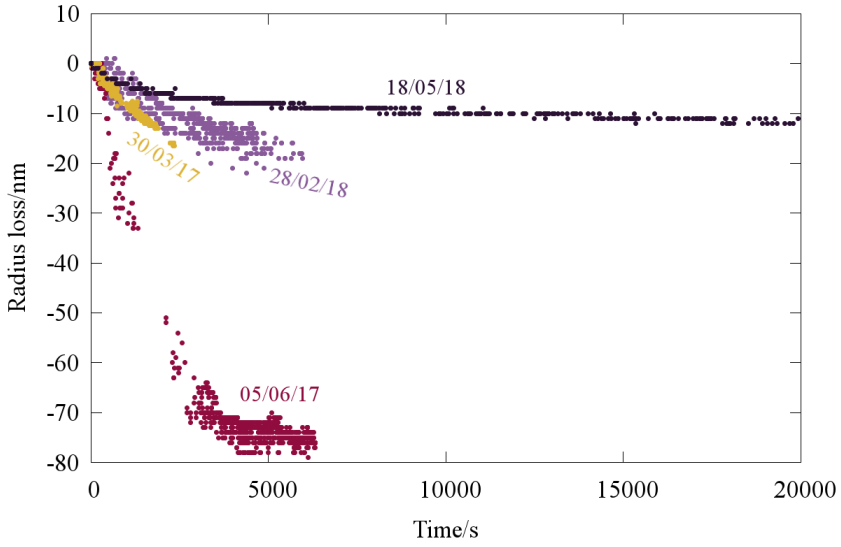

Figure 8.5.2: Comparison of the shell evaporation rate from four experiments, all evaporating at 0% RH. All data is produced from Core-Shell Mie theory.

lose the more volatile components of the accreted SOM product distribution.

8.5.1 Evaporation of Organics into Dry air

Radius data from four experiments under dry conditions have been calculated using a core-shell Mie theory algorithm, fixing the core radius and refractive index to the seed particle values known from the homogeneous algorithm. The evaporation times ranged from approximately 1 to 11 hours. They were converted to express the radius loss relative to the maximum shell width as a function of time, and are presented in Figure 8.5.2. A large degree of variance is observed between the four repeats, for which there are several likely reasons: Each experiment had a slightly different ozone concentration, and took place at slightly varying temperatures.[4] Additionally, the data was not recorded immediately once the ozonolysis was ceased in one case: the WGMs had disappeared during condensation and it took several thousand seconds for them to reappear in the spectrum.

Any evaporation of the organics partitioned onto the seed that does occur seems to be strongly

[4]Temperatures varied between 19 and 22°C.

Date	Seed Composition	Ozone Concentration/ppmv	Evaporation Time/s	Evaporation RH	Notes
30/03/17	Sucrose	71.97	1120,1980	0%,40%	First successful experiment.
28/04/17	$NaNO_3$	73.85	5000	20%	
05/06/17	$NaNO_3$+Na_2SO_4	73.85	6500	0%	
16/06/17	$NaNO_3$	88.60	7000	0%	Ozone flow ceased 1000s after α-pinene flow
27/09/17	$NaNO_3$	62.95	700	0%	
07/11/17	$NaNO_3$	43.0-51.06	11,500	57%	WGM splitting observed
28/02/18	Raffinose	42.36	7400	54-64%	
30/04/18	Raffinose	21.42	54,000	73-84%	
18/05/18	Raffinose	8.35 (may be inaccurate)	20,000	0%	

Table 8.1: Completed experiments presented and discussed in this Chapter.

kinetically controlled: There is noticeable curvature in three of the data sets, despite the fact that no water is present, suggesting that the shell viscosity rapidly increases during the first hour or so. A similar phenomenon was observed in the glycerol + sucrose experiment from the previous chapter. It can be inferred that the small proportion of the shell radius that is lost to volatilisation corresponds to low molecular weight molecules with low O:C ratios. If they were generated at approximately the same rate as the other products, one would expect them to be evenly distributed throughout the shell coating. After the condensation ceases, the high viscosity of the shell effectively stops their diffusion towards the surface on any observable timescale. Initially, only the semivolatile products within the outermost layers are able to evaporate. The others, trapped deeper within the shell, must wait for the surface to recede, until they are exposed to the air/particle interface. Therefore, the pure component vapour pressures of the products cease to be important to the collective motion of the shell.

To put the magnitude of the observed radius changes in context, three of these experiments were analysed from start to finish. They are shown in Figure 8.5.3, presenting, from left to right, the radius dynamics of the seed as the RH is reduced (dark red), followed by the outer radius of the coated particle (orange) during ozonolysis and evaporation. It was observed that the majority of the condensed matter by volume does not re-evaporate within the several hours in each case. This is consistent with existing literature studies of α-pinene SOA, which find that condensation growth at low humidity appears to be mostly irreversible.[366, 349, 70]

One of the rows in Table 8.1 describes an experiment in which a sodium nitrate seed droplet was doped with sodium sulphate (Na_2SO_4). This was to investigate whether any condensed phase reactions would occur during the condensation, potentially forming organosulphates in the process[367]. Unfortunately there was no observable evidence that such molecules were being produced and so it is believed that the evaporative dynamics of this experiment will not be systematically different to any of the others discussed herein.

Consistent with the Yli-Juuti work[301], it was initiallty difficult to say with certainty what the distribution of the vapour presures was as a whole. Given that the dry viscosity of α-pinene

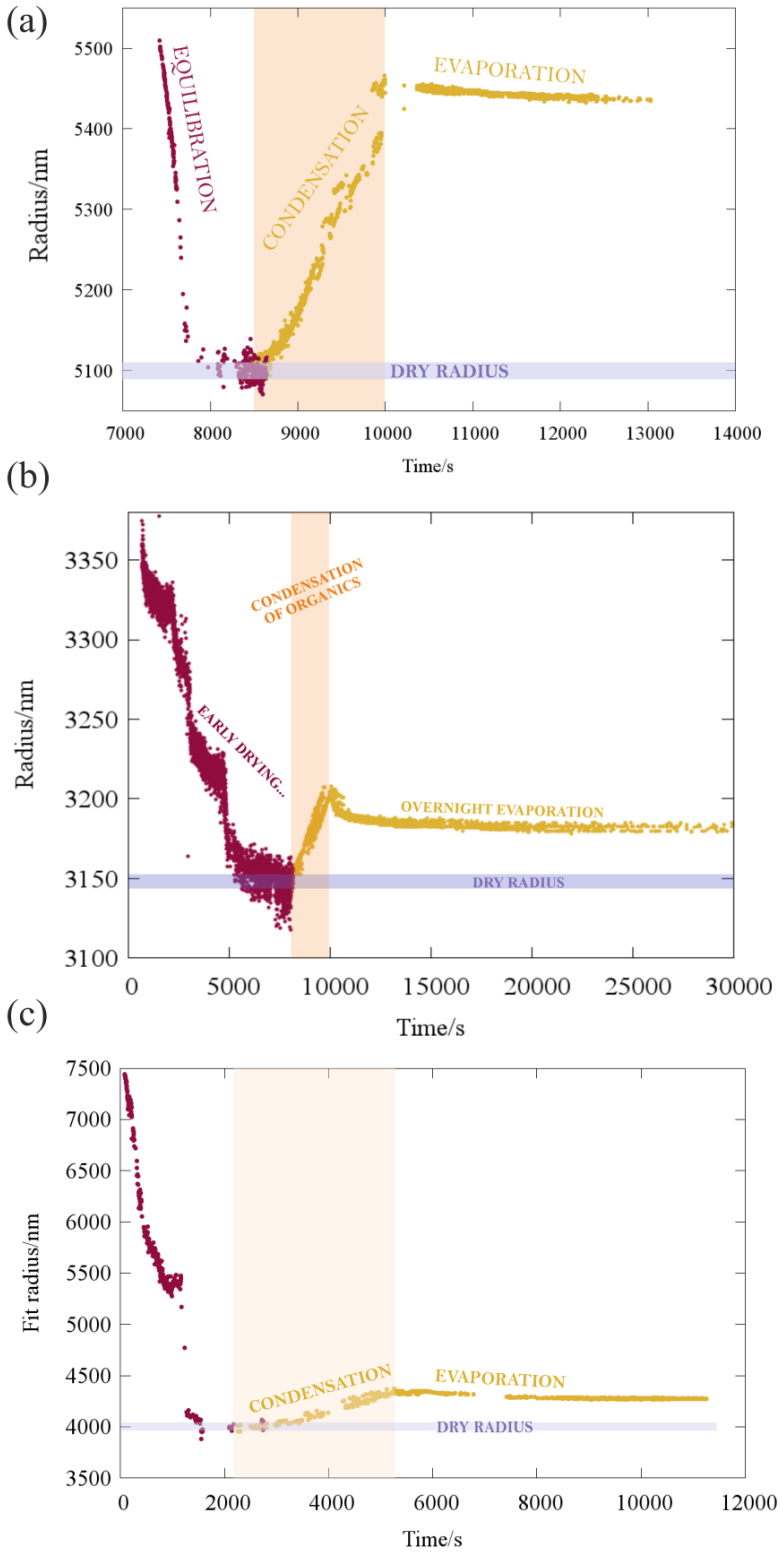

Figure 8.5.3: Particle radii throughout three full experimental datasets, showing drying of the seed particles (homogeneous Mie theory, purple), condensation (core-shell Mie theory, orange envelopes) and overnight evaporation (core-shell Mie theory, yellow points). Experiment dates are (a) 28/04/2017 (b) 18/05/2018 (c) 05/06/2017 (see Table 8.1 for exact details of each experiment).

SOA is known to be in excess of 10^8 Pa s[144], the bulk limitations to evaporation may be masking higher than expected concentrations of semivolatile products in the condensed mass.

8.5.2 Condensation of Water

In order to investigate whether volatile molecules were trapped within the coating, several experiments were conducted in which the outer organic layer was homogenised and dissolved into the core of the seed particle. Again both raffinose and sodium nitrate ($NaNO_3$) were used. The former is a large and highly oxygenated[5] organic molecule, and so as the major component within which the semivolatiles are encased, it should replicate the chemical and physical properties of an SOA particle later in its atmospheric lifetime. $NaNO_3$ is significantly less viscous than raffinose, and is often used as a proxy for sea spray aerosol in the literature[368, 369].

Experiments have been conducted humidifying nitrate coated droplets to RHs of approximately 25 and 80%, and raffinose droplets to 60 and 80%. In some cases, the coating is able to succesfully dissolve inwards and mix with the seed particle. The changing morphologies have been investigated by employing both homogeneous and core-shell Mie theory to fit the WGM trace of the particles either side of the transition. It was also possible to deduce some qualitative information about the changes in internal structure and refractive index the droplets were undergoing by observing their WGM traces, without using Mie theory.

It should be noted that the relative humidities are not as precisely defined in these experiments as those in previous chapters, as such they are better expressed as ranges: Chapter 3 described that the length of tubing through which the humidifed gas flows is substantial. The large surface area absorbs some of the water as it is travelling towards the trapping cell, until it can equilibrate with the gas. Usually there is time to allow the conditions to become stable before an experiment is conducted, but here the re-introduction of the humidified flow after the condensation begins the process again. The mean residence time of the gas in the trapping cell before it is replaced is still low, however.

[5]From the perspective of its O:C ratio, rather than necessarily reactivity or the functional groups present.

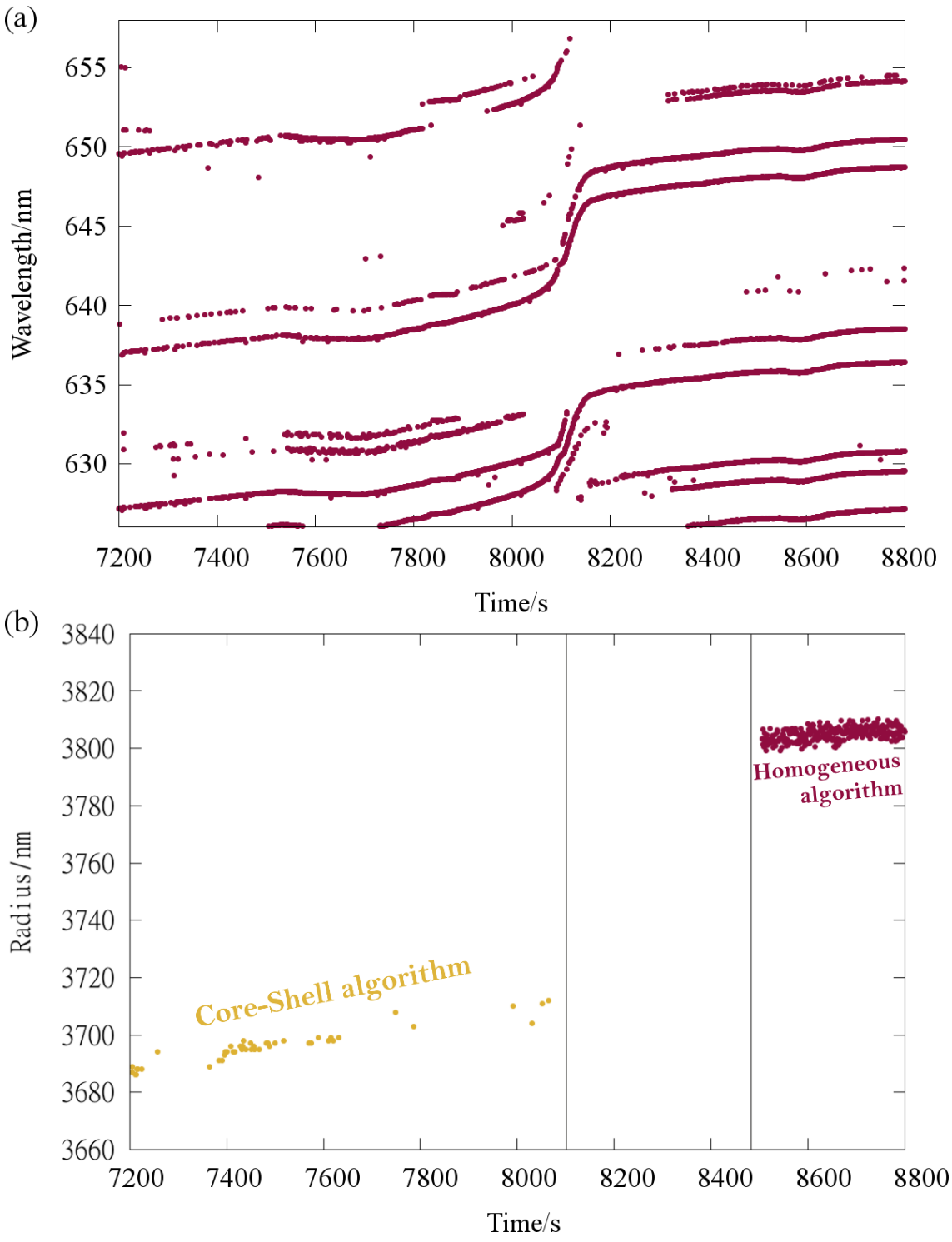

Figure 8.5.4: Observed dissolution of a core-shell droplet upon humidifying. (a) Whispering Gallery Modes observed in the single droplet Raman spectrum. (b) Fit radii using two algorithms either side of the transition. Vertical lines indicate where the core shell fitting was finished and the homogeneous fitting was begun respectively. Time is relative to the beginning of the experiment.

Humidification of a coated raffinose particle to above its glass transition humidity (~40% RH[139]), induces slow uptake of water from the surrounding vapour. The condensed water plasticises both components and the growing particle decreases in viscosity, causing the two phases to internally mix. Interestingly, the α-pinene SOM does not appear to be very hygrosocpic, meaning that initially very little water is absorbed from the newly humidified gas phase. However, once enough water has diffused through the shell and reached the raffinose core, a runaway dissolution process begins, causing a rapid shift in density and refractive index that can be observed in the WGM wavelengths of the particle. An example of this is presented in Figure 8.5.4. The modes move out of concert with each other between time points 8050 and 8150 s, reflecting the fact that the internal surface between the core and the shell disappears during this window, and the organic components mix into the raffinose. The determined radii of the particle using both fitting methods shows that it grows by approximately 90 nm in this time, as shown in the second panel of the Figure.

A different experiment was conducted involving humidification of a coated nitrate droplet to an RH of approximately 60%. It was believed to be an interesting crossover between the core shell and homogeneous regimes: the hygroscopic growth of the SOM layer will be minimal, but the viscosity of sodium nitrate will be low enough that mixing of the two phases should still occur, once it is able to absorb some water. In total the process took nearly 10,000 s to finish. Several unusual features in the Whispering Gallery Mode traces were observed (presented in Figure 8.5.5), whereby multiple changes in morphology occurred before the dissolution was complete.

Initially, one set of modes begins to move whilst the other stays constant in wavelength. This was interpretted as the shell growing but the core staying at a constant size (frames 9000-11500). Next, two of the modes acquired several shoulder peaks, appearing as intense features with increasingly small peaks in between (frames 11500 - 13750). It was determined that these features are an example of mode splitting, which occurs when a core-shell droplet loses its sphericity[352](see inset schematic). The less intense peaks arise from the azimuthal degen-

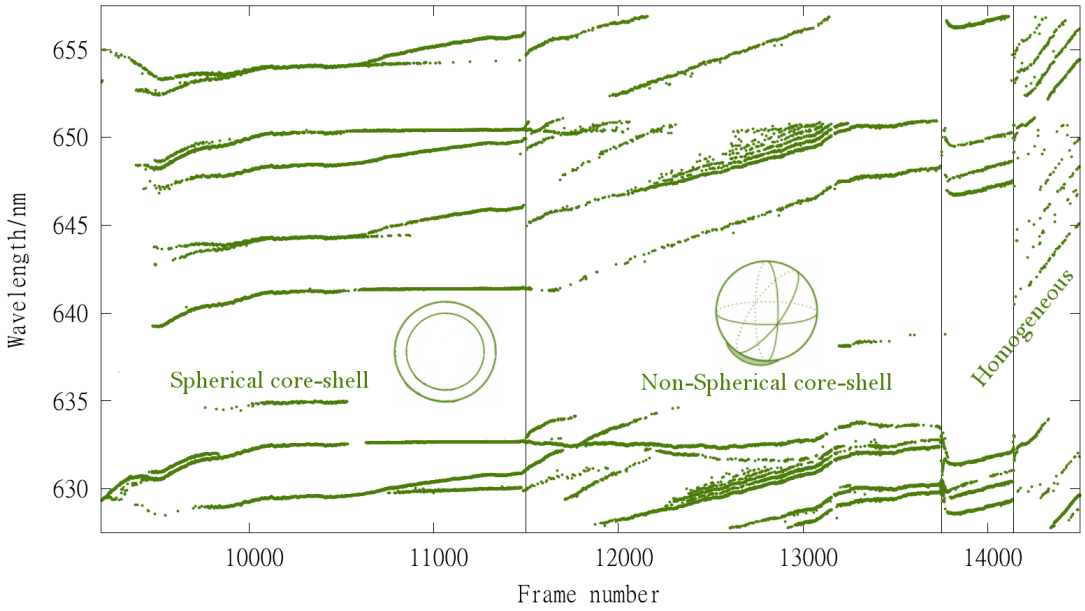

Figure 8.5.5: Consecutive changes in morphology experienced by a sodium nitrate droplet coated in α-pinene SOM as it is humidified to 57% RH, manifested in the motion of whispering gallery mode peaks. See main text for discussion. As before, time is relative to the experiment beginning. Experiment date: 07/11/17).

eracy of a mode being lost. It may be that at this point in the humidification, the dissolution of the sodium nitrate proceeds in an asymmetric way, with water condensing on one side of the droplet and the organics concentrating on the other.

Finally, the droplet regains sphericity (13750) before very rapidly transitioning into a mixed nitrate + organic droplet (14200).

Once the phase transition has ended and the condensed water plasticised both components (raffinose and the SOA shell) such that they can internally mix, it becomes possible to determine the radius as a funtion of time. During the first successful condensation experiment attempted, the SOA coated particle was humidified twice: First to approximately 40%, and then subsequently to 80%. The WGM motion associated to these two events are shown in Figure 8.5.6. Initially it was observed that the hygroscopic growth between these two humidities, inferred from the WGMs by the equation $\triangle\lambda \sim \triangle r$, was less than 2%. Since the growth factor of α-pinene SOA is only

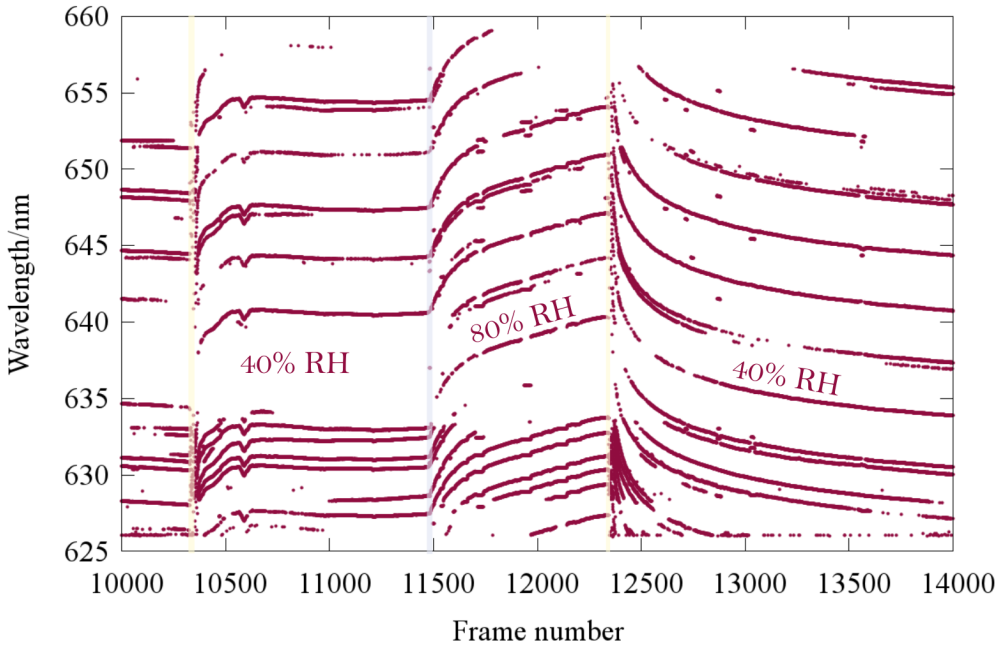

Figure 8.5.6: Hygroscopic growth of an SOA coated sucrose droplet, manifested in the motion of the whispering gallery mode peaks during a two stage water condensation event. As before, time is relative to the beginning of the experiment.

1.02 at 80%[98], it was believed that only the condensed organics took up water.

8.5.3 Evaporation of Organics into Humid air

Once the secondary organic matter has been absorbed and distributed throughout the droplet, the humidified nitrogen flow is maintained, allowing the evaporation of organics to be probed over a period of several hours. Radius dynamics during this experiment are presented in Figure 8.5.7 and clearly show that almost all of the initially condensed volume leaves the particle. The particle was equilibrated with humidified air at 80%, and then dehumidified again to 54%, causing both organics and water to coevaporate in that environment[6] for approximately 18 hr. As a much higher proportion of the organics can diffuse to the particle surface unimpaired and evaporate following this 'phase transition', we can infer that the viscosity of the dry shell is the limiting

[6]Due to the apparatus tubing absorbing some of the water, the trapping cell RH increased from 73% to 84% during the evaporation measurement

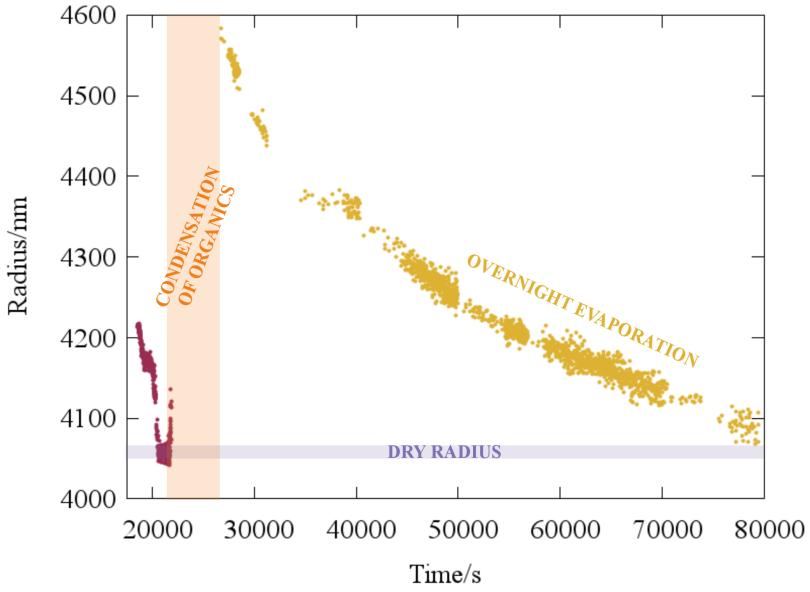

Figure 8.5.7: Homogeneous Mie theory fits of the initial evaporation of a raffinose droplet (19000 - 21000 s) and long term evaporation at 54% RH following condensation of α-pinene and homogenisation of the coated particle.

factor, rather than the volatility of the oxidation products.

The observed radii clearly show that almost all of the initially condensed volume leaves the particle, returning almost to the dry radius of the raffinose seed (light blue envelope) by frame 80,000, a remarkable mass loss given that significantly more water should be present in the particle, even at the moderate humidity of 54%. Converting the $\frac{da^2}{dt}$ gradients to vapour pressures using the Maxwell equations (used in Chapters 6 and 7) was not possible in this instance: No information is available regarding the mole fraction x_{svoc}, mass fraction F_{svoc} or density ρ of the evaporating molecules. Instead, general calculations can be made using some of the maps and trends that have been described previously in this thesis.

The first claim that can be made is that folding time of the radius change is on the order of 10^5 s, suggesting (per Figure 2.2.3) an approximate bulk phase diffusion coefficient for the organics of between 10^{-16} and 10^{-15} m^2s^{-1}. Therefore, the bulk limitation to organic diffusion will be significantly less strong than in the completely dry scenario, and so the magnitude of mass lost

more accurately represents the volatility of the organics. We can infer that the volatility is high while the oxidation products are still fresh, and also that the mass loss into dry air is artificially lower than it would be at equilibrium. The early radius change (26,000 s to 31,000 s) occurs with a gradient of 256 nm^2s^{-1}, which (per section 7.5.2) suggests at most a mean saturation mass concentration, C*, of 10 $\mu g\ m^{-3}$.

8.6 Outlook and Future Studies

To the extent that the studies described in this chapter can replicate the conditions where SOA forms, it has been possible to understand the dynamic behaviour of the generated product mass. While it could also be argued convincingly that the method of VOC oxidation used in these studies is in some respects extreme, the measurements still provide a basis from which we can predict and interpret the behaviour of SOA. Additionally, probing the reaction through the Raman signal of a single seed droplet is a relatively rare technique in this context, and has provided novel information. For example, a high oxygen content within the atmosphere of the trapping cell should have allowed autoxidation to occur frequently, suggesting that the compounds studied had high O:C ratios. The Raman signals of the condensed matter confirm this, with a high degree of oxygenated, electron withdrawing groups clearly present. Conversely, the absence of water, NO_x, or sulphates may have reduced the complexity of the product distribution in comparison to smog chanber studies. That is a secondary concern, as precise reproducing such chemistry is not the purpose of these experiments.

The studies conducted in this chapter describe attempts at understanding the evaporative properties of the SOA product distribution. As this has partly been a tentative exploration of what is possible with this technique, it is difficult to ascertain conclusions to as high a degree of certainty as in previous chapters.

Secondary organic matter is a substance whose properties arise collectively from interactions between the many compounds contained within it and within the oxidation scheme. Hence it is understandable that high variability is observed in the behaviour of the condensed shells, as

there is variability in the relative concentrations of the reactants. Nonetheless, a few tentative outcomes can be stated, with the previously stated caveats regarding the presence of NO_x, water, and sulphate:

1. It is found semivolatiles comprise a large, possibly dominant proportion of the fresh SOA volume. Yet, under dry conditions, the viscosity of the remaining components is so high that they cannot evaporate in significant numbers. Only the SVOCs in the outermost nanometers of the droplet are able to partition back into the gas phase when exposed to air containing no VOCs or chemical reactions. The viscosity suggests the presence of at least some molecules that have high molecular weights, possibly dimers formed in the gas phase[370, 53, 371] or oligomers formed in the particle phase[223, 344, 50].

2. The mean refractive indices (real component) of the organic species have been determined at two wavelengths, and compared to the literature, to generally good agreement. This may have implications for the radiative forcing characteristics of SOA produced freshly above forested areas.

3. Despite being highly oxygenated, the product mass is observed not to be very hygroscopic, which is in broad agreement with the much of the atmospheric literature. One novel implication of the behaviour of these particles is that inorganic aerosol which becomes coated with oxidised organics will have their hygroscopicity drastically reduced; a change that will persist until the outer shell can be in some way plasticised, at which point the two phases will mix and water will be rapidly taken up. Thus, cloud nucleation activity may be sensitive to even small amounts of SOA material in an atmosphere. Interestingly, the dissolution of the core-shell morphology sometimes occurs via a non-spherical intermediate morphology, before the homogeneous particle reverts to a spherical shape.

It has not been possible to fully explore the range of experiments that this apparatus should be capable of in the time available. Instead, a narrow range of conditions were studied, and the sensitivities of the coated particles to those conditions were recorded. The parameter space of

variables that could be added, or different conditions that could be perturbed, is extensive. What follows is a series of suggestions that could be significant and could provide information to the literature that would be difficult to obtain through other experimental methods:

- Determining the hygroscopic growth of the organic layer more precisely is the closest extension of the experiments here. Experiments have only looked at ranges of RH, and not in a systematic manner. At every RH below 40%, a raffinose coated droplet can be assumed to be glassy and so no mixing of the core and shell will occur. The remainder of the growth curve, above 40%, could be prepared by growing a small seed by condensation until the majority of the volume is organic. In that way, it can be assumed that it will act like an SOA particle.

- Particle phase chemistry could be studied by doping the seed droplet with reactive atmospherically relevant molecules, such as ammonium sulphate or glyoxal[372, 373]. In which way the presence of these molecules will change the yield, or indeed properties, of the resultant SOA remains an open question[31, 30, 374]. A related experiment would involve the brown carbon molecule imidazole[94, 375], which absorbs light in the wavelength range of the laser. The change in evaporation rate with and without imidazole present could shed light on droplet heating processes in Brown Carbon particles.

- One area of research that seems to have emerged in the past year (at the time of writing) involves experiments where multiple VOCs are oxidised to SOA, either sequentially[302] or both simultaneously[70]. It is possible to achieve multi-VOC oxidation in this experiment if the two pure liquids are miscible with one another. In that case, a solution of both can be prepared at a range of concentrations and loaded into the organic bubbler in the same way as pure α-pinene was here. Finally Shrivastava et al.[19] have suggested that studies are needed probing middling concentrations of NO_x and HO_x species. If additional mass flow controllers can be sourced, such experiments will be possible.

It may be that there are limitations to what can be achieved via single particle methods, because

each droplet within a larger ensemble will be influenced by the presence of the others. Even so, making measurements such as these more accurate and reproduceable will only help to quantify the differences with ensemble techniques, and to define which regime of particle behaviour the experiment is operating in. It may be that the closer an experiment gets to fully representing what goes on in the atmosphere, the more complex and less explicable the results become.

Summary

It is generally accepted that atmospheric particles, such as secondary organic aerosol (SOA) can become glassy as they are dried. Understanding the impact of such a transition on what occurs within an aerosol particle requires knowledge spanning from the length scale of molecules (nanometers) to the length scale of single particles (hundreds of nanometers to microns). Consequently, each of the studies that have been described in this thesis differ in their scope and the length scale they operate on. A combination of experimental and computational studies have been conducted and it is hoped that, taken together, they reveal a significant amount about diffusional flux within organic aerosol.

Moving backwards from the end of this thesis, we can say that the final chapter contains the study probing aerosol most representative of atmospheric particles. It reveals that treating SOA as a mixture of involatile and semivolatile species is a legitimate assumption, although the interaction of the two with one another can almost completely stop volatilisation if the particles reside in dry air. The optical and hygroscopic properties of the organic mass were investigated, and found to be consistent with previous studies, giving us confidence in the evaporative flux measurements.

Therefore, the results of the previous chapter, which investigated semivolatile species diffusing through a matrix of viscous saccharides in order to evaporate from a particle, can be considered a legitimate proxy for SOA. The droplets were prepared with well defined amounts of the two organic species present, and so the evolving concentrations were able to be simulated precisely with Fickian diffusion modelling. It was found that simple mixing rules for viscos-

ity, when combined with defensible assumptions such as Raoult's Law and the Stokes-Einstein relationship, can accurately reproduce the evaporation rates of single levitated particles. The optimisation schemes sometimes used in conjunction with diffusion modelling did not need to be employed here, and so the model can be considered truly predictive. This result holds across the humidity range studied and a volatility range of the semivolatile extending from 10^{-2} o 10^{-4} Pa.

Water and its dynamics in viscous aerosol remains a non trivial problem to solve, even dating to the original paper of Zobrist[130] proposing glass transitions in atmospheric aeorsol. Nonetheless, three of the chapters presented here have gone some way to revealing new details of the phenomenon, with special attention paid to the nanoscale. In Chapter 7, I considered the water evaporation that happens alongside semivolatile evaporation, to equalise the activity between the gas and particle phases. It was found that in order for the model to accurately reproduce certain experiments, the water content of the particle had to be assumed to rapidly equilibrate between the surface and the core, even when the organic constituents could not.

Several parameterisations of water diffusion through different organic components were produced from a comprehensive study of viscous aerosol in Chapter 6, and inserted with no modifications into the modelling of Chapter 7. The magnitude of the limiting diffusion coefficients are consistent with an emerging concensus in the literature, namely that water equilibration is generally fast in the atmosphere, even when particle viscosities are high.

Meanwhile, the mechanism by which water can diffuse through a stationary organic matrix at the particle surface has been investigated using molecular dynamics simulations, as descibed in Chapter 5. Instead of a continuous Brownian trajectory, the pathway taken by the molecule involves discrete jumps between cavities that do not collapse once they are vacated. It confirms that a decoupling of timescales exists between the motion of water and organics in viscous aerosol, and that the size of the decoupling increases with the molecular weight of the organic. Both results are entirely consistent with the other experimental chapters as well as the wider literature.

From the discoveries made here, there are significant implications for the evaporation of SOA particles later in their atmospheric lifetime, as they will necessarily contain larger, more viscous

and less volatile organic species.

Bibliography

[1] H. Vehkamäki and I. Riipinen, *Chemical Society Reviews*, 2012, **41**, 5160.

[2] M. de Reus, R. Krejci, J. Williams, H. Fischer, R. Scheele and J. Ström, *Journal of Geophysical Research: Atmospheres*, 2001, **106**, 28629–28641.

[3] Nature, *Nature*, 2019, **568**, 433–433.

[4] P. Irvine, K. Emanuel, J. He, L. W. Horowitz, G. Vecchi and D. Keith, *Nature Climate Change*, 2019.

[5] D. K. Farmer, C. D. Cappa and S. M. Kreidenweis, *Chemical Reviews*, 2015, **115**, 4199–4217.

[6] IPCC, in *Climate Change 2013 - The Physical Science Basis*, Cambridge University Press, Cambridge, 2014, ch. 7, pp. 1–147.

[7] C. L. McConnell, E. J. Highwood, H. Coe, P. Formenti, B. Anderson, S. Osborne, S. Nava, K. Desboeufs, G. Chen and M. A. J. Harrison, *Journal of Geophysical Research*, 2008, **113**, D14S05.

[8] A. Molod, L. Takacs, M. Suarez and J. Bacmeister, *Geoscientific Model Development*, 2015, **8**, 1339–1356.

[9] J. Aitken, *Transactions of the Royal Society of Edinburgh*, 1900, **39**, 15–25.

[10] R. J. Weber, P. H. McMurry, F. L. Eisele and D. J. Tanner, *Journal of the Atmospheric Sciences*, 1995, **52**, 2242–2257.

[11] M. Kulmala, A. Toivonen, J. M. Mäkelä and A. Laaksonen, *Tellus B: Chemical and Physical Meteorology*, 1998, **50**, 449–462.

[12] M. Kulmala, H. Vehkamäki, T. Petäjä, M. Dal Maso, A. Lauri, V.-M. Kerminen, W. Birmili and P. McMurry, *Journal of Aerosol Science*, 2004, **35**, 143–176.

[13] C. L. Haman, E. Couzo, J. H. Flynn, W. Vizuete, B. Heffron and B. L. Lefer, *Journal of Geophysical Research: Atmospheres*, 2014, **119**, 6230–6245.

[14] H. B. Fu, R. Ciuraru, Y. Dupart, M. Passananti, L. Tinel, S. Rossignol, S. Perrier, D. J. Donaldson, J. M. Chen and C. George, *Journal of the American Chemical Society*, 2015, **137**, 8348–8351.

[15] V.-M. Kerminen, X. Chen, V. Vakkari, T. Petäjä, M. Kulmala and F. Bianchi, *Environmental Research Letters*, 2018, **13**, 103003.

[16] J. Almeida, S. Schobesberger, A. Kürten, I. K. Ortega, O. Kupiainen-Määttä, A. P. Praplan, A. Adamov, A. Amorim, F. Bianchi, M. Breitenlechner, A. David, J. Dommen, N. M. Donahue, A. Downard, E. Dunne, J. Duplissy, S. Ehrhart, R. C. Flagan, A. Franchin, R. Guida, J. Hakala, A. Hansel, M. Heinritzi, H. Henschel, T. Jokinen, H. Junninen, M. Kajos, J. Kangasluoma, H. Keskinen, A. Kupc, T. Kurtén, A. N. Kvashin, A. Laaksonen, K. Lehtipalo, M. Leiminger, J. Leppä, V. Loukonen, V. Makhmutov, S. Mathot, M. J. McGrath, T. Nieminen, T. Olenius, A. Onnela, T. Petäjä, F. Riccobono, I. Riipinen, M. Rissanen, L. Rondo, T. Ruuskanen, F. D. Santos, N. Sarnela, S. Schallhart, R. Schnitzhofer, J. H. Seinfeld, M. Simon, M. Sipilä, Y. Stozhkov, F. Stratmann, A. Tomé, J. Tröstl, G. Tsagkogeorgas, P. Vaattovaara, Y. Viisanen, A. Virtanen, A. Vrtala, P. E. Wagner, E. Weingartner, H. Wex, C. Williamson, D. Wimmer, P. Ye, T. Yli-Juuti, K. S. Carslaw, M. Kulmala,

J. Curtius, U. Baltensperger, D. R. Worsnop, H. Vehkamäki and J. Kirkby, *Nature*, 2013, **502**, 359–363.

[17] T. Nieminen, H. E. Manninen, S.-L. Sihto, T. Yli-Juuti, R. L. Mauldin, III, T. Petaja, I. Riipinen, V.-M. Kerminen and M. Kulmala, *Environmental Science & Technology*, 2009, **43**, 4715–4721.

[18] B. R. Bzdek, A. J. Horan, M. R. Pennington, J. W. DePalma, J. Zhao, C. N. Jen, D. R. Hanson, J. N. Smith, P. H. McMurry and M. V. Johnston, *Faraday Discussions*, 2013, **165**, 25.

[19] M. Shrivastava, C. D. Cappa, J. Fan, A. H. Goldstein, A. B. Guenther, J. L. Jimenez, C. Kuang, A. Laskin, S. T. Martin, N. L. Ng, T. Petaja, J. R. Pierce, P. J. Rasch, P. Roldin, J. H. Seinfeld, J. Shilling, J. N. Smith, J. A. Thornton, R. Volkamer, J. Wang, D. R. Worsnop, R. A. Zaveri, A. Zelenyuk and Q. Zhang, *Reviews of Geophysics*, 2017, **55**, 509–559.

[20] M. Glasius and A. H. Goldstein, *Environmental Science & Technology*, 2016, **50**, 2754–2764.

[21] A. Guenther, C. N. Hewitt, D. Erickson, R. Fall, C. Geron, T. Graedel, P. Harley, L. Klinger, M. Lerdau, W. A. Mckay, T. Pierce, B. Scholes, R. Steinbrecher, R. Tallamraju, J. Taylor and P. Zimmerman, *Journal of Geophysical Research*, 1995, **100**, 8873.

[22] C. Warneke, J. A. de Gouw, J. S. Holloway, J. Peischl, T. B. Ryerson, E. Atlas, D. Blake, M. Trainer and D. D. Parrish, *Journal of Geophysical Research: Atmospheres*, 2012, **117**, D00V17.

[23] W. Y. Tuet, Y. Chen, L. Xu, S. Fok, D. Gao, R. J. Weber and N. L. Ng, *Atmospheric Chemistry and Physics*, 2017, **17**, 839–853.

[24] X. Zhang, R. C. McVay, D. D. Huang, N. F. Dalleska, B. Aumont, R. C. Flagan and J. H. Seinfeld, *Proceedings of the National Academy of Sciences*, 2015, **112**, 14168–14173.

[25] G. Gržinić, T. Bartels-Rausch, T. Berkemeier, A. Türler and M. Ammann, *Atmospheric Chemistry and Physics*, 2015, **15**, 13615–13625.

[26] B. J. FinlaysonPitts and J. N. Pitts, *Science*, 1997, **276**, 1045–1052.

[27] K. Sindelarova, C. Granier, I. Bouarar, A. Guenther, S. Tilmes, T. Stavrakou, J.-F. Müller, U. Kuhn, P. Stefani and W. Knorr, *Atmospheric Chemistry and Physics*, 2014, **14**, 9317–9341.

[28] J. H. Kroll and J. H. Seinfeld, *Atmospheric Environment*, 2008, **42**, 3593–3624.

[29] Y. B. Lim and B. J. Turpin, *Atmospheric Chemistry and Physics*, 2015, **15**, 12867–12877.

[30] M. Riva, D. M. Bell, A.-M. K. Hansen, G. T. Drozd, Z. Zhang, A. Gold, D. Imre, J. D. Surratt, M. Glasius and A. Zelenyuk, *Environmental Science & Technology*, 2016, **50**, 5580–5588.

[31] K. D. Froyd, S. M. Murphy, D. M. Murphy, J. A. de Gouw, N. C. Eddingsaas and P. O. Wennberg, *Proceedings of the National Academy of Sciences*, 2010, **107**, 21360–21365.

[32] K. Nestorowicz, M. Jaoui, K. J. Rudzinski, M. Lewandowski, T. E. Kleindienst, G. Spólnik, W. Danikiewicz and R. Szmigielski, *Atmospheric Chemistry and Physics*, 2018, **18**, 18101–18121.

[33] Z. Liu, V. S. Nguyen, J. Harvey, J.-F. Müller and J. Peeters, *Phys. Chem. Chem. Phys.*, 2017, **19**, 9096–9106.

[34] J. Peeters, T. L. Nguyen and L. Vereecken, *Physical Chemistry Chemical Physics*, 2009, **11**, 5935.

[35] J. Peeters, J.-F. Müller, T. Stavrakou and V. S. Nguyen, *The Journal of Physical Chemistry A*, 2014, **118**, 8625–8643.

[36] T. Hoffmann, J. R. Odum, F. Bowman, D. Collins, D. Klockow, R. C. Flagan and J. H. Seinfeld, *Journal of Atmospheric Chemistry*, 1997, **26**, 189–222.

[37] A. Alvarado, E. C. Tuazon, S. M. Aschmann, R. Atkinson and J. Arey, *Journal of Geophysical Research: Atmospheres*, 1998, **103**, 25541–25551.

[38] E. G. Stephanou, I. G. Kavouras and N. Mihalopoulos, *Nature*, 1998, **395**, 683–686.

[39] J. Kirkby, J. Duplissy, K. Sengupta, C. Frege, H. Gordon, C. Williamson, M. Heinritzi, M. Simon, C. Yan, J. Almeida, J. Tröstl, T. Nieminen, I. K. Ortega, R. Wagner, A. Adamov, A. Amorim, A.-K. Bernhammer, F. Bianchi, M. Breitenlechner, S. Brilke, X. Chen, J. Craven, A. Dias, S. Ehrhart, R. C. Flagan, A. Franchin, C. Fuchs, R. Guida, J. Hakala, C. R. Hoyle, T. Jokinen, H. Junninen, J. Kangasluoma, J. Kim, M. Krapf, A. Kürten, A. Laaksonen, K. Lehtipalo, V. Makhmutov, S. Mathot, U. Molteni, A. Onnela, O. Peräkylä, F. Piel, T. Petäjä, A. P. Praplan, K. Pringle, A. Rap, N. A. D. Richards, I. Riipinen, M. P. Rissanen, L. Rondo, N. Sarnela, S. Schobesberger, C. E. Scott, J. H. Seinfeld, M. Sipilä, G. Steiner, Y. Stozhkov, F. Stratmann, A. Tomé, A. Virtanen, A. L. Vogel, A. C. Wagner, P. E. Wagner, E. Weingartner, D. Wimmer, P. M. Winkler, P. Ye, X. Zhang, A. Hansel, J. Dommen, N. M. Donahue, D. R. Worsnop, U. Baltensperger, M. Kulmala, K. S. Carslaw and J. Curtius, *Nature*, 2016, **533**, 521–526.

[40] T. Kurtén, K. Tiusanen, P. Roldin, M. Rissanen, J.-N. Luy, M. Boy, M. Ehn and N. Donahue, *The Journal of Physical Chemistry A*, 2016, **120**, 2569–2582.

[41] M. Ehn, T. Berndt, J. Wildt and T. Mentel, *International Journal of Chemical Kinetics*, 2017, **49**, 821–831.

[42] J. D. Rindelaub, J. S. Wiley, B. R. Cooper and P. B. Shepson, *Rapid Communications in Mass Spectrometry*, 2016, **30**, 1627–1638.

[43] T. Berndt, S. Richters, T. Jokinen, N. Hyttinen, T. Kurtén, R. V. Otkjær, H. G. Kjaergaard, F. Stratmann, H. Herrmann, M. Sipilä, M. Kulmala and M. Ehn, *Nature Communications*, 2016, **7**, 13677.

[44] Y. Y. Wei, T. T. Cao and J. E. Thompson, *Atmospheric Environment*, 2012, **62**, 199–207.

[45] J. D. Crounse, L. B. Nielsen, S. Jørgensen, H. G. Kjaergaard and P. O. Wennberg, *Journal of Physical Chemistry Letters*, 2013, **4**, 3513–3520.

[46] M. Ehn, E. Kleist, H. Junninen, T. Petäjä, G. Lönn, S. Schobesberger, M. Dal Maso, A. Trimborn, M. Kulmala, D. R. Worsnop, A. Wahner, J. Wildt and T. F. Mentel, *Atmospheric Chemistry and Physics*, 2012, **12**, 5113–5127.

[47] S. Schobesberger, H. Junninen, F. Bianchi, G. Lonn, M. Ehn, K. Lehtipalo, J. Dommen, S. Ehrhart, I. K. Ortega, A. Franchin, T. Nieminen, F. Riccobono, M. Hutterli, J. Duplissy, J. Almeida, A. Amorim, M. Breitenlechner, A. J. Downard, E. M. Dunne, R. C. Flagan, M. Kajos, H. Keskinen, J. Kirkby, A. Kupc, A. Kurten, T. Kurten, A. Laaksonen, S. Mathot, A. Onnela, A. P. Praplan, L. Rondo, F. D. Santos, S. Schallhart, R. Schnitzhofer, M. Sipila, A. Tome, G. Tsagkogeorgas, H. Vehkamaki, D. Wimmer, U. Baltensperger, K. S. Carslaw, J. Curtius, A. Hansel, T. Petaja, M. Kulmala, N. M. Donahue and D. R. Worsnop, *Proceedings of the National Academy of Sciences*, 2013, **110**, 17223–17228.

[48] T. F. Mentel, M. Springer, M. Ehn, E. Kleist, I. Pullinen, T. Kurtén, M. Rissanen, A. Wahner and J. Wildt, *Atmospheric Chemistry and Physics*, 2015, **15**, 6745–6765.

[49] M. P. Rissanen, T. Kurtén, M. Sipilä, J. A. Thornton, J. Kangasluoma, N. Sarnela, H. Junninen, S. Jørgensen, S. Schallhart, M. K. Kajos, R. Taipale, M. Springer, T. F. Mentel, T. Ruuskanen, T. Petäjä, D. R. Worsnop, H. G. Kjaergaard and M. Ehn, *Journal of the American Chemical Society*, 2014, **136**, 15596–15606.

[50] F. A. Mackenzie-Rae, A. Karton and S. M. Saunders, *Phys. Chem. Chem. Phys.*, 2016, **18**, 27991–28002.

[51] T. Kurtén, M. P. Rissanen, K. Mackeprang, J. A. Thornton, N. Hyttinen, S. Jørgensen, M. Ehn and H. G. Kjaergaard, *The Journal of Physical Chemistry A*, 2015, **119**, 11366–11375.

[52] M. Ehn, J. A. Thornton, E. Kleist, M. Sipilä, H. Junninen, I. Pullinen, M. Springer, F. Rubach, R. Tillmann, B. Lee, F. Lopez-Hilfiker, S. Andres, I.-H. Acir, M. Rissanen, T. Jokinen, S. Schobesberger, J. Kangasluoma, J. Kontkanen, T. Nieminen, T. Kurtén, L. B. Nielsen, S. Jørgensen, H. G. Kjaergaard, M. Canagaratna, M. D. Maso, T. Berndt, T. Petäjä, A. Wahner, V.-M. Kerminen, M. Kulmala, D. R. Worsnop, J. Wildt and T. F. Mentel, *Nature*, 2014, **506**, 476–479.

[53] K. C. Barsanti, J. H. Kroll and J. A. Thornton, *Journal of Physical Chemistry Letters*, 2017, **8**, 1503–1511.

[54] J. Tröstl, W. K. Chuang, H. Gordon, M. Heinritzi, C. Yan, U. Molteni, L. Ahlm, C. Frege, F. Bianchi, R. Wagner, M. Simon, K. Lehtipalo, C. Williamson, J. S. Craven, J. Duplissy, A. Adamov, J. Almeida, A.-K. Bernhammer, M. Breitenlechner, S. Brilke, A. Dias, S. Ehrhart, R. C. Flagan, A. Franchin, C. Fuchs, R. Guida, M. Gysel, A. Hansel, C. R. Hoyle, T. Jokinen, H. Junninen, J. Kangasluoma, H. Keskinen, J. Kim, M. Krapf, A. Kürten, A. Laaksonen, M. Lawler, M. Leiminger, S. Mathot, O. Möhler, T. Nieminen, A. Onnela, T. Petäjä, F. M. Piel, P. Miettinen, M. P. Rissanen, L. Rondo, N. Sarnela, S. Schobesberger, K. Sengupta, M. Sipilä, J. N. Smith, G. Steiner, A. Tomè, A. Virtanen, A. C. Wagner, E. Weingartner, D. Wimmer, P. M. Winkler, P. Ye, K. S. Carslaw, J. Curtius, J. Dommen, J. Kirkby, M. Kulmala, I. Riipinen, D. R. Worsnop, N. M. Donahue and U. Baltensperger, *Nature*, 2016, **533**, 527–531.

[55] T. Jokinen, M. Sipilä, S. Richters, V.-M. Kerminen, P. Paasonen, F. Stratmann, D. Worsnop, M. Kulmala, M. Ehn, H. Herrmann and T. Berndt, *Angewandte Chemie International Edition*, 2014, **53**, 14596–14600.

[56] C. J. Percival, O. Welz, A. J. Eskola, J. D. Savee, D. L. Osborn, D. O. Topping, D. Lowe, S. R. Utembe, A. Bacak, G. McFiggans, M. C. Cooke, P. Xiao, A. T. Archibald, M. E. Jenkin, R. G. Derwent, I. Riipinen, D. W. K. Mok, E. P. F. Lee, J. M. Dyke, C. A. Taatjes and D. E. Shallcross, *Faraday Discussions*, 2013, **165**, 45.

[57] R. Chhantyal-Pun, A. Davey, D. E. Shallcross, C. J. Percival and A. J. Orr-Ewing, *Physical Chemistry Chemical Physics*, 2015, **17**, 3617–3626.

[58] R. L. Caravan, M. A. H. Khan, B. Rotavera, E. Papajak, I. O. Antonov, M.-W. Chen, K. Au, W. Chao, D. L. Osborn, J. J.-M. Lin, C. J. Percival, D. E. Shallcross and C. A. Taatjes, *Faraday Discussions*, 2017, **200**, 313–330.

[59] L. Jia and Y. Xu, *Atmospheric Chemistry and Physics*, 2018, **18**, 8137–8154.

[60] P. Xiao, J.-J. Yang, W.-H. Fang and G. Cui, *Physical Chemistry Chemical Physics*, 2018, **20**, 16138–16150.

[61] Z. J. Buras, R. M. I. Elsamra, A. Jalan, J. E. Middaugh and W. H. Green, *The Journal of Physical Chemistry A*, 2014, **118**, 1997–2006.

[62] S. Enami and Y. Sakamoto, *The Journal of Physical Chemistry A*, 2016, **120**, 3578–3587.

[63] S. Enami and A. J. Colussi, *Phys. Chem. Chem. Phys.*, 2017, **19**, 17044–17051.

[64] L. Vereecken, *Physical Chemistry Chemical Physics*, 2017, **19**, 28630–28640.

[65] Y. Sakamoto, R. Yajima, S. Inomata and J. Hirokawa, *Phys. Chem. Chem. Phys.*, 2017, **19**, 3165–3175.

[66] Q. Mu, M. Shiraiwa, M. Octaviani, N. Ma, A. Ding, H. Su, G. Lammel, U. Pöschl and Y. Cheng, *Science Advances*, 2018, **4**, eaap7314.

[67] A. Zelenyuk, D. Imre, J. Beranek, E. Abramson, J. Wilson and M. Shrivastava, *Environ Sci Technol*, 2012, **46**, 12459–12466.

[68] B. Nozière, M. Kalberer, M. Claeys, J. Allan, B. D'Anna, S. Decesari, E. Finessi, M. Glasius, I. Grgić, J. F. Hamilton, T. Hoffmann, Y. Iinuma, M. Jaoui, A. Kahnt, C. J. Kampf, I. Kourtchev, W. Maenhaut, N. Marsden, S. Saarikoski, J. Schnelle-Kreis, J. D. Surratt, S. Szidat, R. Szmigielski and A. Wisthaler, *Chemical Reviews*, 2015, **115**, 3919–3983.

[69] F. A. Mackenzie-Rae, H. J. Wallis, A. R. Rickard, K. L. Pereira, S. M. Saunders, X. Wang and J. F. Hamilton, *Atmospheric Chemistry and Physics*, 2018, **18**, 4673–4693.

[70] G. McFiggans, T. F. Mentel, J. Wildt, I. Pullinen, S. Kang, E. Kleist, S. Schmitt, M. Springer, R. Tillmann, C. Wu, D. Zhao, M. Hallquist, C. Faxon, M. Le Breton, A. M. Hallquist, D. Simpson, R. Bergstrom, M. E. Jenkin, M. Ehn, J. A. Thornton, M. R. Alfarra, T. J. Bannan, C. J. Percival, M. Priestley, D. Topping and A. Kiendler-Scharr, *Nature*, 2019, **565**, 587–593.

[71] M. Kalberer, D. Paulsen, M. Sax, M. Steinbacher, J. Dommen, A. S. H. Prevot, R. Fisseha, E. Weingartner, V. Frankevich, R. Zenobi and U. Baltensperger, *Science (New York, N.Y.)*, 2004, **303**, 1659–62.

[72] L. Chen, Y. Huang, Y. Xue, J. Cao and W. Wang, *Atmospheric Environment*, 2018, **187**, 218–229.

[73] K. Altieri, S. Seitzinger, A. Carlton, B. Turpin, G. Klein and A. Marshall, *Atmos. Env.*, 2008, **42**, 1476–1490.

[74] M. Rodigast, A. Mutzel and H. Herrmann, *Atmospheric Chemistry and Physics*, 2017, **17**, 3929–3943.

[75] I. Kourtchev, C. Giorio, A. Manninen, E. Wilson, B. Mahon, J. Aalto, M. Kajos, D. Venables, T. Ruuskanen, J. Levula, M. Loponen, S. Connors, N. Harris, D. Zhao, A. Kiendler-Scharr, T. Mentel, Y. Rudich, M. Hallquist, J.-F. Doussin, W. Maenhaut, J. Bäck, T. Petäjä, J. Wenger, M. Kulmala and M. Kalberer, *Scientific Reports*, 2016, **6**, 35038.

[76] W. A. Hall and M. V. Johnston, *Aerosol Science and Technology*, 2011, **45**, 37–45.

[77] M. L. Hinks, J. Montoya-Aguilera, L. Ellison, P. Lin, A. Laskin, J. Laskin, M. Shiraiwa, D. Dabdub and S. A. Nizkorodov, *Atmospheric Chemistry and Physics Discussions*, 2018, **18**, 1643–1652.

[78] F. Couvidat, M. G. Vivanco and B. Bessagnet, *Atmospheric Chemistry and Physics*, 2018, **18**, 15743–15766.

[79] A. C. Aiken, P. F. DeCarlo, J. H. Kroll, D. R. Worsnop, J. A. Huffman, K. S. Docherty, I. M. Ulbrich, C. Mohr, J. R. Kimmel, D. Sueper, Y. Sun, Q. Zhang, A. Trimborn, M. Northway, P. J. Ziemann, M. R. Canagaratna, T. B. Onasch, M. R. Alfarra, A. S. H. Prevot, J. Dommen, J. Duplissy, A. Metzger, U. Baltensperger and J. L. Jimenez, *Environ. Sci. Tech.*, 2008, **42**, 4478–4485.

[80] A. M. J. Rickards, R. E. H. Miles, J. F. Davies, F. H. Marshall and J. P. Reid, *The Journal of Physical Chemistry A*, 2013, **117**, 14120–14131.

[81] P. Tu and M. V. Johnston, *Atmospheric Chemistry and Physics*, 2017, **17**, 7593–7603.

[82] J. H. Kroll, N. M. Donahue, J. L. Jimenez, S. H. Kessler, M. R. Canagaratna, K. R. Wilson, K. E. Altieri, L. R. Mazzoleni, A. S. Wozniak, H. Bluhm, E. R. Mysak, J. D. Smith, C. E. Kolb and D. R. Worsnop, *Nature Chemistry*, 2011, **3**, 133–139.

[83] Q. Chen, C. L. Heald, J. L. Jimenez, M. R. Canagaratna, Q. Zhang, L.-Y. He, X.-F. Huang, P. Campuzano-Jost, B. B. Palm, L. Poulain, M. Kuwata, S. T. Martin, J. P. D. Abbatt, A. K. Y. Lee and J. Liggio, *Geophys. Res. Lett.*, 2015, **42**, 2015GL063693.

[84] R. von Wandruszka, *Geochemical Transactions*, 2000, **1**, 10.

[85] L. Filiciotto, G. de Miguel, A. M. Balu, A. A. Romero, J. C. van der Waal and R. Luque, *Chemical Communications*, 2017, **53**, 7015–7017.

[86] P. Lin, J. Z. Yu, G. Engling and M. Kalberer, *Environmental Science & Technology*, 2012, **46**, 13118–13127.

[87] N. L. Ng, M. R. Canagaratna, Q. Zhang, J. L. Jimenez, J. Tian, I. M. Ulbrich, J. H. Kroll, K. S. Docherty, P. S. Chhabra, R. Bahreini, S. M. Murphy, J. H. Seinfeld, L. Hildebrandt,

N. M. Donahue, P. F. DeCarlo, V. A. Lanz, A. S. H. Prevot, E. Dinar, Y. Rudich and D. R. Worsnop, *Atmospheric Chemistry and Physics*, 2010, **10**, 4625–4641.

[88] Y. Ma, Y. Cheng, X. Qiu, G. Cao, Y. Fang, J. Wang, T. Zhu, J. Yu and D. Hu, *Atmospheric Chemistry and Physics*, 2018, **18**, 5607–5617.

[89] S. Park and S.-C. Son, *Environ. Sci.: Processes Impacts*, 2016, **18**, 32–41.

[90] S. Decesari, S. Fuzzi, M. C. Facchini, M. Mircea, L. Emblico, F. Cavalli, W. Maenhaut, X. Chi, G. Schkolnik, A. Falkovich, Y. Rudich, M. Claeys, V. Pashynska, G. Vas, I. Kourtchev, R. Vermeylen, A. Hoffer, M. O. Andreae, E. Tagliavini, F. Moretti and P. Artaxo, *Atmospheric Chemistry and Physics*, 2006, **6**, 375–402.

[91] D. E. Romonosky, Y. Li, M. Shiraiwa, A. Laskin, J. Laskin and S. A. Nizkorodov, *The Journal of Physical Chemistry A*, 2017, **121**, 1298–1309.

[92] J. Liu, P. Lin, A. Laskin, J. Laskin, S. M. Kathmann, M. Wise, R. Caylor, F. Imholt, V. Selimovic and J. E. Shilling, *Atmospheric Chemistry and Physics*, 2016, **16**, 12815–12827.

[93] S. Rossignol, K. Z. Aregahegn, L. Tinel, L. Fine, B. Nozière and C. George, *Environmental science & technology*, 2014, **48**, 3218–27.

[94] J. Kua, H. E. Krizner and D. O. De Haan, *The Journal of Physical Chemistry A*, 2011, **115**, 1667–1675.

[95] A. Virtanen, J. Joutsensaari, T. Koop, J. Kannosto, P. Yli-Pirilä, J. Leskinen, J. M. Mäkelä, J. K. Holopainen, U. Pöschl, M. Kulmala, D. R. Worsnop and A. Laaksonen, *Nature*, 2010, **467**, 824–827.

[96] M. Shiraiwa, A. Zuend, A. K. Bertram and J. H. Seinfeld, *Physical Chemistry Chemical Physics*, 2013, **15**, 11441.

[97] R. A. Zaveri, R. C. Easter, J. E. Shilling and J. H. Seinfeld, *Atmospheric Chemistry and Physics*, 2014, **14**, 5153–5181.

[98] C. Denjean, P. Formenti, B. Picquet-Varrault, E. Pangui, P. Zapf, Y. Katrib, C. Giorio, A. Tapparo, A. Monod, B. Temime-Roussel, P. Decorse, C. Mangeney and J. F. Doussin, *Atmospheric Chemistry and Physics*, 2015, **15**, 3339–3358.

[99] V. Varutbangkul, F. J. Brechtel, R. Bahreini, N. L. Ng, M. D. Keywood, J. H. Kroll, R. C. Flagan, J. H. Seinfeld, A. Lee and A. H. Goldstein, *Atmos. Chem. Phys.*, 2006, **6**, 2367–2388.

[100] J. Duplissy, P. F. DeCarlo, J. Dommen, M. R. Alfarra, A. Metzger, I. Barmpadimos, A. S. H. Prevot, E. Weingartner, T. Tritscher, M. Gysel, A. C. Aiken, J. L. Jimenez, M. R. Canagaratna, D. R. Worsnop, D. R. Collins, J. Tomlinson and U. Baltensperger, *Atmos. Chem. Phys.*, 2011, **11**, 1155–1165.

[101] M. D. Petters and S. M. Kreidenweis, *Atmospheric Chemistry and Physics*, 2007, **7**, 1961–1971.

[102] D. Hu, D. Topping and G. McFiggans, *Atmospheric Chemistry and Physics*, 2018, **18**, 14925–14937.

[103] D. Topping, P. Connolly and G. McFiggans, *Nature Geoscience*, 2013, **6**, 443–446.

[104] A. J. Prenni, M. D. Petters, A. Faulhaber, C. M. Carrico, P. J. Ziemann, S. M. Kreidenweis and P. J. DeMott, *Geophysical Research Letters*, 2009, **36**, L06808.

[105] R. Wagner, K. H?hler, W. Huang, A. Kiselev, O. M?hler, C. Mohr, A. Pajunoja, H. Saathoff, T. Schiebel, X. Shen and A. Virtanen, *Journal of Geophysical Research: Atmospheres*, 2017, **122**, 4924–4943.

[106] W. Frey, D. Hu, J. Dorsey, M. R. Alfarra, A. Pajunoja, A. Virtanen, P. Connolly and G. McFiggans, *Atmospheric Chemistry and Physics*, 2018, **18**, 9393–9409.

[107] Z. A. Kanji, R. C. Sullivan, M. Niemand, P. J. DeMott, A. J. Prenni, C. Chou, H. Saathoff and O. Möhler, *Atmospheric Chemistry and Physics*, 2019, **19**, 5091–5110.

[108] C. Y. Gao, S. E. Bauer and K. Tsigaridis, *Atmospheric Chemistry and Physics*, 2018, **18**, 14243–14251.

[109] P. J. Connolly, D. O. Topping, F. Malavelle and G. McFiggans, *Atmospheric Chemistry and Physics*, 2014, **14**, 2289–2302.

[110] T. Koop, B. Luo, A. Tsias and T. Peter, *Nature*, 2000, **406**, 611–614.

[111] T. Berkemeier, M. Shiraiwa, U. Pöschl and T. Koop, *Atmospheric Chemistry and Physics*, 2014, **14**, 12513–12531.

[112] D. M. Lienhard, A. J. Huisman, U. K. Krieger, Y. Rudich, C. Marcolli, B. P. Luo, D. L. Bones, J. P. Reid, A. T. Lambe, M. R. Canagaratna, P. Davidovits, T. B. Onasch, D. R. Worsnop, S. S. Steimer, T. Koop and T. Peter, *Atmospheric Chemistry and Physics Discussions*, 2015, **15**, 24473–24511.

[113] Q. Wang, L. Zhao, C. Li and Z. Cao, *Scientific Reports*, 2016, **6**, 26831.

[114] C. R. Ruehl, J. F. Davies and K. R. Wilson, *Science*, 2016, **351**, 1447–1450.

[115] D. J. Cziczo, K. D. Froyd, C. Hoose, E. J. Jensen, M. Diao, M. A. Zondlo, J. B. Smith, C. H. Twohy and D. M. Murphy, *Science*, 2013, **340**, 1320–1324.

[116] L. Nandy and C. S. Dutcher, *The Journal of Physical Chemistry B*, 2018, **122**, 3480–3490.

[117] R. E. O'Brien, B. Wang, S. T. Kelly, N. Lundt, Y. You, A. K. Bertram, S. R. Leone, A. Laskin and M. K. Gilles, *Environmental Science & Technology*, 2015, **49**, 4995–5002.

[118] S. Ham, Z. B. Babar, J. B. Lee, H.-J. Lim and M. Song, *Atmospheric Chemistry and Physics*, 2019, **19**, 9321–9331.

[119] A. Zuend, C. Marcolli, T. Peter and J. H. Seinfeld, *Atmos. Chem. Phys*, 2010, **10**, 7795–7820.

[120] M. Song, C. Marcolli, U. K. Krieger, A. Zuend and T. Peter, *Atmospheric Chemistry and Physics*, 2012, **12**, 2691–2712.

[121] L. Renbaum-Wolff, M. Song, C. Marcolli, Y. Zhang, P. F. Liu, J. W. Grayson, F. M. Geiger, S. T. Martin and A. K. Bertram, *Atmospheric Chemistry and Physics*, 2016, **16**, 7969–7979.

[122] S. Takahama, S. Liu and L. M. Russell, *Journal of Geophysical Research*, 2010, **115**, D01202.

[123] H. Tanaka, T. Kawasaki, H. Shintani and K. Watanabe, *Nature Materials*, 2010, **9**, 324–331.

[124] J. S. Langer, *Reports on Progress in Physics*, 2014, **77**, 042501.

[125] K. Ngai, in *Physical Properties of Polymers*, Cambridge University Press, Cambridge, 3rd edn., 2004, ch. 2, pp. 73–146.

[126] J. F. Douglas and D. Leporini, 1998, **237**, 137–141.

[127] T. Blochowicz, S. Schramm, S. Lusceac, M. Vogel, B. Stühn, P. Gutfreund and B. Frick, *Physical Review Letters*, 2012, **109**, 035702.

[128] F. Fernandez-Alonso, F. J. Bermejo, S. E. McLain, J. F. Turner, J. J. Molaison and K. W. Herwig, *Physical Review Letters*, 2007, **98**, 077801.

[129] M. Tarnacka, W. K. Kipnusu, E. Kaminska, S. Pawlus, K. Kaminski and M. Paluch, *Phys. Chem. Chem. Phys.*, 2016, **18**, 23709–23714.

[130] B. Zobrist, C. Marcolli, D. a. Pedernera and T. Koop, *Atmospheric Chemistry and Physics*, 2008, **8**, 5221–5244.

[131] H. P. Dette and T. Koop, *The Journal of Physical Chemistry A*, 2015, **119**, 4552–4561.

[132] B. Zobrist, V. Soonsin, B. P. Luo, U. K. Krieger, C. Marcolli, T. Peter and T. Koop, *Physical Chemistry Chemical Physics*, 2011, **13**, 3514–26.

[133] N. A. Hosny, C. Fitzgerald, C. Tong, M. Kalberer, M. K. Kuimova and F. D. Pope, *Faraday Discussions*, 2013, **165**, 343.

[134] H. J. Tong, J. P. Reid, D. L. Bones, B. P. Luo and U. K. Krieger, *Atmospheric Chemistry and Physics*, 2011, **11**, 4739–4754.

[135] E. Mikhailov, S. Vlasenko, S. T. Martin, T. Koop and U. Pöschl, *Atmospheric Chemistry and Physics*, 2009, **9**, 9491–9522.

[136] N. Riemer, A. P. Ault, M. West, R. L. Craig and J. H. Curtis, *Reviews of Geophysics*, 2019, 2018RG000615.

[137] T. Koop, J. Bookhold, M. Shiraiwa and U. Pöschl, *Phys. Chem. Chem. Phys.*, 2011, **13**, 19238–55.

[138] B. J. Murray, *Atmospheric Chemistry and Physics*, 2008, **8**, 5423–5433.

[139] Y. C. Song, A. E. Haddrell, B. R. Bzdek, J. P. Reid, T. Bannan, D. O. Topping, C. Percival and C. Cai, *The Journal of Physical Chemistry A*, 2016, **120**, 8123–8137.

[140] C. Fitzgerald, N. A. Hosny, H. Tong, P. C. Seville, P. J. Gallimore, N. M. Davidson, A. Athanasiadis, S. W. Botchway, A. D. Ward, M. Kalberer, M. K. Kuimova and F. D. Pope, *Physical Chemistry Chemical Physics*, 2016, **18**, 21710–21719.

[141] A. Athanasiadis, C. Fitzgerald, N. M. Davidson, C. Giorio, S. W. Botchway, A. D. Ward, M. Kalberer, F. D. Pope and M. K. Kuimova, *Phys. Chem. Chem. Phys.*, 2016, **18**, 30385–30393.

[142] N. A. Hosny, C. Fitzgerald, A. Vyšniauskas, A. Athanasiadis, T. Berkemeier, N. Uygur, U. Pöschl, M. Shiraiwa, M. Kalberer, F. D. Pope and M. K. Kuimova, *Chemical Science*, 2016, **7**, 1357–1367.

[143] A. M. Booth, B. Murphy, I. Riipinen, C. J. Percival and D. O. Topping, *Environmental Science & Technology*, 2014, **48**, 9298–9305.

[144] L. Renbaum-Wolff, J. W. Grayson, A. P. Bateman, M. Kuwata, M. Sellier, B. J. Murray, J. E. Shilling, S. T. Martin and A. K. Bertram, *Proceedings of the National Academy of Sciences*, 2013, **110**, 8014–8019.

[145] Y. Liu, Z. Wu, Y. Wang, Y. Xiao, F. Gu, J. Zheng, T. Tan, D. Shang, Y. Wu, L. Zeng, M. Hu, A. P. Bateman and S. T. Martin, *Environmental Science & Technology Letters*, 2017, **4**, 427–432.

[146] S. Jain, K. B. Fischer and G. A. Petrucci, *Atmosphere*, 2018, **9**, 131.

[147] A. M. Maclean, C. L. Butenhoff, J. W. Grayson, K. Barsanti, J. L. Jimenez and A. K. Bertram, *Atmospheric Chemistry and Physics*, 2017, **17**, 13037–13048.

[148] T. Liu, D. D. Huang, Z. Li, Q. Liu, M. Chan and C. K. Chan, *Atmospheric Chemistry and Physics*, 2018, **18**, 5677–5689.

[149] A. P. Bateman, A. K. Bertram and S. T. Martin, *The Journal of Physical Chemistry A*, 2015, **119**, 4386–4395.

[150] M. Song, P. F. Liu, S. J. Hanna, Y. J. Li, S. T. Martin and a. K. Bertram, *Atmospheric Chemistry and Physics*, 2015, **15**, 5145–5159.

[151] J. W. Grayson, E. Evoy, M. Song, Y. Chu, A. Maclean, A. Nguyen, M. A. Upshur, M. Ebrahimi, C. K. Chan, F. M. Geiger, R. J. Thomson and A. K. Bertram, *Atmospheric Chemistry and Physics*, 2017, **17**, 8509–8524.

[152] B. R. Bzdek, L. Collard, J. E. Sprittles, A. J. Hudson and J. P. Reid, *The Journal of Chemical Physics*, 2016, **145**, 054502.

[153] B. R. Bzdek, R. M. Power, S. H. Simpson, J. P. Reid and P. Royall, *Chem. Sci.*, 2015.

[154] N. E. Rothfuss and M. D. Petters, *Aerosol. Sci. Tech.*, 2016, **50**, 1294–1305.

[155] N. E. Rothfuss and M. D. Petters, *Physical Chemistry Chemical Physics*, 2017, **19**, 6532–6545.

[156] N. E. Rothfuss and M. D. Petters, *Environmental Science & Technology*, 2017, **51**, 271–279.

[157] A. Marsh, S. S. Petters, N. E. Rothfuss, G. Rovelli, Y. C. Song, J. P. Reid and M. D. Petters, *Physical Chemistry Chemical Physics*, 2018, **20**, 15086–15097.

[158] R. A. Zaveri, R. C. Easter, J. D. Fast and L. K. Peters, *Journal of Geophysical Research*, 2008, **113**, D13204.

[159] S. O'Meara, D. O. Topping, R. A. Zaveri and G. McFiggans, *Atmospheric Chemistry and Physics*, 2017, **17**, 10477–10494.

[160] Y. Li and M. Shiraiwa, *Atmospheric Chemistry and Physics*, 2019, **19**, 5959–5971.

[161] M. Shiraiwa and J. H. Seinfeld, *Geophysical Research Letters*, 2012, **39**, 2012GL054008.

[162] M. Kanakidou, J. H. Seinfeld, S. N. Pandis, I. Barnes, F. J. Dentener, M. C. Facchini, R. Van Dingenen, B. Ervens, A. Nenes, C. J. Nielsen, E. Swietlicki, J. P. Putaud, Y. Balkanski, S. Fuzzi, J. Horth, G. K. Moortgat, R. Winterhalter, C. E. L. Myhre, K. Tsigaridis, E. Vignati, E. G. Stephanou and J. Wilson, *Atmospheric Chemistry and Physics*, 2005, **5**, 1053–1123.

[163] L. T. Molina, J. E. Spencer and M. J. Molina, *Chemical Physics Letters*, 1977, **45**, 158–162.

[164] U. Pöschl, T. Letzel, C. Schauer and R. Niessner, *The Journal of Physical Chemistry A*, 2001, **105**, 4029–4041.

[165] M. J. Ezell, S. N. Johnson, Y. Yu, V. Perraud, E. A. Bruns, M. L. Alexander, A. Zelenyuk, D. Dabdub and B. J. Finlayson-Pitts, *Aerosol. Sci. Technol.*, 2010, **44**, 329–338.

[166] M. Sarrafzadeh, J. Wildt, I. Pullinen, M. Springer, E. Kleist, R. Tillmann and A. Kiendlerscharr, *Atmos. Chem. Phys.*, 2016, **16**, 11237–11248.

[167] W. Huang, H. Saathoff, A. Pajunoja, X. Shen, K.-H. Naumann, R. Wagner, A. Virtanen, T. Leisner and C. Mohr, *Atmospheric Chemistry and Physics*, 2018, **18**, 2883–2898.

[168] K. L. Pereira, R. Dunmore, J. Whitehead, M. R. Alfarra, J. D. Allan, M. S. Alam, R. M. Harrison, G. McFiggans and J. F. Hamilton, *Atmospheric Chemistry and Physics*, 2018, **18**, 11073–11096.

[169] J. F. Hamilton, M. T. Baeza-Romero, E. Finessi, A. R. Rickard, R. M. Healy, S. Peppe, T. J. Adams, M. J. S. Daniels, S. M. Ball, I. C. A. Goodall, P. S. Monks, E. Borrás and A. Muñoz, *Faraday Discussions*, 2013, **165**, 447.

[170] J. Duplissy, M. B. Enghoff, K. L. Aplin, F. Arnold, H. Aufmhoff, M. Avngaard, U. Baltensperger, T. Bondo, R. Bingham, K. Carslaw, J. Curtius, A. David, B. Fastrup, S. Gagne, F. Hahn, R. G. Harrison, B. Kellett, J. Kirkby, M. Kulmala, L. Laakso, A. Laaksonen, E. Lillestol, M. Lockwood, J. Makela, V. Makhmutov, N. D. Marsh, T. Nieminen, A. Onnela, E. Pedersen, J. O. P. Pedersen, J. Polny, U. Reichl, J. H. Seinfeld, M. Sipila, Y. Stozhkov, F. Stratmann, H. Svensmark, J. Svensmark, R. Veenhof, B. Verheggen, Y. Viisanen, P. E. Wagner, G. Wehrle, E. Weingartner, H. Wex, M. Wilhelmsson and P. M. Winkler, *Atmos. Chem. Phys.*, 2010, **10**, 1635–1647.

[171] J. Kirkby, J. Curtius, J. Almeida, E. Dunne, J. Duplissy, S. Ehrhart, A. Franchin, S. Gagné, L. Ickes, A. Kürten, A. Kupc, A. Metzger, F. Riccobono, L. Rondo, S. Schobesberger, G. Tsagkogeorgas, D. Wimmer, A. Amorim, F. Bianchi, M. Breitenlechner, A. David, J. Dommen, A. Downard, M. Ehn, R. C. Flagan, S. Haider, A. Hansel, D. Hauser, W. Jud, H. Junninen, F. Kreissl, A. Kvashin, A. Laaksonen, K. Lehtipalo, J. Lima, E. R. Lovejoy, V. Makhmutov, S. Mathot, J. Mikkilä, P. Minginette, S. Mogo, T. Nieminen, A. Onnela, P. Pereira, T. Petäjä, R. Schnitzhofer, J. H. Seinfeld, M. Sipilä, Y. Stozhkov, F. Stratmann, A. Tomé, J. Vanhanen, Y. Viisanen, A. Vrtala, P. E. Wagner, H. Walther, E. Weingartner,

H. Wex, P. M. Winkler, K. S. Carslaw, D. R. Worsnop, U. Baltensperger and M. Kulmala, *Nature*, 2011, **476**, 429–433.

[172] F. Riccobono, S. Schobesberger, C. E. Scott, J. Dommen, I. K. Ortega, L. Rondo, J. Almeida, A. Amorim, F. Bianchi, M. Breitenlechner, A. David, A. Downard, E. M. Dunne, J. Duplissy, S. Ehrhart, R. C. Flagan, A. Franchin, A. Hansel, H. Junninen, M. Kajos, H. Keskinen, A. Kupc, A. Kurten, A. N. Kvashin, A. Laaksonen, K. Lehtipalo, V. Makhmutov, S. Mathot, T. Nieminen, A. Onnela, T. Petaja, A. P. Praplan, F. D. Santos, S. Schallhart, J. H. Seinfeld, M. Sipila, D. V. Spracklen, Y. Stozhkov, F. Stratmann, A. Tome, G. Tsagkogeorgas, P. Vaattovaara, Y. Viisanen, A. Vrtala, P. E. Wagner, E. Weingartner, H. Wex, D. Wimmer, K. S. Carslaw, J. Curtius, N. M. Donahue, J. Kirkby, M. Kulmala, D. R. Worsnop and U. Baltensperger, *Science*, 2014, **344**, 717–721.

[173] D. L. Bones, J. P. Reid, D. M. Lienhard and U. K. Krieger, *Proc. Nat. Acad. Sci.*, 2012, **109**, 11613–8.

[174] E. Abramson, D. Imre, J. Beránek, J. Wilson and A. Zelenyuk, *Physical Chemistry Chemical Physics*, 2013, **15**, 2983.

[175] S. Bastelberger, U. K. Krieger, B. Luo and T. Peter, *Atmospheric Chemistry and Physics*, 2017, **17**, 8453–8471.

[176] R. M. Power, S. H. Simpson, J. P. Reid and A. J. Hudson, *Chemical Science*, 2013, **4**, 2597–2604.

[177] L. Renbaum-Wolff, J. W. Grayson, A. P. Bateman, M. Kuwata, M. Sellier, B. J. Murray, J. E. Shilling, S. T. Martin and A. K. Bertram, *Proceedings of the National Academy of Sciences*, 2013, **110**, 8014–8019.

[178] P. Struntz and M. Weiss, *Physical Chemistry Chemical Physics*, 2018, **20**, 28910–28919.

[179] D. A. Ullmann, M. L. Hinks, A. Maclean, C. Butenhoff, J. Grayson, K. Barsanti, J. L. Jimenez, S. A. Nizkorodov, S. Kamal and A. K. Bertram, *Atmospheric Chemistry and Physics*, 2019, **19**, 149–1503.

[180] D. M. Lienhard, A. J. Huisman, D. L. Bones, Y.-F. Te, B. P. Luo, U. K. Krieger and J. P. Reid, *Physical Chemistry Chemical Physics*, 2014, **16**, 16677.

[181] H. C. Price, J. Mattsson, Y. Zhang, A. K. Bertram, J. F. Davies, J. W. Grayson, S. T. Martin, D. O'Sullivan, J. P. Reid, A. M. J. Rickards and B. J. Murray, *Chem. Sci.*, 2015, **6**, 4876–4883.

[182] J. F. Davies and K. R. Wilson, *Analytical Chemistry*, 2016, **88**, 2361–2366.

[183] X. Li, T. Hede, Y. Tu, C. Leck and H. Ågren, *Atmospheric Chemistry and Physics*, 2011, **11**, 519–527.

[184] H. C. Price, B. J. Murray, J. Mattsson, D. O'Sullivan, T. W. Wilson, K. J. Baustian and L. G. Benning, *Atmospheric Chemistry and Physics*, 2014, **14**, 3817–3830.

[185] H. C. Price, J. Mattsson and B. J. Murray, *Phys. Chem. Chem. Phys.*, 2016, **18**, 19207–19216.

[186] D. Hegg, S. Gao, W. Hoppel, G. Frick, P. Caffrey, W. Leaitch, N. Shantz, J. Ambrusko and T. Albrechcinski, *Atmospheric Research*, 2001, **58**, 155–166.

[187] K. E. Huff Hartz, T. Rosenørn, S. R. Ferchak, T. M. Raymond, M. Bilde, N. M. Donahue and S. N. Pandis, *Journal of Geophysical Research: Atmospheres*, 2005, **110**, D14208.

[188] X. Tang, D. R. Cocker and A. Asa-Awuku, *Atmospheric Chemistry and Physics*, 2012, **12**, 8377–8388.

[189] R. R. Dickerson, S. Kondragunta, G. Stenchikov, K. L. Civerolo, B. G. Doddridge and B. N. Holben, *Science*, 1997, **278**, 827–830.

[190] R.-J. Huang, Y. Zhang, C. Bozzetti, K.-F. Ho, J.-J. Cao, Y. Han, K. R. Daellenbach, J. G. Slowik, S. M. Platt, F. Canonaco, P. Zotter, R. Wolf, S. M. Pieber, E. A. Bruns, M. Crippa, G. Ciarelli, A. Piazzalunga, M. Schwikowski, G. Abbaszade, J. Schnelle-Kreis, R. Zimmermann, Z. An, S. Szidat, U. Baltensperger, I. E. Haddad and A. S. H. Prévôt, *Nature*, 2014, **514**, 218–222.

[191] A. Valenzuela, J. P. Reid, B. R. Bzdek and A. J. Orr-Ewing, *Journal of Geophysical Research-Atmospheres*, 2018, **123**, 6469–6486.

[192] S. N. Pandis, N. M. Donahue, B. N. Murphy, I. Riipinen, C. Fountoukis, E. Karnezi, D. Patoulias and K. Skyllakou, *Faraday Discuss.*, 2013, **165**, 9–24.

[193] S. Takahama and L. M. Russell, *Journal of Geophysical Research*, 2011, **116**, D02203.

[194] N. Fukuta and L. A. Walter, *Journal of the Atmospheric Sciences*, 1970, **27**, 1160–1172.

[195] A. T. Liu, R. A. Zaveri and J. H. Seinfeld, *Atmospheric Environment*, 2014, **89**, 651–654.

[196] A. Moridnejad and T. C. Preston, *The Journal of Physical Chemistry A*, 2016, **120**, 9759–9766.

[197] K. Gatzsche, Y. Iinuma, A. Tilgner, A. Mutzel, T. Berndt and R. Wolke, *Atmospheric Chemistry and Physics*, 2017, **17**, 13187–13211.

[198] S. O'Meara, D. Topping and G. McFiggans, *Atmospheric Chemistry and Physics*, 2016, **16**, 5299–5313.

[199] H. Mai, M. Shiraiwa, R. C. Flagan and J. H. Seinfeld, *Environmental Science & Technology*, 2015, **49**, 11485–11491.

[200] Y. Ma, T. R. Willcox, A. T. Russell and G. Marston, *Chem. Commun.*, 2007, 1328–1330.

[201] G. Duporté, M. Riva, J. Parshintsev, E. Heikkinen, L. M. F. Barreira, N. Myllys, L. Heikkinen, K. Hartonen, M. Kulmala, M. Ehn and M.-L. Riekkola, *Environmental Science & Technology*, 2017, **51**, 5602–5610.

[202] X. Li, T. Hede, Y. Tu, C. Leck and H. Ågren, *The Journal of Physical Chemistry Letters*, 2010, **1**, 769–773.

[203] Seinfeld, John H. and S. N. Pandis, *Atmospheric Chemistry and Physics*, John Wiley & Sons Ltd., 1st edn., 1998.

[204] M. Shiraiwa, M. Ammann, T. Koop and U. Poschl, *Proceedings of the National Academy of Sciences*, 2011, **108**, 11003–11008.

[205] M. Shiraiwa and J. H. Seinfeld, *Geophysical Research Letters*, 2012, **39**, L24801.

[206] T. Berkemeier, S. S. Steimer, U. K. Krieger, T. Peter, U. Pöschl, M. Ammann and M. Shiraiwa, *Phys. Chem. Chem. Phys.*, 2016, **18**, 12662–12674.

[207] R. Krishna, *Chemical Society Reviews*, 2015, **44**, 2812–2836.

[208] K. L. Ngai, *The European Physical Journal E - Soft Matter*, 2003, **12**, 93–100.

[209] N. Ramesh, P. K. Davis, J. M. Zielinski, R. P. Danner and J. L. Duda, *Journal of Polymer Science Part B: Polymer Physics*, 2011, **49**, 1629–1644.

[210] F. H. Marshall, T. Berkemeier, M. Shiraiwa, P. B. Ohm, S. Dutcher and J. P. Reid, *Phys. Chem. Chem. Phys.*, 2018, **20**, 15560–15573.

[211] M. Song, P. F. Liu, S. J. Hanna, R. A. Zaveri, K. Potter, Y. You, S. T. Martin and A. K. Bertram, *Atmospheric Chemistry and Physics*, 2016, **16**, 8817–8830.

[212] U. Pöschl, Y. Rudich and M. Ammann, *Atmospheric Chemistry and Physics*, 2007, **7**, 5989–6023.

[213] A. C. Vander Wall, P. S. J. Lakey, E. Rossich Molina, V. Perraud, L. M. Wingen, J. Xu, D. Soulsby, R. B. Gerber, M. Shiraiwa and B. J. Finlayson-Pitts, *Environmental Science: Processes & Impacts*, 2018, **20**, 1593–1610.

[214] T. Berkemeier, M. Ammann, U. K. Krieger, T. Peter, P. Spichtinger, U. Pöschl, M. Shiraiwa and A. J. Huisman, *Atmospheric Chemistry and Physics*, 2017, **17**, 8021–8029.

[215] R. Symes, R. M. Sayer and J. P. Reid, *Physical Chemistry Chemical Physics*, 2004, **6**, 474.

[216] L. Mitchem and J. P. Reid, *Chemical Society Reviews*, 2008, **37**, 756.

[217] J. P. Reid and L. Mitchem, *Annual Review of Physical Chemistry*, 2006, **57**, 245–271.

[218] J. B. Wills, K. J. Knox and J. P. Reid, *Chemical Physics Letters*, 2009, **481**, 153–165.

[219] A. Ashkin and J. M. Dziedzic, *Applied Physics Letters*, 1971, **19**, 283–285.

[220] A. Ashkin, J. M. Dziedzic, J. E. Bjorkholm and S. Chu, *Optics Letters*, 1986, **11**, 288–290.

[221] J. E. Hawkins and G. T. Armstrong, *Journal of the American Chemical Society*, 1954, **76**, 3756–3758.

[222] F. H. Marshall, R. E. H. Miles, Y.-C. Song, P. B. Ohm, R. M. Power, J. P. Reid and C. S. Dutcher, *Chem. Sci.*, 2016, **7**, 1298–1308.

[223] K. Kristensen, T. Cui, H. Zhang, A. Gold, M. Glasius and J. D. Surratt, *Atmospheric Chemistry and Physics*, 2014, **14**, 4201–4218.

[224] V. Gorshelev, A. Serdyuchenko, M. Weber, W. Chehade and J. P. Burrows, *Atmospheric Measurement Techniques*, 2014, **7**, 609–624.

[225] S. Nie, *Science*, 1997, **275**, 1102–1106.

[226] B. Pettinger, B. Ren, G. Picardi, R. Schuster and G. Ertl, *Physical Review Letters*, 2004, **92**, 096101.

[227] P. Nissenson, C. J. H. Knox, B. J. Finlayson-Pitts, L. F. Phillips and D. Dabdub, *Physical Chemistry Chemical Physics*, 2006, **8**, 4700–4710.

[228] A. Moridnejad, T. C. Preston and U. K. Krieger, *The Journal of Physical Chemistry A*, 2017, **121**, 8176–8184.

[229] A. K. Ray, A. Souyri, E. J. Davis and T. M. Allen, *Applied Optics*, 1991, **30**, 3974.

[230] J. Archer, *Ph.D. thesis*, Polish Academy of Sciences, 2017.

[231] T. C. Preston and J. P. Reid, *Journal of the Optical Society of America B*, 2013, **30**, 2113.

[232] K. Gorkowski, N. M. Donahue and R. C. Sullivan, *Environmental Science: Processes & Impacts*, 2018, **20**, 1512–1523.

[233] O. B. Toon and T. P. Ackerman, *Applied Optics*, 1981, **20**, 3657.

[234] A. K. Ray and R. Nandakumar, *Applied Optics*, 1995, **34**, 7759.

[235] D. J. Stewart, C. Cai, J. Nayler, T. C. Preston, J. P. Reid, U. K. Krieger, C. Marcolli and Y. H. Zhang, *The Journal of Physical Chemistry A*, 2015, **119**, 4177–4190.

[236] K. Gorkowski, H. Beydoun, M. Aboff, J. S. Walker, J. P. Reid and R. C. Sullivan, *Aerosol Science and Technology*, 2016, **50**, 1327–1341.

[237] K. Gorkowski, N. M. Donahue and R. C. Sullivan, *Environmental Science & Technology*, 2017, **51**, 12154–12163.

[238] S. Lyu, V. Mathai, Y. Wang, B. Sobac, P. Colinet, D. Lohse and C. Sun, *Science Advances*, 2019, **5**, eaav8081.

[239] F. H. Stillinger and A. Rahman, *The Journal of Chemical Physics*, 1974, **60**, 1545–1557.

[240] J. A. McCammon, B. R. Gelin and M. Karplus, *Nature*, 1977, **267**, 585–590.

[241] E. Braun, J. Gilmer, H. B. Mayes, D. L. Mobley, J. I. Monroe, S. Prasad and D. M. Zuckerman, *Living Journal of Computational Molecular Science*, 2019, **1**, 5957.

[242] J. VandeVondele, M. Krack, F. Mohamed, M. Parrinello, T. Chassaing and J. Hutter, *Computer Physics Communications*, 2005, **167**, 103–128.

[243] L. Verlet, *Physical Review*, 1967, **159**, 98–103.

[244] M. P. Allen and D. J. Tildesley, *Computer Simulation of Liquids*, Oxford University Press, 2017, vol. 1.

[245] G. Bussi, D. Donadio and M. Parrinello, *The Journal of Chemical Physics*, 2007, **126**, 014101.

[246] M. Parrinello and A. Rahman, *Journal of Applied Physics*, 1981, **52**, 7182–7190.

[247] B. Hess, H. Bekker, H. J. C. Berendsen and J. G. E. M. Fraaije, *Journal of Computational Chemistry*, 1997, **18**, 1463–1472.

[248] U. Essmann, L. Perera, M. L. Berkowitz, T. Darden, H. Lee and L. G. Pedersen, *The Journal of Chemical Physics*, 1995, **103**, 8577.

[249] C. Oostenbrink, A. Villa, A. E. Mark and W. F. Van Gunsteren, *Journal of Computational Chemistry*, 2004, **25**, 1656–1676.

[250] M. Bonomi, D. Branduardi, G. Bussi, C. Camilloni, D. Provasi, P. Raiteri, D. Donadio, F. Marinelli, F. Pietrucci, R. A. Broglia and M. Parrinello, *Computer Physics Communications*, 2009, **180**, 1961–1972.

[251] J. L. F. Abascal and C. Vega, *The Journal of chemical physics*, 2005, **123**, 234505.

[252] K. B. Koziara, M. Stroet, A. K. Malde and A. E. Mark, *Journal of Computer-Aided Molecular Design*, 2014, **28**, 221–233.

[253] A. K. Malde, L. Zuo, M. Breeze, M. Stroet, D. Poger, P. C. Nair, C. Oostenbrink and A. E. Mark, *Journal of Chemical Theory and Computation*, 2011, **7**, 4026–4037.

[254] N. Schmid, A. P. Eichenberger, A. Choutko, S. Riniker, M. Winger, A. E. Mark and W. F. van Gunsteren, *European Biophysics Journal*, 2011, **40**, 843–856.

[255] L. Martínez, R. Andrade, E. G. Birgin and J. M. Martínez, *Journal of Computational Chemistry*, 2009, **30**, 2157–64.

[256] S. Páll and B. Hess, *Computer Physics Communications*, 2013, **184**, 2641–2650.

[257] M. Mezei, *Journal of Computational Physics*, 1987, **68**, 237–248.

[258] N. Metropolis, A. W. Rosenbluth, M. N. Rosenbluth, A. H. Teller and E. Teller, *The Journal of Chemical Physics*, 1953, **21**, 1087–1092.

[259] M. A. Gonzalez, E. Sanz, C. McBride, J. L. F. Abascal, C. Vega and C. Valeriani, *Phys. Chem. Chem. Phys.*, 2014, **16**, 24913–24919.

[260] S. Kumar, J. M. Rosenberg, D. Bouzida, R. H. Swendsen and P. A. Kollman, *Journal of Computational Chemistry*, 1992, **13**, 1011–1021.

[261] J. S. Hub, B. L. de Groot and D. van der Spoel, *Journal of Chemical Theory and Computation*, 2010, **6**, 3713–3720.

[262] M. J. Abraham, T. Murtola, R. Schulz, S. Páll, J. C. Smith, B. Hess and E. Lindahl, *SoftwareX*, 2015, **1-2**, 19–25.

[263] H. S. Hansen and P. H. Hünenberger, *Journal of Computational Chemistry*, 2011, **32**, 998–1032.

[264] M. L. S. Batista, G. Pérez-Sánchez, J. R. B. Gomes, J. A. P. Coutinho and E. J. Maginn, *The Journal of Physical Chemistry B*, 2015, **119**, 15310–15319.

[265] L. Sun, T. Hede, Y. Tu, C. Leck and H. Agren, *J. Phys. Chem. A*, 2013, **117**, 10746–52.

[266] K. S. Karadima, V. G. Mavrantzas and S. N. Pandis, *Phys. Chem. Chem. Phys.*, 2017, **19**, 16681–16692.

[267] R. Bahadur and L. M. Russell, *The Journal of chemical physics*, 2008, **129**, 094508.

[268] A. M. J. Rickards, Y.-C. Song, R. E. H. Miles, T. C. Preston and J. P. Reid, *Phys. Chem. Chem. Phys.*, 2015, **17**, 10059–10073.

[269] I. N. Tang and H. R. Munkelwitz, *Aerosol Science and Technology*, 1991, **15**, 201–207.

[270] S. S. Steimer, U. K. Krieger, Y.-F. Te, D. M. Lienhard, A. J. Huisman, B. P. Luo, M. Ammann and T. Peter, *Atmospheric Measurement Techniques*, 2015, **8**, 2397–2408.

[271] A. Zaragoza, M. A. Gonzalez, L. Joly, I. López-Montero, M. A. Canales, A. L. Benavides and C. Valeriani, *Physical Chemistry Chemical Physics*, 2019, **21**, 13653–13667.

[272] S. R. Becker, P. H. Poole and F. W. Starr, *Physical Review Letters*, 2006, **97**, 055901.

[273] Z. Shi, P. G. Debenedetti and F. H. Stillinger, *The Journal of Chemical Physics*, 2013, **138**, 12A526.

[274] E. J. Saltzman and K. S. Schweizer, *The Journal of Chemical Physics*, 2006, **125**, 044509.

[275] T. Savin and P. S. Doyle, *Biophysical Journal*, 2005, **88**, 623–638.

[276] X. Michalet, *Physical Review E*, 2010, **82**, 041914.

[277] T. Murata, M.-S. Lee and A. Tanioka, *Journal of Colloid and Interface Science*, 1999, **220**, 250–254.

[278] N. Nikulsin, E. R. Azhagiya Singam, G. Elliott and D. Jacobs, *Physical Chemistry Chemical Physics*, 2018, **20**, 20899–20909.

[279] N. Alcázar-Cano and R. Delgado-Buscalioni, *Soft Matter*, 2018, **14**, 9937–9949.

[280] R. Zwanzig, *Proceedings of the National Academy of Sciences*, 1988, **85**, 2029–2030.

[281] M. L. Meste, D. Champion, G. Roudaut, G. Blond and D. Simatos, *Journal of Food Science*, 2002, **67**, 2444–2458.

[282] Y. Liu, B. Bhandari and W. Zhou, *Glass transition and enthalpy relaxation of amorphous food saccharides: A review*, 2006.

[283] R. Krishna and J. Wesselingh, *Chemical Engineering Science*, 1997, **52**, 861–911.

[284] J.-P. Ryckaert, G. Ciccotti and H. J. Berendsen, *Journal of Computational Physics*, 1977, **23**, 327–341.

[285] C. Cai, R. E. H. Miles, M. I. Cotterell, A. Marsh, G. Rovelli, A. M. J. Rickards, Y. H. Zhang and J. P. Reid, *Journal of Physical Chemistry A*, 2016, **120**, 6604–6617.

[286] W. Huang, H. Saathoff, A. Pajunoja, X. Shen, K.-H. Naumann, R. Wagner, A. Virtanen, T. Leisner and C. Mohr, *Atmospheric Chemistry and Physics*, 2018, **18**, 2883–2898.

[287] C. L. Jackson and G. B. McKenna, *Journal of Non-Crystalline Solids*, 1991, **131-133**, 221–224.

[288] M. Alcoutlabi and G. B. McKenna, *Journal of Physics: Condensed Matter*, 2005, **17**, R461–R524.

[289] A. A. Zardini, S. Sjogren, C. Marcolli, U. K. Krieger, M. Gysel, E. Weingartner, U. Baltensperger and T. Peter, *Atmospheric Chemistry and Physics Discussions*, 2008, **8**, 5235–5268.

[290] G. Adler, T. Koop, C. Haspel, I. Taraniuk, T. Moise, I. Koren, R. H. Heiblum and Y. Rudich, *Proceedings of the National Academy of Sciences*, 2013, **110**, 20414–20419.

[291] D. Jakubczyk, G. Derkachov, M. Kolwas and K. Kolwas, *Journal of Quantitative Spectroscopy and Radiative Transfer*, 2013, **126**, 99–104.

[292] M. M. Fard, U. K. Krieger and T. Peter, *The Journal of Physical Chemistry A*, 2017, **121**, 9284–9296.

[293] S. Sengupta and S. Karmakar, *Journal of Chemical Physics*, 2014, **140**, 224505.

[294] A. Wisitsorasak and P. G. Wolynes, *The Journal of Physical Chemistry B*, 2014, **118**, 7835–7847.

[295] R. Baeza, A. Pérez, V. Sánchez, M. C. Zamora and J. Chirife, *Food and Bioprocess Technology*, 2010, **3**, 87–92.

[296] M. L. Hinks, M. V. Brady, H. Lignell, M. Song, J. W. Grayson, A. K. Bertram, P. Lin, A. Laskin, J. Laskin and S. A. Nizkorodov, *Phys. Chem. Chem. Phys.*, 2016, **18**, 8785–8793.

[297] A. P. Bateman, Z. Gong, T. H. Harder, S. S. de Sá, B. Wang, P. Castillo, S. China, Y. Liu, R. E. O'Brien, B. B. Palm, H.-W. Shiu, G. G. Cirino, R. Thalman, K. Adachi, M. L. Alexander, P. Artaxo, A. K. Bertram, P. R. Buseck, M. K. Gilles, J. L. Jimenez, A. Laskin, A. O. Manzi, A. Sedlacek, R. A. F. Souza, J. Wang, R. Zaveri and S. T. Martin, *Atmospheric Chemistry and Physics*, 2017, **17**, 1759–1773.

[298] Q. Ye, E. S. Robinson, X. Ding, P. Ye, R. C. Sullivan and N. M. Donahue, *Proceedings of the National Academy of Sciences*, 2016, **113**, 12649–12654.

[299] L. Berthier, G. Biroli, J.-P. Bouchaud, L. Cipelletti and W. Van Saarloos, *Dynamical Heterogeneities in Glasses, Colloids, and Granular Media*, Oxford University Press, 2011.

[300] K. Atwi, M. Baassiri, M. Fawaz and A. Shihadeh, *Atmospheric Chemistry and Physics Discussions*, 2018, 1–29.

[301] T. YliJuuti, A. Pajunoja, O.-P. Tikkanen, A. Buchholz, C. Faiola, O. Väisänen, L. Hao, E. Kari, O. Peräkylä, O. Garmash, M. Shiraiwa, M. Ehn, K. Lehtinen and A. Virtanen, *Geophysical Research Letters*, 2017, **44**, 2562–2570.

[302] Q. Ye, M. A. Upshur, E. S. Robinson, F. M. Geiger, R. C. Sullivan, R. J. Thomson and N. M. Donahue, *Chem*, 2018, **4**, 318–333.

[303] S. Ingram, C. Cai, Y.-C. Song, D. R. Glowacki, D. O. Topping, S. O'Meara and J. P. Reid, *Physical Chemistry Chemical Physics*, 2017, **19**, 31634–31646.

[304] T. C. Preston and J. P. Reid, *Journal of the Optical Society of America A*, 2015, **32**, 2210.

[305] S. Sengupta, S. Karmakar, C. Dasgupta and S. Sastry, *The Journal of Chemical Physics*, 2013, **138**, 12A548.

[306] M. Potuzak, R. C. Welch and J. C. Mauro, *The Journal of Chemical Physics*, 2011, **135**, 214502.

[307] J. C. Phillips, *Reports on Progress in Physics*, 1996, **59**, 1133–1207.

[308] J. S. Langer, *Physical Review E*, 2012, **85**, 051507.

[309] J. H. Wu and Q. Jia, *Scientific Reports*, 2016, **6**, 2–11.

[310] J. Trzmiel, K. Weron, J. Janczura and E. Placzek-Popko, *Journal of Physics: Condensed Matter*, 2009, **21**, 345801.

[311] P. G. Debenedetti and F. H. Stillinger, *Nature*, 2001, **410**, 259–267.

[312] J. F. Davies, A. E. Haddrell and J. P. Reid, *Aerosol Science and Technology*, 2012, **46**, 666–677.

[313] M. Starzak and S. D. Peacock, *Zuckerindustrie*, 1997, **122**, 380–387.

[314] M. McGlashan, *Journal of Chemical Education*, 1963, **40**, 516–518.

[315] J. W. Lu, A. M. J. Rickards, J. S. Walker, K. J. Knox, R. E. H. Miles, J. P. Reid and R. Signorell, *Phys. Chem. Chem. Phys.*, 2014, **16**, 9819–9830.

[316] U. K. Krieger, C. Marcolli and J. P. Reid, *Chemical Society Reviews*, 2012, **41**, 6631.

[317] J. Julin, M. Shiraiwa, R. E. H. Miles, J. P. Reid, U. Pöschl and I. Riipinen, *The Journal of Physical Chemistry A*, 2013, **117**, 410–420.

[318] J. P. Reid, A. K. Bertram, D. O. Topping, A. Laskin, S. T. Martin, M. D. Petters, F. D. Pope and G. Rovelli, *Nature Communications*, 2018, **9**, 956.

[319] D. M. Saylor, S. Jawahery, J. S. Silverstein and C. Forrey, *The Journal of Chemical Physics*, 2016, **145**, 031106.

[320] G. Tarjus and D. Kivelson, *The Journal of Chemical Physics*, 1995, **103**, 3071.

[321] P. Kumar, *Proceedings of the National Academy of Sciences*, 2006, **103**, 12955–12956.

[322] M. A. Gonzalez, J. L. F. Abascal, C. Valeriani and F. Bresme, *The Journal of Chemical Physics*, 2015, **142**, 154903.

[323] P. Kumar, *Proceedings of the National Academy of Sciences*, 2006, **103**, 12955–12956.

[324] F. Mallamace, C. Branca, M. Broccio, C. Corsaro, N. Gonzalez-Segredo, J. Spooren, H. E. Stanley and S.-H. Chen, *The European Physical Journal Special Topics*, 2008, **161**, 19–33.

[325] B. Chen, E. E. Sigmund and W. P. Halperin, *Physical Review Letters*, 2006, **96**, 145502.

[326] Q. Liu, S. Huang and Z. Suo, *Physical Review Letters*, 2015, **114**, 224301.

[327] H. Švajdlenková, S. Arrese-Igor, Z. Nógellová, A. Alegría and J. Bartoš, *Phys. Chem. Chem. Phys.*, 2017, **19**, 15215–15226.

[328] K. R. Harris, *Journal of Chemical Physics*, 2009, **131**, 054503.

[329] J. D. Rindelaub, J. S. Wiley, B. R. Cooper and P. B. Shepson, *Rapid Communications in Mass Spectrometry*, 2016, **30**, 1627–1638.

[330] D. Bosse, *Ph.D. thesis*, Kaiserslautern University of Technology, 2004.

[331] R. E. H. Miles, J. S. Walker, D. R. Burnham and J. P. Reid, *Physical Chemistry Chemical Physics*, 2012, **14**, 3037.

[332] G. Rovelli, Y.-C. Song, A. M. Maclean, D. O. Topping, A. K. Bertram and J. P. Reid, *Analytical Chemistry*, 2019, **91**, 5074–5082.

[333] J. W. Grayson, E. Evoy, M. Song, Y. Chu, A. Maclean, A. Nguyen, M. A. Upshur, M. Ebrahimi, C. K. Chan, F. M. Geiger, R. J. Thomson and A. K. Bertram, *Atmospheric Chemistry and Physics*, 2017, **17**, 8509–8524.

[334] C. Cai, D. J. Stewart, T. C. Preston, J. S. Walker, Y.-H. Zhang and J. P. Reid, *Physical Chemistry Chemical Physics*, 2014, **16**, 3162.

[335] G. D. Kinzer and R. Gunn, *Journal of Meteorology*, 1951, **8**, 71–83.

[336] C. S. Dutcher, X. L. Ge, A. S. Wexler and S. L. Clegg, *Journal of Physical Chemistry C*, 2012, **116**, 1850–1864.

[337] P. B. Ohm and C. S. Dutcher, *Journal of Physical Chemistry A*, 2016, **120**, 4147 4154.

[338] H. Wex, F. Stratmann, D. Topping and G. McFiggans, *Journal of the Atmospheric Sciences*, 2008, **65**, 4004–4016.

[339] P. Massoli, A. T. Lambe, A. T. Ahern, L. R. Williams, M. Ehn, J. Mikkila, M. R. Canagaratna, W. H. Brune, T. B. Onasch, J. T. Jayne, T. Petaja, M. Kulmala, A. Laaksonen, C. E. Kolb, P. Davidovits and D. R. Worsnop, *Geophys. Res. Lett.*, 2010, **37**, 5.

[340] W.-S. W. DeRieux, Y. Li, P. Lin, J. Laskin, A. Laskin, A. K. Bertram, S. A. Nizkorodov and M. Shiraiwa, *Atmospheric Chemistry and Physics*, 2018, **18**, 6331–6351.

[341] V. Soonsin, A. A. Zardini, C. Marcolli, A. Zuend and U. K. Krieger, *Atmospheric Chemistry and Physics*, 2010, **10**, 11753–11767.

[342] O.-P. Tikkanen, V. Hämäläinen, G. Rovelli, A. Lipponen, M. Shiraiwa, J. P. Reid, K. E. J. Lehtinen and T. Yli-Juuti, *Atmospheric Chemistry and Physics*, 2019, **19**, 9333–9350.

[343] G. Rovelli, R. E. H. Miles, J. P. Reid and S. L. Clegg, *The Journal of Physical Chemistry A*, 2016, **120**, 4376–4388.

[344] F. D. Lopez-Hilfiker, C. Mohr, M. Ehn, F. Rubach, E. Kleist, J. Wildt, T. F. Mentel, A. J. Carrasquillo, K. E. Daumit, J. F. Hunter, J. H. Kroll, D. R. Worsnop and J. A. Thornton, *Atmospheric Chemistry and Physics*, 2015, **15**, 7765–7776.

[345] K. Sato, Y. Fujitani, S. Inomata, Y. Morino, K. Tanabe, S. Ramasamy, T. Hikida, A. Shimono, A. Takami, A. Fushimi, Y. Kondo, T. Imamura, H. Tanimoto and S. Sugata, *Atmospheric Chemistry and Physics*, 2018, **18**, 5455–5466.

[346] M. Shrivastava, A. Zelenyuk, D. Imre, R. Easter, J. Beranek, R. A. Zaveri and J. Fast, *Journal of Geophysical Research: Atmospheres*, 2013, **118**, 3328–3342.

[347] C. Meusinger, U. Dusek, S. M. King, R. Holzinger, T. Rosenørn, P. Sperlich, M. Julien, G. S. Remaud, M. Bilde, T. Röckmann and M. S. Johnson, *Atmospheric Chemistry and Physics*, 2017, **17**, 6373–6391.

[348] R. L. Mauldin III, T. Berndt, M. Sipilä, P. Paasonen, T. Petäjä, S. Kim, T. Kurtén, F. Stratmann, V.-M. Kerminen and M. Kulmala, *Nature*, 2012, **488**, 193–196.

[349] V. Perraud, E. A. Bruns, M. J. Ezell, S. N. Johnson, Y. Yu, M. L. Alexander, A. Zelenyuk, D. Imre, W. L. Chang, D. Dabdub, J. F. Pankow and B. J. Finlayson-Pitts, *Proceedings of the National Academy of Sciences*, 2012, **109**, 2836–2841.

[350] W. Wang and S. Ye, *Phys. Chem. Chem. Phys.*, 2017, **19**, 4488–4493.

[351] Y. Ma, T. Luciani, R. A. Porter, A. T. Russell, D. Johnson and G. Marston, *Physical Chemistry Chemical Physics*, 2007, **9**, 5084.

[352] J. Buajarern, L. Mitchem and J. P. Reid, *Journal of Physical Chemistry A*, 2007, **111**, 9054–9061.

[353] Y. Wu and M. V. Johnston, *Environmental Science & Technology*, 2017, **51**, 4445–4451.

[354] F. K. A. Gregson, J. F. Robinson, R. E. H. Miles, C. P. Royall and J. P. Reid, *The Journal of Physical Chemistry B*, 2019, **123**, 266–276.

[355] C. Giorio, S. J. Campbell, M. Bruschi, F. Tampieri, A. Barbon, A. Toffoletti, A. Tapparo, C. Paijens, A. J. Wedlake, P. Grice, D. J. Howe and M. Kalberer, *Journal of the American Chemical Society*, 2017, **139**, 3999–4008.

[356] C. Yuan, Y. Ma, Y. Diao, L. Yao, Y. Zhou, X. Wang and J. Zheng, *Journal of Geophysical Research: Atmospheres*, 2017.

[357] V. G. Khamaganov and R. A. Hites, *The Journal of Physical Chemistry A*, 2001, **105**, 815–822.

[358] R. C. d. M. Oliveira and G. F. Bauerfeldt, *The Journal of Physical Chemistry A*, 2015, **119**, 2802–2812.

[359] D. M. Bell, D. Imre, S. T. Martin and A. Zelenyuk, *Phys. Chem. Chem. Phys.*, 2017, **19**, 6497–6507.

[360] A. A. Chew and R. Atkinson, *Journal of Geophysical Research: Atmospheres*, 1996, **101**, 28649–28653.

[361] T. Berndt, O. Böge and F. Stratmann, *Atmospheric Environment*, 2003, **37**, 3933–3945.

[362] D. Johnson and G. Marston, *Chemical Society Reviews*, 2008, **37**, 699.

[363] G. Socrates, *Infrared and Raman Characteristic Group Frequencies: Tables and Charts*, Wiley, 3rd edn., 2004, p. 366.

[364] M. S. Claflin, J. E. Krechmer, W. Hu, J. L. Jimenez and P. J. Ziemann, *ACS Earth and Space Chemistry*, 2018, **2**, 1196–1210.

[365] H. Kim and S. E. Paulson, *Atmospheric Chemistry and Physics*, 2013, **13**, 7711–7723.

[366] T. D. Vaden, D. Imre, J. Beranek, M. Shrivastava and A. Zelenyuk, *Proceedings of the National Academy of Sciences*, 2011, **108**, 2190–2195.

[367] Y. Iinuma, C. Müller, T. Berndt, O. Böge, M. Claeys and H. Herrmann, *Environmental Science & Technology*, 2007, **41**, 6678–6683.

[368] R. C. Hoffman, A. Laskin and B. J. Finlayson-Pitts, *Journal of Aerosol Science*, 2004, **35**, 869–887.

[369] B. Jing, Z. Wang, F. Tan, Y. Guo, S. Tong, W. Wang, Y. Zhang and M. Ge, *Atmospheric Chemistry and Physics*, 2018, **18**, 5115–5127.

[370] K. J. Heaton, M. A. Dreyfus, S. Wang and M. V. Johnston, *Environmental Science & Technology*, 2007, **41**, 6129–6136.

[371] C. Mohr, F. D. Lopez-Hilfiker, T. Yli-Juuti, A. Heitto, A. Lutz, M. Hallquist, E. L. D'Ambro, M. P. Rissanen, L. Hao, S. Schobesberger, M. Kulmala, R. L. Mauldin, U. Makkonen, M. Sipilä, T. Petäjä and J. A. Thornton, *Geophysical Research Letters*, 2017.

[372] S. Myriokefalitakis, M. Vrekoussis, K. Tsigaridis, F. Wittrock, A. Richter, C. Brühl, R. Volkamer, J. P. Burrows and M. Kanakidou, *Atmos. Chem. Phys.*, 2008, **8**, 4965–4981.

[373] B. M. Connelly, D. O. De Haan and M. A. Tolbert, *The Journal of Physical Chemistry A*, 2012, **116**, 6180–6187.

[374] J. Ye, J. P. D. Abbatt and A. W. H. Chan, *Atmospheric Chemistry and Physics*, 2018, **18**, 5549–5565.

[375] S. Rossignol, L. Tinel, A. Bianco, M. Passananti, M. Brigante, D. J. Donaldson and C. George, *Science*, 2016, **353**, 699–702.

[376] C. Cai, A. Marsh, Y.-H. Zhang and J. P. Reid, *Environmental Science & Technology*, 2017, **51**, 9683–9690.

[377] Y. Liu and P. H. Daum, *J. Aerosol Sci.*, 2008, **39**, 974–986.

Appendices

A. Analysis of MD Trajectories of Water in Sucrose

Sucrose - sucrose decorrelation time

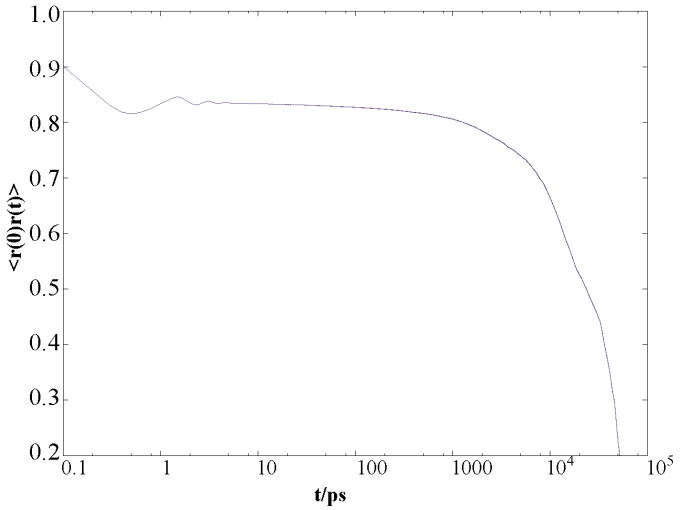

Figure 8.6.1: Position-position autocorrelation function of a single succrose molecule within one 1 μs simulation, showing very little motion in the interval 0.1 - 1000 ps. This plot suggests that it is reasonable to cluster the data (i.e. to determine potentials of mean force, as in Figure 5.1.4) in increments of 1 ns.

Comparison of experimental and computed MD densities

One sanity check that can be employed is to compare predicted and observed densities. The two sets of values may be the inverse of what the reader is expecting: the densities are *observed* from the simulations and the *predictions* are generated by a polynomial parametrisation of experimental data by Cai et al.[285]: Experiments performed on several dozen sucrose droplets were included in this paper and three functions were assessed to determine which represented the particle densities most effectively. A scatter plot of the equilibrium densities extracted from the trajectories are presented against these determinations in Figure 8.6.2, showing generally good agreement. While the more dehydrated simulation boxes tend to be slightly less dense than the single particle measurements predict them to be, the mean deviation is still very low (2.05%).

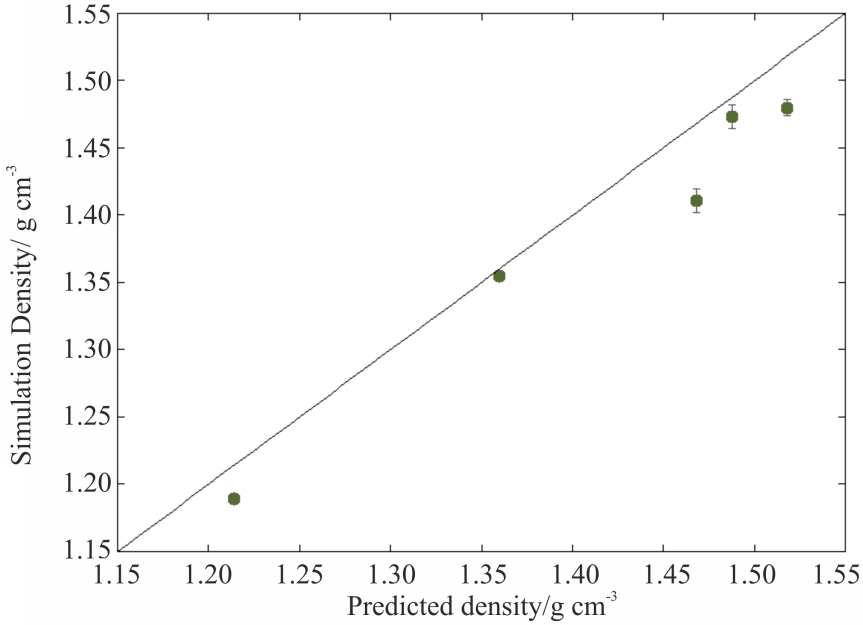

Figure 8.6.2: Comparison of simulation box densities (y axis) with a cubic parametrisation of sucrose aerosol (x axis) at the same water activities (calculated by equation 5.2.1). The black line denotes $y = x$. Error bars are calculated from the standard deviation of the simulation box density, and the fit error reported in the original publication respectively[285].

This gives us additional confidence in the data extracted from the trajectories.

Dynamic Heterogeneity in water displacement

The 95% by mole fraction sucrose simulation, which is the system with the highest proportion of confinement, was analysed to determine the extent of dynamic heterogeneity during the trajectory. Briefly, the positions of every oxygen atom belonging to the water molecules present in the box were plotted at intervals of one picosecond. Each is coloured according to its net displacement relative to its starting position, which was initialised at 20 ns through the 100 ns trajectory.

Two snapshots are presented in Figure 8.6.3, showing a range of displacements observed between the various water molecules within each frame. Unfortunately, computational constraints meant that only a small subset of the trajectory could be analysed in this manner.

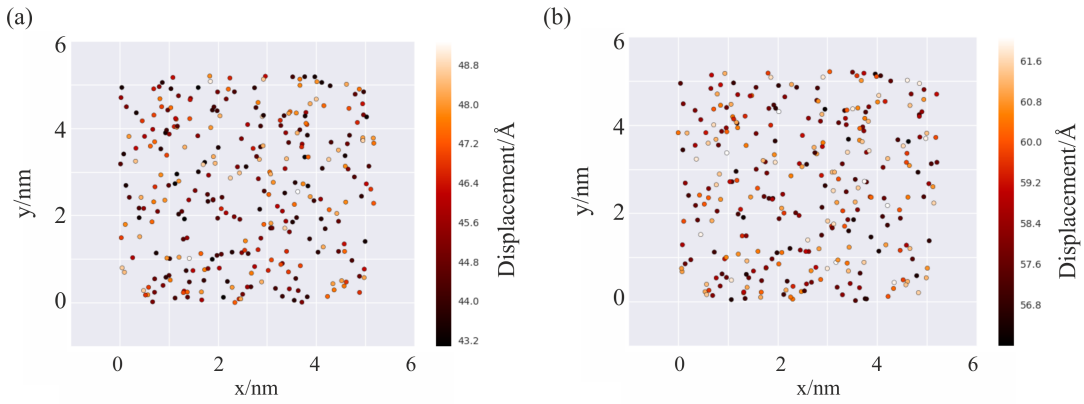

Figure 8.6.3: Water displacements calculated *per molecule* from their starting positions in a simulation with a sucrose mole fraction of 0.95. The frame presented in Panel (b) (168ps) shows a larger range within the MD frame than panel (a) (130 ps).

Several clusters of slow diffusing molecules are observed to remain less mobile for extended periods. It may be that the molecules experiencing confinement within cavities are those that that achieve the least displacement, although it is difficult to extrapolate from a small time frame. Crucially, these figures are reminiscent of theoretical work on glasses[294], and of fluorescence imaging of viscous aerosol[142]. In this sense, the analysis presented here further validates computational studies of this type as a legitimate method to investigate the dynamics of dehydrated organic systems.

B. Fickian Modelling of Viscous Aerosol

Fi-PaD modelling of water evaporation from sucrose

KM-GAP modelling of semivolatile evaporation from sucrose

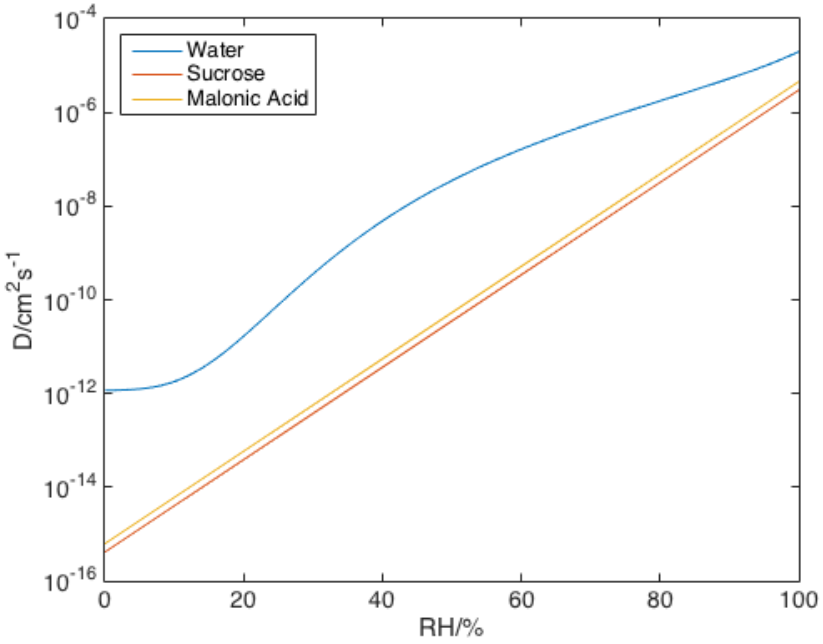

Figure 8.6.5: Composition dependent diffusion coefficients of the components of ternary particles. Water (blue) is taken from Figure 6.4.8(a). Sucrose and malonic acid (red, orange respectively) are determined using equation 5.1.1 in conjunction with viscosity data from Song et al.[139]

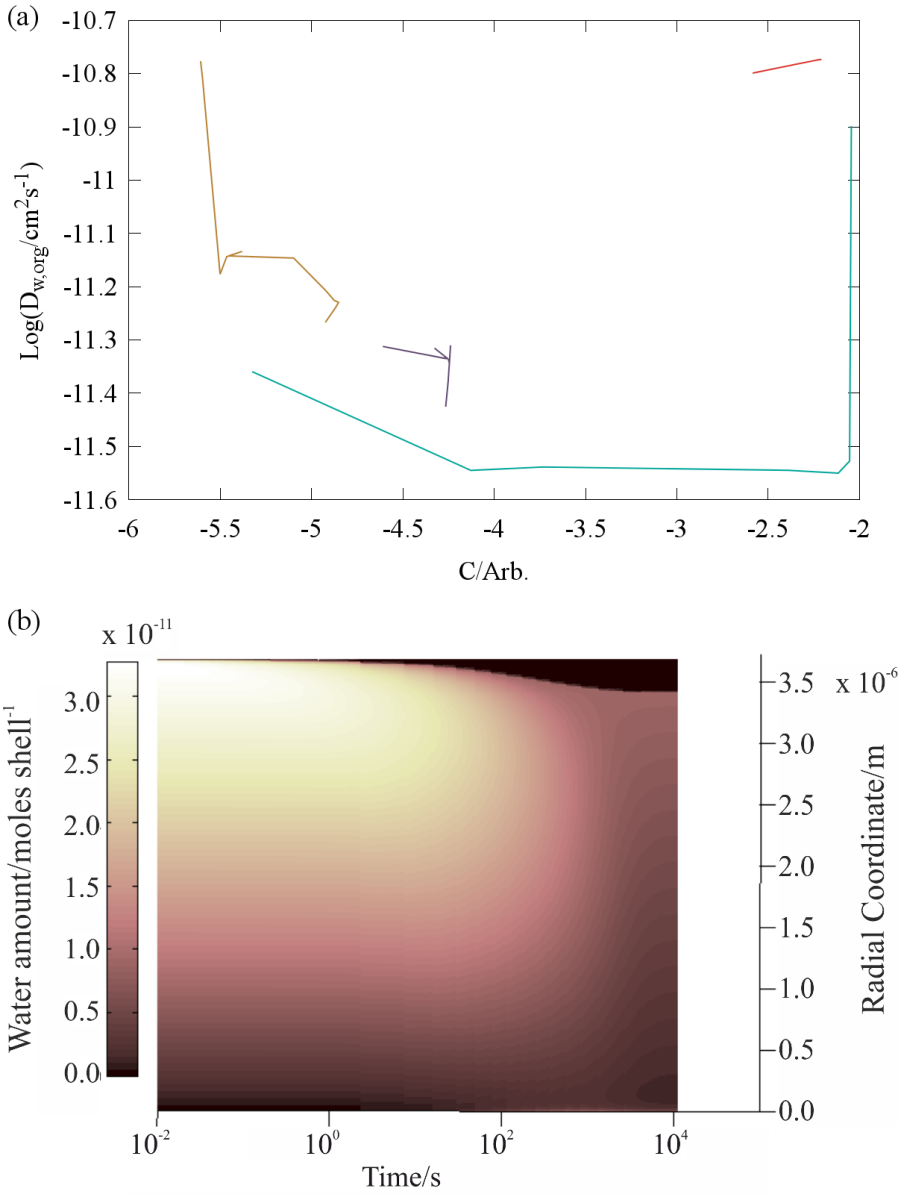

Figure 8.6.4: (a) Trajectories of four independent solvers through ($D_{w,org}$, C) space, converging to the lowest error solution of a Sucrose Glucose droplet experiencing an RH change of 52-18%, resulting in the radius prediction shown in the previous figure. The optimum solution is only found by the orange solver. (b) The internal concentration profile of the particle predicted according to the lowest error radius fit.

C. Corrected Refractive Indices for Ternary Organic Aerosol

The associated radii of both of these data sets were discussed in Section 7.5.3. The amount of water and semivolatile remaining in the particle was a key component of the analysis, as it allowed consecutive experiments conducted on the same particle to be modelled correctly. Refractive index can also be used as a proxy for droplet composition, and is extracted simultaneously during the fittting process. The Mie fit values for the raffinose + malonic acid system are shown in Figure 8.6.4. For comparison, a prediction of the refractive index of the organic mass at the starting ratio is shown, across the same range in water activity. The prediction relies on mixing rules that extrapolate the mass density into the supersaturated regime accesses in the aerosol state[376], and then sum the molar refractions of the constituent solutes[377]. Here the starting molar ratio of semivolatile to nonvolatile, 3:2, was used in the calculation. Both the initial values of m are shown, for a spectrum wavelength of 645 nm, and the corrected values for the prediction wavelength of 589 nm. The correction was done in the way described in section 3.2.5.

While the prediction and the observed data points both increase from high to low RH, beyond this there is little agreement, especially between 40 and 80%. In this humidity region, many of the particles exhibit refractive indices lower than the prediction, which may be the result of residual water trapped within them. It is tempting to say that the water will be trapped in the core, but the fact that it seems to be affecting the whispering gallery mode positions (and hence the experimentally determined refractive index) strongly implies the excess water is at least partly near the surface. Such a phenomenon has been described in the thesis of Andrew M.J. Rickards, in very long experiments dehydrating sugar droplets[268], in which he found that equilibrium is not achieved on any reasonable timescale and there is always residual water in viscous aerosol. The values which are not corrected for dispersion were fit by the core-shell model, running in homogeneous mode, which operated with a fixed dispersion term during calculations.

Values for malonic acid in sucrose are also shown in Figure 8.6.5, and there is much better agreement with the prediction. The red points are the same values as those plotted as colours in Ingram et al. 2017[303], Figure 9.

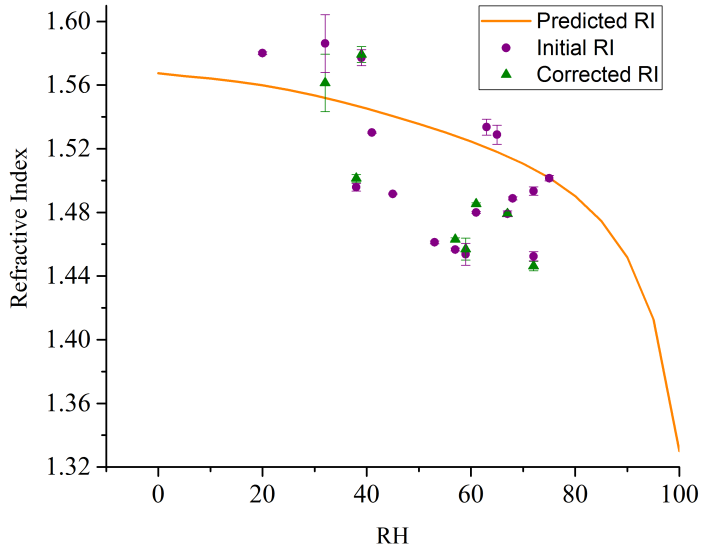

Figure 8.6.6: Mie fit refractive indices (points) of particles containing raffinose and malonic acid. Molar refraction predictions for the starting molar ratio of 3:2, at an incident wavelength of 650nm is shown in orange.

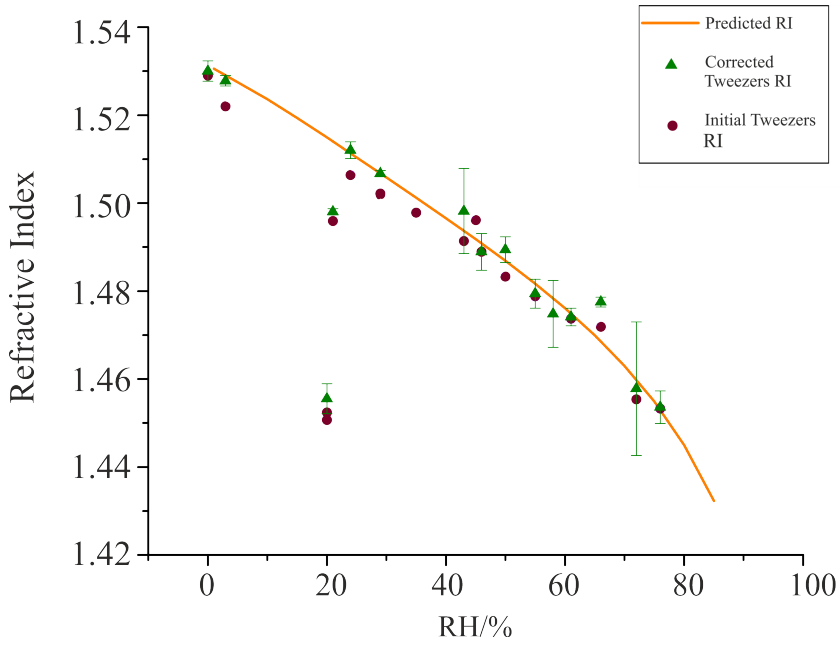

Figure 8.6.7: Mie fit refractive indices (points) of particles containing sucrose and malonic acid. Molar refraction predictions for the starting molar ratio are also (yellow line).